

**ELECTRON AND PHONON TRANSPORT IN NANOSTRUCTURED
EXFOLIATED GRAPHENE NANOPATELETS AND ITS POTENTIAL IN
THERMAL ENERGY CONVERSION**

By

Jinglei Xiang

A DISSERTATION

**Submitted to
Michigan State University
in partial fulfillment of the requirements
for the degree of**

DOCTOR OF PHILOSOPHY

Materials Science and Engineering

2012

ABSTRACT

ELECTRON AND PHONON TRANSPORT IN NANOSTRUCTURED EXFOLIATED GRAPHENE NANOPATELETS AND ITS POTENTIAL IN THERMAL ENERGY CONVERSION

By

Jinglei Xiang

Graphene nanoplatelets (GNP), produced from microwave assisted thermal exfoliation of graphite intercalated compounds, possess exceptional electrical and thermal properties thanks to the well preserved conjugation in the graphene basal plane as a result of this production method. The potential of these intriguing physical properties can only be realized if these nanoparticles are assembled on a macroscopic scale. However, numerous interfaces thus created between nanoparticles could have a large impact on the physical properties of GNP based nanocomposites. This research is dedicated to the investigation of the difference of electron and phonon transport at the interfaces and how to make use of this unique distinction to nanostructure and assemble GNP for thermoelectric application which requires a high electrical to thermal conductivity ratio σ/κ as well as high Seebeck coefficient S of the material.

In the first part of the discussion, the effect of incorporating GNP into a polymer to improve its electrical and thermal conductivity is discussed. It is found that there are distinct property enhancements around percolation threshold in the nanocomposites originating from the different mechanisms of electron and phonon transport across the GNP/polymer interface. In order to take full advantage of the excellent in-plane physical properties of GNP, a highly

ordered, highly flexible binder free GNP paper was prepared by a simple filtration technology and annealing that shows much enhanced electrical and thermal conductivity.

The second part of this research is dedicated to separation of electron and phonon transport in GNP paper by various nanostructuring techniques in order to enhance σ/κ ratio. In the first approach, monodispersed metal nanoparticle spacers were synthesized on the surface of GNP particles. The Au/GNP hybrid film prepared by filtration shows decoupled electron and phonon transport. As a result, the in-plane electrical conductivity increased by 70% while a 7% reduction in thermal conductivity was observed in comparison to a neat GNP paper. In the second approach, polyaniline (PANI) was synthesized by in-situ chemical oxidative polymerization in the presence of GNP where GNP served as a template for nucleation and growth of PANI. Depending on the composition and protonation ratio of PANI, σ/κ increased from 2.5 for neat GNP paper to 4.7 for the as-made PANI/GNP and further to 11 for the reprotionated PANI/GNP film. The optimal thermoelectric properties was achieved at a protonation of 0.2 with approximately 40wt% of PANI in the nanocomposite, reaching an electrical conductivity of 59 S/cm, a thermal conductivity of 12W/mK and a Seebeck coefficient of 33 $\mu\text{V/K}$ at 300K. In the third approach, three dimensional folding of a core-shell nanostructure based on PANI/GNP paper was adopted to take advantage of the high anisotropic conduction in a GNP paper, its high flexibility and foldability, but more importantly the strong phonon scattering at the corner of the folds as compared to a much lower disruption in the electron flow.

Taken together, the ability to produce and nanostructure these inexpensive graphene nanoplatelets opens up numerous opportunities for the development of plastic thermoelectrics in the future.

**Copyright by
Jinglei Xiang
2012**

To my parents and beloved fiancée Weijun Lu

ACKNOWLEDGEMENTS

First of all, I would like to express my sincere gratitude to my research advisor Prof. Lawrence. T. Drzal for his continuous and kind support, patience and guidance throughout my study. It has been a wonderful experience working in Prof. Drzal's research group and I benefited a lot from his personal suggestions and words of encouragement.

I would also like to thank my committee member Prof. Don Morelli for his support and guidance during my graduate studies. I learned a great deal from discussing my research with him. Likewise, I am also grateful for Prof. Neil Wright, Prof. Jeff Sakamoto and Prof. Phillip Duxbury for their kind support and valuable advice for me as my committee members.

I thank all the staff members in CMSC, Mike Rich, Per Askeland, Brian Rook, Ed Drown, Wanjun Liu, Hwanman Park, Hazel-Ann Hosein, Saswata Bose, Inhwan Do, Hiroyuki Fukushima, Xiaobing Li as well as Karen Lillis, Inger Weitlauf for their generous assistance to my research.

I am also deeply thankful to my officemates and friends who have shared time with me during my graduate study and shared with me their joys and sorrows in our lives. Special thanks go to Anchita Monga, Xian Jiang, Deb Saha, Dee Rollins, Yan Li, Pat Aderhold, Tao Wang, Huang Wu, Sanjib Biswas, Kevin Zhou, Chang Liu, Shaowen Ji, Leyun Wang, Xueling Fei and Dafei Kang.

Lastly, I would like to thank my parents and my beloved fiancée for their unconditional love and support in the course of my life. My life is full of hope and joy with you around.

TABLE OF CONTENTS

LIST OF TABLES	xi
LIST OF FIGURES	xii
Chapter 1 Introduction and Background	1
1.1 The rise of graphene:	1
1.2 An alternative material: exfoliated graphene nanoplatelets (GNP).....	4
1.3 Multifunctional graphene-based polymer nanocomposites (electrical and thermal properties)6	
1.3.1 Electron transport:	10
1.3.2 Phonon transport:.....	13
1.4 Bi-continuous paper like graphene based nanocomposites	16
1.5 Background in thermoelectric energy conversion materials:.....	17
1.6 Motivation and objective of research:.....	21
References:.....	23
Chapter 2 Investigation of GNP in Improving the Thermal and Electrical Conductivity of Paraffin Wax and Its Use in Thermal Energy Storage	32
2.1 Abstract:.....	32
2.2 Introduction.....	32
2.3 Experimental:	34
2.4 Characterization:	36
2.5 Results and discussions:.....	40
2.5.1 Morphology	40
2.5.2 Electrical conductivity of paraffin/GNP nanocomposites:.....	43
2.5.3 Thermal conductivity paraffin/GNP nanocomposites:.....	44
2.5.4 Thermal interface resistance:.....	46
2.5.5 Effect of GNP particles on other thermo physical properties of nanocomposites:	51
2.5.6 Thermal gravimetric analysis:	52

2.6 Conclusions:.....	54
Acknowledgements.....	55
References.....	56

Chapter 3 Thermal Conductivity of a Monolayer of Exfoliated Graphene Nanoplatelets Prepared by Liquid-Liquid Interfacial Self-Assembly..... 59

3.1 Abstract:.....	59
3.2 Introduction.....	60
3.3 Experimental details:	61
3.4 Results and discussions:.....	63
3.4.1 Scanning electron microscopy:.....	63
3.4.2 Optical Transmission and Absorption of GNP Monolayers:.....	66
3.4.3 Confocal Micro-Raman Spectroscopy Analysis:	68
3.4.5 Calculation of the Thermal Conductivity of GNP Monolayers:.....	70
3.5 Conclusions:.....	73
Acknowledgement:	74
References:.....	76

Chapter 4 Thermal Conductivity of Exfoliated Graphene Nanoplatelet Paper 78

4.1 Abstract.....	78
4.2 Introduction:.....	78
4.3 Experimental.....	80
4.4 Results and discussions:.....	83
4.4.1 Morphology	83
4.4.2 Thermogravimetric analysis of GNP paper	88
4.4.3 Thermal diffusivity and thermal conductivity of GNP paper under various treatments	89
4.5 Conclusions:.....	94
References.....	97

Chapter 5 Electron and Phonon Transport in Gold Nanoparticle Decorated Graphene Nanoplatelet Nanostructured Paper	99
5.1 Abstract:	99
5.2 Introduction:	99
5.3 Experimental:	102
5.4 Results and discussions:	104
5.4.1 Morphology	104
5.4.2 Thermal diffusivity and thermal conductivity of Au/GNP hybrid paper	113
5.4.3 Electrical properties of Au/GNP hybrid paper	119
5.5 Conclusion:	123
Supporting information	125
References	130
Chapter 6 Templated Growth of Polyaniline on GNP and Its Thermoelectric Properties	134
6.1 Abstract:	134
6.2 Introduction:	134
6.3 Experimental:	137
6.4 Results and discussions:	143
6.4.1 Synthesis of PANi/GNP and characterizations:	143
6.4.2 Thermoelectric properties of PANi/GNP:	157
6.4.3 Effect of protonation on thermoelectric properties of PANi/GNP nanocomposites: ..	164
6.5 Conclusion:	168
Acknowledgement:	169
References	170
Chapter 7 Improving Thermoelectric Properties of Exfoliated Graphene Nanoplatelets Paper by Folding	174
7.1 Abstract:	174
7.2 Introduction:	174
7.3 Experiments:	176
7.4 Results and discussions:	181

7.4.1 GNP paper folded	181
7.4.2 Electronic conduction of the folded paper.....	186
7.4.3 Folded PANi/GNP paper as a p-type thermoelectric material	188
7.5 Conclusion:	196
References:.....	197
Chapter 8 Summary and Recommended Studies	200
8.1 Summary:.....	200
8.2 Recommended future works:	204
8.2.1 Solvent processing of PANi/GNP:	204
8.2.2 Carrier transport analysis for PANi/GNP:.....	205
References:.....	208

LIST OF TABLES

Table 2-1: Heating and cooling characteristics of GNP-15 composite PCM (average of three samples)	52
Table 2-2: Heating and cooling characteristics of GNP-1 composite PCM (average of three samples)	52
Table 4-1: Density variation of GNP paper under different conditions.....	90
Table 5-1: Average densities of GNP and Au/GNP hybrid papers measured as-made, annealed, annealed & cold compacted (standard deviation < 0.05g/cm ³).	113
Table 6-1: Typical atomic percentage of nitrogen and chlorine species on PANi/GNP samples at different protonations prepared at 0.05M aniline and estimation of the protonation level.....	152
Table 6-2: The thermoelectric properties, σ/κ and ZT of neat PANi, neat GNP and PANi/GNP (50mM aniline, as-made) and PANi/GNP(50mM aniline, reprotonated) at room temperature.	168
Table 7-1: Electrical resistance measurement on the folded paper (1 fold between voltage probes)	187
Table 7-2: Electrical resistance measurement on the folded paper (2 folds between voltage probes).....	187
Table 7-3: Electrical conductivity of the folded PANi/GNP paper with and without compaction	192

LIST OF FIGURES

Figure 1-1: Electrical percolation, as applied to conductive composites. The formation of the first complete particle linkage results in a significant drop in resistivity at V_c . For interpretation of the references to color in this and all other figures, the reader is referred to the electronic version of this dissertation.	13
Figure 1-2: Schematic representation of Seebeck effect when a sample is subjected to a temperature gradient, in this case, holes are the dominant carriers.	18
Figure 1-3: Schematic representation of a thermoelectric uncouple consisting of a p and n type semiconductor materials connected electrically in series and thermally in parallel operating under power generation mode (left) or refrigeration mode (right)	19
Figure 2-1: (a) Photograph of the customized aluminum mold; (b) Photograph of Bolling two roll mill; (c) Scheme for the sample preparation routes: casting and two roll milling.....	35
Figure 2-2: (a) Schematics for in plane thermal conductivity measurement of the two roll milled sample; (b) Photograph of the sample prepared from compressing the two roll milled sheets to a desired thickness (1 inch) and a circular cross section of that was produced by a punch.	39
Figure 2-3: a: 4wt% GNP-1/paraffin by casting; b: 4wt% GNP-15/paraffin by casting; c: 4wt% GNP-15/paraffin by two roll mill; d: 10wt% GNP-15/paraffin by two roll mill; e: enlarged edge view of the nanoplatelets (scale bar 100 nm); f: enlarged edge view of one platelet (scale bar: 10 nm)	41
Figure 2-4: Electrical resistivity of GNP/paraffin composite PCM.....	44
Figure 2-5: (a) Through plane thermal conductivity of GNP/paraffin prepared by casting; (b) Through-plane (left column) and in-plane (middle column) thermal conductivity of GNP-15/paraffin prepared by two roll mill and through-plane thermal conductivity by casting (right column).	45
Figure 2-6: overview of the dominate factors in interfacial thermal conductance in carbon based nanocomposites as well as possible techniques to reduce interface resistance. Adapted from ref. 15.....	47
Figure 2-7: Thermal conductivity of paraffin/GNP-15 fitted with effective medium theory below electrical percolation.....	50
Figure 2-8: (a) TGA analysis of GNP-1/paraffin nanocomposites in N_2 . (b) TGA analysis of GNP-15/paraffin nanocomposites in N_2	53
Figure 3-1: (a) SEM image of a LSA GNP monolayer film supported on a glass substrate. (b) SEM image of a HSA GNP monolayer film supported on a glass substrate.....	65

Figure 3-2: Percent transmission of light for LSA and HSA monolayers scanning from 350 nm to 1000 nm. Inset is the photo of LSA and HSA coated monolayers supported on glass substrates as well as the blank slide.....	66
Figure 3-3: Raman G band shift of GNP with temperature and linear curve fitting with Microsoft Excel. Two measurements were conducted indicated by blue and red marks.....	67
Figure 3-4: (a) Raman G peak shift of the LSA monolayer at different laser power levels. (b) Raman G peak shift of the HSA monolayer using different laser power levels.	69
Figure 3-5: (a) Local temperature of an individual GNP at the center of a LSA monolayer vs. the absorbed laser power with x50 and x100 objectives. The solid lines represent the linear curve fittings. (b) Local temperature of an individual GNP at the center of a HSA monolayer vs. the absorbed laser power with x50 and x100 objectives. The solid lines represent the linear curve fittings.	72
Figure 4-1: Typical Raman spectrum of GNP particles showing D peak, G peak and 2D peak. .	81
Figure 4-2: Schematic representation of the GNP paper making process by vacuum assisted self assembly and actual photos of GNP paper peeled off the ANODISC filter paper after drying. ..	84
Figure 4-3: (a) SEM micrographs of cross section of the as-made GNP-15 paper (scale bar: 10 μm), (b) annealed and cold pressed GNP-15 paper (scale bar: 10 μm), (c) as-made GNP-1 paper (scale bar: 5 μm), (d) annealed and cold pressed GNP-1 paper (scale bar: 1 μm).	85
Figure 4-4: (a): TGA weight loss curves of GNP-15 paper before and after annealing, (b) TGA weight loss curves of GNP-1 paper before and after annealing.....	88
Figure 4-5: (a) Through-plane thermal diffusivity of GNP-1 and GNP-15 papers. (b) Through-plane conductivity of GNP-1 and GNP-15 papers. (c) In-plane diffusivity of GNP-1 and GNP-15 papers. (d) In-plane conductivity of GNP-1 and GNP-15 papers. (note: left column represents GNP1, right column represents GNP15)	92
Figure 5-1: Schematics of experimental procedures and the interactions between the metal ions and the active sites on PEI coated GNP and formation of Au nanoparticles.....	105
Figure 5-2 (a): Low magnification SEM image of Au nanoparticle decorated GNP prepared at 0.3wt% PEI concentration (scale bar: 1 μm). b: High magnification SEM image of Au nanoparticle decorated GNP prepared at 0.3wt% PEI (scale bar: 100 nm) c: Low magnification SEM image of Au nanoparticle decorated GNP prepared at 0.6wt% PEI concentration (scale bar: 1 μm). d: High magnification SEM image of Au nanoparticle decorated GNP prepared at 0.6wt% PEI concentration (scale bar: 100nm).....	107
Figure 5-3: (a) Size and distribution of Au nanoparticles on GNP prepared at 0.3wt% PEI concentration. (b) Size and distribution of Au nanoparticles on GNP prepared at 0.6wt% PEI concentration.	109

Figure 5-4: Schematics of the experiment showing the Au nanoparticle decorated GNP dispersed in water for subsequent vacuum assisted self assembly.	110
Figure 5-5: Photos of the as-made GNP paper showing flexibility and mechanical robustness under bending and the Au/GNP hybrid sample used for thermal diffusivity measurement (1 inch diameter)	111
Figure 5-6: (a) Representative cross sectional SEM image of “as-made” GNP paper (scale bar: 5 μm). (b) as-made Au/GNP hybrid paper prepared at 0.3wt% PEI (scale bar: 5 μm).	111
Figure 5-7: (a) Through-plane thermal diffusivity of GNP and Au/GNP paper. b: Through-plane thermal conductivity of GNP and Au/GNP paper. c: In-plane thermal diffusivity of GNP and Au/GNP paper. d: In-plane thermal conductivity of GNP and Au/GNP paper. Note: left column represents GNP15, middle column represents GNP15/Au(0.3wt% PEI), right column represents GNP15/Au(0.6wt% PEI)	116
Figure 5-8: (a) In-plane electrical conductivity of anneal & cold compacted GNP and Au/GNP paper. (b) Through-plane electrical resistivity of anneal & cold compacted GNP and Au/GNP paper.....	121
Figure 5-9: TGA curve of neat PEI in air	125
Figure 5-10: TGA curves of annealed GNP paper, as-made GNP paper and as-made Au/GNP paper in air.	126
Figure 5-11: Example SEM images analyzed by Image-Pro to determine the distribution of nanoparticle size (scale bar 100nm).....	127
Figure 5-12: Particle size distribution obtained from Figure 5-11.	128
Figure 5-13: Schematic representation of through-plane resistivity measurement of thin film sample	129
Figure 6-1: A schematic representation of replacing the Au nanoparticle spacers in the highly ordered GNP paper with a layer of polymer.	135
Figure 6-2: Schematic representation of the experimental setup for measuring the Seebeck coefficient and thermal conductivity of thin film sample. Inset is the photo of the actual sample mounted to the "L-shaped" copper block.....	141
Figure 6-3: Schematic representation of in-situ polymerization of aniline in the presence of GNP particles and a photo showing the flexibility of the final nanocomposite film.....	145
Figure 6-4: (a,b) SEM micrographs of neat polyaniline salt showing the granular structure and small needle-like nanostructure growing out of the surface. (c,d) surface morphology of PANi/GNP particles (in-situ polymerization of aniline in the presence of GNP particles in 1M HCl at 0.03M aniline). (e,f) surface morphology of PANi/GNP particles (in-situ polymerization of aniline in the presence of GNP particles in 1M HCl at 0.05M aniline).	146

Figure 6-5: a: TGA of neat polyaniline salt, neat GNP, and PANi/GNP synthesized at 0.03M and 0.05M initial concentration of aniline. b: Derivative of weight loss vs. temperature for neat PANi, neat GNP, and PANi/GNP synthesized at 0.03M and 0.05M initial concentration of aniline. ... 150

Figure 6-6: (a) Regional scans of N1s core-level spectra of as-made polyaniline salt showing the presence of imine nitrogen(-N=), amine nitrogen (-NH-) and positively charged nitrogen (N^+) (b): regional scan of Cl2p core-level spectra of as-made polyaniline salt showing Cl anions. (c): regional scans of N1s core-level spectra of as-made PANi/GNP prepared at 0.05M of aniline. (d): regional scans of Cl2p of PANi/GNP(0.05M). 153

Figure 6-7: Raman shift of neat PANi powder, neat GNP film and the as-made PANi/GNP film prepared at 50mM aniline concentration. 157

Figure 6-8: (a) Seebeck coefficient of GNP/PANi nanocomposites prepared at different aniline concentrations (0.03M and 0.05M) as well as the performance for neat GNP paper and neat polyaniline salt measured from 200K to 300K. (b). Thermal conductivity of GNP/PANi (0.03M and 0.05M) as well as neat GNP paper and neat polyaniline salt from 200K to 300K. 160

Figure 6-9: (a) Proposed polymerization process for polyaniline in the absence of GNP and the charge transport mechanism by inter and intrachain hopping. (b) Proposed polymerization of PANi in the presence of GNP and the proposed charge transport mechanism in the composites. 162

Figure 6-10: Electrical conductivity of GNP/PANi (0.03M and 0.05M) as well as neat GNP paper and neat polyaniline salt at room temperature. 163

Figure 6-11: (a) Seebeck coefficient of PANi/GNP prepared at 0.05M aniline with different protonation levels. (b) Thermal conductivity of PANi/GNP (50mM) with different levels of protonations..... 165

Figure 6-12: Electrical conductivity of PANi/GNP samples prepared at 0.05M aniline with different protonation ratio. 167

Figure 7-1: Schematic representation of experimental procedures to prepare PANi coated GNP paper by rapid mixture polymerization..... 176

Figure 7-2: custom made mold for paper folding, and stacking of folded paper strips into desired thickness for subsequent measurements. 178

Figure 7-3: (a) schematic representation of experiment setup for Seebeck coefficient, thermal conductivity, electrical conductivity measurement for the folded sample. (b) a photo of the folded PANi/GNP paper mounted on the cryostat before measurement. 179

Figure 7-4: schematic representation of electron transport within the folded paper, the air gaps between individual fold is exaggerated..... 182

Figure 7-5: Photos of flat GNP paper, GNP paper cut to strips, folding the GNP strips on the custom-made acrylic mold, and the folded paper.(from top left to bottom right) 183

Figure 7-6: (a) SEM micrographs of a folded strip at low magnification (scale bar: 1mm), (b) the convex side of the folding edge (scale bar: 100 μ m), (c) the concave side of the folding edge (scale bar: 100 μ m), (d) a magnified view of the tip of the folding edge (scale bar: 20 μ m)..... 184

Figure 7-7: (a) Photos of four-point electrical resistance measurement on the slightly folded GNP paper and (b) a heavily folded GNP paper with one fold between the voltage probes..... 186

Figure 7-8: (a) Photo of the as-synthesized PANi/GNP paper (5 cm \times 5 cm). (b) An overview of the surface morphology of PANi/GNP paper by SEM (scale bar: 10 μ m). (c) SEM micrograph of PANi nanofibrils grown on the surface of GNP (scale bar: 100 nm). (d) folding edge of the PANi/GNP paper showing the interconnected "core" (scale bar: 100 μ m). 189

Figure 7-9: TGA analysis of the as synthesized PANi/GNP paper and the neat polyaniline in air. 191

Figure 7-10: (a) Seebeck coefficient of the folded PANi/GNP paper (pressed vs. unpressed) from 270K to 320K (b) Thermal conductivity of the folded PANi/GNP paper (pressed vs. unpressed) from 270K to 320K..... 193

Figure 7-11: schematic representation of the folded paper for estimating the bulk electrical conductivity and mathematic derivation. 194

Figure 8-1: Schematics and actual photo of the quantum design versalab module and wiring, CH1 measures the Hall voltage, CH2 measures the in-plane resistivity of the sample. z direction: coming out of the paper. 206

Chapter 1 Introduction and Background

1.1 The rise of graphene:

Graphene consists of a single layer of atomic carbon arranged in a honeycomb lattice structure. Although graphene has been known for over one hundred years, the recent attention given to graphene is largely due to the Nobel Prize winning work by Geim and Novoselov in 2004 [1-5]. The graphene structure is the building block for graphitic carbon materials of all other dimensionalities (such as 0D buckyball, 1D carbon nanotubes and 3D graphite). Ever since its discovery, graphene or few-layer graphene (FLG) quickly attracts great interest from research communities all over the world. It has been shown that graphene has exceptional electrical, thermal and mechanical properties. For example, it is one of the strongest materials with a Young's modulus exceeding 1 TPa [6]. An ideal graphene sheet has extremely high electrical conductivity and it was shown that charge carriers behave like massless Dirac Fermions with carrier mobility measured between 3000 and 10,000 cm²/Vs at room temperature [7,8]. Thermal conductivity of graphene, measured by a non-contact optical method, is reported to reach values of up to $(5.3 \pm 0.48) \times 10^3$ W/mK [9]. Research conducted in the past few years has shown great promise for the use of graphene in multifunctional composites, electrochemical energy storage and electronics, as well as in dye sensitized solar cells [10-13]. It is expected that this novel lightweight nanomaterial will have a huge impact on our society given all these possible technological applications demonstrated so far.

Large-scale, economical production of graphene or FLG is a significant challenge for its wide spread application. Currently, there are four major routes to synthesize graphene or FLG. First, graphene has been prepared by micromechanical cleavage from a highly oriented pyrolytic

graphite (HOPG). This is also widely known as the "scotch tape" method in which a single sheet of graphene is lifted from the HOPG because of the weak van der Waals interaction between adjacent graphene sheets in bulk graphite [2]. Second, graphene has been grown by chemical vapor deposition of hydrocarbons on a metal substrate (such as Ni and Cu) [14,15]. Third, epitaxial graphene was grown on single-crystal silicon carbide by vacuum graphitization [16]. Last, a colloidal suspension of graphene sheets can be prepared by converting graphite to graphite oxide (GO) followed by reduction with strong reducing agents. Among all these methods, the "scotch tape" method is capable of producing high quality graphene, but the yield is extremely low. It is not a suitable method to adopt if a large quantity of graphene is needed. The chemical vapor deposition and vacuum graphitization methods are energy intensive, producing single or FLG with a large size best suited for the electronics industry [17,18].

Production of graphene through reduction of GO is a popular route because of its high yield. GO is produced by an oxidative treatment of graphite using a method developed by Hummers, which is less time consuming and hazardous compared with earlier approaches [19]. In general, oxidation of graphite is accomplished by treating graphite with a water-free mixture of concentrated sulfuric acid, sodium nitrate and potassium permanganate. It takes less than two hours to complete the oxidation at a temperature less than 45°C given reasonable safety precautions during the process. After oxidation, the interlayer distance between adjacent graphene sheets expands as a result of accommodation of various oxygen functional groups such as the epoxide, hydroxyl as well as carbonyl and carboxyl groups introduced during oxidation [20]. Depending on the degree of drying, the interlayer distance varies from 0.63 nm for dried GO to 1.2 nm for hydrated GO [21,22]. Oxidation transforms the highly hydrophobic graphene basal plane to a more hydrophilic derivative. Therefore, it is also reasonable to think of GO as a

graphite intercalation compound with covalently bound oxygen and non-covalently bound water molecules between graphene layers. The increased hydrophilicity of GO makes it easy to disperse it in water with ultrasonication.

Much research has been done in reducing GO chemically to graphene [23]. One of the most commonly reported methods is chemical reduction of GO in the presence of strong reducing agents such as hydrazine monohydrate, sodium borohydride (NaBH_4) etc. During the reduction process, the yellow brown color of GO dispersion gradually turned black due to elimination of oxygen functional groups and partial restoration of sp^2 carbon. The basal plane becomes increasingly hydrophobic and eventually precipitated out forming irreversible agglomerates as a result of strong van der Waals force between individual graphene. The resulting graphene agglomerates appear to be insoluble in water and organic solvents, making further processing rather difficult [24]. The restacking of graphene sheets can be effectively prevented if a charged polyelectrolyte such as PSS (polystyrenesulfonate) or a small organic molecule (e.g. pyrenebutyric acid) is present during the reduction process [25,26]. The adsorption of the polyelectrolyte or small molecules on the basal plane of graphene surface due to π electron interaction overcomes the strong van der Waals force between graphene sheets. However, foreign stabilizers are not always desirable in many applications. Recently, Li et al found that GO reduced by hydrazine can be electrostatically stabilized by the negatively charged carboxylic acid group without using a polymer or a surfactant and the same functional group which may not be easily reduced by hydrazine can facilitate the dispersion of reduced graphene oxide (RGO) given careful control over the pH of the solution as well as the initial concentration of GO [27].

Apart from colloidal reduction of GO to graphene using strong reducing agents, thermal treatment of GO is another route to produce thin graphene nanosheets. Rapid heating to 1050°C (>2000 °C/min) resulted in expansion and delamination of GO caused by vaporization of intercalated water molecules and thermal pyrolysis of oxygen containing functional groups [28-31]. The functionalized graphene sheets produced by this method have similar C/O ratio (C/O:10.3 by elemental analysis) to graphene reduced in the presence of hydrazine. However, it is expected that structural defects formed during the exfoliation process, leaving behind numerous vacancies on the RGO sheet which might adversely affect its properties.

After the reduction, the change of color from yellow brown typical of GO to black indicates partial restoration of electronic conjugation in the reduced material, making it electrically conductive. Jung et al. measured the electrical conductivity of individually reduced graphene oxide with three different reduction routes (i.e. vacuum annealing, hydrazine reduction or a sequential combination of the two). It is found that an additional thermal treatment led to a further reduction in the degree of functionalization and dramatically increased the electrical conductivity. The reported range of electrical conductivity of these individually reduced GO is only 33-85 S/m [32]. One of the reasons for this low level of conductivity is the remaining oxygen groups clustering into rows and islands, resulting in graphitic regions intermixed with islands of oxygen-functionalized species [33]. These point defects act as scattering centers, changing the ballistic transport of electrons to a "hop-like" transport similar to electron tunneling.

1.2 An alternative material: exfoliated graphene nanoplatelets (GNP)

The unique properties of graphene are likely to be compromised because of the irreversible structural damages incurred during oxidation and reduction process of GO. It is by

far almost impossible to restore the perfect sp^2 carbon in the basal plane of graphene once graphite has been oxidized. Researchers are currently investigating alternative routes to produce thin sheet of graphene while still maintaining the strong and robust carbon scaffold intact during the production process. Research led by Drzal et al. has successfully produced exfoliated graphene nanoplatelets (GNP) of tens of nanometers in thickness and 100-10000 nm in diameter using a microwave assisted thermal exfoliation followed by pulverization [34,35]. The idea is similar to splitting graphite oxide to produce functionalized graphene sheet. In this case, the starting material is graphite intercalated compound (GIC). The intercalates are usually a combination of nitric and sulfuric acids at certain proportion. The advantage of using microwave irradiation instead of conventional furnace is that graphite is an excellent microwave absorber and heats instantly. The rapid heating rate caused vaporization of intercalated acids giving rise to a huge pressure that overcomes the interlayer van der Waals interaction. The volume of the exfoliated graphite is several hundred that of the original GIC and is known as "worm". The accordion-like worms that are several hundred micrometers were then broken down to smaller nanoplatelets by controlled combination of ultrasonication and ball milling. The diameter of GNP after ultrasonication for 2 h is reduced to approximately 15 μm known as GNP-15. GNP-15 can be further downsized to approximately 1 μm or less with rotary ball milling for 72 h. The thickness of individual nanoplatelets is less than 10 nm as measured by TEM. The surface area of GNP was measured by Brunauer-Emmet-Teller (BET) using N_2 adsorption at 77K which is approximately 20-40 m^2/g for GNP-15 and 100-130 m^2/g for GNP-1. Although these particles consist of multiple layers of graphene, It still has an extremely large length-to-thickness ratio which can be very desirable in many applications. Most importantly, the intercalation and exfoliation process leave the basal plane of graphene intact as evidenced by very high C/O ratio

in X-ray photoelectron spectroscopy (XPS) and Raman spectroscopy. It is reasonable to expect that the intrinsic properties of graphene such as electrical and thermal conductivity persist in these nanoplatelets.

While the single or few-layer graphene has promising application in electronics industry due to their unique band structure (zero bandgap) that can be tuned by applying a gate bias [36,37], the band structure of as-produced GNP particles approaches that of the bulk graphite, which might restrict its application in electronics. However, the ease of mass production at a relatively low cost of these GNP particles might find its entry point to the market through composites application, much earlier than all other graphene nanomaterials. Multifunctional graphene-based polymer composites is one of the most exciting research topics during the past decade because of their tremendous potential in various technological applications.

1.3 Multifunctional graphene-based polymer nanocomposites (electrical and thermal properties)

Polymers and their composites have found wide spread applications in automobiles, aerospace, consumer products, electronic packaging, etc. due to their low cost, light-weight, good chemical resistance and high performance [38,39]. The properties of a polymer matrix can be completely modified by adding micrometer or nanometer sized fillers. For example, the insulating polymer can be made conductive with the addition of metal particles, carbon blacks, carbon fibers or carbon nanotubes, which could be very useful for electrostatic charge dissipation, EMI shielding, and bipolar plates in fuel cells applications [40,41]. On the other hand, the thermal conductivity of polymers is very low, which poses great limitations in certain applications that require fast heat dissipation such as in electronic packaging, engine components

in automobiles or in airplanes. Addition of thermally conductive metal particles, carbon fibers and carbon nanotubes have been proved useful in increasing the thermal conductivity of the resulting composites [42]. In addition, mechanical properties, gas permeability as well as fire retardancy can also be greatly enhanced by incorporation of the fillers into the polymer host [43,44].

The use of graphite based fillers can be traced back to Aylsworth [45,46] who first developed and proposed exfoliated graphite as a reinforcement for polymers in the 1910s while others proposed the dispersion of intercalated graphite in polymer resins by conventional composite processing techniques [47]. It was only recently that carbon nanomaterials such as carbon nanotubes and graphene nanosheets thanks to their exceptional physical properties started to gain momentum in replacing conventional fillers to introduce multifunctionalities to polymer hosts. However, the high surface area of these carbon nanomaterials also gives rise to a strong van der Waals interaction between individual nanoparticles. Therefore, their maximum contribution to the properties of composites can only be achieved if they remain reasonably dispersed inside the polymer without significant agglomeration. Typically, thermoplastic polymer composites were made by one of the three processing routes: solvent blending, in situ polymerization and melt extrusion.

1. Solvent blending:

In this approach, graphene based fillers are dispersed in a suitable solvent such as water, acetone, chloroform, tetrahydrofuran (THF), dimethyl formamide (DMF) or toluene. The polymer was then added and solubilized. Ultrasonication was usually used to homogenize the dispersion of nanofillers in the polymer host. It is also important to note that long time exposure to ultrasonication can introduce defects to graphene sheets which might be detrimental to the

properties. During solvent blending, graphene sheets were coated with polymers and remained separate. Solvent was then removed by evaporation at a temperature around or below the boiling point of the solvent during which graphene sheets reassemble, sandwich the polymer to form nanocomposites. However, several possible drawbacks associated with this approach is that the nanofillers tend to agglomerate during slow solvent evaporation, resulting in inhomogeneous distribution of graphene sheets in the polymer. In addition, residue solvent molecule might remain on the surface of GNP, which cannot be easily removed. Various polymer composites such as expanded graphite (EG)-PMMA[48], functionalized graphene-PS[49], graphene-PVA[50], graphene-PVC[51], PVDF-reduced graphene [52] have been prepared using this technique.

2. in situ polymerization

In this approach, graphene based fillers were dispersed together with monomers in the presence of a solvent. Polymerization reaction took place with the addition of certain amount of initiators at a controlled temperature for certain amount of time. This technique enables not only the covalent bonding between functionalized graphene with the polymer matrix but also non covalent bonding such as PMMA-GO [53], PP-GO nanocomposites [54]. For graphite-based layered structure in a polymer matrix, this technique further facilitated the exfoliation of expanded graphite into thinner platelets by intercalation of the monomers, forming well-dispersed graphene in the polymer. While this approach has offered a good technique to achieve a homogeneous dispersion of graphene inside the polymer host and possibly enhanced interactions, it requires careful control over the conditions used in the synthesis of nanocomposites such as reaction temperature, concentration of monomer vs. the initiator,

reaction time, as well as the pH of the solution. Examples of using in situ polymerization to fabricate nanocomposites are EG-PMMA[55], graphene-PMMA[56], graphene-PS[57], EG-nylon 6[58,59], and EG-PANi [60].

3. Melt extrusion

Melt extrusion uses strong shearing forces to disperse the reinforcement phase at an elevated temperature that liquefies the polymer. Compared with the previous two approaches, melt extrusion has its unique advantage because of its environmental friendliness and versatility, making it more commercially attractive. This strategy usually involves mixing graphene sheets and melted polymer in a twin-screw extruder. The temperature, screw speed, screw rotation and mixing time are the major parameters to adjust for optimal dispersion of the nanofiller in the matrix. Several disadvantages associated with this approach is that it is confined by the viscosity of the nanocomposites especially at a high filler loading which prevents uniform dispersion of graphene nanosheets in the polymer, compromising the physical properties of the composites. A variety of graphene reinforced composites prepared by this methods are EG-polyester[61], EG-PPS[62], graphene-PP[63], graphene-PC[64].

The resulting physical properties of graphene reinforced nanocomposites vary widely depending on the processing methods, concentration of fillers, aspect ratio, presence of functional groups, inter-particle contact as well as the filler orientation in the polymer matrix. The next section focuses on the electrical and thermal properties of conductive particle (especially those filled by graphene) filled nanocomposites in general and discusses the fundamental difference between the two.

1. 3. 1 Electron transport:

The addition of electrically conductive fillers into an insulating polymer matrix results in a significant drop in its resistivity at a certain filler loading. This mechanism of electronic transport in composite materials has been discussed previously and is described by a phenomenon called percolation. When the number of conductive filler is enough to form continuous linkage that span the entire specimen, the resistivity experiences a significant drop, turning an insulator into a semiconductor at the percolation threshold [65]. Figure 1-1 illustrates the percolation phenomenon as applied to conductive composites. In spite of the high electrical conductivity of the individual filler, it is difficult to obtain composites with resistivity within five orders of magnitude of the filler itself [66,67]. The resistance of the composite specimen consists of three independent components: 1) contact resistance (constriction resistance), 2) quantum mechanical electron tunneling resistance, and 3) intrinsic resistivity of the fillers. Contact resistance, also known as constriction resistance (R_{cr}), results from a resistance associated with the constriction of electron flow through the contact of two conductive spheres. R_{cr} derived from the ohmic conduction and electric fields can be expressed as:

$$R_{cr} = \frac{\rho_i}{d} \tag{1.1}$$

where ρ_i is the intrinsic resistivity of the fillers, d is the diameter of the contact spot. Assume the size of the conductive filler particle is D , when D/d is >10 , equation (1.1) begins to diverge and a very high resistance results even when the conductive particles are in close contact with each other [68]. On the other hand, if the conductive particles are coated with a thin insulating film during material processing, such as the residual organic film that may remain on the conductive

powder surface after milling, or in a conductor-filled polymer composites, the polymer may completely cover the surface of the filler. In both cases, tunneling resistance arises that increases the resistivity of the composites. In particular, the magnitude of tunneling resistance (or the probability of electrons to tunnel through a potential barrier) is directly related to the work function of the conductor, the thickness of the insulating film, and the relative dielectric permittivity of the film. Since tunneling is independent of the resistivity of the film itself, it is believed that the organics, polymers, oxides with similar work functions, permittivity as well as film thickness will have similar tunneling resistance. Dietrich has shown mathematically in his pioneer work that described the tunneling resistivity on insulating film thicknesses and presented a general tunneling curve based on TiO₂ film on Ti, which is considered applicable to all other materials [69]. Generally speaking, quantum mechanical tunneling can occur for thin films on the order of 10 nm or less. If the film thickness is known, tunneling resistivity (ρ_t) can be estimated, therefore the tunneling resistance R_t which is inversely proportional to the contact area A can be described by:

$$R_t = \frac{\rho_t}{A} \quad 1.2$$

The resistance of a contact R_c is the sum of the two separate effects given by:

$$R_c = \frac{\rho_i}{d} + \frac{\rho_t}{A} \quad 1.3$$

However, determination of either the contact diameter d or the contact area A is the major challenge in estimating the overall contact resistance primarily because both parameters are dependent on the morphology, dispersion state and more importantly the elastic modulus of the

conductive particles due to possible mechanical deformation as a result of the change in the hydrostatic pressure and temperature at which the sample is kept at [65]. For carbon based nanocomposites, contact resistance dominates when filler loading is high and physical contacts are present while tunneling resistance becomes significant when filler loading is low and there is an insulating polymer film coated on the fillers. Due to the temperature dependent differences involved in the origin of constriction and tunneling resistances (i.e. contact resistance increases with temperature while tunneling resistance decreases with temperature [70]), Jovic et al reported a "phase transition" from predominately "contact conductivity" to "tunneling conductivity" by measuring the conductivity temperature coefficient ($CTC=d\sigma/dT$) in an epoxy/expanded graphite composites with intermediate filler contents when heated from room temperature to 120°C [71]. While this phenomenon depends largely on the starting polymer matrix, the filler loading as well as the processing history of composites, It did offer a nice technique to separate the individual component's contribution to overall interfacial contact resistance and determine which one is dominating from temperature dependence resistivity of the composites.

In general, the electronic transport of a graphene based composites depends not only on the intrinsic properties of graphene, but also on the interfacial contact resistance which is directly related to the concentration, dispersion, and the interaction of the filler with the polymer host.

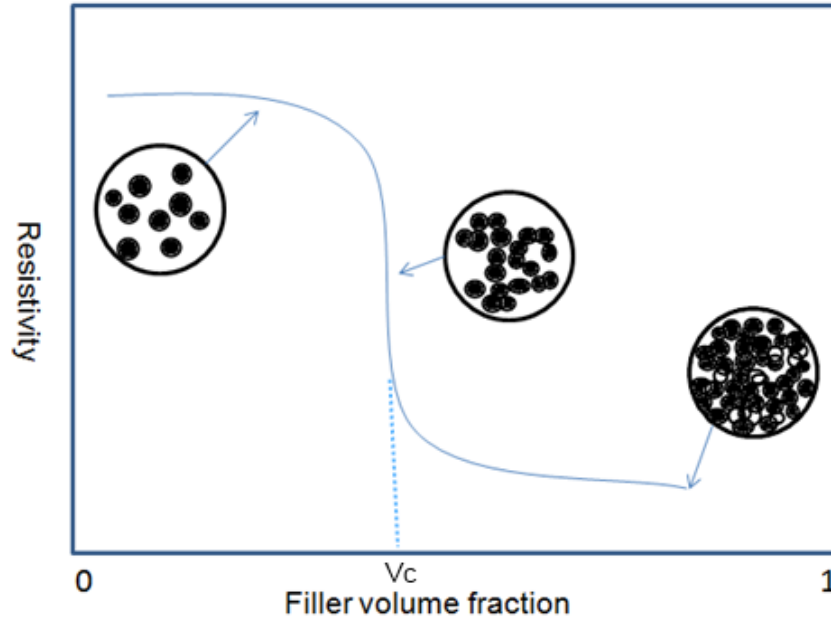


Figure 1-1: Electrical percolation, as applied to conductive composites. The formation of the first complete particle linkage results in a significant drop in resistivity at V_c . For interpretation of the references to color in this and all other figures, the reader is referred to the electronic version of this dissertation.

1. 3. 2 Phonon transport:

Heat transport involves movement of energy from one place to another by energy carriers. For example, molecules in the liquid or gas phase bump into each other due to Brownian motion, transferring their kinetic energy (thermal energy) at the same time. Energy can also be transported by an ordered drift of molecules in certain direction such as advection. In polymers, heat is predominantly transported by phonons, which are quantized modes of lattice vibration [72]. The theoretical prediction of thermal conductivity (λ) of polymers can be calculated by the kinetic formula:

$$\lambda = \frac{C_p v l}{3} \tag{1.4}$$

where C_p is the specific heat capacity, v is the average phonon velocity, l is the phonon mean free path. In particular, l is a very small number (usually a few angstroms) for polymers because of the numerous structural defects along the chains of the polymers that act as phonon scattering centers, leading to a very low thermal conductivity. Thermally conductive composites can be used in a variety of applications such as automobiles, aerospace, electronic circuit boards, heat sinks, electronic packaging, protective clothing, etc. There has been plenty of research directed at enhancing thermal conductivity of polymers by adding thermally conductive fillers such as carbon blacks, carbon fibers, graphite, metal or ceramic particles [73-77]. However, it typically requires a very high filler loading (30 vol%) to achieve a thermal conductivity suitable for certain applications, which poses great challenges in composite processing as a result of increased viscosity of the nanocomposites. Moreover, the mechanical properties and density of resulting composites are altered after the introduction of a high loading of fillers.

Graphene-based nanomaterials recently have shown promising results in terms of enhancing the thermal conductivity of composites [78,79]. Taking epoxy as the polymer matrix, thermal conductivity of graphene filled epoxy has been reported to achieve different levels of enhancement depending on the composition of the filler, the aspect ratio, the filler size distribution, as well as its chemical compatibility with the matrix [80-83]. Due to the 2D platelet morphology of graphene sheets, thermal conductivity of composites is also dependent on the orientation of the filler in the matrix. Heat flow in the direction perpendicular to the platelet is significantly restricted as compared to the heat flow in the direction parallel to the platelets [84,85]. This unique anisotropic heat conduction in graphene sheets filled composites can be very useful in directional thermal management for electronics and protective clothings.

Theoretical prediction and modelling:

Two basic models have been used to represent the upper and lower bound for thermal conductivity of composites, referred to as the parallel and the series model. In the parallel model, each phase is considered to contribute to conductivity independently, proportional to its volume fraction:

$$\mathbf{K}_c = \mathbf{K}_f \phi_f + \mathbf{K}_m \phi_m \quad (1.5)$$

where \mathbf{K}_c , \mathbf{K}_f , \mathbf{K}_m are the thermal conductivity of the composite, filler, matrix, respectively, and ϕ_f and ϕ_m are the volume fractions of the filler and the matrix. This model assumes perfect contact between the fillers in a percolated network and has some relevance to the case of continuous fiber composites in the direction parallel to the fibers. However, it usually results in a large overestimation with respect to experimental values. The series model, on the other hand, assumes no contact between the filler and the matrix, thermal resistance of the composite is considered the sum of the resistance from the filler and that of the matrix arranged in series. Depending on the volume fractions, thermal conductivity is predicted by:

$$\mathbf{K}_c = \frac{1}{\left(\frac{\phi_f}{\mathbf{K}_f}\right) + \left(\frac{\phi_m}{\mathbf{K}_m}\right)} \quad (1.6)$$

The experimental values obtained usually falls between these two predictions, with the true value being closer to the series model prediction. More complicated models have been proposed and developed that take into account the filler geometry, aspect ratio, alignment, as well as the interfacial thermal resistance for better description of thermal behaviors of various systems.

Among all these parameters that play a role in heat transport in composites, the interfacial thermal resistance (or Kapitza resistance) seems to be drawing most of the attention. Kapitza resistance, named after the Russian physicist who discovered a temperature discontinuity at metal-liquid interface, can be calculated theoretically or by means of computer simulation as a result of the technical challenges involved in accurately measuring the interfacial heat flow in nanocomposites directly [86,87]. Monte-Carlo based methods and molecular dynamics offer the advantage of manipulating the interaction of nanofiller in the matrix on a molecular scale, simulation results can later be fitted with experimental data to back calculate the parameter of interest [88,89].

As suggested by the previous discussion on the mechanism of energy transport in composites, It is believed that no matter electronic or phononic conduction, both are affected by the existence of interfaces in the composites (i.e. mostly the matrix-filler, filler-filler interfaces). However, the conduction mechanisms are quite different when it comes to interfacial phases when electron tunneling occurs while phonon tunneling is still not fully verified or understood . Therefore, failing to consider the effect of interfacial transport of phonons might explain the discrepancies observed in the estimation of thermal conductivity by the parallel and series model described above.

1.4 Bi-continuous paper like graphene based nanocomposites

Very different from the approach taken in the previous section to fabricate bulk nanocomposites, a highly ordered, highly flexible paper-like nanocomposite can be prepared using a very inexpensive way such as vacuum assisted self assembly. In this case, graphene sheets were dispersed in an aqueous or organic solvent and then filtrated on a filter membrane to

create a paper. For example, carbon nanotubes mat (buckypaper)[90], graphene oxide (GO) paper[91,92], and reduced graphene paper [93-95] have been reported by various research groups. The electrical conductivity can reach as high as 200 S/cm for aligned buckypaper [90] and 350 S/cm for reduced graphene paper [95]. A highly aligned, bi-continuous paper-based nanocomposite can be prepared by vacuum infiltration of a polymer resin or simply immerse the porous paper structure in a solution containing the polymer of interest followed by solvent evaporation, leaving the polymer intercalated in the pores of the paper. Due to the already established interconnectivity of the filler and its preferential alignment, the thermal and electrical conductivity in the aligned direction can be much higher than if the fillers are randomly distributed in the polymer matrix due to the reduced contact resistance [84,85,96,97]. Depending on the initial dispersion state of graphene based fillers, the paper-like nanocomposites still possess certain flexibility and mechanical robustness. While most of graphene paper reported in the literature consist of reduced graphene oxide that has to go through an extra chemical reduction that cannot fully restore the conjugation of graphene, the electrical and thermal properties of the resulting paper is compromised. For GNP developed in Drzal's group, the highly aromatic graphene basal plane remains intact during the intercalation-expansion fabrication route, offering another ideal starting material for the preparation of flexible, robust paper based structure that can be used in a variety of applications.

1.5 Background in thermoelectric energy conversion materials:

The multi-functionality that can be introduced to a polymer matrix by incorporation of graphene nanosheets has opened up numerous opportunities in the field of renewable energy generation and conversion. One of the promising technologies that could potentially benefit from

the development of graphene based polymer nanocomposites is thermoelectric energy conversion. The thermoelectric effect was first discovered in 1821 by Thomas Seebeck who reported that heating a junction between two dissimilar metals produced a potential difference. The Seebeck coefficient (S), is defined as the ratio of voltage generated per unit temperature change:

$$S = \frac{\Delta V}{\Delta T} \quad (1.7)$$

Figure 1-2 is a schematic representation of the potential difference generated due to the diffusion of charge carriers from the hot to the cold side of the sample. An equilibrium is reached when the carriers drifting back due to a built in electric field balances the carrier diffusion induced by the temperature gradient. Seebeck coefficient is determined by the dominant charge carriers present in the materials and is positive for holes and negative for electrons.

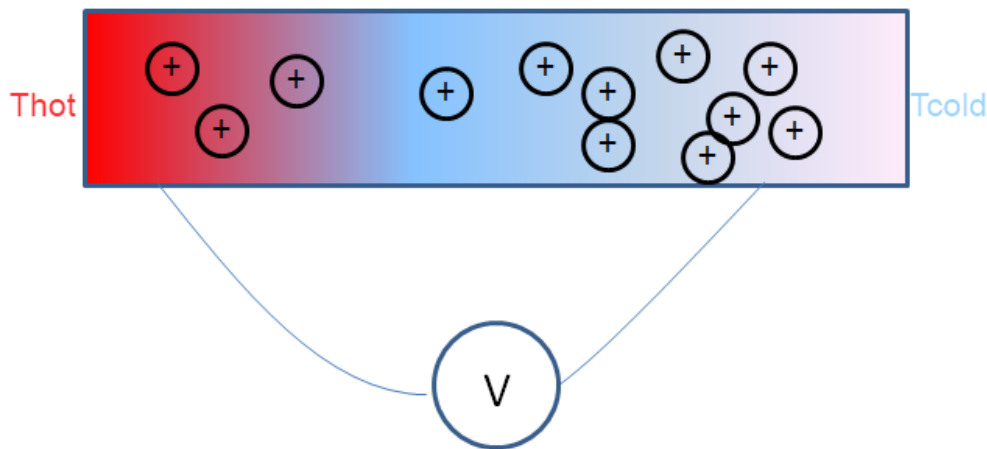


Figure 1-2: Schematic representation of Seebeck effect when a sample is subjected to a temperature gradient, in this case, holes are the dominant carriers.

Another thermoelectric effect is discovered by a French watchmaker Peltier who found that when a current is passed through a junction of different metals, heat can be either absorbed or released at the junction depending on the direction of the current. The Seebeck effect and the

Peltier effect are the theoretical foundations for the state of the art solid state heating and cooling technology.

In order to illustrate how a thermoelectric device work, it is essential to understand the basic configuration of a thermoelectric unicouple composed of a n-type and p-type material connected in series. If a heat source is applied to one end of the couple, charge carriers become energized and diffuse down toward the cold side causing a Seebeck voltage to be generated across the couple, this thermally induced voltage gives rise to a current when a resistive load is connected to the couple. On the other hand, a current passing through the unicouple causes the electrons and holes to move away from one end of the couple, effectively cooling it down. A thermoelectric module can be fabricated by connecting many unicouples electrically in series but thermally in parallel so as to maintain the effective temperature difference. Figure 1-3 is a schematic depiction of a thermoelectric unicouple that operates under either a power generation mode (Seebeck effect) or refrigeration mode (Peltier effect).

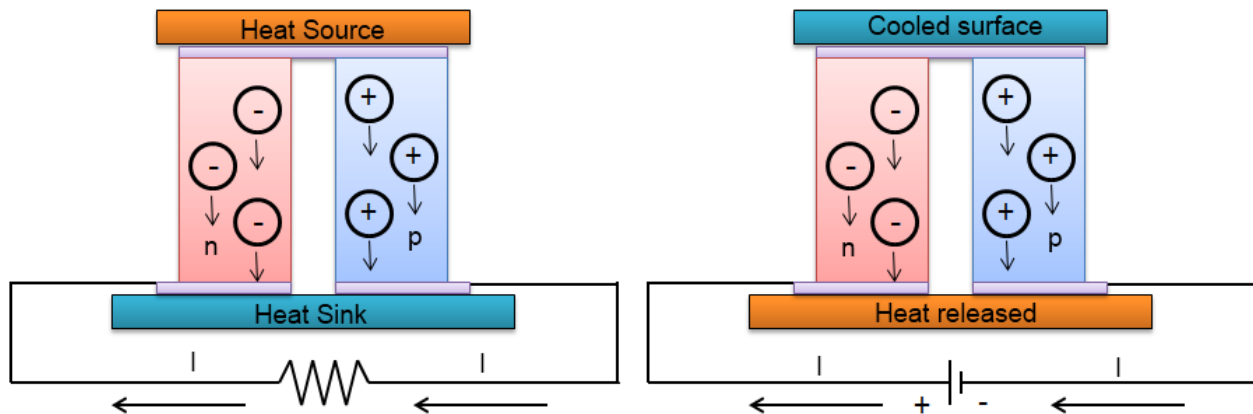


Figure 1-3: Schematic representation of a thermoelectric unicouple consisting of a p and n type semiconductor materials connected electrically in series and thermally in parallel operating under power generation mode (left) or refrigeration mode (right)

The conversion efficiency η of the thermoelectric device defined as the ratio between power W delivered to the load to the heat supplied Q from the source can be expressed as:

$$\eta = \frac{W}{Q} = \frac{\Delta T}{T_h} \cdot \frac{\sqrt{1 + Z\bar{T}} - 1}{\sqrt{1 + Z\bar{T} + \frac{T_c}{T_h}}} \quad (1.8)$$

where Z is a material dependent parameter, \bar{T} , T_h and T_c are the average operating temperature, hot side temperature and cold side temperature respectively. Parameter Z , also referred to as the thermoelectric figure of merit is the quantity to be maximized for higher conversion efficiency. The most commonly used dimensionless figure of merit ZT is obtained by multiplying Z by the operating temperature T which is expressed as:

$$ZT = \frac{S^2 \sigma}{\kappa} \cdot T \quad (1.9)$$

where S is the Seebeck coefficient, σ is the electrical conductivity, κ is the thermal conductivity of the material. From the definition of Z , a good thermoelectric material should have a high Seebeck coefficient, a high electrical conductivity and a low thermal conductivity. Apparently, in addition to having a high Seebeck coefficient, a large electrical to thermal conductivity ratio σ/κ is highly desired. Current research activities are primarily focused on inorganic semiconductors and developing complex material structures that behave like phonon glass electron crystals (i.e. allowing electrons to flow undisturbed while blocking phonon transport in the materials)[98-100]. Certain approaches such as impurity atom substitution [101], introduction of rattler atoms[102,103] or use of low dimensional materials[104,105] have been shown to be successful in reducing the thermal conductivity while causing less disruption to electrical conductivity. However, the delicate nanostructures that are intentionally introduced to the bulk could be very difficult to maintain due to their susceptibility to stoichiometry, temperature, pressure, sintering

time and etc, making it almost impractical in large scale production. In addition, large consumption of raw materials could also impose added risk and cost when faced with a dwindling mining and production of rare earth metals.

Recently, research in polymer based thermoelectric materials have been on the rise because of its intrinsic low thermal conductivity, light-weight, low cost as well as ease of large scale production. During the course of this research, polymer composites based on carbon nanotubes have also been proposed to show promising thermoelectric properties [106-109]. The combination of a polymer matrix having low thermal conductivity and highly electrically conductive fillers such as graphene nanoplatelets seems to be an interesting and viable route to explore in terms of increasing the σ/κ ratio so as to achieve a higher figure of merit.

1.6 Motivation and objective of research:

Graphene nanoplatelets are produced by acid intercalation and thermal exfoliation of graphite intercalated compounds. These nanoplatelets have excellent electrical, thermal and mechanical properties as a result of preservation of the pristine aromatic character of the graphene basal plane during production. However, the benefits of GNP can only be realized if they can be assembled macroscopically or into a bulk. In this case, it is reasonable to assume that the numerous contacts or the interfaces created play an important role in the performance and behavior of the resulting nanocomposites. Based on this premise, this dissertation is dedicated to the investigation of the difference in energy transport (electron and phonon in particular) occurring at the interfaces and discusses several useful nanostructuring techniques to modify the behavior of carrier transport in GNP-based nanocomposites with a focus on developing an inexpensive, lightweight, flexible nanocomposites for thermoelectric application.

In the first part of the research, the effect of incorporating GNP on the electrical and thermal properties of an insulating polymer is studied and the distinction between conduction of electrons and phonons across GNP/polymer interfaces is illustrated. A novel method based on micro-Raman spectroscopy that investigates the effect of particle-particle junctions on phonon transport is proposed.

With the previous learning in mind, as well as an aim to maximize the potential of individual GNP particles, the second part of the research is based on a highly ordered, highly flexible multilayer GNP paper prepared by vacuum assisted self assembly and focuses on the modification and separation of electron and phonon transport by various nanostructuring techniques in order to design a nanocomposite thermoelectric material with a high σ/κ ratio and Seebeck coefficient. In particular, a facile, one-pot synthesis of metal nanoparticles on the surface of GNP is proposed with microwave assisted heating and the effect of metal nanoparticles on carrier transport is explored. In another approach, a conductive polymer (polyaniline) was synthesized on the surface of GNP by in situ polymerization forming a core-shell nanostructure. The effect of polymer interaction with GNP, the concentration as well as protonation ratio of polyaniline on the thermoelectric properties of PANi/GNP nanocomposites is discussed. The last part explores a novel approach that completely alters the way electrons and phonons transport inside a PANi decorated GNP paper by a simple folding, the potential of creating an electrically connected thermally disconnected structure from this approach for thermoelectric application is discussed.

REFERENCES

References

1. Geim, A.K.; Graphene: status and prospects, *Science*, **2009**, *324*, 1530.
2. Geim, A.K. and Novoselov. K.S. The rise of graphene, *Nature Materials*, **2007**, *6*, 183-191.
3. Rao, C. N. R.; Sood, A. K.; Subrahmanyam, K. S.; Govindaraj, A. Graphene: the new two-dimensional nanomaterial. *Angew. Chem. Int. Ed.* **2009**, *48*, 7752-7777.
4. Allen, M. J.; Tung, V. C.; Kaner, R. B. Honeycomb carbon: a review of graphene. *Chem. Rev.* **2010**, *110*, 132-145.
5. Singh, V.; Joung, D.; Zhai, L.; Das, S.; Khondaker, S. I.; Seal, S. Graphene based materials: Past, present and future. *Prog. Mater. Sci.* **2011**, *56*, 1178-1271.
6. Lee, C.; Wei, X.; Kysar, J. W.; Hone, J. Measurement of the elastic properties and intrinsic strength of monolayer graphene. *Science*, **2008**, *321*, 385-388.
7. Novoselov, K. S. Geim, A.K.; Morozov, S.V.; Jiang, D.; Katsnelson, M.I.; Grigorieva, I. V.; Dubonos, S. V.; Firsov, A. A. Two-dimensional gas of massless Dirac fermions in graphene, *Nature*, **2005**, *438*, 197-200.
8. Novoselov, K.S.; Geim, A.K.; Morozov, S.V.; Jiang, D.; Zhang. Y.; Dubonos, S. V.; Grigorieva, I. V. and Firsov. A. A. Electric field effect in atomically thin carbon films, *Science* **2004**, *306*, 666-669.
9. Balandin, A.A.; Ghosh, S.; Bao, W.; Calizo, I.; Teweldebrhan, D.; Miao, F et al. Superior thermal conductivity of single-layer graphene. *Nano Lett.* **2008**, *8*, 902-907.
10. Kuilla, T.; Bhadra, S.; Yao, D.; Kim, N. H.; Bose, S.; Lee, J. H. Recent advances in graphene based polymer composites. *Prog. Polym. Sci.* **2010**, *35*, 1350-1375.
11. Roy-Mayhew, J.D.; Bozym, D. J.; Punckt, C.; Aksay, I. A. Functionalized graphene as a catalytic counter electrode in dye-sensitized solar cells. *ACS Nano*, **2010**, *4*, 6203-6211.
12. Brownson, D. A. C.; Kampouris, D. K.; Banks, C. E. An overview of graphene in energy production and storage applications. *J Power Sources.* **2011**, *196*, 4873-4885.
13. Wang, S.; Ang, P. K.; Wang, Z.; Tang, A. L. L.; Thong, J. T. L.; Loh, K. P. High mobility, printable, and solution-processed graphene electronics. *Nano Lett.* **2010**, *10*, 92-98.
14. Eizenberg, M.; & Blakely, J. M.; Carbon monolayer phase condensation on Ni (111). *Surf. Sci.* **1970**, *82*, 228-236.
15. Li, X.; Cai, W.; An, J.; Kim, S.; Nah, J.; Yang, D et al. Large-Area synthesis of high-quality and uniform graphene films on copper foils. *Science*, **2009**, *324*, 1312-1314.

16. Berger, C.; Song, Z.; Li, X.; Wu, X.; Brown, N.; Naud, C et al. Electronic confinement and coherence in patterned epitaxial graphene, *Science*, **2006**, *312*, 1191-1196.
17. Reina, A.; Jia, X.; Ho, J.; Nezich, D.; Son, H.; Bulovic, V et al. Large area, few-layer graphene films on arbitrary substrates by chemical vapor deposition. *Nano Lett.* **2009**, *9*, 30-35.
18. Chen, J. H.; Ishigami, M.; Jang, C.; Hines, D. R.; Fuhrer, M. S.; Williams, E. D. Printed graphene circuits. *Adv. Mater.* **2007**, *19*, 3623-3627.
19. Hummers W, Offeman R. Preparation of graphite oxide. *JACS*, **1958**, *80*,1339.
20. Dreyer, D. R.; Park, S.; Bielawski, C. W.; Ruoff, R. S. The chemistry of graphene oxide. *Chem. Soc. Rev.* **2010**, *39*, 228-240.
21. Szabo, T.; Berkesi O.; Dekany, I.; DRIFT study of deuterium-exchanged graphite oxide. *Carbon*, **2005**, *43*, 3186-3189.
22. de Boer JH.; Van Doorn ABC.; Graphite oxide I: The adsorption of water. *Koninkl Ned Akad Wetenschap. Proc* **1958**; *61B*, 242-252.
23. Park, S.; Ruoff, R. S. Chemical methods for the production of graphenes. *Nat. Nanotechnol.* **2009**, *4*, 217-224.
24. Stankovich, S.; Dikin, D. A.; Piner, R. D.; Kohlhaas, K. A.; Kleinhammes, A.; Jia, Y et al. Synthesis of graphene-based nanosheets via chemical reduction of exfoliated graphite oxide, *Carbon*, **2007**, *45*, 1558-1565.
25. Stankovich. S.; Piner. R.D.; Chen, X.; Wu, N.; Nguyen, S. T.; Ruoff. R.S.; Stable aqueous dispersions of graphitic nanoplatelets via the reduction of exfoliated graphite oxide in the presence of poly(sodium 4-styrenesulfonate), *J. Mater. Chem.* **2006**, *16*, 155-158.
26. Xu, Y.; Bai, H.; Lu, G.; Li, C.; Shi, G. Flexible graphene films via the filtration of water-soluble noncovalent functionalized graphene sheets. *JACS*, **2008**, *130*, 5856-5857.
27. Li, D.; Muller, M. B.; Gilje, S.; Kaner, R. B.; Wallace, G.G.; Processable aqueous dispersions of graphene nanosheets. *Nat. Nanotechnol*, **2008**, *3*, 101-105.
28. Schniepp, H. C.; Li, J. L.; McAllister, M. J.; Sai, H.; Alonso, M. H.; Adamson, D. H et al. Functionalized single graphene sheets derived from splitting graphite oxide, *J. Phys. Chem. B.* **2006**, *110*, 8535-8539.
29. McAllister, M.J.; Li, J. L.; Adamson, D. H.; Schniepp, H. C.; Abdala, A. A.; Liu, J et al. Single sheet functionalized graphene by oxidation and thermal expansion of graphite. *Chem. Mater.* **2007**, *19*, 4396-4404.
30. Larciprete, R.; Lacovig, P.; Gardonio, S.; Baraldi, A.; Lizzit, S. Atomic oxygen on graphite: chemical characterization and thermal reduction. *J. Phys. Chem. C.* **2012**, *116*, 9900-9908.

31. Li, J-L.; Kudin, K. N.; McAllister, M. J.; Prud'homme, R.K.; Aksay, I.A.; Car, R.; Oxygen-driven unzipping of graphitic materials, *Phys. Rev. Lett.* **2006**, *96*, 176101.
32. Jung, I.; Dikin, D.; Park, S.; Cai, W.; Mielke, S. L.; Ruoff, Rodney.; Effect of water vapor on electrical properties of individual reduced graphene oxide sheets. *J. Phys. Chem. C*, **2008**, *112*, 20264-20268.
33. Navarro, C. G.; Weitz, T. R.; Bittner, A. M.; Scolari, M.; Mews, A.; Burghard, M et al. Electronic transport properties of individual chemically reduced graphene oxide sheets. *Nano Lett.* **2007**, *7*, 3499-3503.
34. Drzal, L.T.; Fukushima, H.; Expanded graphite and products produced therefrom, U.S Patent Application 11/363,336, **2006**.
35. Fukushima, H.; Graphite reinforcements in polymer nanocomposites. Ph.D dissertation, Michigan State University, East Lansing, Michigan, **2003**.
36. Castro, E.V.; Novoselov, K. S.; Morozov, S. V.; Peres, N. M. R.; Lopes dos Santos, J. M. B.; Nilsson, J et al. Biased bilayer graphene: semiconductor with a gap tunable by the electric field effect. *Phys. Rev. Lett.* **2007**, *99*, 216802.
37. Zhang, Y.; Tang, T. T.; Girit, C.; Hao, Z.; Martin, M. C.; Zellt, A et al. Direct observation of a widely tunable bandgap in bilayer graphene. *Nature* **2009**, *459*, 820-823.
38. Vaia, R. A.; Giannelis E. P. Polymer melt intercalation in organically-modified layered silicates: model predictions and experiment. *Macromolecules*, **1997**, *30*, 8000-8009.
39. Okamoto, M.; Nam, P. H.; Maiti, P.; Kotaka, T.; Nakayama, T.; Takada, M et al. Biaxial flow-induced alignment of silicate layers in polypropylene/clay nanocomposite foam. *Nano Lett*, **2001**, *1*, 503-505.
40. Chung, D. D. L. Electrical applications of carbon materials. *J. Mater. Sci.* **2004**, *39*, 2645-2661.
41. Cho, E. A.; Jeon, U. S.; Ha, H. Y.; Hong, S. A.; Oh, I. H. Characteristics of composite bipolar plates for polymer electrolyte membrane fuel cells. *J Power Sources*. **2004**, *125*, 178-182.
42. Thostenson, E. T.; Ren, Z.; Chou, T. W. Advances in the science and technology of carbon nanotubes and their composites: a review. *Compos Sci Technol*, **2001**, *61*, 1899-1912.
43. Coleman, J. N.; Khan, U.; Blau, W. J.; Gun'ko, Y. K. Small but strong: A review of the mechanical properties of carbon nanotube-polymer composites. *Carbon*, **2006**, *44*, 1624-1652.
44. Wu, Q.; Zhu, W.; Zhang, C.; Liang, Z.; Wang, B. Study of fire retardant behavior of carbon nanotube membranes and carbon nanofiber paper in carbon fiber reinforced epoxy composites. *Carbon*, **2010**, *48*, 1799-1806.
45. Aylsworth, J. W. Expanded graphite and composition thereof. US Patent 1,137,373, **1915**.

46. Aylsworth, J. W. Expanded graphite. US Patent 1,191,383; **1916**.
47. Lincoln, V. F.; Claude, Z. Inventors, organic matrix composites reinforced with intercalated graphite. US Patent 4,414,142; **1983**.
48. Zheng, W.; Wong, S. C. Electrical conductivity and dielectric properties of PMMA/expanded graphite composites. *Compos Sci Technol.* **2003**, *63*, 225-235.
49. Liu, N.; Luo, F.; Wu, H.; Liu, Y.; Zhang, C.; Chen, J. One step ionic-liquid-assisted electrochemical synthesis of ionic-liquid functionalized graphene sheets directly from graphite. *Adv Funct. Mater.* **2008**, *18*, 1518-1525.
50. Jiang, L.; Shen, X. P.; Wu, J. L.; Shen, K. C Preparation and characterization of graphene/poly(vinyl alcohol) nanocomposites. *J Appl Polym Sci*, **2010**, *118*, 275-279.
51. Vadukumpully, S.; Paul, J.; Mahanta, N.; Valiyaveetil, S. Flexible conductive graphene/poly(vinyl chloride) composite thin films with high mechanical strength and thermal stability. *Carbon*, **2011**, *49*, 198-205.
52. Ansari, S.; Giannelis, E. P. Functionalized graphene sheet-poly(vinylidene fluoride) conductive nanocomposites. *J Polym Sci Part B-Polym Phys*, **2009**, *47*, 888-897.
53. Jang, J. Y.; Kim, M. S.; Jeong, H. M.; Shin, C. M. Graphite oxide/poly(methyl methacrylate) nanocomposites prepared by a novel method utilizing macroazoinitiator. *Compos Sci Technol*, **2009**, *69*, 186-191.
54. Huang, Y.; Qin, Y.; Zhou, Y.; Niu, H.; Yu, Z. Z.; Dong, J. Y. Polypropylene/graphene oxide nanocomposites prepared by in-situ Ziegler-Natta polymerization. *Chem Mater*, **2010**, *22*, 4096-4102.
55. Chen, G.; Weng, W.; Wu, D.; Wu, C. PMMA/graphite nanosheets composite and its conducting properties. *Eur. Polym. J.* **2003**, *39*, 2329-2335.
56. Chen, G. H.; Wu, D. J.; Weng, W. G.; Yan, W. L. Dispersion of graphite nanosheets in a polymer matrix and the conducting property of the nanocomposites. *Polym. Engng. Sci.* **2001**, *41*, 2148.
57. Hu, H.; Wang, X.; Wang, J.; Wan, L.; Liu, F.; Zheng, H et al. Preparation and properties of graphene nanosheets-polystyrene nanocomposites via in situ emulsion polymerization. *Chem. Phys. Lett.* **2010**, *484*, 247-253.
58. Pan, Y. X.; Yu, Z. Z.; Ou, Y.C.; Hu, G. H. A new process of fabricating electrically conducting nylon 6/graphite nanocomposites via intercalation polymerization. *J. Polym. Sci. Part B, Polym. Phys.* **2000**, *38*, 1626-1633.
59. Weng, W.; Chen, G.; Wu, D.; Chen, X.; Lu, J.; Wang, P.; Fabrication and characterization of nylon 6/foiliated graphite electrically conducting nanocomposites. *J Polym Sci Part B, Polym Phys.* **2004**, *42*, 2844-2856.

60. Du, X. S.; Xiao, M.; Meng, Y. Z.; Facile synthesis of highly conductive polyaniline/graphite nanocomposites. *Eur Polym J.* **2004**, *40*, 1489-1493.
61. Kim, H.; Macosko, C. W. Morphology and properties of polyester/exfoliated graphite nanocomposites. *Macromolecules*, **2008**, *41*, 3317-3327.
62. Zhao, Y. F.; Xiao, M.; Wang, S. J.; Ge, X. C.; Meng, Y. Z. Preparation and properties of electrically conductive PPS/expanded graphite nanocomposites. *Compos Sci Technol* 2007, *67*, 2528-2534.
63. Kalaitzidou, K.; Fukushima, H.; Drzal, L. T. A new compounding method for exfoliated graphite-polypropylene nanocomposites with enhanced flexural properties and low percolation threshold. *Compos Sci Technol*, 2007, *67*, 2045-2051.
64. Kim, H.; Macosko C. W. Processing-property relationships of polycarbonate/graphene nanocomposites. *Polymer* 2009, *50*, 3797-3809.
65. Ruschau, G. R.; Yoshikawa, S.; Newnham, R. E. Resistivities of conductive composites. *J. Appl. Phys.* **1992**, *72*, 953-959.
66. Hu, K. A.; Moffatt, D.; Runt, J.; Safari, A.; Newnham, R. E. V₂O₃-polymer composite thermistors. *J. Am. Ceram. Soc.* **1987**, *70*, 583-585.
67. Bhattacharya, S. K. *Metal-filled polymers* (Marcel-Dekker, New York, 1986)
68. R. Holm, *Electric contacts*. (Springer, Berlin, 1967)
69. Dietrich, L. *Z. Phys.* **1952**, *132*, 231.
70. Sheng, P.; Sichel, E. K.; Gittleman, J. I. Fluctuation-induced tunneling conduction in carbon-polyvinylchloride composites. *Phys. Rev. Lett.* **1978**, *40*, 1197-1200.
71. Jovic, N.; Dudic, D.; Montone, A.; Antisari, M. V.; Mitric, M.; Djokovic, V. Temperature dependence of the electrical conductivity of epoxy/expanded graphite nanosheet composites. *Scripta Mater*, **2008**, *58*, 846-849.
72. Majumdar A.; *Microscale transport phenomena*, In: Rohsenow WM, Hartnett, J. R. Cho, Y. I, editors. *Handbook of heat transfer*, 3rd ed. New York; McGraw-Hill; **1998**, p.8.1-8.
73. Pierson, H.O.; *Handbook of carbon, graphite, diamond and fullerenes: properties. Processing and applications*. New Jersey: Noyes Publications; **1993**.
74. Wypych, G. *Handbook of fillers: physical properties of fillers and filled materials*. Toronto: ChemTec Publishing; **2000**.
75. Wolff, S.; Wang, M. J.; *Carbon black science & technology*. 2nd ed, New York; Marcel Dekker; **1993**.
76. Kelly, B. T.; *Physics of graphite*. Barking (UK): Applied science publishers; **1981**.

77. Kuriger, R. J.; Alam, M. K.; Thermal conductivity of thermoplastic composites with submicrometer carbon fibers. *Exp Heat Trans*, **2002**, *15*, 19-30.
78. Tu, H.; Ye, L. Thermal conductive PS/graphite composites. *Polym. Adv. Technol.* **2009**, *20*, 21-27.
79. Fukushima, H.; Drzal, L. T.; Rook, B. P.; Rich, M. J. Thermal conductivity of exfoliated graphite nanocomposites. *J. Therm. Anal. Calorim.* **2006**, *85*, 235-238.
80. Hung, M. T.; Choi, O.; Ju, Y. S.; Hahn, H. T. Heat conduction in graphite-nanoplatelet reinforced polymer nanocomposites. *Appl. Phys. Lett.* **2006**, *89*, 023117.
81. Yu, A.; Ramesh, P.; Itkis, M. E.; Bekyarova, E.; Haddon, R. C. Graphite nanoplatelet-epoxy composite thermal interface materials. *J. Phys. Chem. C.* **2007**, *111*, 7565-7569.
82. Sun, X.; Ramesh, P.; Itkis, M. E.; Bekyarova, E.; Haddon, R. C. Dependence of the thermal conductivity of two-dimensional graphite nanoplatelet-based composites on the nanoparticle size distribution. *J. Phys.: Condens. Matter*, **2010**, *22*, 334216 (9pp).
83. Ganguli, S.; Roy, A. K.; Anderson, D. P. Improved thermal conductivity for chemically functionalized exfoliated graphite/epoxy composites. *Carbon*, **2008**, *46*, 806-817.
84. Veca, L. M.; Mezziani, M. J.; Wang, W.; Wang, X.; Lu, F.; Zhang, P et al. Carbon nanosheets for polymeric nanocomposites with high thermal conductivity. *Adv. Mater.* **2009**, *21*, 2088-2092.
85. Marconnet, A. M.; Yamamoto, N.; Panzer, M. A.; Wardle, B. L.; Goodson, K. E. Thermal conduction in aligned carbon-nanotube-polymer nanocomposites with high packing density. *ACS Nano*, **2011**, *5*, 4818-4825.
86. Huxtable, S. T.; Cahill, D. G.; Shenogin, S.; Xue, L.; Ozisik R.; Barone, P et al. Interfacial heat flow in carbon nanotube suspensions. *Nat Mater.* **2003**, *2*, 731-734.
87. Shenogin S.; Xue, L.; Ozisik R.; Keblinski, P.; Cahill, D. G.; Role of thermal boundary resistance on the heat flow in carbon-nanotube composites. *J Appl Phys*, **2004**, *95*, 8136-8144.
88. Duong, H. M.; Yamamoto, N.; Papavassiliou, D. V.; Maruyama, S.; Wardle, B. L. Inter-carbon nanotube contact in thermal transport of controlled morphology polymer nanocomposites. *Nanotechnology*, **2009**, *20*, 155702.
89. Duong, H. M.; Papavassiliou, D. V.; Mullen, K. J.; Maruyama, S. Computational modelling of the thermal conductivity of single-walled carbon nanotube-polymer composites. *Nanotechnology*, **2008**, *19*, 065702.
90. Wang, D.; Song, P.; Liu, C.; Wu, W.; Fan, S. Highly oriented carbon nanotube papers made of aligned carbon nanotubes. *Nanotechnology*, **2008**, *19*, 075609 (1-6)
91. Dmitriy, A. D.; Stankovich, S.; Zimney, E. J.; Piner, R. D.; Dommett, G. H. B.; Evmenenko, G et al. Preparation and characterization of graphene oxide paper. *Nature*, **2007**, *448*, 457-460.

92. Park, S.; Lee, K. S.; Bozoklu, G.; Cai, W.; Nguyen, S. T.; Ruoff, R. S. Graphene oxide papers modified by divalent ions-enhancing mechanical properties via chemical cross-linking. *ACS Nano*, **2008**, *2*, 572-578.
93. Li, D.; Kaner, R. B. Graphene-based materials. *Science*, **2008**, *320*, 1170-1171.
94. Xu, Y.; Bai, H.; Lu, G.; Li, C.; Shi, G. Flexible graphene films via the filtration of water-soluble noncovalent functionalized graphene sheets. *JACS*, **2008**, *130*, 5856-5857.
95. Chen, H.; Muller, M. B.; Gilmore, K. J.; Wallace, G. G.; Li, D. Mechanically strong, electrically conductive, and biocompatible graphene paper. *Adv. Mater.* **2008**, *20*, 3557-3561.
96. Du, F.; Guthy, C.; Kashiwagi, T.; Fischer, J. E.; Winey, K. I. An infiltration method for preparing single-walled nanotube/epoxy composites with improved thermal conductivity. *J. Polym Sci: Part B: Polym Phys*, **2006**, *44*, 1513-1519.
97. Liang, Q.; Yao, X.; Wang, W.; Liu, Y.; Wong, C. P. A three-dimensional vertically aligned functionalized multilayer graphene architecture: an approach for graphene-based thermal interface materials. *ACS Nano*, **2011**, *5*, 2392-2401.
98. Sales, B. C.; Mandrus, D.; Chakoumakos, B. C.; Keppens, V.; Thompson, J. R. Filled skutterudite antimonides: electron crystals and phonon glasses. *Phys. Rev. B*, **1997**, *56*, 15081-15089.
99. Nolas, G.S.; Morelli, D.T.; Tritt, T.M.; Skutterudites: A phonon-glass-electron crystal approach to advanced thermoelectric energy conversion applications. *Annu. Rev. Mater. Sci.* **1999**, *29*, 89-116.
100. Nolas, G.S.; Slack, G.A.; Schujman, S. B. Semiconductor clathrates: a phonon glass electron crystal material with potential for thermoelectric applications. *Semiconduct Semimet.* **2001**, *69*, 255-300.
101. Ioffe, A. F. Heat transfer in semiconductors, *Can. J. Phys*, **1956**, *34*, 1342-1355.
102. Slack, G. A.; Tsoukala, V. G. Some properties of semiconducting IrSb₃. *J. Appl. Phys.* **1994**, *76*, 1665-1671.
103. Morelli, D. T.; Meisner, G. P. Low temperature properties of the filled skutterudite CeFe₄Sb₁₂. *J. Appl. Phys*, **1995**, *77*, 3777-3781.
104. Hicks, L. D.; Dresselhaus, M. S. Effect of quantum well structures on the thermoelectric figure of merit. *Phys. Rev. B*, **1993**, *47*, 12727-12731.
105. Harmon, T. C.; Walsh, M. P.; Laforge, B. E.; Turner, G. W. Nanostructured thermoelectric materials. *J Electron. Mater.* **2005**, *34*, L19-L22.
106. Meng C.; Liu, C.; Fan, S. A promising approach to enhanced thermoelectric properties using carbon nanotube networks. *Adv. Mater.* **2009**, *21*, 1-5.

107. Yao, Q.; Chen, L.; Zhang, W.; Liufu, S.; Chen, X. Enhanced thermoelectric performance of single-walled carbon nanotubes/polyaniline hybrid nanocomposites. *ACS Nano*, **2010**, *4*, 2445-2451.
108. Kim, D.; Kim, Y.; Choi, K.; Grunlan, J.C.; Yu, C. Improved thermoelectric behavior of nanotube-filled polymer composites with poly(3,4-ethylenedioxythiophene) polystyrenesulfonate. *ACS Nano*, **2010**, *4*, 513-523.
109. Yu, C.; Choi, K.; Liang, Y.; Grunlan, J.C. Light-weight flexible carbon nanotube based organic composites with large thermoelectric power factors. *ACS Nano*, **2011**, *5*, 7885-7892.

Chapter 2 Investigation of GNP in Improving the Thermal and Electrical Conductivity of Paraffin Wax and Its Use in Thermal Energy Storage

2.1 Abstract:

This chapter serves as a primer to explore the physical properties of GNP and its effect on an insulating polymer matrix (i.e. paraffin wax). In particular, nanocomposites consisting of GNP and paraffin wax with high latent heat have great potential for high efficiency phase change materials (PCM) for thermal energy storage application. Composite PCMs were made by mixing two different kinds of GNP (GNP-1 and GNP-15) into paraffin wax. Direct casting and two roll milling were used to prepare samples. The investigation on the thermal and electrical conductivity of nanocomposites with these two nanofillers was performed. Higher thermal conductivity of composite PCM can be achieved with nanofillers of larger aspect ratio, higher particle alignment. The thermal physical properties of the nanocomposites were investigated by differential scanning calorimetry and thermal gravimetric analysis. It was found that the latent heat of the nanocomposites was not adversely affected by the presence of GNP and the thermal stability improved. This chapter is based on a journal publication: Xiang, J., Drzal, L. T. (2011). Investigation of exfoliated graphite nanoplatelets (xGnP) in improving thermal conductivity of paraffin wax-based phase change material. *Solar Energy Materials and Solar Cells*, 95(7), 1811–1818.

2.2 Introduction

Latent heat storage materials have been reported in the literature as useful for thermal

energy storage applications because of their high energy density [1-3]. Heat is stored through the phase transition within the material, such as solid-solid or solid-liquid transitions. Paraffin wax has attracted numerous attentions for its low cost, moderate energy densities, low vapor pressure, negligible supercooling and chemical inertness [4]. However, one of the intrinsic disadvantages associated with paraffin wax and other organic PCM are their low thermal conductivity, which severely limited the rate of absorbing and releasing heat from and to the environment. Various high thermally conductive fillers (e.g. metallic fins [5], ceramic powder fillers, graphitic carbon fibers [6], carbon nanofibers [7], graphite particles [8] and exfoliated graphite [9]) have been reported to improve the effective thermal conductivity of phase change materials. However, one usually needs a very high concentration of these traditional conductive fillers to achieve a noticeable improvement in thermal conductivity, resulting in increased density of the composites, processing difficulties and increased cost.

In this work, GNP-1 and GNP-15 were mixed with paraffin wax. The viscosity of paraffin wax is low and is thus conducive to dispersing conductive particles uniformly in the polymer matrix. The thermal and electrical conductivities of nanocomposites with nanofillers of different sizes were investigated. Different samples were prepared to study the effect of particle orientation on the conductivities of nanocomposites. Furthermore, the experimental results were compared with effective medium theory first proposed by Nan [10] on carbon nanotubes to estimate the interfacial thermal resistance. In addition, the effect of adding different GNP particles on melting/crystallization enthalpies, latent heat and thermal stability of paraffin wax is also discussed.

2.3 Experimental:

Materials:

GNP-15 and GNP-1 were produced by the acid intercalation and microwave-assisted exfoliation process described in the previous chapter. Paraffin wax (*n*-docosane) with melting temperature of 53-57°C, xylenes (reagent grade) were purchased from Sigma-Aldrich and used directly.

Sample preparation:

Casting:

Paraffin wax was melted at 80°C. GNP were then added to the liquid paraffin under constant stirring at 1wt%, 2wt%, 4wt%, 6wt%, 8wt%, and 10wt%. At higher loadings (i.e. >6wt%), xylenes were used as a solvent to dissolve wax first, reducing the melt viscosity and facilitate the uniform dispersion of GNP. The liquid composite was sonicated for 1 h prior to solvent evaporation. Samples were poured into a customized aluminum mold (shown in Figure 2-1a) and solidified at room temperature. Disk samples of 1'' in diameter and 5 mm in average thickness were used for subsequent experiments.

Two roll milling:

In order to study the effect of particle orientation on thermal conductivity, composite samples from cast molding was further processed by two roll mill (shown in Figure 2-1b) in which extensive shear force and compression at the nip point of the rolls allow particles to align within the plane. In two roll mill processing, the quality of the composite film depends on the temperature of the rolls, a higher temperature yet still below the melting point of paraffin reduces the chance of film shrinkage by giving the wax molecules enough thermal energy to undergo stress relaxation while the film is still wrapped around the rolls. The speed of the roll is adjusted

so that the front roll rotates faster than the rear roll. It is worth noting that the speed difference between the rolls effectively creates enough shear force at the gap of the two rolls, facilitating the dispersion of GNP and their alignment in the matrix. The composite materials were processed in the rolls for 10 minutes before they were removed. The final product composite sheet is around 0.4-0.5 mm in thickness. Both the through plane and in plane thermal conductivity was measured. Figure 2-1c is the schematic representation of sample preparation routes:

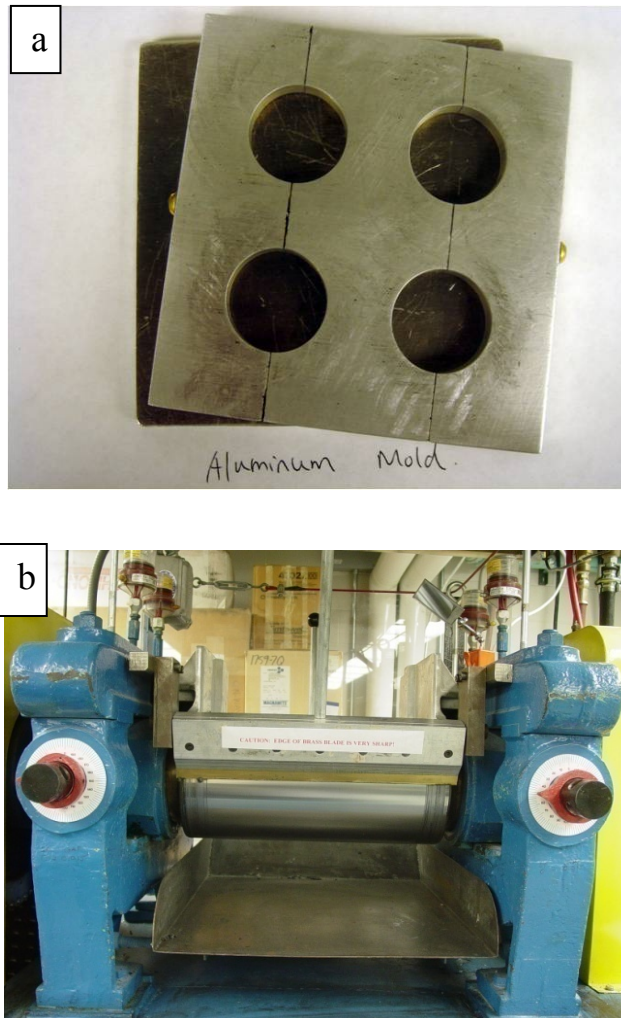
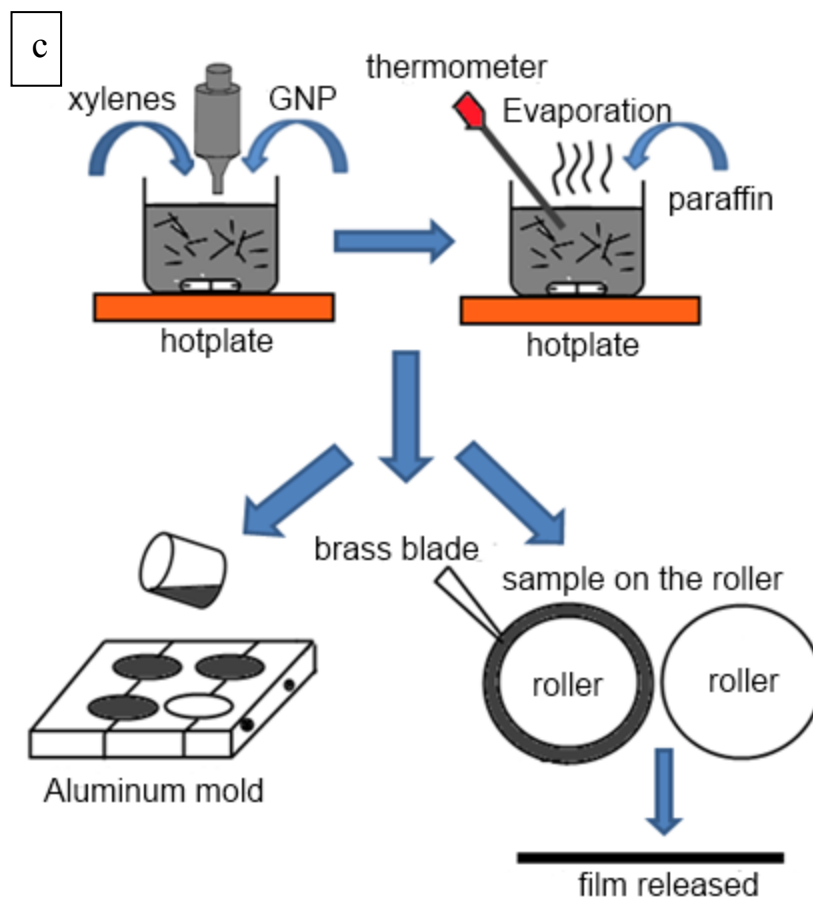


Figure 2-1: (a) Photograph of the customized aluminum mold; (b) Photograph of Bolling two roll mill; (c) Scheme for the sample preparation routes: casting and two roll milling.

Figure 2-1 (cont'd)



2.4 Characterization:

Scanning electron microscopy (SEM)

To investigate the dispersion of GNP particles in paraffin matrix at different loadings, disk samples prepared by casting and two roll milling were liquid nitrogen fractured. The fractured surface was oxygen plasma treated for 5 minutes with a Radio Frequency power at

550W. The treated sample was later gold coated with the Denton Vacuum sputter coater to ensure that the sample is electrically conductive. A JEOL (JSM 6400) scanning electron microscope with an accelerating voltage of 15kV was used to examine the fractured composite surface at a working distance of 15 mm.

Thermal conductivity

The thermal conductivity of paraffin/GNP composites was measured with a Unitherm (TM) Model 2022 (Anter Corporation, Pittsburgh, PA). The test was performed according to ASTM E1530. For samples prepared by cast molding, the average thickness of the sample is 5 mm, and it can be directly used for through-plane thermal conductivity measurement. However, for the samples prepared by two roll mill, the through plane thermal resistance is too small to be measured due to the very small thickness of the composite thin film (0.4-0.5 mm). 4 or 5 sheets were stacked in parallel so that the resistance falls in the range of the instrument. As for the in-plane measurement, the sample was made by compressing the thin sheets released from the roll mills in a closed rectangular mold to a desired thickness, and used a circular iron punch to produce a 1'' disk sample from the cross section of the block (shown in Figure 2-2a,b). All the samples were tested at 20 °C under an applied load of 20 psi.

Electrical conductivity

The resistivity of paraffin/GNP nanocomposites was measured with a Gamry instrument under FAS2™ Femtostat plug system and potentiostatic mode. A rectangular portion was fabricated by a Buehler Isomet™ low speed saw from the cast molded disk samples for the measurements. The resistance of the sample was measured in the frequency range from 0.6Hz to 100kHz and resistivity of samples were calculated by taking the geometry of the sample into account using equation (2.1):

$$\rho = R \times A / L \quad (2.1)$$

R is the resistance of the sample at 1Hz, A is the cross section area of the sample and L is the length of the sample.

Differential scanning calorimetry (DSC)

A sample size of around 5-10 mg was loaded to the DSC sample cell and the data was collected for the 2nd run at a scanning rate of 5°C/min. The solid-solid transformation in paraffin wax, the melting temperature, the crystallization temperature, and the latent heat of paraffin were analyzed by Universal Analysis 2000 Version 4.5A.

Thermogravimetric analysis (TGA)

A sample of 10-15 mg of composite samples was loaded to the Pt pan and the experiments were conducted in nitrogen atmosphere. The temperature range scanned was from 25°C to 500°C with a 25°C/min ramp rate and a 4°C/min resolution upon thermal decomposition events.

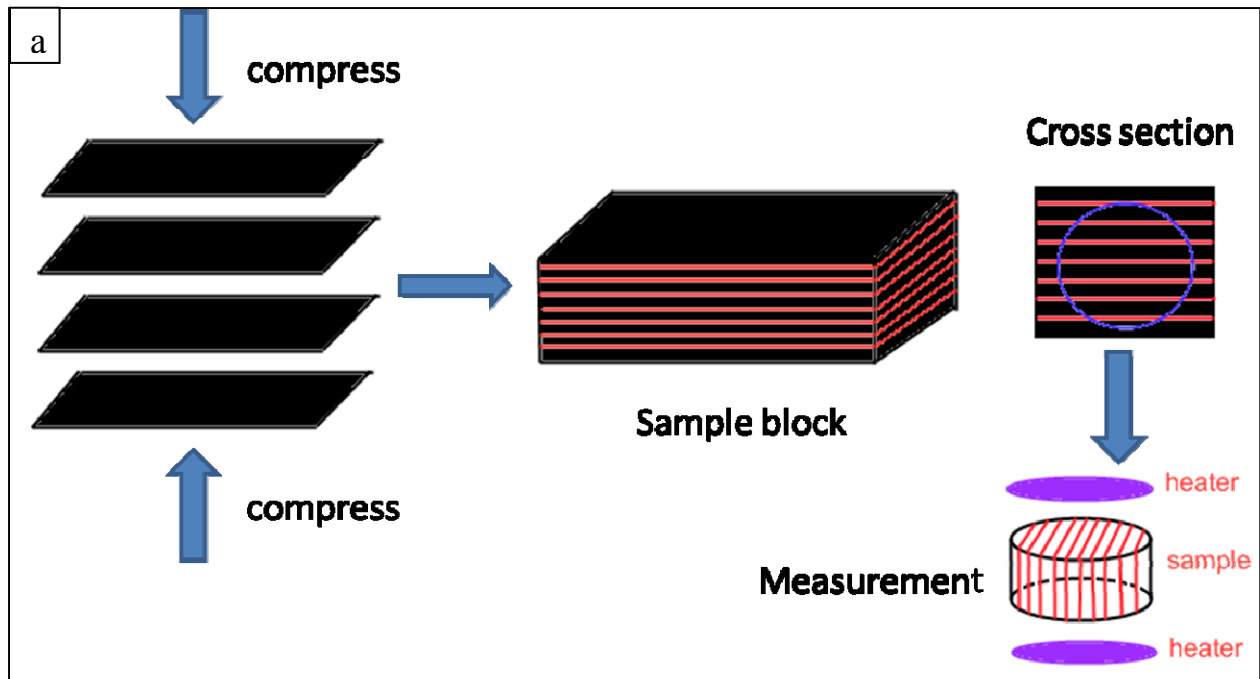


Figure 2-2: (a) Schematics for in plane thermal conductivity measurement of the two roll milled sample; (b) Photograph of the sample prepared from compressing the two roll milled sheets to a desired thickness (1 inch) and a circular cross section of that was produced by a punch.

2.5 Results and discussions:

2.5.1 Morphology

Figure 2-3(a) shows the fractured cross section of the 4wt% GNP-1/paraffin nanocomposites prepared by casting. GNP are either embedded in the paraffin matrix evidenced by the white lines protruding from the background or lying on the surface indicated by their irregular but sharp edges different from the smooth and soft paraffin wax. At the same nanofiller loading, GNP-15 particles in the nanocomposites are more easily recognized due to their larger size shown in Figure 2-3(b). It is also found that unlike the morphology reported by Kalaitzidou [11] in PP/GNP nanocomposites that most nanoplatelets tend to roll up or fold on itself during sample preparation (melt extrusion), GNP in paraffin maintained their platelet shape as a result of the low viscosity of the polymer matrix and thus the high aspect ratio of GNP is not negatively affected in sample fabrication. In the samples prepared by two roll mill with GNP loading at 4wt%, 10wt% shown in Figure 2-3(c-d). It is very clear that particles assumed a preferential alignment as indicated by the white lines in SEM. Figure 2-3(e-f) shows the magnified edge views of the nanoplatelets, it is also evident that the individual nanoplatelet is thin with thickness less than 10 nm and thus they have a very high aspect ratio. The distance between particles was increased due to the expansion of material at the rolling nip point and it is the same compressive and shearing force that contributed to the alignment of the particles.

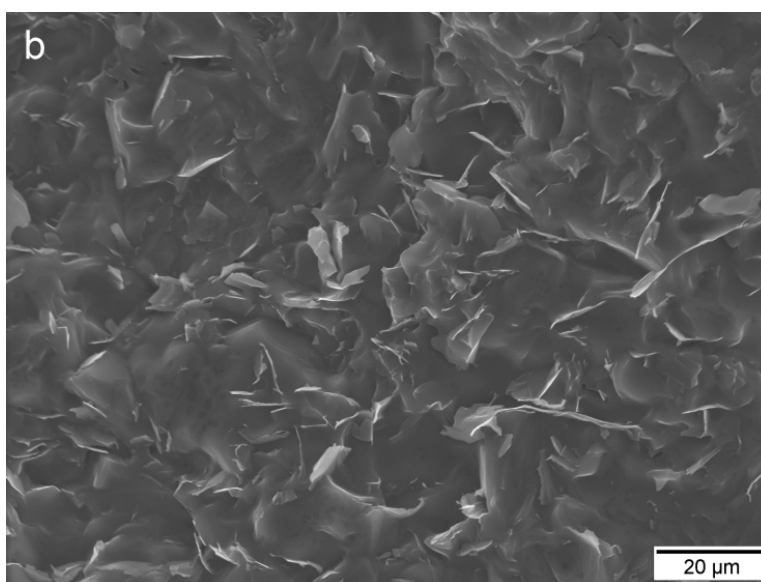
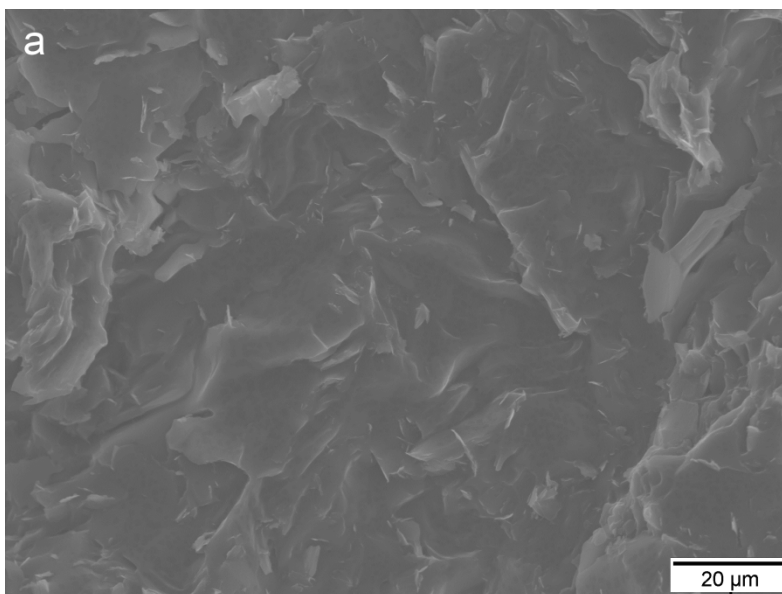


Figure 2-3: a: 4wt% GNP-1/paraffin by casting; b: 4wt% GNP-15/paraffin by casting; c: 4wt% GNP-15/paraffin by two roll mill; d: 10wt% GNP-15/paraffin by two roll mill; e: enlarged edge view of the nanoplatelets (scale bar 100 nm); f: enlarged edge view of one platelet (scale bar: 10 nm)

Figure 2-3 (cont'd)

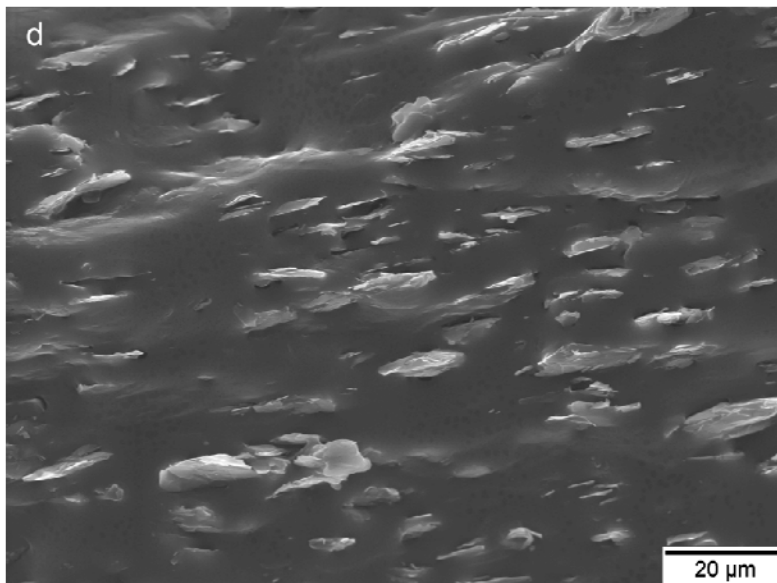
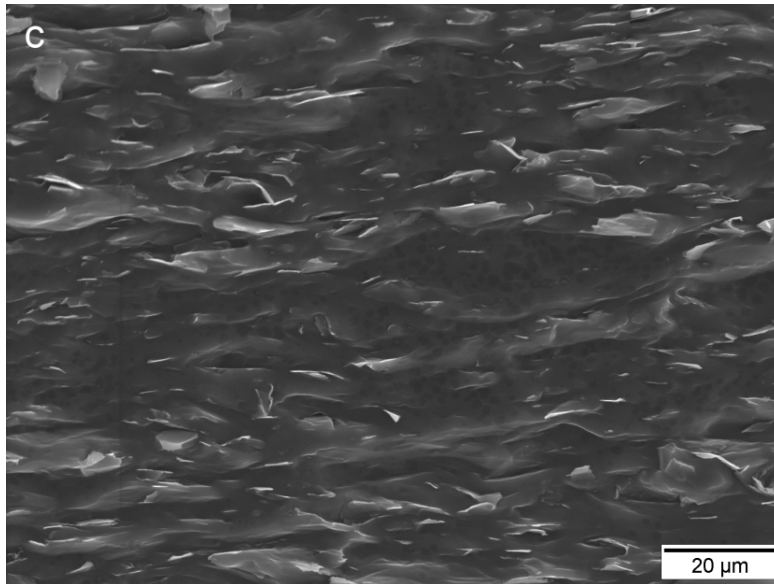
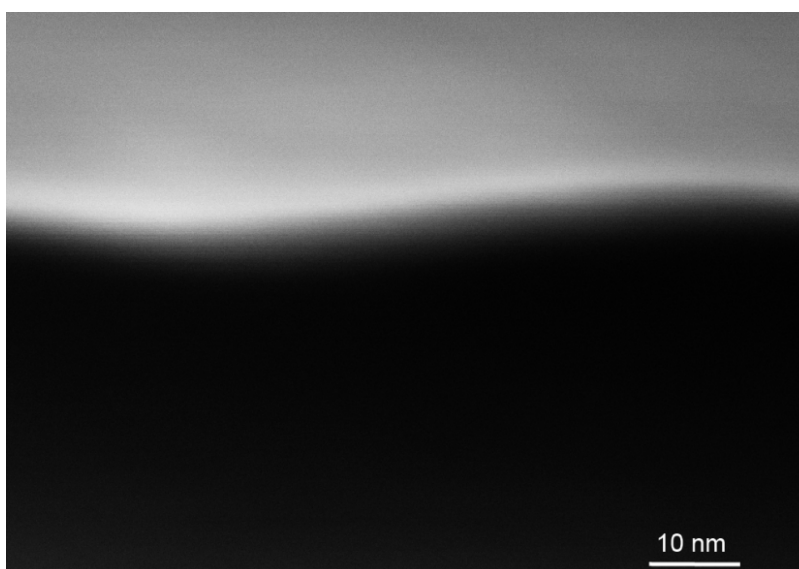
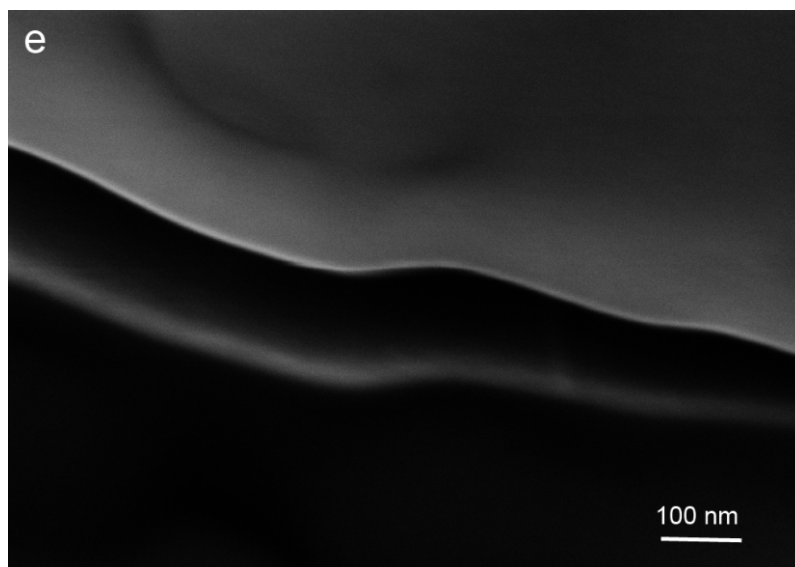


Figure 2-3 (cont'd)



2.5.2 Electrical conductivity of paraffin/GNP nanocomposites:

In order to find out the effect of dispersion of GNP on electrical conductivity of the resulting nanocomposites, the resistivity of paraffin/GNP-1 and paraffin/GNP-15 samples were measured and compared in Figure 2-4. For nanocomposites with GNP-15 as fillers, resistivity

undergoes a sharp decrease from 10^{10} (ohm cm) to around 10^3 (ohm cm) at 1 vol% which suggests that conductive paths were formed in paraffin. However, GNP-1 nanocomposites did not percolate even at 2 vol%. Despite the fact that the absolute number of GNP-1 is almost 250 (15×15) times more than GNP-15 in the composites at the same loading level, the aspect ratio of is much smaller (100 vs. 1000). It can be seen from SEM micrographs that the platelet like morphology for larger nanoplatelets were maintained better than smaller ones, which suggests the importance of filler morphology and aspect ratio on the electrical conductivity of nanocomposites.

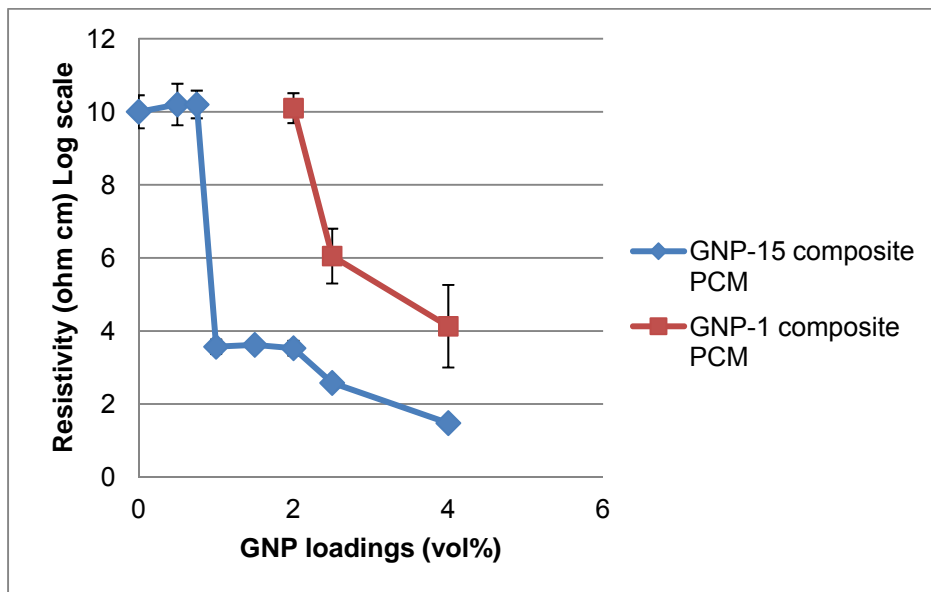


Figure 2-4: Electrical resistivity of GNP/paraffin composite PCM

2.5.3 Thermal conductivity paraffin/GNP nanocomposites:

Thermal conductivity of paraffin/GNP nanocomposites prepared by casting at different filler concentrations was measured and shown in Figure 2-5(a). The thermal conductivity increased linearly for GNP-15 samples up to 2 vol% beyond which the data exhibits super linear behavior. In GNP-1 composites, thermal conductivity also increased linearly with GNP loading,

but the improvement is not as effective as GNP-15 although the absolute number of nanofiller particles is much larger at the same loading level. Given the fact that GNP-15 is superior to GNP-1 in improving the thermal conductivity of paraffin nanocomposites, two samples prepared by two roll mill containing 2vol% and 5vol% GNP-15 in paraffin matrix were used for the measurements. Both samples show higher thermal conductivity in the in-plane direction rather than in the through-plane direction shown in Figure 2-5(b). Aligning the particles in its basal plane direction effectively utilizes the high in-plane thermal conductivity of the graphite nanoplatelets. However, thermal conductivity of the two roll milled sample is not as high as the cast mold samples at the same loading level.

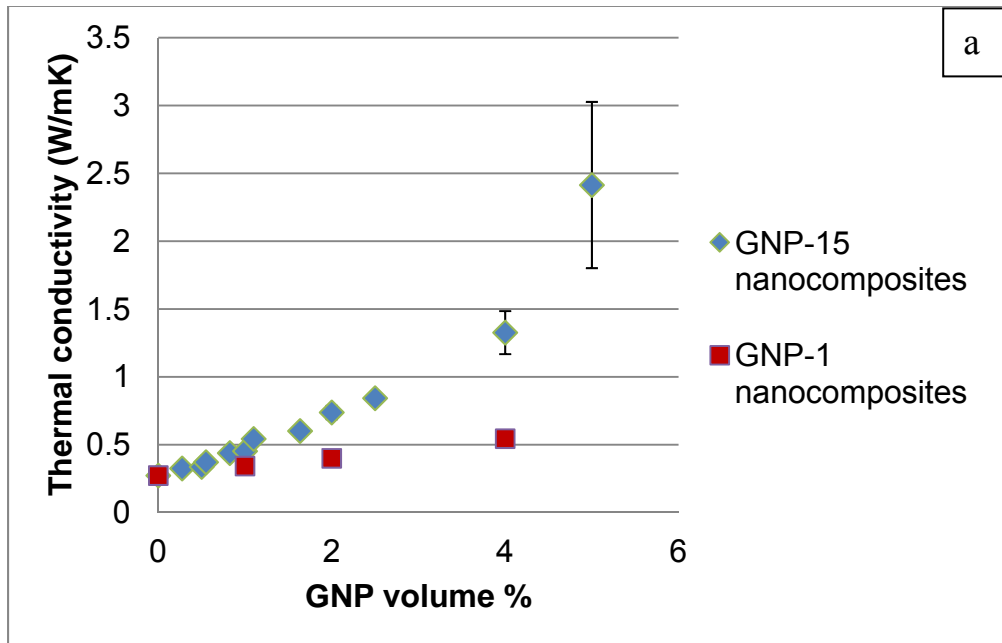
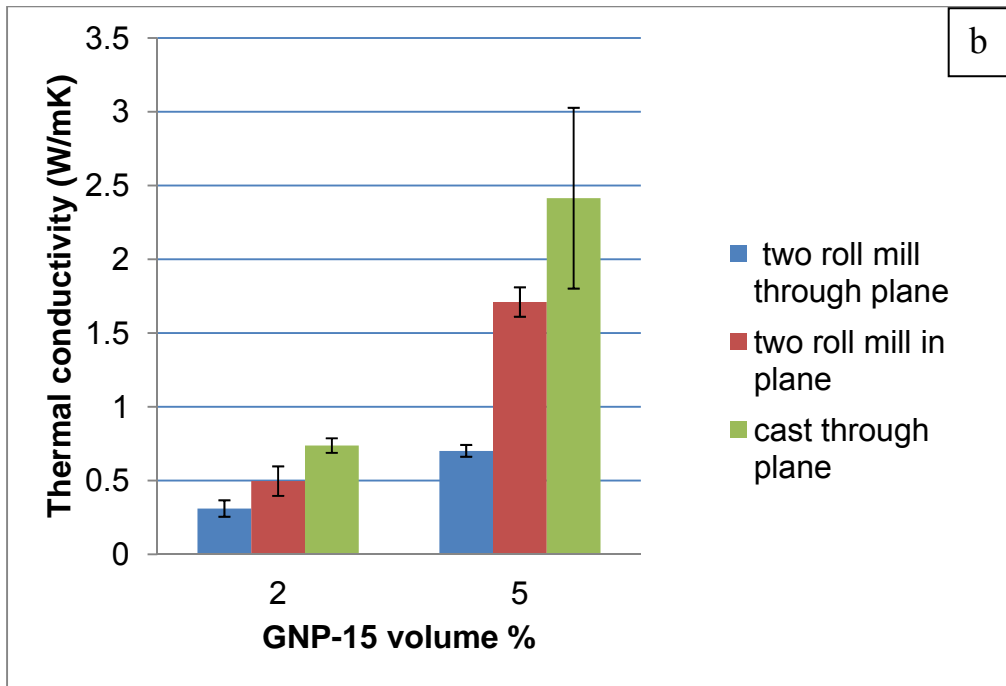


Figure 2-5: (a) Through plane thermal conductivity of GNP/paraffin prepared by casting; (b) Through-plane (left column) and in-plane (middle column) thermal conductivity of GNP-15/paraffin prepared by two roll mill and through-plane thermal conductivity by casting (right column).

Figure 2-5(cont'd)



2.5.4 Thermal interface resistance:

It is obvious that the formation of a continuous chain structure of highly thermally conductive GNP particles inside the polymer is not making a large contribution to the heat conduction of the composites. In fact, similar phenomenon where thermal percolation is not observed or even a slight drop in thermal conductivity in the vicinity of electrical percolation threshold has been reported by other research groups in carbon nanotubes based nanocomposites [12-14]. This interesting effect can be explained by two counteracting processes: incorporation of GNP particles into the matrix introduces new interfaces between the filler and the matrix giving rise to a thermal interfacial resistance (Kapitza resistance). On the other hand, noticeable increase in the number of GNP particles creates a highly conducting phase in the matrix contributing to a better heat conduction. The fact that thermal conductivity only shows a slight

increase in GNP/paraffin possibly indicates that the latter process still dominates. Many researchers have attributed the lack of thermal percolation to the presence of a high thermal interfacial resistance resulting from a weak coupling between the filler and the polymer matrix. In order to find out different parameters that might result in a large interfacial resistance, Xu et al. used molecular dynamics simulation to investigate heat conduction in carbon nanotubes based nanocomposites and the author proposed two major approaches to improve interfacial thermal conductivity (i.e. phonon spectrum matching and better interfacial coupling) as shown in Figure 2-6 [15].

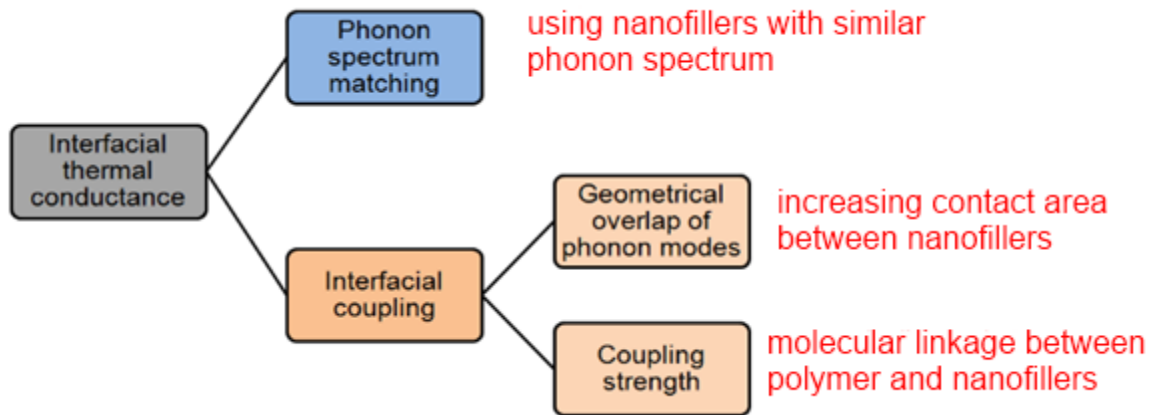


Figure 2-6: overview of the dominate factors in interfacial thermal conductance in carbon based nanocomposites as well as possible techniques to reduce interface resistance. Adapted from ref. 15.

With the above two approaches in mind, we proposed the following discussion for GNP/paraffin nanocomposites studied here. Heat transport in graphene nanoplatelets takes place by phonons of varying frequencies. Phonons are transported from one platelet to another via the polymer in between. Since there is a difference in acoustic properties, the phonon spectrum will be different in these two materials. In addition, due to the weak van der Waals interaction between paraffin and GNP, it is believed that only low frequency phonon vibration modes are

available to carry heat energy. The high frequency phonons, which also carry heat energy, need to interact with other phonons before they can be transferred to low energy vibration states to couple with the polymer matrix according to a theoretical study conducted by Luo et al. [16]. As a result of this combined effect of phonon mismatch as well as weak coupling with the matrix, strong phonon scattering occur at the interfaces that corresponds to a high thermal interface resistance reducing the efficiency of heat transfer in nanocomposites. This process would be more prevalent in nanocomposites containing finer filler particles due to a greater density of interfaces because the chance of phonon scattering at the interface is greater as in the case of GNP-15 and GNP-1 composites.

In terms of nanofiller alignment, random orientations of GNP in paraffin especially at higher GNP loading for the cast molded samples led to significant overlapping among particles which increased the geometric overlap of phonon modes due to a larger physical contact area. On the other hand, two roll mill process not only aligned the particles in the matrix, but also broke GNP aggregates and separated them, disrupting the percolating networks and introducing more phonon scattering at GNP/paraffin interfaces.

As already mentioned previously, thermal interface resistance presents a significant barrier for phonons to transport from one conductive filler particle to another surrounded by a polymer matrix, it is interesting to predict the thermal interface resistance from experimental data. Many models have been proposed to predict the thermal conductivity of nanocomposites, but few have taken the interfacial resistance into account. Nan proposed a model based on carbon nanotubes and assumed an interfacial barrier layers between the nanotubes and the polymer, a Maxwell-Garnett type effective medium approach was used to predict the thermal interface resistance [10]. For the case of isotropically oriented ellipsoidal particles including platelets, the

thermal conductivity ratio K_e/K_m (defined as effective thermal conductivity vs. matrix thermal conductivity) can be expressed by Equation (2.2):

$$\frac{K_e}{K_m} = \frac{3 + f(\beta_x + \beta_z)}{3 - f\beta_x}$$

$$\beta_x = \frac{2(K_{11}^g - K_m)}{K_{11}^g + K_m}; \beta_z = \frac{K_{33}^g}{K_m} - 1 \quad (2.2)$$

where f is the volume fraction of graphite platelets, Assume individual GNP is coated with a very thin interfacial thermal barrier layer, K_{11}^g and K_{33}^g are the equivalent thermal conductivities along transverse and longitudinal axes of a nanoplatelet, and can be expressed in Equation (2.3):

$$K_{11}^g = \frac{K_g}{1 + \frac{2a_k K_g}{tK_m}}; K_{33}^g = \frac{K_g}{1 + \frac{2a_k K_g}{dK_m}} \quad (2.3)$$

where t and d are the thickness and diameter of GNP; a_k is the Kapitza radius defined by:

$$a_k = R_k K_m \quad (2.4)$$

where R_k is the thermal interface resistance. The model described above assumes that the nanofiller particles are completely surrounded by the polymer matrix and they do not touch each other. Since the percolation threshold for GNP/paraffin composites is approximately 1 vol% as suggested by electrical resistivity measurement, the experimental data used for curve fitting are

limited to those below 1 vol%. Assume the diameter and thickness of the GNP-15 particles are 15 μm and 10 nm and the in-plane and through-plane thermal conductivities are 3000 W/m K and 10 W/m K. The thermal interface resistance of approximately 7 to $9 \times 10^{-8} \text{m}^2 \text{K/W}$ produces the best fit with experimental results. This R_k value is very close to the interfacial resistance across the carbon nanotube matrix reported by Cahill and Keblinski group which is about $8.3 \times 10^{-8} \text{m}^2 \text{K/W}$ [17]. Figure 2-7 shows the curve fitting result using this model assuming various interfacial resistances.

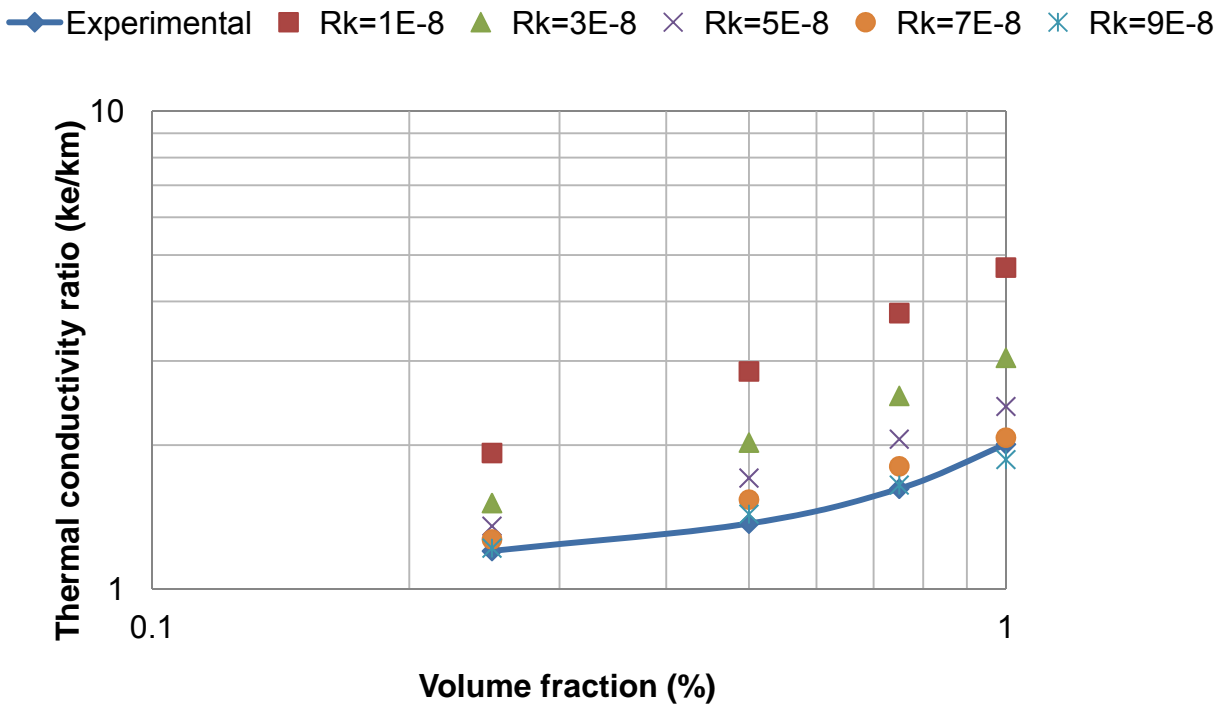


Figure 2-7: Thermal conductivity of paraffin/GNP-15 fitted with effective medium theory below electrical percolation.

2.5.5 Effect of GNP particles on other thermophysical properties of nanocomposites:

Differential scanning calorimetry was used to investigate the effect of GNP on thermo - physical properties of paraffin nanocomposites and its capacity to store thermal energy. Both the melting and cooling behaviors of paraffin/GNP were recorded, two peaks were observed from the DSC analyses which correspond to solid-solid transformation and melting/crystallization of paraffin wax. The relevant enthalpies were calculated by integration the peaks above the base line given by the software itself.

The temperatures that characterize the melting and crystallization peak are not affected significantly by addition of GNP particles. The melting and crystallization enthalpies for paraffin nanocomposites at low GNP concentration did not deviate from neat paraffin very much as opposed to the samples at high loading levels when the composite's ability to absorb and release heat is degraded because of the increasing replacement of paraffin wax with GNP particles. However, the presence of more GNP in the paraffin matrix did not negatively affect the thermal physical properties of wax itself. This can be further supported by compensating the presence of GNP in the composites and recalculating the melting and crystallization enthalpies for paraffin wax alone in the nanocomposites using Equation (2.7). It is found that for both nanocomposites, the heat absorbing and releasing capacity during heating and cooling for paraffin did not degrade but improve slightly with GNP loadings.

$$\Delta H_{wax} = \frac{\Delta H_{comp}}{1 - x_G} \quad (2.7)$$

where ΔH_{comp} is latent heat of composite PCM with GNP. ΔH_{wax} is latent heat of wax in PCM. X_G is the weight fraction of xGnP. Table 2-1 and Table 2-2 collected data from paraffin nanocomposites containing 0wt%, 2wt%, 4wt% and 8wt% GNP-15 or GNP-1.

Table 2-1: Heating and cooling characteristics of GNP-15 composite PCM (average of three samples)

Sample names	Melt peak(°C)	Melting enthalpy of composite (J/g)	Melting enthalpy of wax (J/g)	Cryst. peak(°C)	Cryst. enthalpy of composite (J/g)	Cryst. enthalpy of wax (J/g)
Neat	54.54	185.9	185.9	51.73	186.8	186.8
2wt%	54.82	188.6	192.4	51.27	189.9	193.7
4wt%	55.13	183.5	191.1	51.87	185	192.7
8wt%	54.9	171.9	186.8	51.63	172.9	187.9

Table 2-2: Heating and cooling characteristics of GNP-1 composite PCM (average of three samples)

Sample names	Melt peak(°C)	Melting enthalpy of composite (J/g)	Melting enthalpy of wax (J/g)	Cryst. peak(°C)	Cryst. enthalpy of composite (J/g)	Cryst. enthalpy of wax (J/g)
Neat	54.54	185.9	185.9	51.73	186.8	186.8
2wt%	54.33	186.05	189.85	52.09	187.15	191
4wt%	53.97	180.4	187.9	52.22	180.2	187.7
8wt%	54.35	176.65	192	51.94	178.1	193.5

2.5.6 Thermal gravimetric analysis:

Since graphite is known for its chemical inertness and resistance to thermal degradation, thermal decomposition of paraffin nanocomposites upon addition of GNP was analyzed by TGA in N_2 shown in Figure 2-8. It is shown in the analysis that thermal decomposition of paraffin nanocomposites gradually shifted to higher temperature with increasing GNP. Although the interaction between GNP and paraffin is weak, they still interact with the surrounding matrix and

improve the overall stability of composite PCM. The remaining weight at 500°C, at which temperature paraffin wax was completely thermally decomposed but GNP were unaffected, was close to the initial loadings 0wt%, 2wt%, 4wt% and 8wt% respectively.

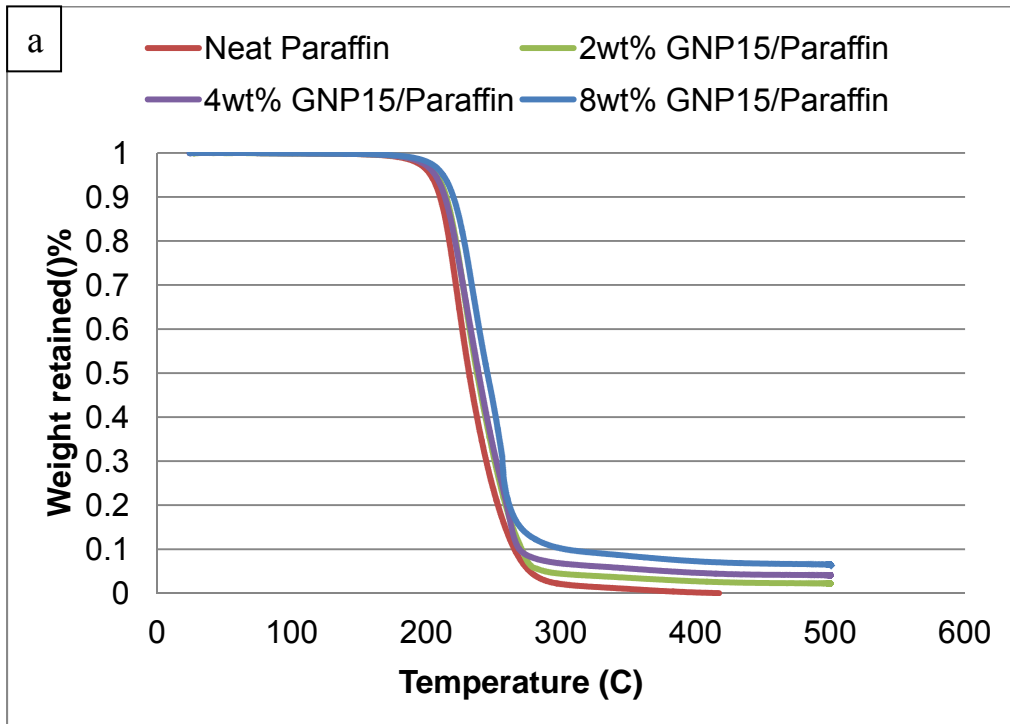
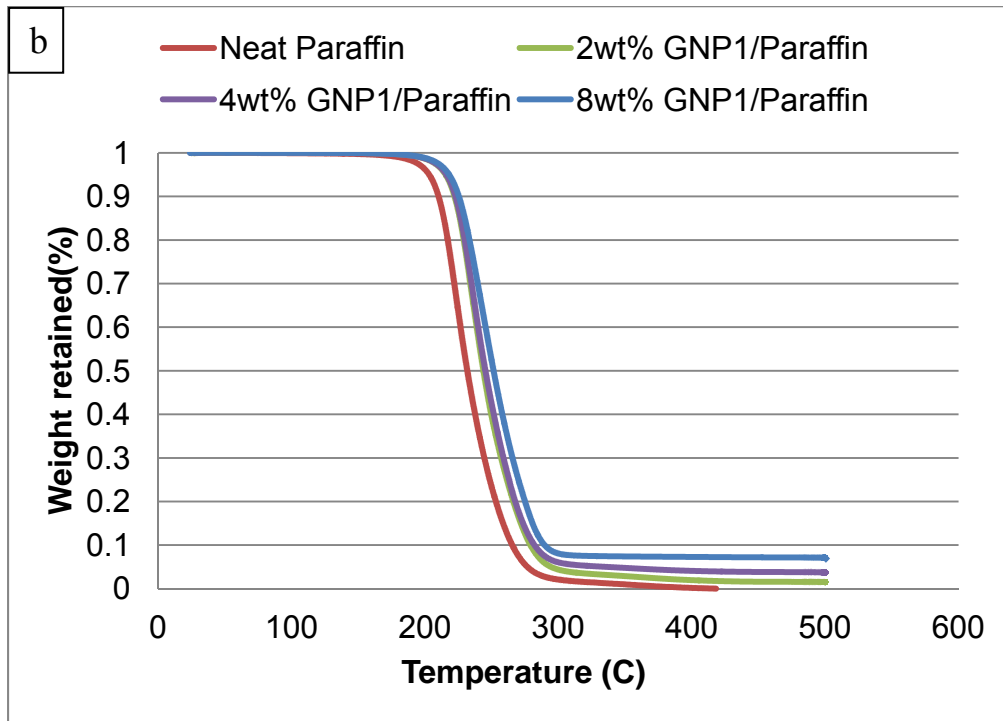


Figure 2-8: (a) TGA analysis of GNP-1/paraffin nanocomposites in N₂. (b) TGA analysis of GNP-15/paraffin nanocomposites in N₂

Figure 2-8(cont'd)



2.6 Conclusions:

GNP of two different sizes (GNP-1 and GNP-15) were successfully mixed with paraffin wax to make a composite phase change materials (PCM) of high latent heat and high thermal and electrical conductivity. In particular, GNP-15 nanocomposites prepared by casting show lower electrical percolation and higher thermal conductivity than GNP-1 counterparts possibly because of the large difference in the aspect ratio of the two nanofillers. The distinctive property enhancements was also observed at the electrical percolation where electrical conductivity increased by many orders of magnitude while thermal conductivity remained almost the same. Lack of thermal conductivity in the nanocomposites can be explained by different mechanisms for electron and phonon transport across the polymer/GNP interface. In particular, phonon

transport is dependent on the physical properties (phonon spectra) of the two components as well as their coupling strength, a high interfacial resistance due to phonon scattering is the major reason for inefficient heat transfer. In comparison, electron transport across interfaces takes place by electron tunneling where physical contact between filler particles is not required. The interfacial contact resistance is believed to account for the much lower than expected improvement in thermal conductivity of the nanocomposites. The interfacial thermal resistance estimated by Nan's model to be 7 to $9 \times 10^{-8} \text{ m}^2 \text{ K/W}$, was found to be comparable to that of carbon nanotubes. For the purpose of thermal energy storage, DSC results show the latent heat of paraffin nanocomposites were not degraded by adding GNP. Latent heat of paraffin alone and the thermal stability of the composite PCM measured by TGA actually improved slightly in the presence of GNP.

Acknowledgements

The author appreciated the generous help from Brian Rook from Composite Materials and Structures Center on operating the two roll mill. Financial support for this project was provided by the Michigan Economic Development Corporation through the 21st Century Jobs Fund.

REFERENCES

References

1. Hasnain, S.M. Review on sustainable thermal energy storage technologies, Part I: heat storage materials and techniques. *Energy Convers Manage.* **1998**, *39*, 1127-1138.
2. Telkes. M. Thermal storage for solar heating and cooling, in: *Proceedings of the Workshop on Solar Energy Storage Subsystems for the Heating and Cooling of Buildings*, Charlottesville, Virginia, USA, 1975.
3. Pillai, K.K.; Brinkworth, B.J.; The storage of low grade thermal energy using phase change materials. *Appl. Energy.* **1976**, *2*, 205-216.
4. Luyt, A. S. Role of polymers in developing phase change materials for energy storage. *eXpress Polym. Lett.* **2008**, *2*, 147-147.
5. Velraj, R.; Seeniraj, R.V.; Hafner, B.; Faber, C.; Schwarzer, K.; Experimental analysis and numerical modeling of inward solidification on a finned vertical tube for a latent heat storage unit. *Sol Energy.* **1997**, *60*, 281-290.
6. Fukai, J.; Kanou, M.; Kodama, Y.; Miyatake, O.; Thermal conductivity enhancement of energy storage media using carbon fibers. *Energy Convers Manage.* **2000**, *41*, 1543-1556.
7. Elgafy, A.; Lafdi, K.; Effect of carbon nanofiber additives on thermal behavior of phase change materials. *Carbon.* **2005**, *43*, 3067-3074.
8. Pincemin, S.; Olives, R.; Py, X.; Highly conductive composites made of phase change materials and graphite for thermal storage. *Sol Energy Mater Sol C.* **2008**, *92*, 603-613.
9. Kim, S.; Drzal, L. T.; High latent heat storage and high thermal conductive phase change materials using exfoliated graphite nanoplatelets. *Sol Energy Mater Sol C.* **2009**, *93*, 136-142.
10. Nan, C. W.; Liu, G.; Lin, Y.; Li, M. Interface effect on thermal conductivity of carbon nanotube composites. *App Phys Lett*, **2004**, *85*, 3549-3551.
11. Kalaitzidou, K.; Fukushima, H.; Drzal, L. T.; Multifunctional polypropylene composites produced by incorporation of exfoliated graphite nanoplatelets. *Carbon.* **2007**, *45*, 1446-1452.
12. Mamunya, Y.; Boudenne, A.; Lebovka, N.; Ibos, L.; Candau, Y.; Lisunova, M. Electrical and thermophysical behavior of PVC-MWCNT nanocomposites. *Compos Sci Technol* **2008**, *68*, 1981-1988.

13. Grunlan J. C.; Kim, Y. S.; Ziaee, S.; Wei, X.; Abdel-Magid, B.; Tao, K. Thermal and mechanical behavior of carbon-nanotube-filled latex. *Macromol Mater Eng* **2006**, *291*, 1035-1043.
14. Moisala, A.; Li, Q.; Kinloch, I. A.; Windle, A. H. Thermal and electrical conductivity of single and multi-walled carbon nanotube-epoxy composites. *Compos Sci Technol* **2006**, *66*, 1285-1288.
15. Xu, Z.; Buehler, M.J. Nanoengineering heat transfer performance at carbon nanotube interfaces. *ACS Nano*, **2009**, *3*, 2767-2775.
16. Luo. T.; Lloyd, J. R. Non-equilibrium molecular dynamics study of thermal energy transport in Au-SAM-Au junctions. , *Int. J. Heat Mass Transfer*, **2010**. *53*, 1-11.
17. Huxtable, S.; Cahill, D. G.; Shenogin, S.; Xue L.; Ozisik, R.; Barone, P et al. Interfacial heat flow in carbon nanotube suspensions. *Nat Mater*. **2003**, *2*, 731-734.

Chapter 3 Thermal Conductivity of a Monolayer of Exfoliated Graphene Nanoplatelets Prepared by Liquid-Liquid Interfacial Self-Assembly

3.1 Abstract:

A monolayer film composed of exfoliated graphene platelets GNP was extracted from a chloroform-water interface and supported on a glass substrate. The nanoplatelets are interconnected at the edges without overlapping forming a very densely packed structure with uniform thickness. Micro-Raman spectroscopy with a 50 mW 532 nm laser generating heat at the center of the sample was used to probe the thermal conductivity of the GNP monolayer at different power levels. The Raman G peak shift of graphite was used to record the local temperature rise in the monolayer. The cross sectional area of heat conduction is determined by the thickness of individual platelets. A UV-Vis spectrometer was used to measure the absorption of light by the monolayer. Depending on the interface density, thermal conductivities are estimated to be 380 W/m K and 290 W/m K for monolayers with average particle size of 10 μm and 5 μm , respectively. This chapter is based on a journal publication: Xiang, J., Drzal, L. T (2010) Thermal Conductivity of a Monolayer of Exfoliated Graphite Nanoplatelets Prepared by Liquid-Liquid Interfacial Self-Assembly. *Journal of Nanomaterials*, 2010,1-6.

3.2 Introduction

This chapter discusses a novel approach to visually inspect the heat conduction in a percolated network of pure GNP, providing insights into the effect of interfacial resistance on thermal conductivity.

Earlier work has shown that graphene supports 2D phonon propagation giving rise to a remarkably high thermal conductivity in its basal plane [1]. It is difficult to use conventional techniques such as 3ω , laser flash, and thermal bridge to measure thermal conductivity of this very delicate system such as single layer graphene without causing physical damage during sample preparation and handling. Confocal micro-Raman microscopy, a non-destructive, optical technique has been successfully used to extract thermal properties of thin films [2,3]. Balandin et al. successfully measured thermal conductivity of a mechanically cleaved single layer graphene ribbon with Raman spectroscopy that uses the Raman G peak of graphene as a probe for local temperature determination at the laser spot. The measured thermal conductivity of graphene is 4400-5300 W/m K [4]. Similarly with Raman spectroscopy, Geim et al used temperature readout obtained from the intensity ratio of Stokes to anti-Stokes signal to study the thermal properties of a large circular shaped graphene membrane also obtained from micromechanical cleavage and they concluded thermal conductivity to be 600 W/m K [5]. These single layer graphene were all suspended over a micro trench with their edges connecting to either bulk graphite or gold heat sinks. Recently, Ruoff et al reported a CVD grown graphene monolayer suspended or supported over a holey Au/SiN substrate. The thermal conductivity of graphene was measured by monitoring the graphene G peak shift with laser heating. The measured conductivities for suspended and supported graphene are 2500+1100/-1050 W/m K and 370+650/-320 W/m K respectively [6]. It was surmised that the huge difference is due to the phonon leakage and

scattering at the substrate-graphene interface. More recently, Balandin et al investigated the dimensional crossover of thermal transport in few-layer graphene (FLG) using the same technique, they showed that the room temperature thermal conductivity changes from 2800 W/m K to 1300 W/m K as the number of atomic planes in FLG increases from 2 to 4 [7].

Despite the numerous literature that focus on the thermal conductivity of graphene and few-layer graphene, there is no report that investigates the thermal conductivity of a monolayer film consisting of individual graphene nanoplatelets. Here, a monolayer film of GNP was extracted from a liquid-liquid interface following the procedures reported by Biswas [8] and deposited on a substrate for thermal conductivity measurement by confocal Raman spectroscopy that shed light on the effectiveness of those highly conductive nanoplatelets in heat conduction. In a monolayer, individual GNP is lying flat on the glass substrate and densely connected to each other resembling a percolated conductive network in a nanocomposite except that the nanoparticles are highly ordered with well defined contacts instead of a random distribution of particles with uncontrolled contacts. Heat spreads in a 2D plane in the monolayer and the efficiency of heat conduction of such monolayers was studied.

3.3 Experimental details:

Materials:

Two kinds of GNP produced from different graphite sources were measured and their surface areas were determined by Brunauer-Emmet-Teller (BET) using N₂ adsorption at 77K to be 20-40 m²/g and 200-220 m²/g, and are referred to as low surface area (LSA) GNP and high surface area (HSA) GNP in later discussion. Chloroform, used for liquid-liquid interface

extraction of a monolayer of GNP was purchased from J.T. Baker and used directly without purification.

Extraction of a Monolayer GNP at the Liquid-Liquid Interface:

A monolayer of densely packed GNP particles was prepared on the glass substrate following the procedure by Biswas [8]. To summarize the process, GNP were dispersed in chloroform at 0.1 mg/ml. The supernatant of the suspension was obtained by 10 min centrifugation at 5000 rpm. Then water was added to the supernatant solution followed by high power sonication. GNP particles then quickly adsorbed at the chloroform-water interface and a monolayer was extracted on a glass slide. The samples were dried in air and then annealed at 250 °C for 2 h. The area of GNP coated region is 3 cm × 2.5 cm.

UV/Vis Spectroscopy:

The optical transparency of the monolayer coated glass slide was measured by UV-Vis spectrometer (Perkin Elmer Lambda 900) to determine the amount of light absorbed by the monolayer. The amount of light transmitted was measured and the light absorbed by GNP monolayer was calculated from subtracting the percentage transmitted from the total light source.

Scanning Electron Microscopy

A JEOL JSM-7500F scanning electron microscope was used to examine the morphology of the monolayer on the glass slide. The sample was not gold coated and the imaging was done at 5kV at working distance of 4.5 mm.

Confocal Raman Spectroscopy:

A LabRAM ARAMIS laser Raman spectrometer (Horiba Scientific) with 532 nm 50mW DPSS laser was used to probe the G band of GNP particles. To determine the temperature

dependence of G peak, an INSTEC (STC 200) heating stage was used to heat the sample and a very low laser power was used to collect the Raman signal to avoid laser induced heating. Monolayers of both LSA and HSA GNP were prepared on the microscopic glass slides for subsequent measurements. The laser was focused on the center of the monolayer and a filter that controls different amount of laser coming through the objective lens was used to induce different levels of heating in the samples. A D1, D06, D03, D0 filter was used in each experiment that corresponds to 10%, 25%, 50% and 100% laser power. Both the 50× and 100× objective lenses were used for each sample measured. The laser spot size r_0 was 0.24 μm and 0.19 μm for the 50× and 100× respectively which were determined using $r_0 = \lambda/\pi\text{NA}$, where NA is the numerical aperture value of 0.9 and 0.75 for the ×100 and ×50 objectives.

3.4 Results and discussions:

3.4.1 Scanning electron microscopy:

The formation of a stable monolayer of GNP particles that were closely connected without overlapping was driven by the gain in interfacial energy that enables the nanoplatelets to be adsorbed to the oil-water interface [9-11]. Since these graphene nanosheets are highly hydrophobic on their basal planes while the oxygen functional groups on the edges render them hydrophilic, it is expected that a meniscus will be generated around the particles and ‘like’ menisci overlap to generate large attractive capillary force to form a close packed structure at the liquid-liquid interface [11,12]. While the magnitude of this lateral capillary force is negligible for spherical particles with diameter less than 10 μm [13], Bowden et al showed that, for planar shaped particles at the liquid-liquid interface, the lateral capillary force is quite significant even

for particles with thicknesses of few nanometers [11]. Depending on the starting material and intercalation and exfoliation conditions, the average thickness of individual nanoplatelets may vary which will be reflected in the optical transparency measurement.

Figure 3-1(a,b) shows the SEM images of the two glass substrates coated with LSA and HSA GNP monolayers. From SEM micrographs, individual platelets come into contact with each other at the edges (indicated by arrows in the figures) so well that there is no noticeable gap left between them thanks to the more regular geometry of the platelet edges. In some portions of the glass substrate, gaps can be observed between nanoplatelets but every single one is connected to the adjacent particle without overlapping for both the LSA and HSA monolayers which proves both interfacial energy minimization and the strong edge interaction among nanoplatelets. With multiple inspection of different parts of the monolayers, it is concluded that the LSA monolayer has an average particle size of around 5-10 μm . In the HSA monolayer, however, more gaps exist among individual platelets and the average size of the platelet is within 1-5 μm . It is obvious from the SEM images that the interface density in the HSA monolayer is higher than the LSA monolayer.

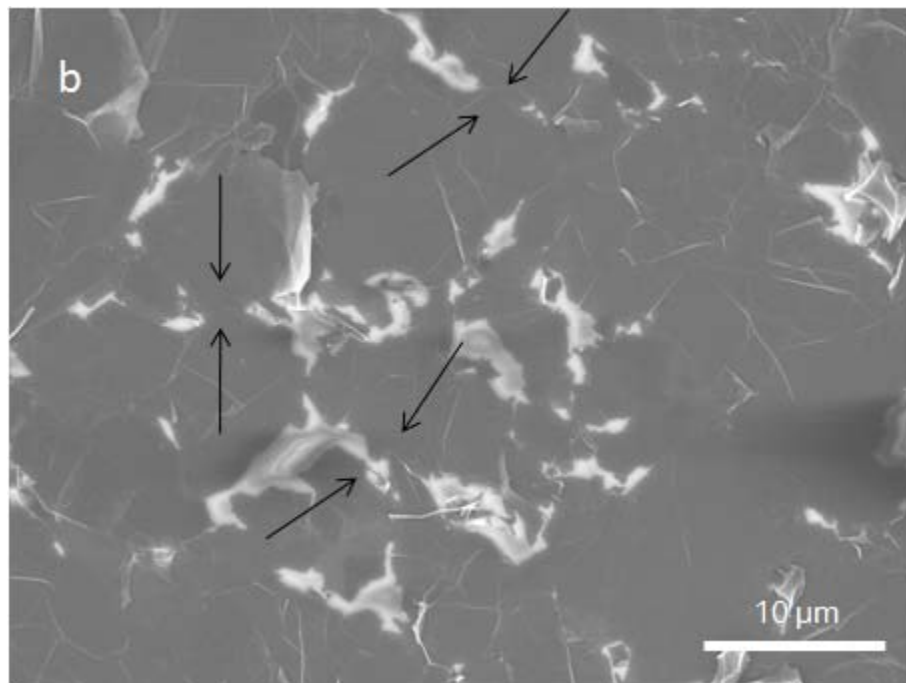
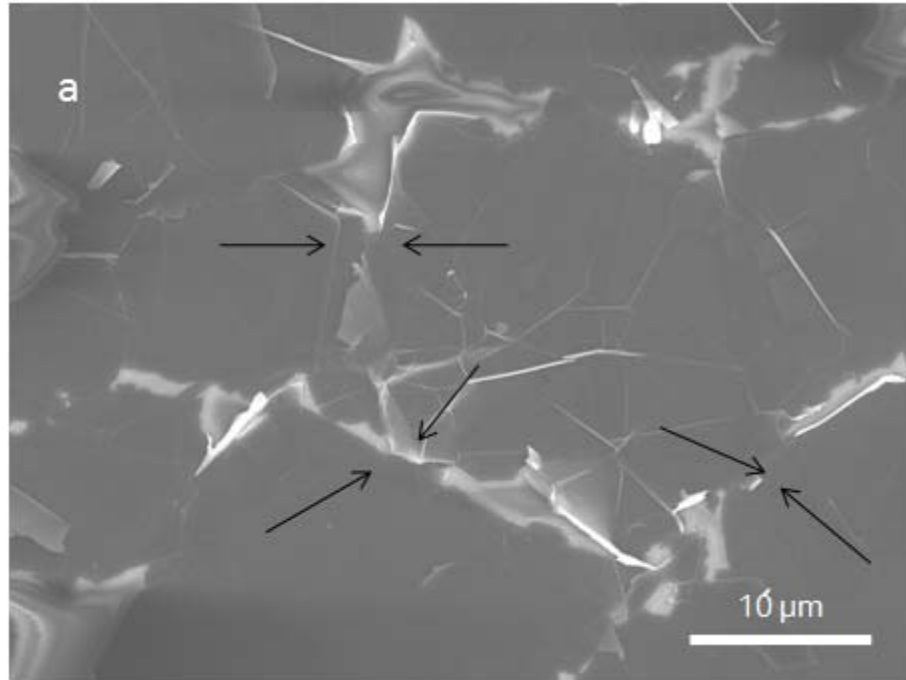


Figure 3-1: (a) SEM image of a LSA GNP monolayer film supported on a glass substrate. (b) SEM image of a HSA GNP monolayer film supported on a glass substrate.

3.4.2 Optical Transmission and Absorption of GNP Monolayers:

The optical transparency of those monolayers was determined by scanning a blank glass slide and a GNP coated slide to eliminate the effect of reflective loss from the slides. Since the reflection of the graphite nanosheets is negligibly small [14], it is not accounted for in this calculation. The amount of light absorbed was calculated by subtracting the light transmitted through the glass slide:

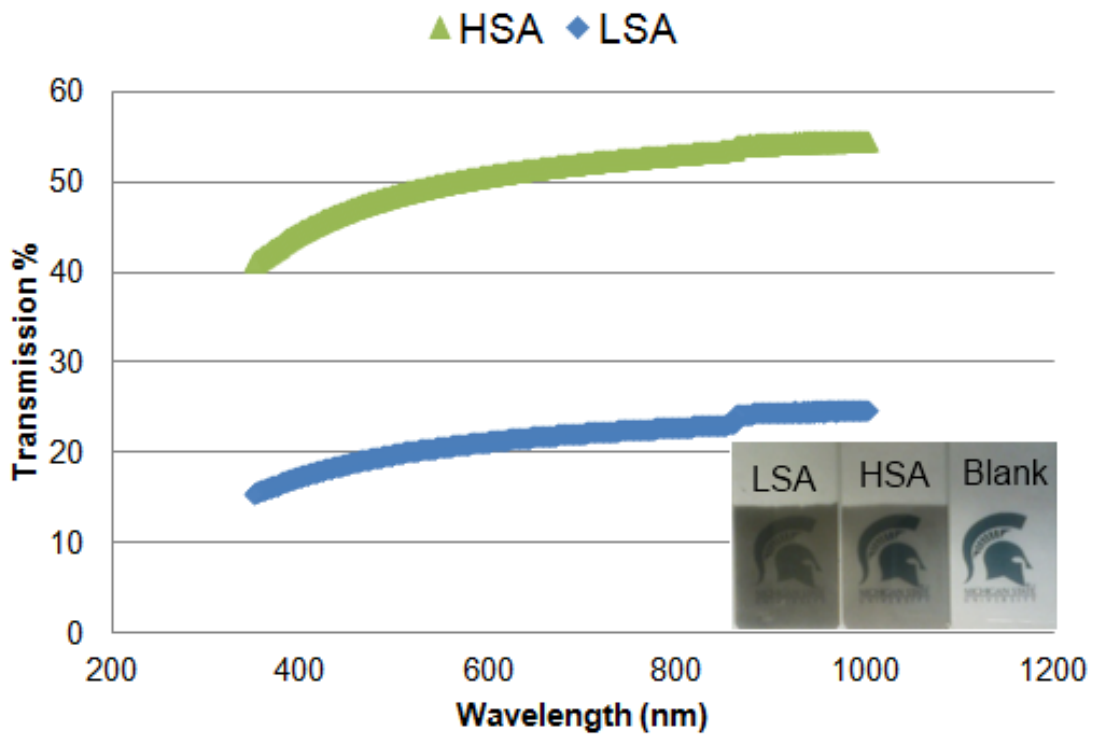


Figure 3-2: Percent transmission of light for LSA and HSA monolayers scanning from 350 nm to 1000 nm. Inset is the photo of LSA and HSA coated monolayers supported on glass substrates as well as the blank slide.

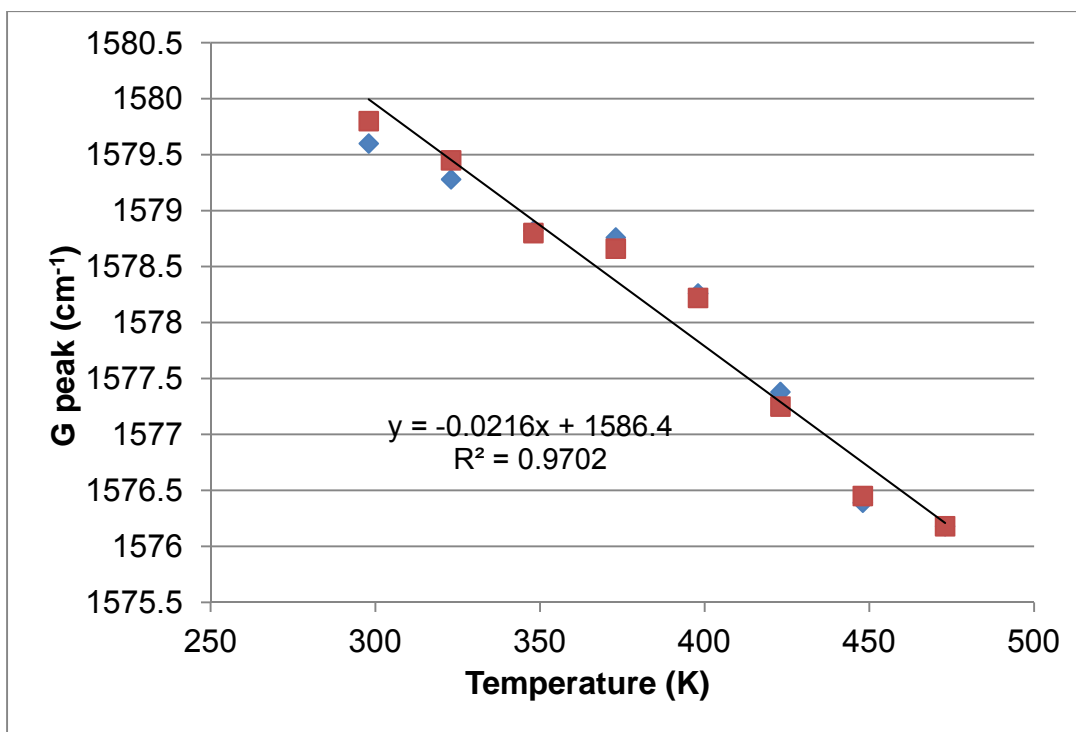


Figure 3-3: Raman G band shift of GNP with temperature and linear curve fitting with Microsoft Excel. Two measurements were conducted indicated by blue and red marks.

A (absorption) = $1 - T$ (transmission). Figure 3-2 shows the percentage transmission of light for both the LSA and HSA monolayers from 350 nm to 1000 nm. The optical transparency for the LSA and HSA monolayer is 20.5 % and 49.6 %, respectively at the 532 nm. The absorption is then calculated to be 79.5 % and 50.4 % for the LSA and HSA monolayers. The fact that the HSA GNP went through better intercalation and exfoliation contributes to the production of much thinner nanoplatelets, which boosts the optical transparency. The thickness of the individual HSA GNP and LSA GNP were previously measured to be around 10 nm and 20 nm respectively by AFM [8].

3.4.3 Confocal Micro-Raman Spectroscopy Analysis:

The laser induced heating of the graphene nanoplatelets causes a red shift of the G band because of bond softening. The G band shift is believed to be linearly dependent on the temperature of the sample [15]. A heating stage was used to heat individual GNP and the Raman signal was collected at a very low laser power. Two measurements were taken at each temperature up to 473K. The slope of the temperature dependence of G peak was determined to be $-0.021 \text{ cm}^{-1}/\text{K}$ shown in Figure 3-3. However, in the monolayer samples, heat absorbed by GNP propagates to the edge of the platelet and the large thermal interface resistance is expected to scatter the phonons (lattice vibrations). This is in stark contrast to constructing a graphite or Au heat sink around an individual nanoplatelet. A phonon being transported along the monolayer encounters numerous interfaces that reduce the heat conduction efficiency. It is necessary to focus the laser on the center of the monolayer to ensure that heat spreads uniformly in a circular geometry. In fact, if the laser beam was focused on the edge of the sample, the local temperature will increase much higher due to the presence of a boundary that impedes heat dissipation. During the experiment, the edges of the monolayer sample was kept at ambient temperature at around 300K, additional heat sinks were not used because of the huge surface area of the monolayer compared with the laser spot size. The Raman G-peak shift was collected at different laser power levels (i.e. 100%, 50%, 25% and 10%) with the selection of a proper filter. Figure 3-4(a,b) shows the G-peak shift at different power levels for both the LSA and HSA monolayers. The presence of oxygen functional groups on the edges of GNP are likely to alter the carbon bonding from sp^2 to sp^3 type and this gives rise to a D band in the Raman signal (1350 cm^{-1}). Due to the difference in the size of the nanoplatelets in LSA and HSA monolayer, the HSA

sample has more edge areas exposed to the laser and this provides a possible explanation to a higher D band observed in HSA samples.

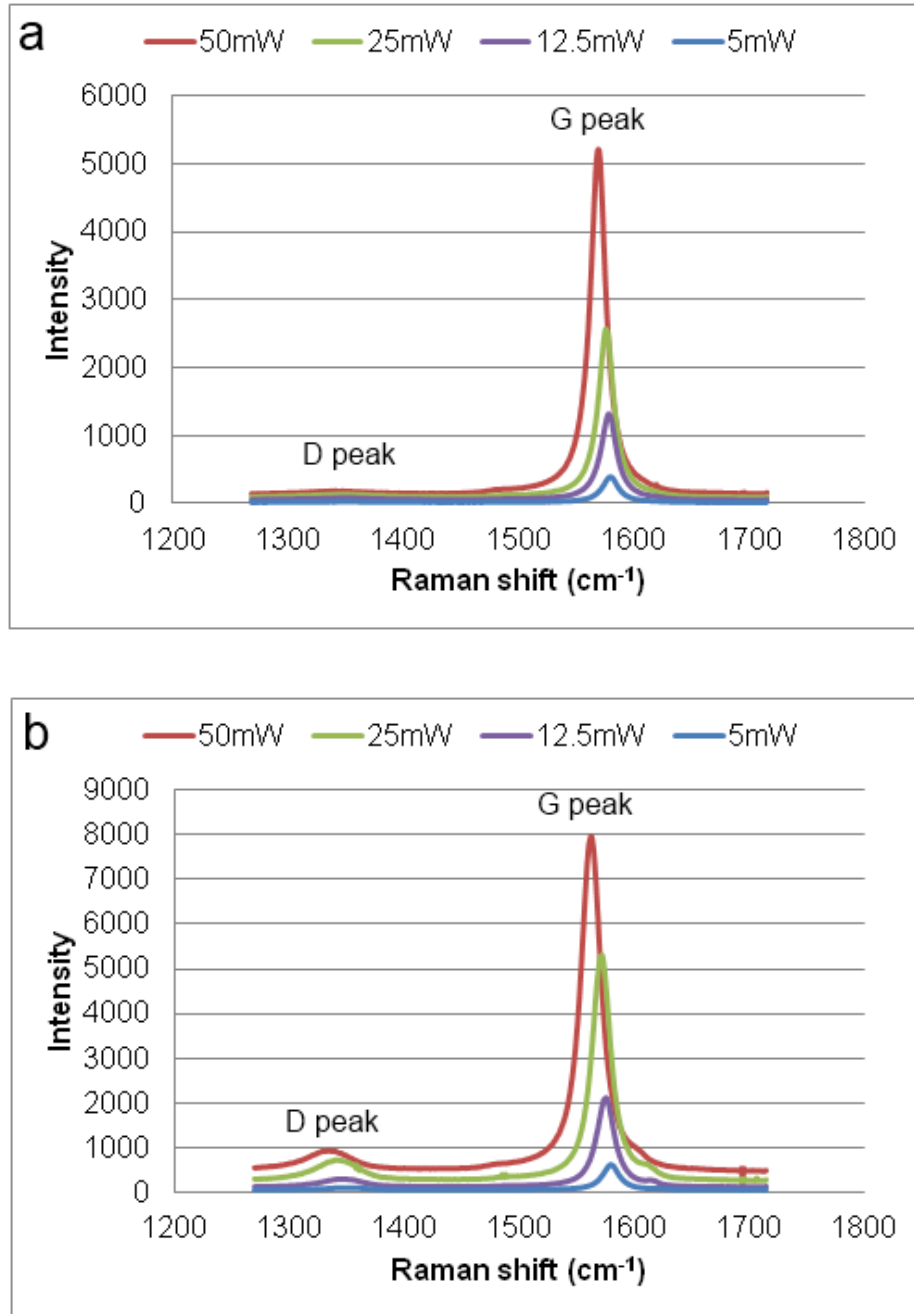


Figure 3-4: (a) Raman G peak shift of the LSA monolayer at different laser power levels. (b) Raman G peak shift of the HSA monolayer using different laser power levels.

3.4.5 Calculation of the Thermal Conductivity of GNP Monolayer:

The temperature rise at the center of the monolayer caused by the Gaussian-shaped laser heating is proportional to the absorbed laser power and inversely proportional to the efficiency of heat conduction. The volumetric laser heating is $q_v = q_0/t \exp(-r^2/r_0^2)$ with r_0 being the laser spot size, r being the radial position measured from the center of the laser beam. Here, q_0 is the absorbed laser power per unit area at the laser spot and t is the thickness of monolayer thickness which is the same as the thickness of individual platelets. The glass substrate ($\kappa = 1$ W/m K) interacts with the phonons and causes phonon leakage which reduces the thermal conductivity. The temperature distribution of the supported monolayer can be obtained by the steady state form of the heat diffusion equation in cylindrical coordinate following Cai's approach [6]:

$$\frac{1}{r} \frac{d}{dr} \left(r \frac{dT}{dr} \right) - \frac{g}{\kappa t} (T - T_a) + \frac{q_v}{\kappa} = 0 \quad (3.1)$$

where g is the interfacial thermal conductance per unit area between the monolayer and the substrate as well as the air molecules. κ is the thermal conductivity of the monolayer, T_a is the ambient temperature. From the Gaussian-shaped laser heating, the total absorbed power by the monolayer Q is:

$$Q = t \int q_v 2\pi r dr = q_0 \pi r_0^2 \quad (3.2)$$

Let $\theta = T - T_a$ and $Z = (g/\kappa t)^{1/2} r$, equation (3.1) can be converted to a nonhomogeneous Bessel's equation:

$$\frac{\partial^2 \theta}{\partial z^2} + \frac{1}{z} \frac{\partial \theta}{\partial z} - \theta = -\frac{q_0}{g} \exp\left(-\frac{z^2}{z_0^2}\right) \quad (3.3)$$

The solution to the above equation is:

$$\theta(z) = C_1 I_0(z) + C_2 K_0(z) + \theta_p(z) \quad (3.4)$$

where $I_0(z)$ and $K_0(z)$ are the zero-order modified Bessel functions of the first and second kind.

The particular solution $\theta_p(z)$ can be obtained using the variation of parameters method and is found to depend on q_0/g [16]. The temperature rise in the monolayer measured by Raman laser

is:

$$\theta_m = \frac{\int_0^{\infty} \theta(z) \exp\left(-\frac{z^2}{z_0^2}\right) z dz}{\int_0^{\infty} \exp\left(-\frac{z^2}{z_0^2}\right) z dz} \quad (3.5)$$

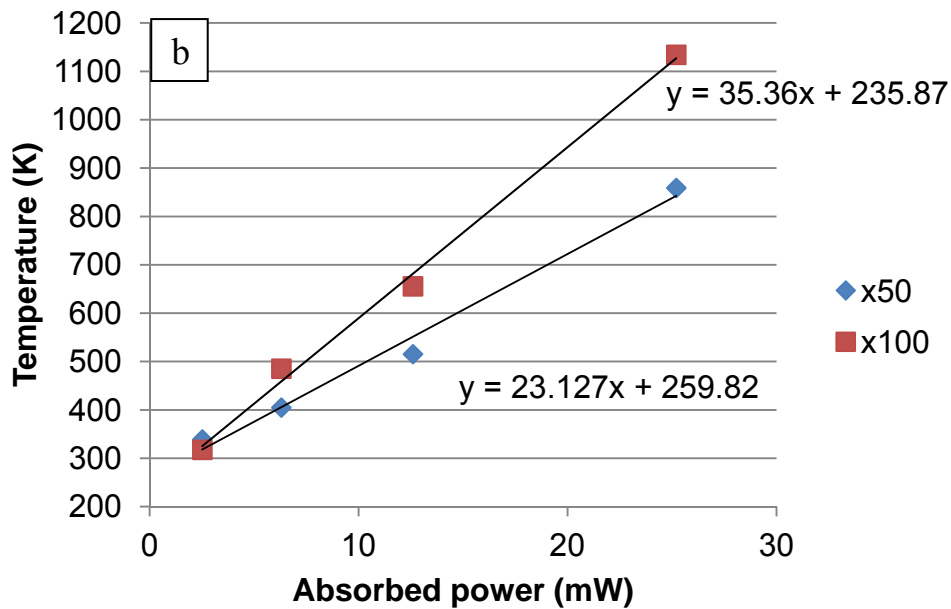
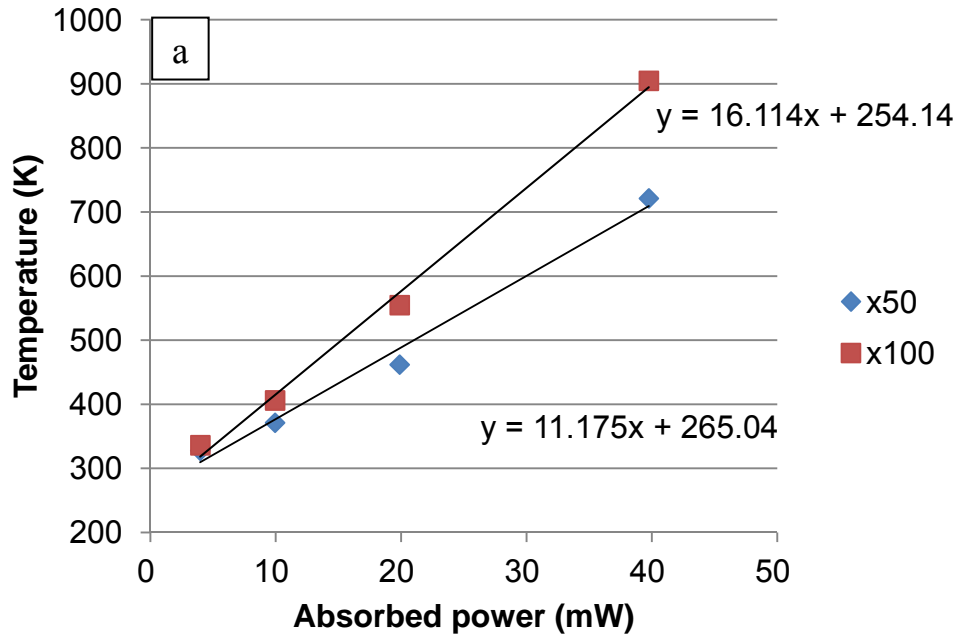


Figure 3-5: (a) Local temperature of an individual GNP at the center of a LSA monolayer vs. the absorbed laser power with x50 and x100 objectives. The solid lines represent the linear curve fittings. (b) Local temperature of an individual GNP at the center of a HSA monolayer vs. the absorbed laser power with x50 and x100 objectives. The solid lines represent the linear curve fittings.

The measured thermal resistance defined as $R = \theta_m / Q$ can be calculated from equation 3.2 and 3.5. Given the temperature dependence of Raman G peak, the temperature rise θ_m and absorbed power Q is found to be linearly related as is shown in Figure 3-5(a,b) and the slope of which yields R_{LSA} equal to 1.12×10^4 K/W and 1.61×10^4 K/W respectively for the LSA monolayer with 50 \times and 100 \times objectives. Similarly, R_{HSA} equals to 2.31×10^4 K/W and 3.54×10^4 K/W for the HSA monolayer with 50 \times and 100 \times objectives. The ratio of the two R values is found to be dependent only on g/κ . With one of the R values measured with either objective, g^2/κ can be further obtained. After a curve fitting procedure for g/κ and g^2/κ , it is found that $g \approx 50$ MW/m²K and $\kappa_{LSA} \approx 380$ W/m K for the LSA monolayer while $g \approx 30$ MW/m²K and $\kappa_{HSA} \approx 290$ W/m K for the HSA monolayer. Due to the difference in GNP size, the HSA monolayer has a higher interface density than the LSA monolayer which might cause the reduction in overall efficiency of heat conduction due to strong phonon scattering at the particle interfaces.

3. 5 Conclusions:

A densely packed monolayer of GNP was successfully extracted from a chloroform-water interface driven by interfacial energy minimization and attractive capillary interactions. Confocal micro-Raman spectroscopy was used as a heater and a thermometer to probe the heat conduction efficiency of monolayers made from GNP of different sizes and thicknesses. The presence of interfaces in the monolayers significantly affects thermal conductivity, reducing the thermal conductivity in this assembly of graphene nanoplatelets by almost an order of magnitude lower than the highest reported value in the literature measured by the same technique. However,

the in-plane thermal conductivities of both monolayers are still high with negligible cross plane conduction making it a promising candidate for applications that require fast heat dissipation to reduce hot spots.

Acknowledgement:

The authors wish to acknowledge the support of the State of Michigan 21st Century Jobs Fund for partial support of this research.

REFERENCES

References

1. Nika, D. L.; Ghosh, S.; Pokatilov, E. P.; Balandin, A. A. Lattice Thermal Conductivity of Graphene Flakes: Comparison with Bulk Graphite. *Appl. Phys. Lett.* **2009**, *94*, 203103.
2. Perichon, S.; Lysenko, L.; Remaki, B.; Barbier, D.; Champagnon, B. Measurement of Porous Silicon Thermal Conductivity by Micro-Raman Scattering, *Appl. Phys. Lett.* **1999**, *86*, 4700-4702.
3. Lysenko, V.; Perichon, S.; Remaki, B.; Barbier, D.; Champagnon, B. Thermal Conductivity of Thick Meso-Porous Silicon Layers by Micro-Raman Scattering. *Appl. Phys. Lett.* **1999**, *86*, 6841-6846.
4. Balandin, A. A.; Ghosh, S.; Bao, W.; Calizo, I.; Teweldebrhan, D.; Miao, F et al. Superior Thermal Conductivity of Single-Layer Graphene, *Nano Lett.* **2008**, *8*, 902-907.
5. Faugeras, C.; Faugeras, B.; Orlita, M.; Potemski, M.; Nair, R. R.; Geim, A. K. Thermal Conductivity of Graphene in Corbino Membrane Geometry. *ACS Nano*, **2010**, *4*, 1889-1892.
6. Cai, W.; Moore, A. L.; Zhu, Y.; Li, X.; Chen, S.; Shi, L et al. Thermal Transport in Suspended and Supported Monolayer Graphene Grown by Chemical Vapor Deposition. *Nano Lett.* **2010**, *10*, 1645-1651.
7. Ghosh, S.; Bao, W.; Nika, D. L.; Subrina, S.; Pokatilov, E. P.; Lau, C. N et al. Dimensional Crossover of Thermal Transport in Few-Layer Graphene. *Nat Mater*, **2010**, *9*, 555-558.
8. Biswas, S.; Drzal, L. T. A Novel Approach to Create a Highly Ordered Monolayer Film of Graphene Nanosheets at the Liquid-Liquid Interface, *Nano Lett.* **2009**, *9*, 167-172.
9. Lin, Y.; Skaff, H.; Emrick, T.; Dinsmore, A. D.; Russell, T. P. Nanoparticle Assembly and Transport at Liquid-Liquid Interfaces. *Science*, **2003**, *299*, 226-229.
10. Binder, W. H. Supramolecular Assembly of Nanoparticles at Liquid-Liquid Interfaces. *Angew, Chem. Int. Ed*, **2005**, *44*, 5172-5175.
11. Bowden, N.; Terfort, A.; Carbeck, J.; Whitesides, G. M. Self-Assembly of Mesoscale Objects into Ordered Two-Dimensional Arrays. *Science*, **1997**, *276*, 233-235.
12. Bowden, N.; Oliver, S. R. J.; Whitesides, G. M. Mesoscale Self-Assembly: Capillary Bonds and Negative Menisci. *J. Phys. Chem. B*, **2000**, *104*, 2714-2724.

13. Kralchevsky, P. A.; Paunov, V. N.; Denkov, N. D.; Ivanov, I. B.; Nagayama, K. Energetical and Force Approaches to the Capillary Interactions between Particles Attached to a Liquid-Fluid Interface, *J. Colloidal Interface Sci*, **1993**, *155*, 420-437.
14. Nair, R. R.; Blake, P.; Grigorenko, A. N.; Novoselov, K. S.; Booth, T. J.; Stauber, T et al. Fine Structure Constant Defines Visual Transparency of Graphene. *Science*, **2008**, *320*, 1308-1308.
15. Calizo, I.; Balandin, A. A.; Bao, W.; Miao, F.; Lau, C. N. Temperature Dependence of the Raman Spectra of Graphene and Graphene Multilayers. *Nano Lett.* **2007**, *7*, 2645-2649.
16. Greenberg M. *Advanced Engineering Mathematics*, 2nd ed, Prentice Hall, Upper Saddle River, NJ. 1998.

Chapter 4 Thermal Conductivity of Exfoliated Graphene Nanoplatelet Paper

4.1 Abstract

Instead of making a monolayer GNP film with only a few tens of nanometer in thickness, a novel method was proposed to make multilayer GNP film. In particular, these highly hydrophobic nanoparticles were dispersed and stabilized in a DI water/polyethyleneimine (PEI, a cationic polyelectrolyte) solution. A free standing, mechanically robust paper of GNP was prepared by vacuum filtration. The effect of GNP size, polyelectrolyte coating and paper porosity on thermal transport properties was investigated. It was found that thermal annealing improved thermal conductivity by decomposing the PEI molecule that was adsorbed on the GNP particles while still maintaining the porosity of the paper. Mechanically compressing the sample effectively reduced the pore volumes within the paper and increased the contact area among individual platelet. The strong alignment effect and larger contact area was evidenced by a 80% increase in in-plane thermal conductivity (207 ± 12 W/m·K) and a through-plane conductivity of only 1.7 ± 0.12 W/m·K. This flexible, lightweight, low-cost, paper material made of GNP particles is a promising candidate for applications requiring 2D heat conduction. This chapter is based on a journal publication: Xiang, J., Drzal, L. T. (2011). Thermal conductivity of exfoliated graphite nanoplatelet paper. *Carbon*, 49(3), 773-778.

4.2 Introduction:

Free-standing paper-like graphitic materials have great technological importance to modern society because of their chemical inertness, good mechanical properties, and impermeability to gases and fluids. Early work has shown that these exfoliated graphite flakes

can be rolled into flexible thin sheets and used as gaskets [1-4], flow field plates in fuel cells*, and electrodes for Li ion batteries [5]. The discovery of carbon nanotubes leads to densely packed CNT mats prepared by vacuum filtration and their superior strength and electrical conductivity are useful in many applications [6-8]. More recently, it is shown that graphite oxide can be exfoliated in water to yield hydrophilic, oxygenated graphene oxide nanosheet that can be assembled macroscopically to a paper-like structure through flow directed assembly [9]. Ruoff et al also shows that these graphite oxide nanosheets can be chemically reduced to graphene with hydrazine in the presence of a strong base such as KOH to restore the outstanding mechanical and electrical properties of graphene [10].

However, there are very few reports on thermal transport properties of those papers. Hone reported the thermal conductivity of densely packed CNT paper to be a few tens W/m·K, [11] much lower than conventional inorganic materials for heat dissipation although individual carbon nanotube is believed to have very high thermal conductivity [12]. A. Balandin et al. recently used micro-Raman spectroscopy, a non-contact, optical method to determine the thermal conductivity of single layer graphene, they concluded $\kappa=4400-5300\text{W/m}\cdot\text{K}$, among the highest in nature [13]. Yet, it remains elusive how well a paper-like material composed of individual graphite nanosheet conducts heat and how to tailor the thermal conductivity of these papers for various purposes.

To make a paper with GNP particles, these highly hydrophobic nanoparticles were dispersed in a polyethyleneimine/water solution. The cationic polyelectrolyte induces steric and electrostatic stabilization [14] between the nanoplatelets [15] and a paper was prepared by

*Grafcell (<http://www.graftechaet.com/GRAFCELL/GRAFCELL-Home.aspx>)

subsequent vacuum filtration and drying. The thermal conductivity of the as-made GNP paper consisting of individual platelets of different sizes and made with various processing steps (e.g. thermal annealing, cold pressing) was measured and related to the heat conduction in this paper-like structure.

4.3 Experimental

Materials:

GNP were prepared as usual by exfoliating the H₂SO₄/HNO₃ intercalated natural graphite (GIC, A3772) purchased from Asbury Graphite Mills, Inc, NJ. Microwave exfoliation proves superior to conventional thermal treatments due to the fast heating process and high energy density, which vaporizes the acids within the layers of graphite causing a significant and rapid expansion of the graphite gallery. The measured surface area is 20-40 m²/g for GNP-15 and 100-130 m²/g for GNP-1.

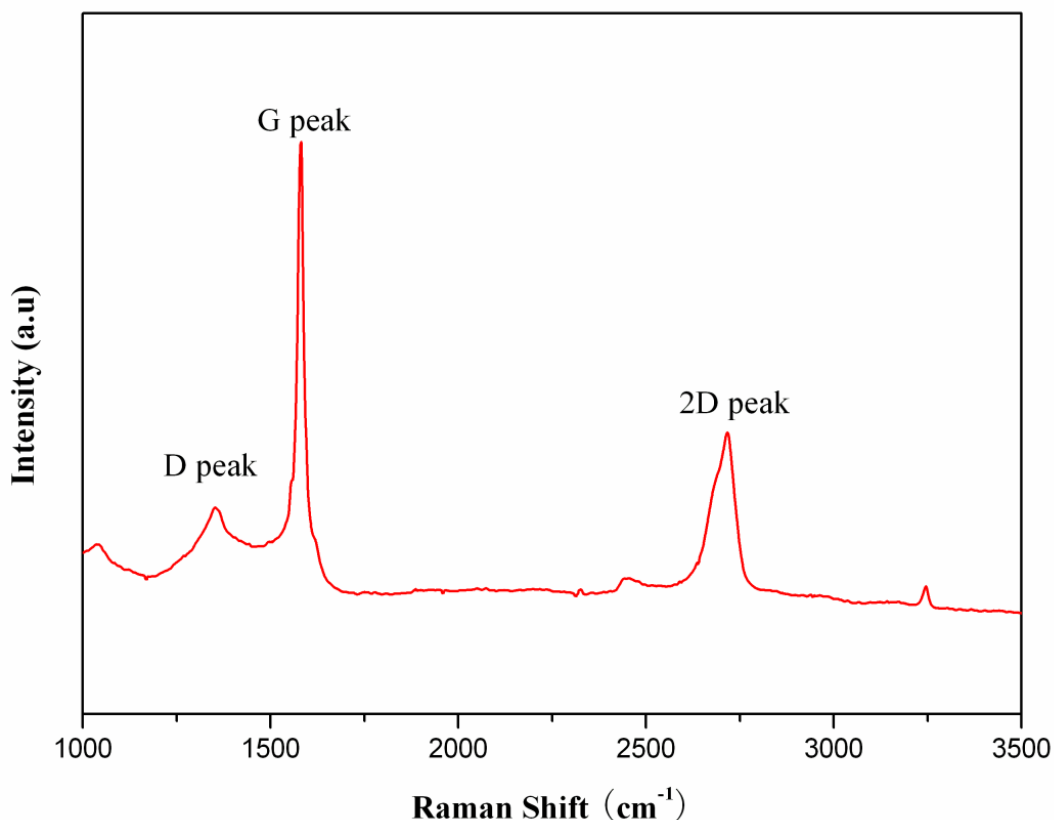


Figure 4-1: Typical Raman spectrum of GNP particles showing D peak, G peak and 2D peak.

The Raman spectrum of the GNP particle is shown in Figure 4-1, the small D band and a sharp G band confirms the sp^2 type bonding of the carbon atoms in the basal plane. It is thus believed that the intercalation process and subsequent pulverization processes did not oxidize the surface of the GNP which might degrade the electrical and thermal conductivity of an individual platelet [16].

GNP paper preparation:

Polyethyleneimine (PEI) was purchased from Aldrich. (branched, $M_w=25,000$). PEI solution was prepared containing 0.1wt% of the polymer in DI water. 0.1g GNP was dispersed in 100ml PEI solution and bath sonicated for 30 mins under constant stirring. The suspension was

kept stirring for 24 h before the excess polyelectrolyte was washed away by filtering through the 0.2 μm Durapore PVDF filter paper and re-dispersed in water at 1mg/ml. The pH of the suspension was adjusted to around 5-6 to induce positive charges on the polyelectrolyte [17]. The GNP-15 particles, due to larger effect of gravitational sedimentation, settled in few days, while the GNP-1 particles could be stabilized in the suspension for weeks.

An ANODISC membrane (0.2 μm , Whatman) was used for paper making by vacuum filtration. A controlled multi-filtration process (5 ml at a time) was used to minimize the disordered layering structure caused by water flow. 50 ml of the suspension was filtered to make one paper. The paper was then suction dried for 1h and then put into a vacuum oven and dried at 60° C overnight before peeling the GNP paper off the membrane. This paper was then referred to as “as-made” in later discussions. The free-standing paper was then thermally annealed at a furnace at 340° C for 2h and is identified as “annealed”. The annealed paper was then cold-pressed at 100 psi at room temperature for 1h and is identified as “annealed and cold-pressed”.

Scanning electron microscopy:

A JEOL JSM-7500F was used to image both the top surface and cross section of the GNP paper. The as-made, annealed and cold pressed papers prepared from both GNP-1 and GNP-15 were examined. For the cross sectional imaging, a portion of the GNP paper was mounted by epoxy and maintained at a position perpendicular to the polishing surface by a Buehler Sampl-Klip. Then the sample surface was polished and O₂ plasma treated for 45 mins at a RF power of 225W and gold coated for 2 mins before imaging.

Thermogravimetric analysis (TGA):

To investigate the effect of thermal annealing on sample thermal conductivity, a sample of 10-15 mg of GNP paper before and after annealing was loaded to the Pt pan and the experiments were conducted in a nitrogen atmosphere. The temperature range scanned was from 25°C to 700°C with a 10°C/min ramp rate and a 4°C/min resolution for thermal decomposition events.

Flash lamp laser diffusivity (Netzsch 447 NanoFlash)

The thermal diffusivity (α , m²/s) of the 1'' diameter GNP paper was measured by a LFA Nanoflash 447 Light flash system. Both the in-plane and through-plane thermal diffusivity were measured for the as-made, annealed, and anneal and cold pressed samples. To calculate the thermal conductivity of the samples, the apparent densities (ρ : kg/m³) of the samples were measured by dividing the mass over the volume, and the specific heat capacity (C_p : J/kg K) was measured by DSC (Q2000, TA instruments). The thermal conductivity (κ) is calculated according to the equation: $\kappa = \alpha \times \rho \times C_p$.

4.4 Results and discussions:

4.4.1 Morphology

To create a more ordered layer structure, a multi-filtration process (5 ml at a time) is necessary. During each filtration, water easily flows through the pores within the paper and the highly hydrophobic nanoplatelet floats at the water-air interface forming a very densely packed structure to minimize the interfacial energy. The first few layers were stacked more orderly because of the uniformity of water flow rate through the tubular shaped pores in the filter paper.

However, as the thickness of the paper builds up, the flow of water became more chaotic since more pores are blocked by the planar shaped GNP particles. It is thus recommended that the total filtration volume do not exceed 100 ml (at a concentration of 1 mg/ml) for maintaining the layered structure within the paper. Figure 4-2 shows schematic representation of filtration and the photos of the as-made self-standing, and mechanically robust GNP paper after being peeled off the filter paper.

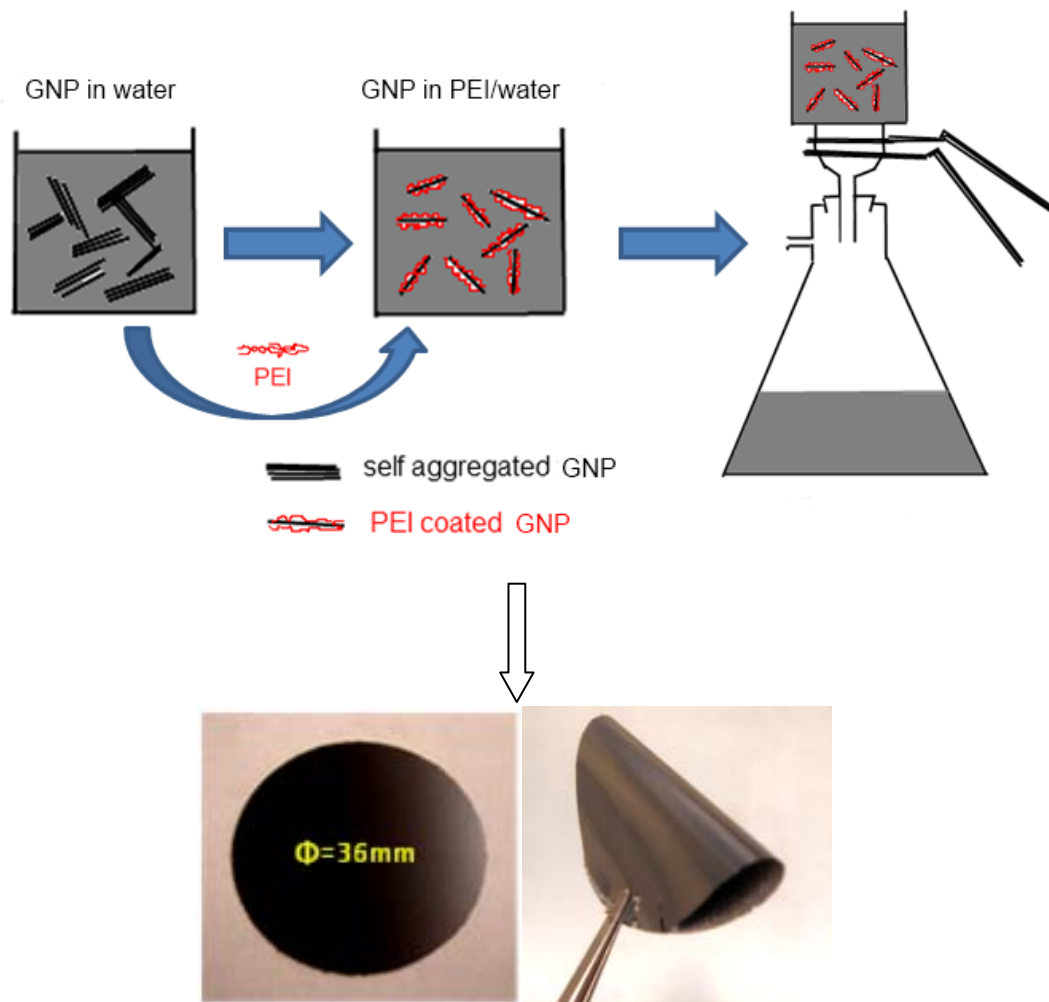


Figure 4-2: Schematic representation of the GNP paper making process by vacuum assisted self assembly and actual photos of GNP paper peeled off the ANODISC filter paper after drying.

In order to examine the stacking condition of the GNP particles in the paper-like structure, FESEM images of the cross sections of GNP papers are shown for both the as-made samples and the annealed and cold-pressed samples shown in Figure 4-3.

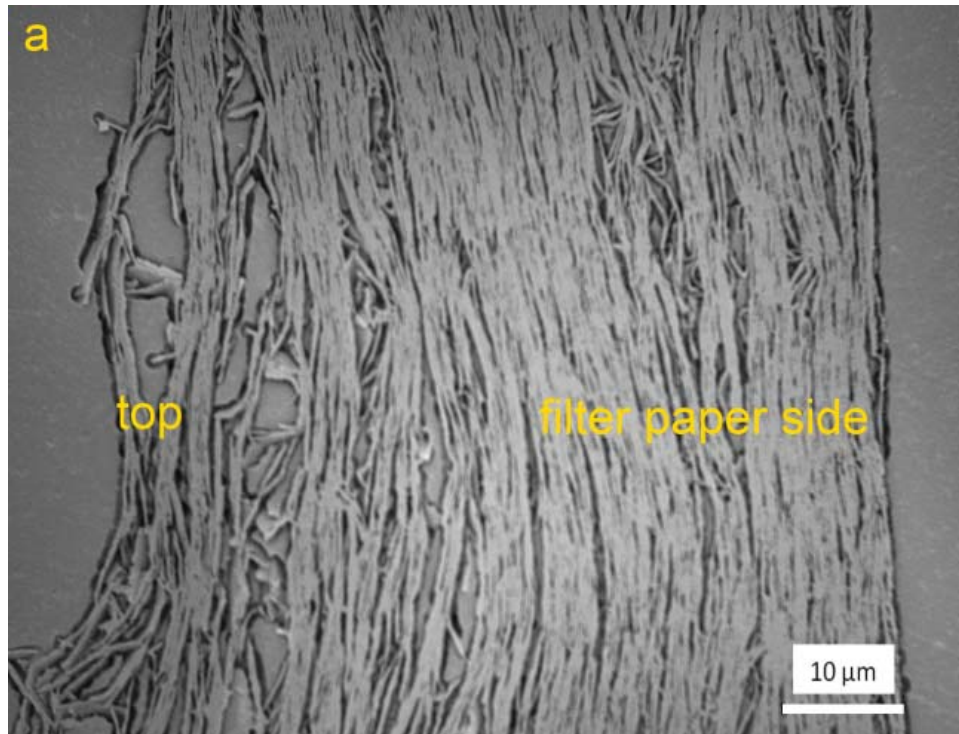


Figure 4-3: (a) SEM micrographs of cross section of the as-made GNP-15 paper (scale bar: 10 μm), (b) annealed and cold pressed GNP-15 paper (scale bar: 10 μm), (c) as-made GNP-1 paper (scale bar: 5 μm), (d) annealed and cold pressed GNP-1 paper (scale bar: 1 μm).

Figure 4-3(cont'd)

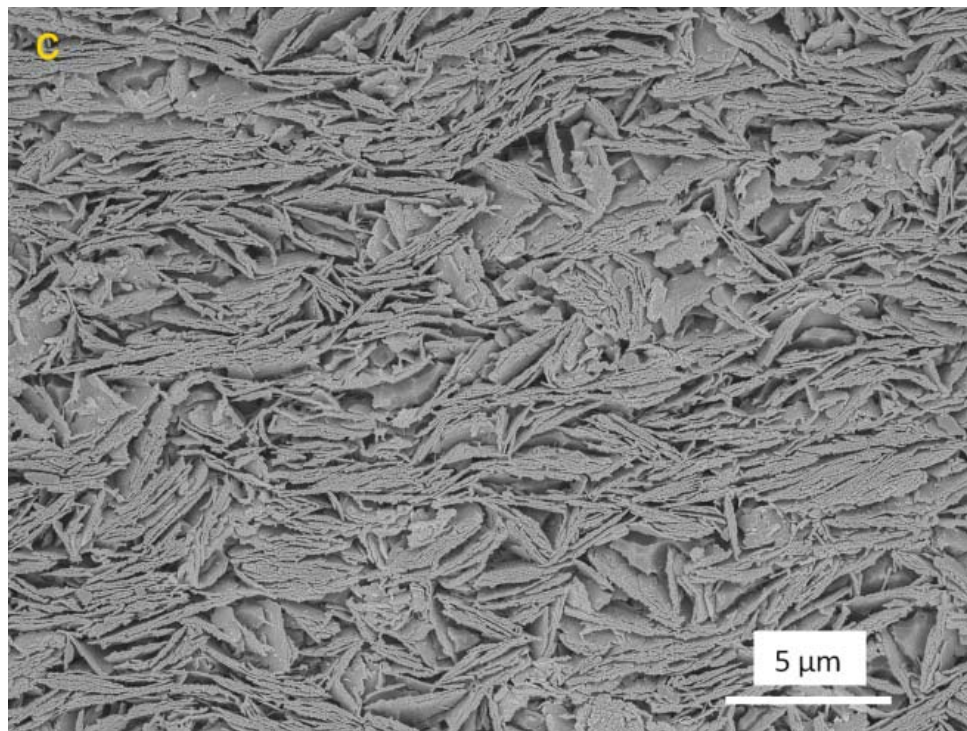
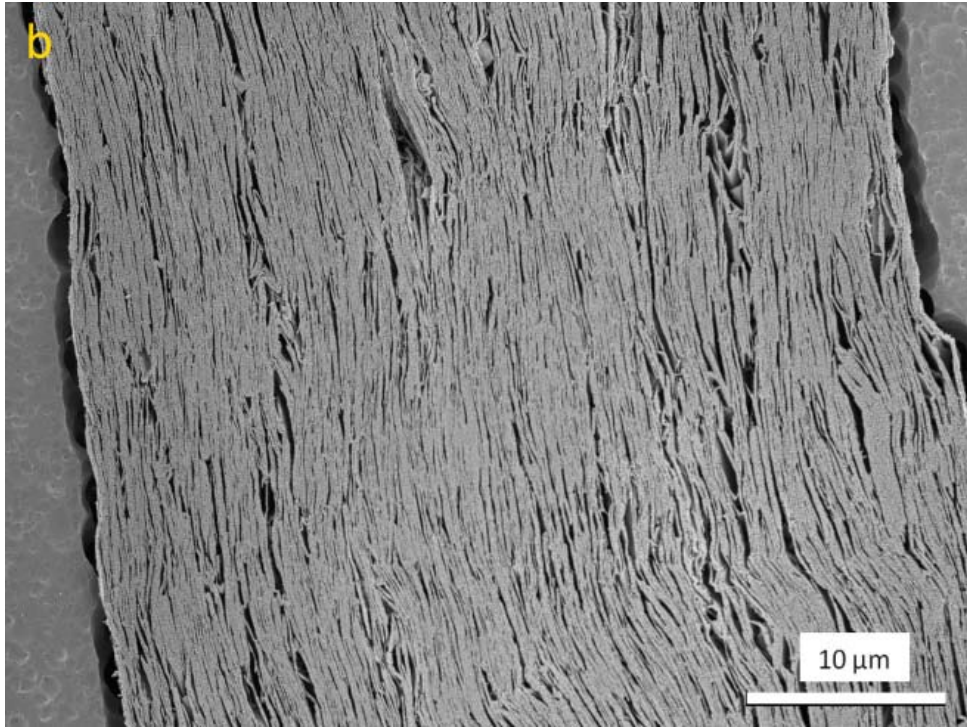
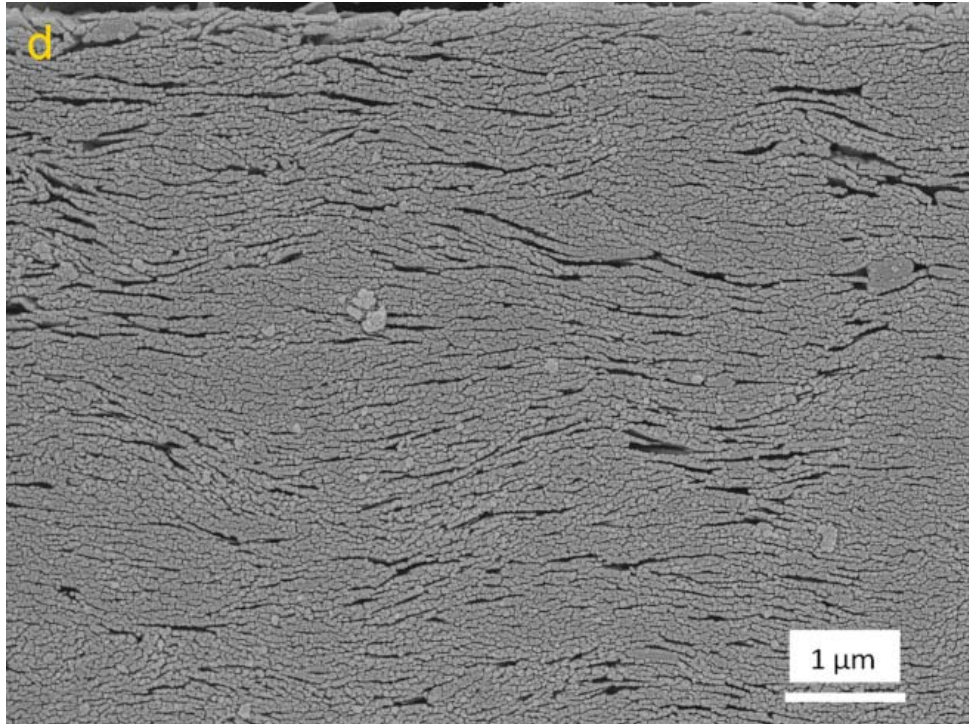


Figure 4-3 (cont'd)



It is noted in Figure 4-3a that the bottom side of the paper (the side attached to the filter paper) has a better layered structure than the top part due to the changing flow conditions of the water. Figure 4-3(a,c) shows the porosity of the as-made paper, the layering is more obvious in GNP-15 due to the larger platelet size. The thermal annealing process facilitates the decomposition of polyelectrolyte adsorbed on the surface of GNP and the same process will lead to a slight disruption of the layered structure inside the paper as a result of decomposition of PEI from the interior of the paper. It is necessary to cold-press the sample to restore the structure and alignment of the paper, eliminate porosity, and increase contact areas among GNP shown in Figure 4-3(b,d).

4.4.2 Thermogravimetric analysis of GNP paper

The TGA curves for GNP paper before and after annealing are shown in Figure 4-4. It is obvious that there is a slope change at around 300°C which marks the decomposition of PEI. At around 600 °C when GNP is starting to oxidize, the difference in the weight retained before and after annealing is 1.5wt% and 2.5wt% for GNP-15 and GNP-1 papers respectively which also corresponds to the amount of PEI coated on the GNP surface. In addition, the thermal annealing process effectively “cleans” the GNP by removing the water molecules adsorbed on the surface and the edges as is seen by the initial weight loss below 250 °C for the as-made samples.

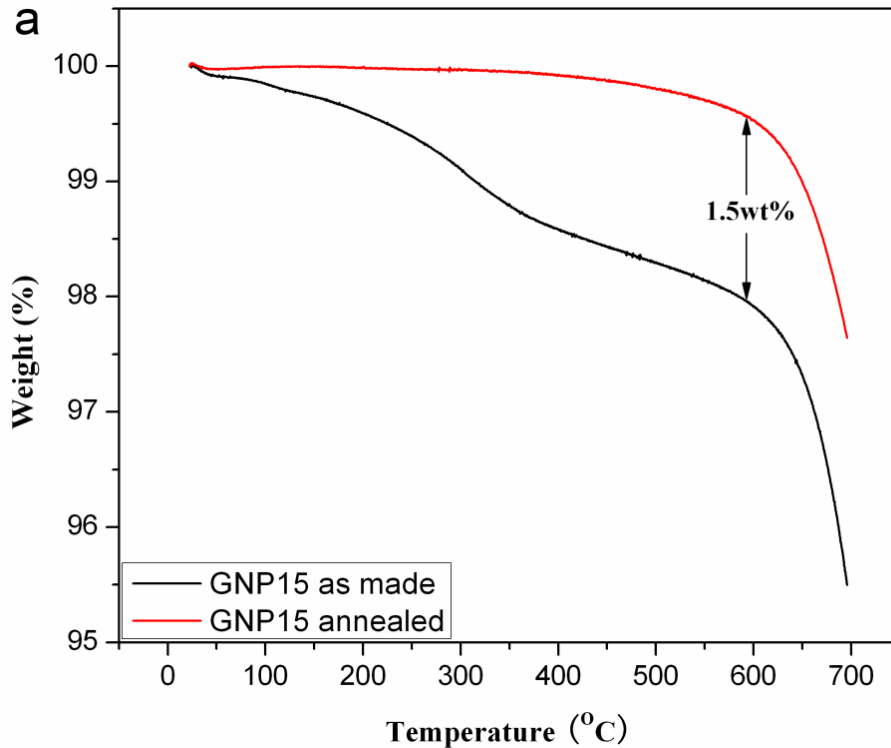
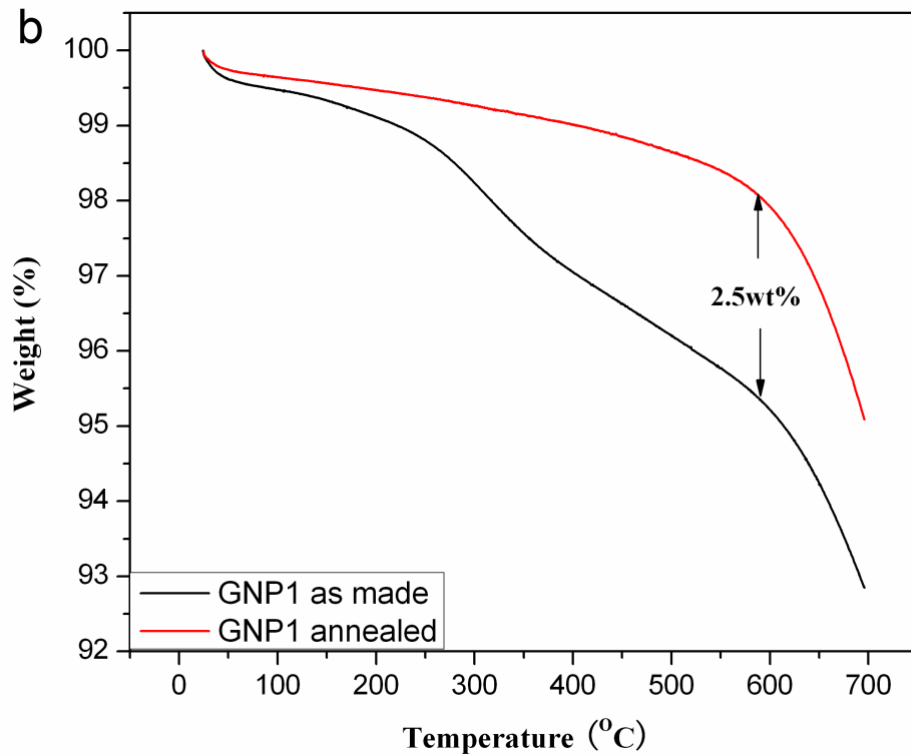


Figure 4-4: (a): TGA weight loss curves of GNP-15 paper before and after annealing, (b) TGA weight loss curves of GNP-1 paper before and after annealing.

Figure 4-4 (cont'd)



4.4.3 Thermal diffusivity and thermal conductivity of GNP paper under various treatments

A 1'' disk was punched out from the 36 mm diameter GNP paper for both the through-plane and in-plane thermal diffusivity measurement. Results for through-plane, in-plane thermal diffusivity and conductivity were compared for GNP-1 and GNP-15 paper for the as-made, the annealed, and the annealed and cold-pressed samples in Figure 4-5(a-d). The specific heat capacity of GNP particles in all the experiments was measured to be 710 J/kg K. Table 4-1 shows the densities of different samples.

Table 4-1: Density variation of GNP paper under different conditions

Density (ρ : g/cm ³)	as-made	annealed	annealed & cold pressed
GNP-15 paper	0.73 \pm 0.08	0.73 \pm 0.08	1.15 \pm 0.2
GNP-1 paper	0.71 \pm 0.03	0.71 \pm 0.05	1.3 \pm 0.2

For the through-plane measurement, the 1'' GNP paper was placed in the sample holder covered by a ring shaped mask to block any leakage of light from sample edges. The entire bottom surface of the sample was irradiated and the heat propagated to the top surface was collected by the IR camera. The Cowan + pulse model provided by the software package (Netzsch Proteus) was used to calculate the thermal diffusivity. It is believed that the existence of thermally insulating polymers (PEI) either on the GNP surface or at the interfaces hinders phonon transport, increasing the thermal interface resistance which is believed to play a major role in nanoscale heat transfer. Thus, the heat treatment above the decomposition temperature of polymer would remove most of the PEI, improving the "thermal contact" among platelets and evidenced by a 20% improvement in thermal diffusivity and hence the conductivity given the fact that the density of the sample remains the same before and after annealing for GNP-15 and GNP-1 paper. However, after the cold pressing process, the density of the sample increases because most of the pores created during filtration and annealing were eliminated, but the compressive stress effectively aligns the particles within a plane perpendicular to the force direction as shown in the SEM images. In addition, the nanointerfaces among individual platelet scatter phonons and further impede the heat transfer from particle to particle. The dual effects of both strong alignment and multiple nanointerfaces results in a through plane thermal conductivity less than 2 W/mK. Also, there is noticeable difference in the heat conducting

capability of GNP-15 and GNP-1 papers. The mere fact that the number of nanointerfaces in GNP-1 paper are a few hundred times greater in number than for the larger GNP-15 illustrates that the boundary phonon scattering will reduce thermal conductivity significantly.

The in-plane diffusivity and conductivity were measured using a method that employs a mask to collimate the laser beam and heat an approximately 5 mm diameter spot at the bottom of a 1'' disk sample. Heat will flow through the thickness of the sample and spread out in the plane. Another mask with embedded annulus of 9 to 12 mm in diameter was placed on the sample to allow heat radiation to be collected by the IR detector. In this case, the large anisotropy of the graphitic material (GNP) in heat conduction would affect the in-plane measurement, i.e. the time for the heat to reach the slit in the mask will depend on both the radial diffusion time and the axial diffusion time. Thus, the through-plane diffusivity of the sample was measured first and input to the in-plane analysis and used in the axial part of the heat flow calculation. Then an iterative scheme is used to separate the axial and radial diffusivities. The model that considers all this is "anisotropic + heat loss". For both GNP-15 and GNP-1 samples, a modest 10% improvement in thermal diffusivity and conductivity were observed due to thermal annealing. For the cold-pressed samples, a dramatic enhancement in thermal conductivity from 71 W/m·K to 207 W/m·K for GNP-15 paper implies that the strong alignment of particles and solid "thermal contact" induced by large compressive stress improves thermal conductivity and reduces thermal contact resistance. The same trend applies to the GNP-1 sample, but the GNP size reduction from 15 μm to 1 μm introduces multiple interfaces that reduce phonon transport significantly. As a result, the thermal conductivity is only 10 percent of the GNP-15 for all the samples measured at three different conditions. Despite the promising results reported here, it is still worth noting

that there are some commercial exfoliated graphite products with thermal conductivity as high as 1500W/m·K.*

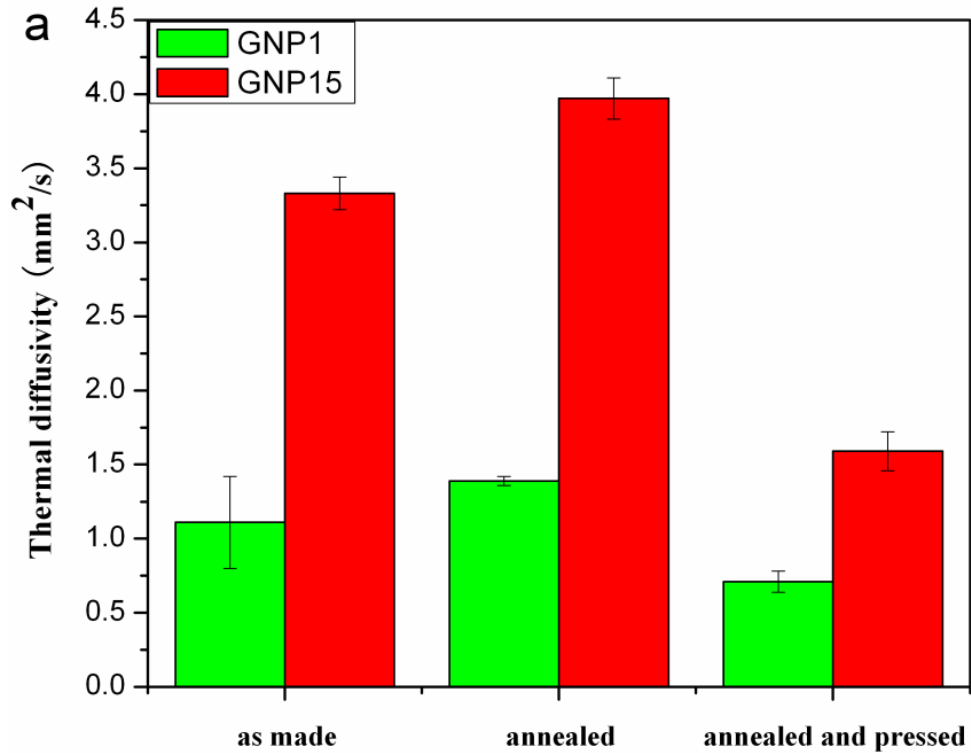


Figure 4-5: (a) Through-plane thermal diffusivity of GNP-1 and GNP-15 papers. (b) Through-plane conductivity of GNP-1 and GNP-15 papers. (c) In-plane diffusivity of GNP-1 and GNP-15 papers. (d) In-plane conductivity of GNP-1 and GNP-15 papers. (note: left column represents GNP1, right column represents GNP15)

* Graftech International (<http://www.graftech.com/MARKETS/Lighting-Thermal-Management.aspx>)

Figure 4-5(cont'd)

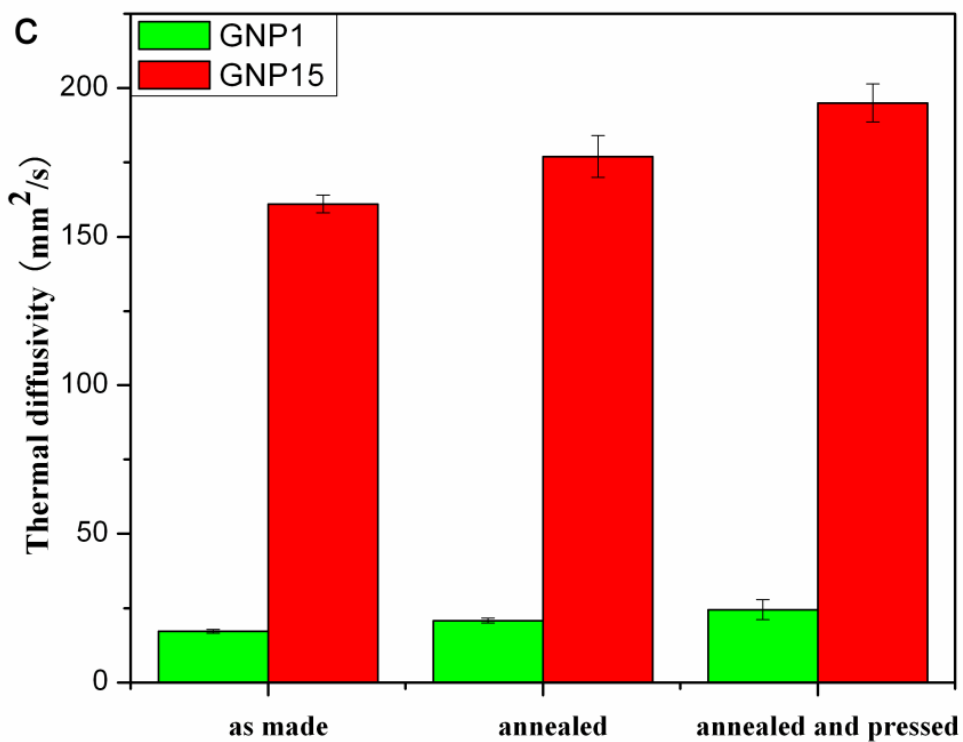
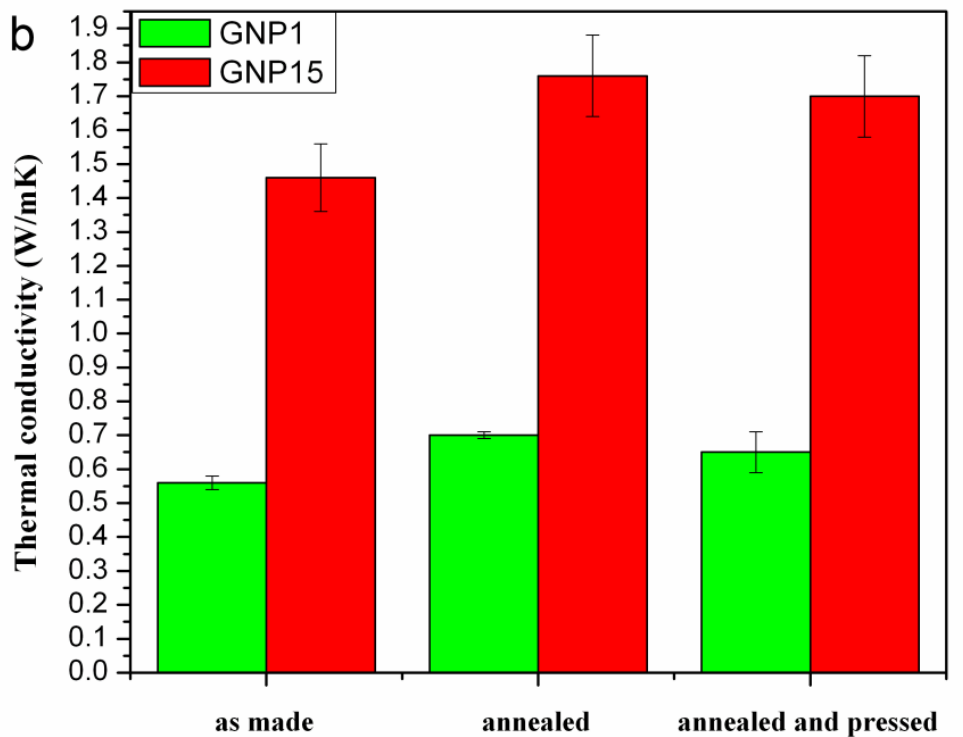
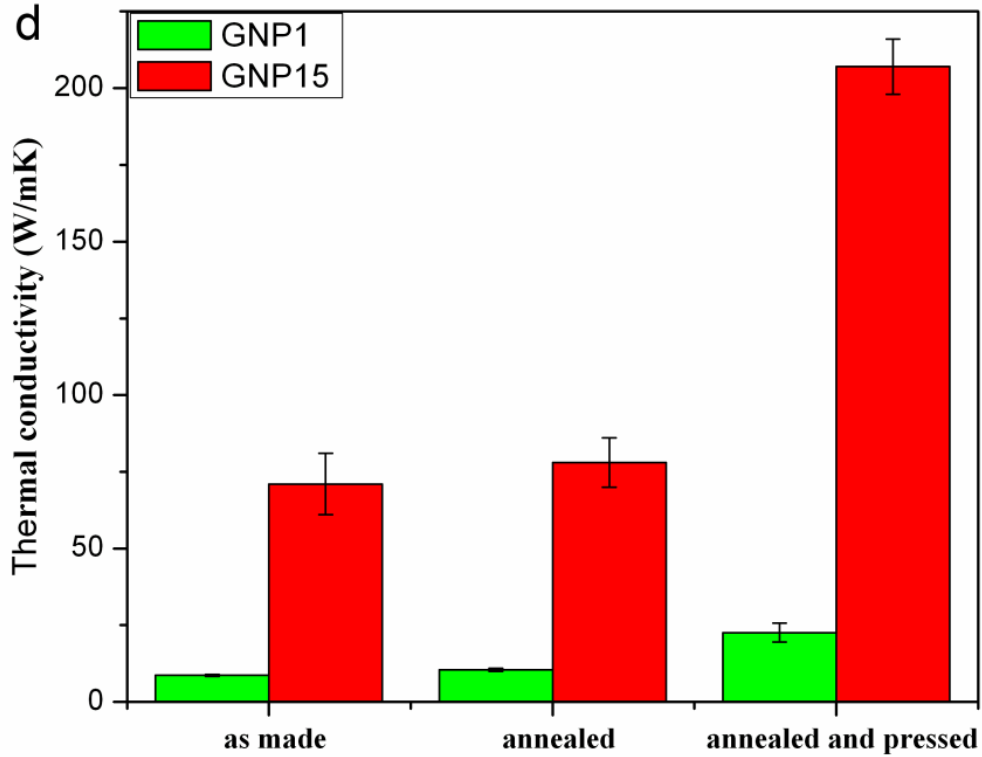


Figure 4-5(cont'd)



4.5 Conclusions:

GNP stabilized by PEI were successfully dispersed in water and a paper-like structure was prepared by flow directed self assembly. Thermal diffusivity and conductivity of both GNP-15 and GNP-1 papers were measured at three different conditions. Annealing that helps decompose the polymer enhances thermal conductivity possibly due to the reduction of thermal interface resistance. However, the dominant factor in nanoscale heat transfer is the density of nanointerfaces within the paper which gives rise to phonon boundary scattering. Cold pressing restores the strong alignment of individual particle, improves the thermal contact by eliminating the pores in the paper. After annealing and pressing, the GNP papers are very anisotropic in heat

conduction, which is very promising for applications that require moving heat in a particular direction (e.g. 2D heat spreader) or to reduce the maximum temperature at a “hotspot” by spreading heat laterally for protective purposes.

REFERENCES

References

1. Dowell, M. B.; Howard, R.A.; Tensile and compression properties of flexible graphite foils. *Carbon* **1986**, *24*, 311-323.
2. Leng, Y.; Gu, J.; Cao, W.; Zhang, T.Y.; Influences of density and flake size on the mechanical properties of flexible graphite. *Carbon* **1998**, *36*, 875-881.
3. Reynolds, R. A.; Greinke, R. A.; Influence of expansion volume of intercalated graphite on tensile properties of flexible graphite. *Carbon* **2001**, *39*, 479-481.
4. Chung, D. Flexible graphite for gasketing, adsorption, electromagnetic interference shielding, vibration damping, electrochemical applications, and stress sensing. *J Mater Eng Perform* **2000**, *9*, 161-163.
5. Yazici, M. S.; Krassowski, D.; Prakash, J. Flexible graphite as battery anode and current collector. *J. Power Sources* **2005**, *141*, 171-176.
6. Baughman, R. H.; Cui, C.; Zakhidov, A. A.; Iqbal, Z.; Barisci, J. N.; Spinks, G. M et al. Carbon nanotube actuators. *Science* **1999**, *284*, 1340-1344.
7. Hennrich, F.; Lebedkin, S.; Malik, S.; Tracy, J.; Barczewski, M.; Rosner, H et al. Preparation, characterization and applications of free-standing single walled carbon nanotube thin films. *Phys Chem Chem Phys* **2002**, *4*, 2273-2277.
8. Coleman, J. N.; Blau, W. J.; Dalton, A. B.; Munoz, E.; Collins, S.; Kim, B. G et al. Improving the mechanical properties of single-walled carbon nanotubes sheets by intercalation of polymeric adhesives. *Appl. Phys. Lett* **2003**, *82*, 1682-1684.
9. Dmitriy, A. D.; Stankovich, S.; Zimney, E. J.; Piner, R. D.; Dommett, G. H. B.; Evmenenko, G et al. Preparation and characterization of graphene oxide paper. *Nature* **2007**, *448*, 457-460.
10. Park, S.; An, J.; Piner, R. D.; Jung, I.; Yang, D.; Velamakanni, A. Aqueous suspension and characterization of chemically modified graphene sheets. *Chem. Mater* **2008**, *20*, 6592-6594.
11. Hone, J.; Whitney, M.; Zettl, A. Thermal conductivity of single-walled carbon nanotubes. *Synth Met* **1999**, *103*, 2498-2499.
12. Li, Q.; Liu, C.; Wang, X.; Fan, S.; Measuring the thermal conductivity of individual carbon nanotubes by the Raman shift method. *Nanotechnology* **2009**, *20*, 145702.
13. Balandin, A. A.; Ghosh, S.; Bao, W.; Calizo, I.; Teweldebrhan, D.; Miao, F et al. Superior thermal conductivity of single-layer graphene. *Nano Lett* **2008**, *8*, 902-907.
14. Hiemenz, P. C.; Rajagopalan, R. *Principles of Colloid and Surface Chemistry*, 3rd edition, revised and expanded, Marcel Dekker, New York: 1997: 575-614.

15. Yu, D.; Dai, L.; Self-assembled graphene/carbon nanotube hybrid films for supercapacitors. *J. Phys. Chem. Lett* **2010**, *1*, 467-470.
16. Padgett, C. W.; Brenner, B. W. Influence of chemisorption on the thermal conductivity of single-wall carbon nanotubes. *Nano Lett* **2004**, *4*, 1051-1053.
17. Zhang, J.; Xu, Q.; Ye, F.; Lin, Q.; Jiang, D.; Iwasa, M. Effect of citric acid on the adsorption behavior of polyethyleneimine (PEI) and the relevant stability of SiC slurries. *Colloid Surface A* **2006**, *276*, 168-175.

Chapter 5 Electron and Phonon Transport in Gold Nanoparticle Decorated Graphene Nanoplatelet Nanostructured Paper

5.1 Abstract:

Monodispersed Au nanoparticles were synthesized on the surface of GNP in the presence of polyethyleneimine (PEI) with microwave assisted heating. A highly structured layered Au/GNP “paper” with good flexibility and mechanical robustness was prepared by vacuum assisted self assembly. The thermal and electrical conductivity of the hybrid paper with and without the Au nanoparticles were investigated after different experimental processing conditions including thermal annealing and cold compaction. Annealing effectively removed the adsorbed PEI molecules and improved thermal contact between Au/GNP particles while cold compaction reduced porosity and induced stronger alignment of the Au/GNP within the hybrid paper. Both approaches led to improvement in electrical and thermal conductivity. It was also found that adjacent GNP particles were electrically connected by metal nanoparticles but thermally disconnected. It is believed that phonons are scattered at the Au/GNP interfaces while electrons tunnel across this interface, resulting in a separation of electron and phonon transport within this hybrid paper. This chapter is based on a journal publication: Xiang, J., Drzal, L. T. (2011) Electron and phonon transport in Au nanoparticle decorated graphene nanoplatelet nanostructured paper. *ACS applied materials & interfaces*, 3(4), 1325-1332.

5.2 Introduction:

Chapter 4 discussed in detail the electrical and thermal transport of a highly ordered GNP paper prepared by vacuum assisted self assembly. It was found that both annealing and cold compaction is beneficial in improving the electron and phonon transport in the paper as a result

of reduced contact resistance. This chapter continues to investigate this paper-like structure but with an aim to separate the carrier transport within the GNP paper for thermoelectric application which requires a decoupled electron and phonon transport. In particular, metal nanoparticles such as gold was deposited on the surface of GNP and a hybrid Au/GNP paper was prepared. Decoration of GNP with metal nanoparticles changes to some extent the nature of GNP-GNP interfaces from a surface contact to a point to point contact, the question this chapter attempts to answer is how these nanoparticles would change the electron and phonon transport within this hybrid paper.

The graphene-metal hybrid systems have already been discussed in the literature to have various engineering applications such as fuel cell catalysis [1-5], electrochemical sensing [6, 7] and electrochemical energy storage [8,9]. Methods to synthesize metal nanoparticles on the basal plane surface of graphene have been explored quite extensively. Among those, solution and supercritical liquid approaches have the advantage of covering the entire surface area of graphene nanosheets with nanoparticles. For example, one common method is to chemically functionalize the graphitic surface in order to introduce anchoring sites for the metal precursors. The metal precursor is then reduced in the presence of a reducing agent to produce nanoparticles that covalently attaches to the basal plane of the graphene [10-12]. The disadvantage of this approach is the disruption of the sp^2 bonded carbon atoms in the basal plane which leads to reduced transport properties of graphene because of additional scattering sites [13]. Another widely adopted technique involves non-covalent encapsulation of the graphitic surface with a surfactant or a polymer and subsequent growth of nanoparticles on the surfactant in the presence of a reducing agent [14, 15]. This technique induces minimum chemical perturbation of the basal planes, preserving the conjugated system for undisrupted carrier transport. Other techniques of

metal nanoparticle decoration on graphitic nanostructure include electro-deposition [16], evaporation [17], and solventless bulk synthesis [18]. While these methods have some processing advantages over solution-phase techniques, they are usually quite expensive and energy intensive. In order to synthesize nanoparticles using the solution-phase approach with a narrow size distribution, several factors need to be controlled carefully which include the concentration of metal salt and reducing agent [19,20], the presence of a protecting agent [21], the reaction time [22] and reaction temperature [23].

Here, monodispersed gold nanoparticles were synthesized on individual GNP in the presence of polyethyleneimine with microwave assisted heating. Previous publications have reported on the deposition of Au nanoparticles on graphene nanosheets through simultaneous reduction of graphene oxide and Au(III) by microwave heating and sonolysis [24,25]. This chapter demonstrates a fast, one-pot, aqueous synthesis of Au nanoparticles directly on pristine graphene nanosheets. Polyethyleneimine, a hydrophilic polymer with primary, secondary and tertiary amino groups and an overall positive charge in the neutral aqueous solution, adsorbs on the highly hydrophobic GNP surface and stabilizes the GNP particles in water. The adsorption of PEI on GNP effectively induces both electrostatic and steric stabilization. In addition, PEI contains one of the highest densities of amino groups among all polymers, donating electrons that help reduce metal ions [26-28]. Gold nanoparticles were chosen here because of their strong resistance to oxidation and excellent thermal and electrical properties. Gold nanoparticle decorated GNP was prepared into a paper form by vacuum assisted self-assembly. The electrical and thermal conductivity of the Au/GNP paper was characterized under different conditions such as annealing and compaction similar to Chapter 4. The impact of gold nanoparticles on both electron and phonon transport in this hybrid paper is discussed.

5.3 Experimental:

Preparation of exfoliated graphene nanoplatelets (GNP)

GNPs were produced from a commercial graphite intercalated compound (Asbury Mills, NJ). Thermal exfoliation was carried out in a microwave oven followed by mechanical size reduction with a combination of ultra-sonication and ball milling to produce nanoplatelets with the desired aspect ratios. GNP-15 particles are used throughout the experiment and are simply referred as GNP.

Decoration of GNP with Au nanoparticles

Polyethyleneimine (PEI) was purchased from Sigma Aldrich. (Branched, $M_w=25,000$). The GNP particles were dispersed in a PEI/water solution containing 0.3wt% and 0.6wt% PEI. The suspensions were bath sonicated for 1 h and kept stirred overnight to ensure sufficient interaction between PEI and GNP. Tetrachloroauric acid ($\text{HAuCl}_4 \cdot 3\text{H}_2\text{O}$) purchased from Sigma Aldrich (> 99.9% trace metal basis) was then added into the suspension and mixed thoroughly. The suspension was irradiated with microwave radiation for a short period of time and then centrifuged at 6000 rpm and washed with copious amount of water to produce Au nanoparticle decorated GNP. The resulting Au/GNP product was dried under vacuum at 70 °C overnight.

Preparations of Au/GNP hybrid paper (as made, annealed, anneal and cold compacted):

The Au/GNP hybrid paper was prepared by vacuum filtration with an ANODISC 47 mm filter membrane. (0.2 μm , Whatman) The hybrid paper was then washed with water and dried at 60 °C under vacuum overnight before being removed from the filter. These were identified as “as-made” samples. The paper identified as “annealed” sample was placed in a furnace and

annealed at 340°C in air for 2 h to decompose the PEI. The “annealed and cold compacted” paper was mechanically compressed in a hydraulic press at 100 psi at room temperature for 1 h. For comparison, a neat GNP paper without Au nanoparticles was prepared in the same way.

Flash lamp thermal diffusivity measurement by Nanoflash 447 (Netzsch Instruments)

For through-plane thermal diffusivity measurement, the 1 inch disk sample was placed in the sample holder covered by a ring shaped mask to block any leakage of light from sample edges. The entire bottom surface of the sample was irradiated and the heat propagating to the top surface was collected by the IR camera. The “cowan + pulse” model provided by the software package (Netzsch Proteous) was used to calculate thermal diffusivity. The in-plane diffusivity was measured using a method that employs a mask that collimates the laser beam at a 5 mm diameter spot at the bottom of the 1 inch disk sample. Another mask with embedded annulus of 9 to 12 mm was placed on the sample allowing heat propagating radially to be collected. The “in-plane, anisotropic + heat loss” model incorporated in the software was used for subsequent diffusivity calculation.

Electrical conductivity characterizations of hybrid papers:

In-plane electrical conductivity was measured with a Keithley 2400 SourceMeter in a four point configuration with a probe spacing of 1 cm on thin rectangular films. Electric current was scanned from 20 mA to 100 mA with 20 mA intervals. Voltage drops on the sample were recorded and plotted against the current to obtain the resistance. The through-plane conductivity of thin film samples was measured by using 2 instead of 4 leads. Electrical resistance of the sample was obtained by calculating the slope of the voltage vs. current data. Taking the

geometry of the samples into account, the in-plane electrical conductivity and through-plane resistivity (see supporting information) were calculated.

5.4 Results and discussions:

5.4.1 Morphology

Dispersion of GNP particles in water proves difficult and results in an immediate floating and aggregation of the particles at the air-water interface because of the highly hydrophobic nature of the basal plane. Polyethyleneimine, a cationic polyelectrolyte, adsorbs on the GNP surface due to a thermodynamic driving force to reduce the hydrophobic interface between GNP and the polar solvent and minimize the interfacial energy. At pH <10, the positively charged polymer chain also induced electrostatic repulsion that contributed to good dispersion of the nanoplatelets. As the tetra-chloroauric acid dissolved in water was mixed with the GNP suspensions, the AuCl_4^- ions complex with the positive functional groups of PEI adsorbed on the GNP surface (chloride ligands were replaced by amine groups of PEI). The adsorbed PEI chains, in this case, serve as templates for subsequent Au nanoparticle growth on the surface of GNP. The addition of H^+ ions also lowered the pH of the solution to around 6, inducing more positive charges on the chain of PEI and more electrostatic attraction with AuCl_4^- [29]. The reduction of Au^{3+} to Au^0 was then carried out in a microwave oven where the heating rate was fast enough to cause a rapid temperature increase in the solution due to the high polarity of water molecules, creating a high concentration of radicals which facilitated the electron transfer from the radicals of PEI to the metal precursor. As soon as the solution was supersaturated with metal atoms, Au atoms formed nuclei. The critical size of the nucleus as well as nucleation activation energy control the nucleation rate and depend on the surface tension of the nuclei-solvent interface when

the radius of nuclei is small [30, 31]. Therefore, a higher surface tension corresponds to a larger critical nucleus size and a lower nucleation rate, which should be avoided in synthesizing monodispersed small nanoparticles. Upon formation of the nucleus, polyethyleneimine, with a lower surface tension than Au atoms, adsorbed on the surface of the metal atoms reducing the nucleation energy barrier and critical nucleus size. As a result, more primary particles with low surface energy were formed leading to generation of smaller secondary particles whose growth and coarsening were also affected by surface tension [32]. Figure 5-1 represents the typical procedures and the interactions between the metal ions and the active sites on GNP particles and subsequent formation of nanoparticles on GNP.

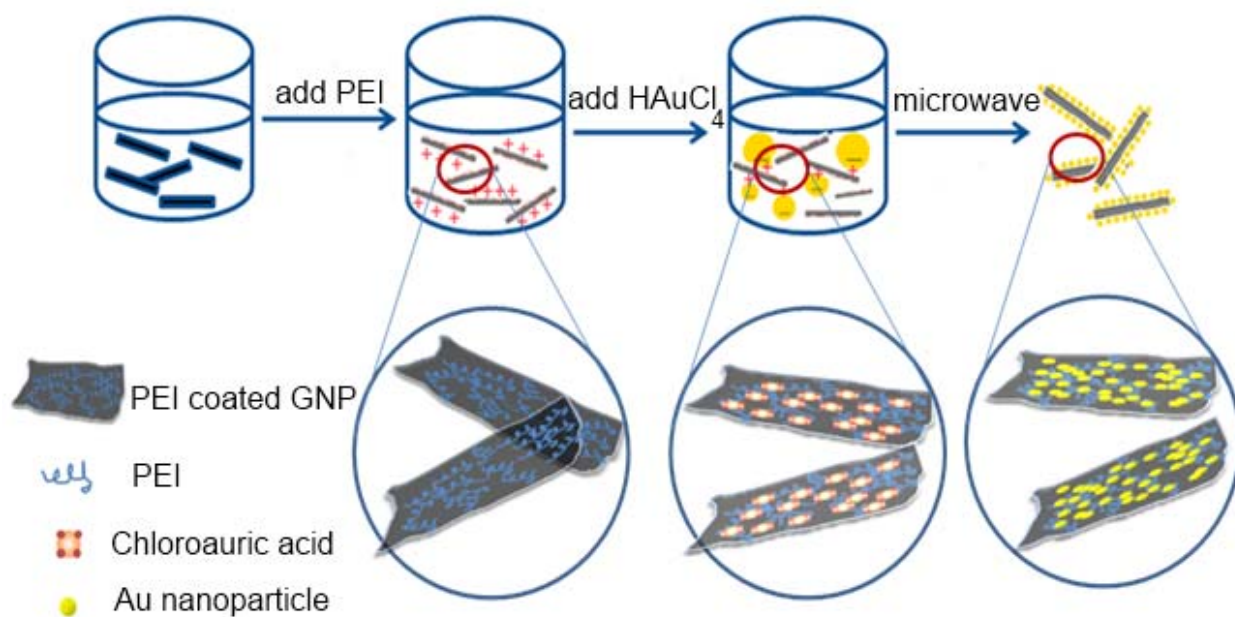


Figure 5-1: Schematics of experimental procedures and the interactions between the metal ions and the active sites on PEI coated GNP and formation of Au nanoparticles

From SEM micrographs shown in Figure 5-2, it was found that the size and loading of the Au nanoparticles synthesized by this technique correlated with the concentration of PEI in the solution. The size of the nanoparticles was reduced while the loading increased with higher

concentration of PEI in the solution. With a higher concentration of PEI in the solution, the number of nuclei with a lower surface energy increased which leads to formation of more primary and secondary particles. In addition, more PEI chains would adsorb on to the surface of GNP acting as templates for Au nanoparticle growth. There is no obvious agglomeration of Au nanoparticles on the surface of GNP, which is also believed to be the result of PEI encapsulation that stabilizes the nanoparticles in the solution electrostatically. Figure 5.3 shows the size and distribution of Au nanoparticles on the GNP surface at 0.3wt% and 0.6wt% PEI concentrations. This is obtained by analyzing representative SEM images of magnifications at 80k or higher in Image-Pro, a commercially available software. (See Supporting Information). It is clear that the whole spectrum shifts to a smaller size range while the number of nanoparticles increased for samples prepared in 0.6wt% PEI. The size of the Au nanoparticles prepared at 0.3wt% PEI is 10.8 ± 2.4 nm while they are reduced in size to 8.3 ± 2.1 nm at 0.6wt% PEI.

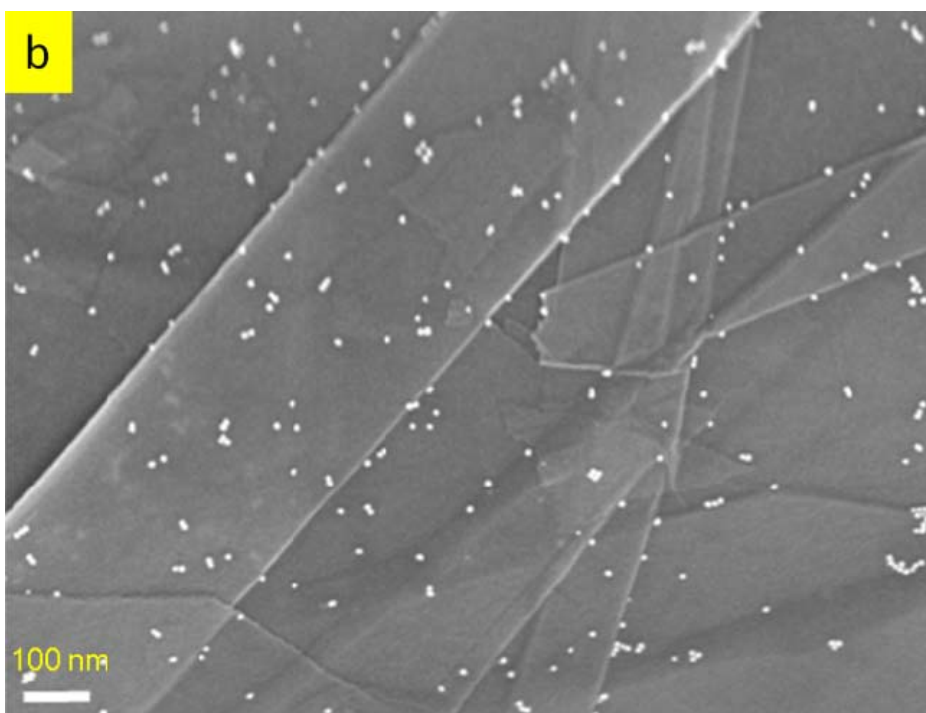
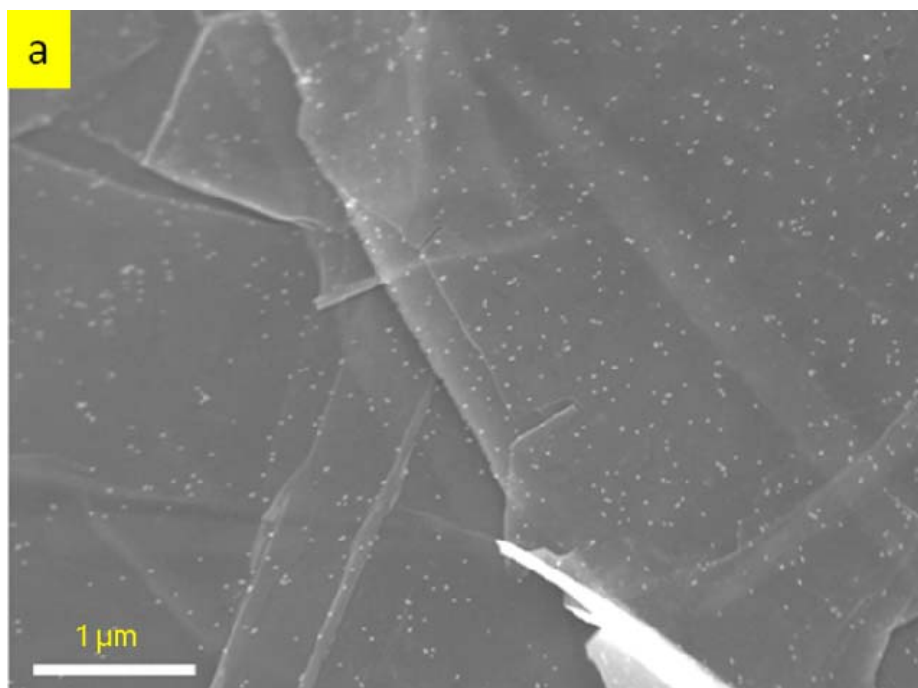
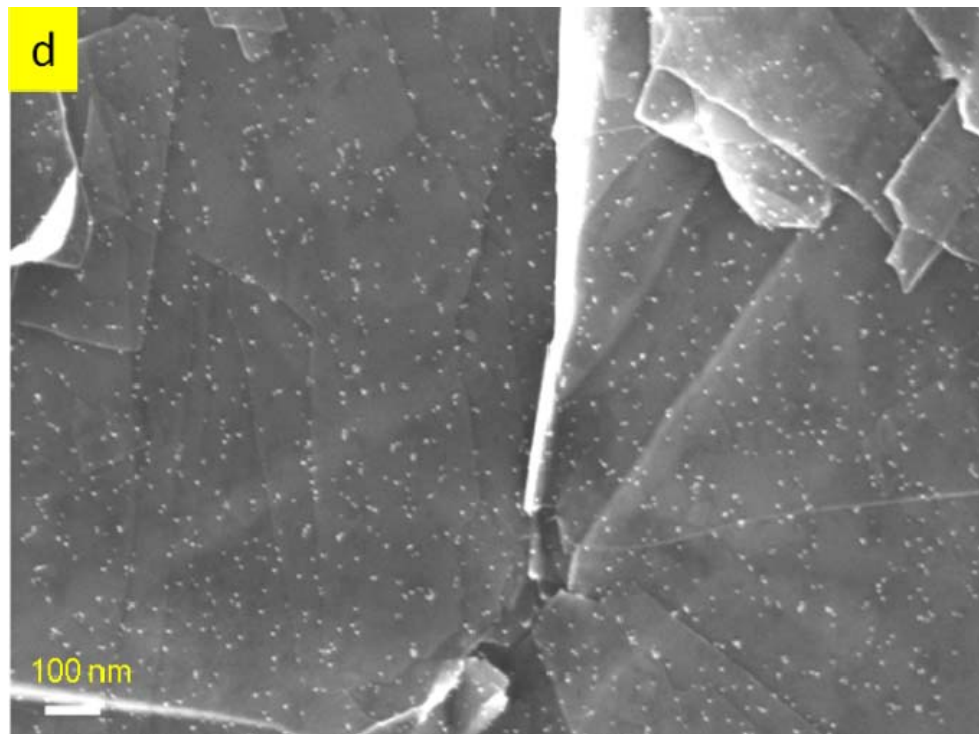
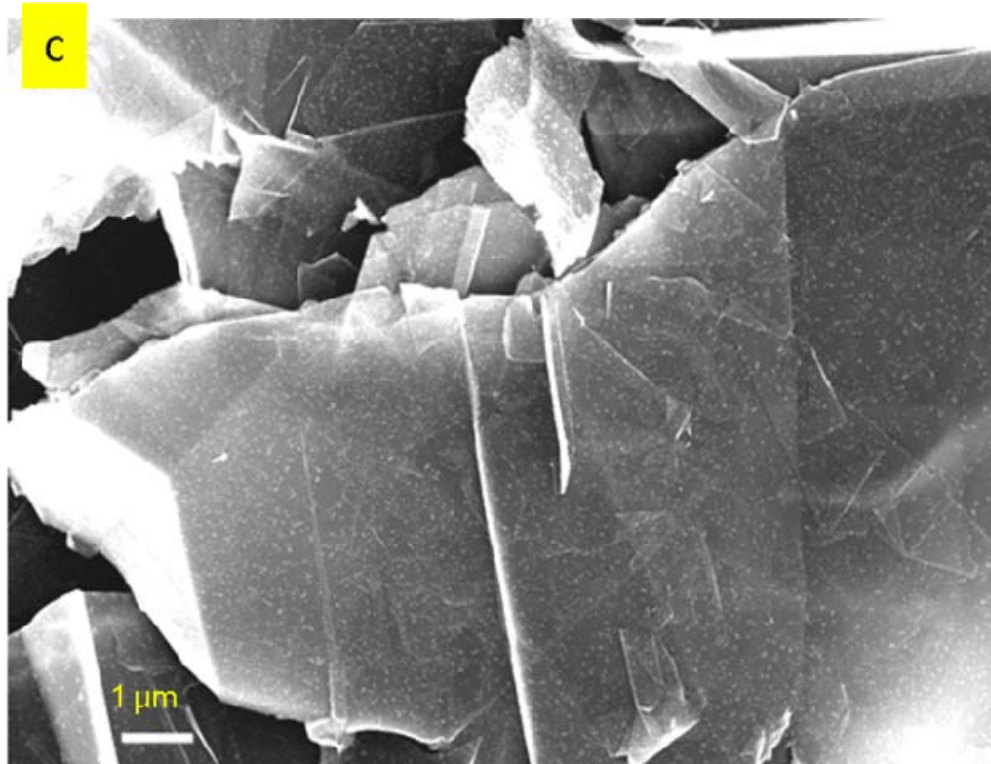


Figure 5-2 (a): Low magnification SEM image of Au nanoparticle decorated GNP prepared at 0.3wt% PEI concentration (scale bar: 1 μm). b: High magnification SEM image of Au nanoparticle decorated GNP prepared at 0.3wt% PEI (scale bar: 100 nm) c: Low magnification SEM image of Au nanoparticle decorated GNP prepared at 0.6wt% PEI concentration (scale bar: 1 μm). d: High magnification SEM image of Au nanoparticle decorated GNP prepared at 0.6wt% PEI concentration (scale bar: 100nm)

Figure 5-2(cont'd)



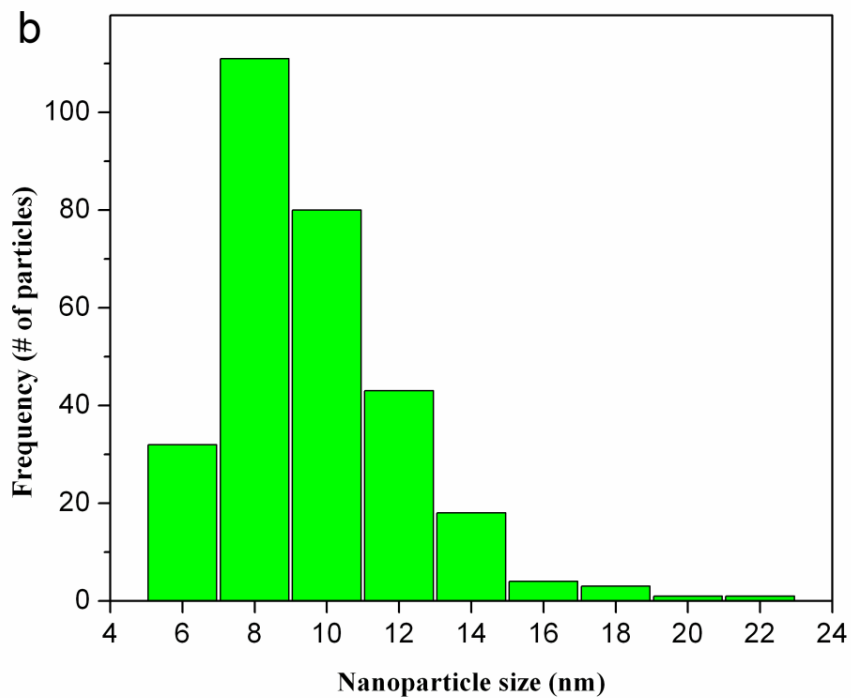
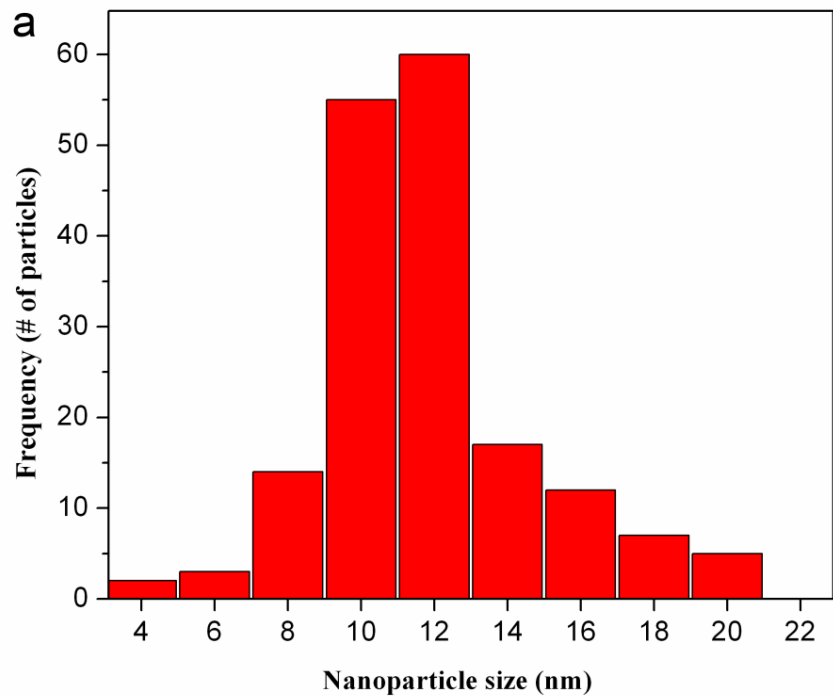


Figure 5-3: (a) Size and distribution of Au nanoparticles on GNP prepared at 0.3wt% PEI concentration. (b) Size and distribution of Au nanoparticles on GNP prepared at 0.6wt% PEI concentration.

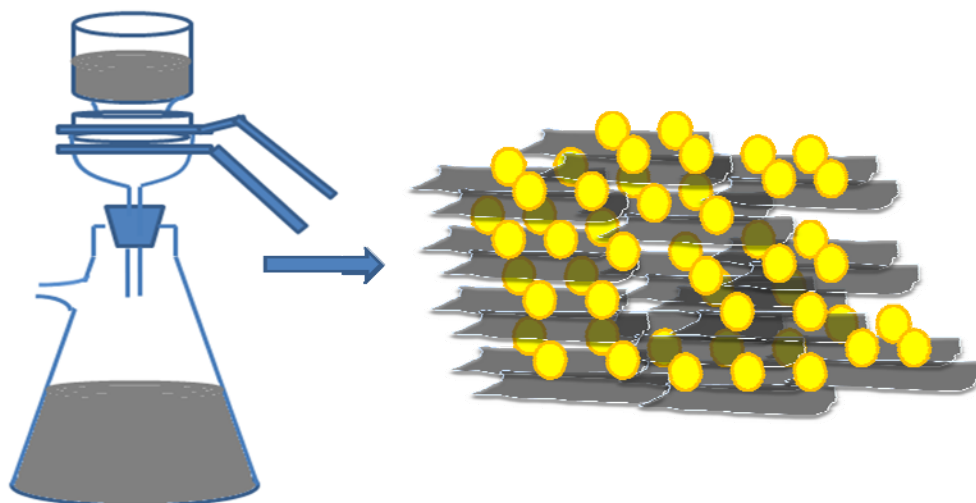


Figure 5-4: Schematics of the experiment showing the Au nanoparticle decorated GNP dispersed in water for subsequent vacuum assisted self assembly.

Figure 5-4 shows the vacuum assisted self assembly process to prepare Au/GNP hybrid paper. To create a more ordered multilayer structure within the paper, it is important to do multi-filtration (5 ml at a time) instead of filtration all at once. After the filtration process, it was found that the bottom few layers in contact with the filter membrane is more ordered than the top layers as a result of a non-uniform pressure difference in the paper during filtration as thickness builds up. Therefore, 30 – 40 ml of Au/GNP suspension at 1 mg/ml concentration was filtered to achieve a better aligned structure within the hybrid paper. Figure 5-5 shows the photos of the as-made papers after being removed from the filter membrane. The as-made paper is very flexible and shows certain mechanical robustness under bending.



Figure 5-5: Photos of the as-made GNP paper showing flexibility and mechanical robustness under bending and the Au/GNP hybrid sample used for thermal diffusivity measurement (1 inch diameter)

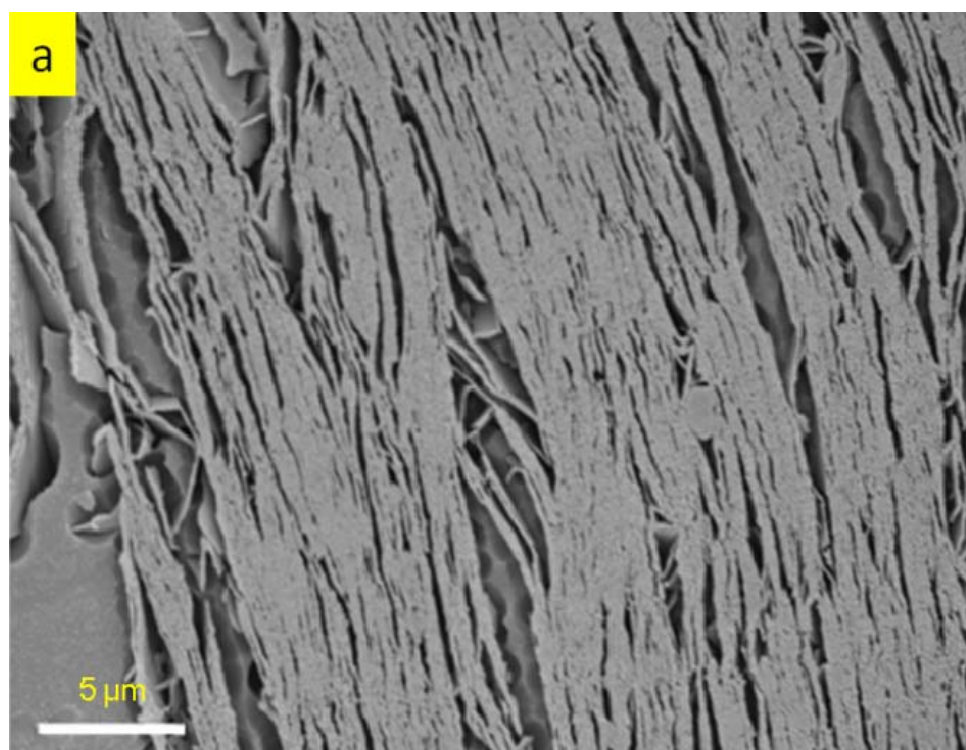
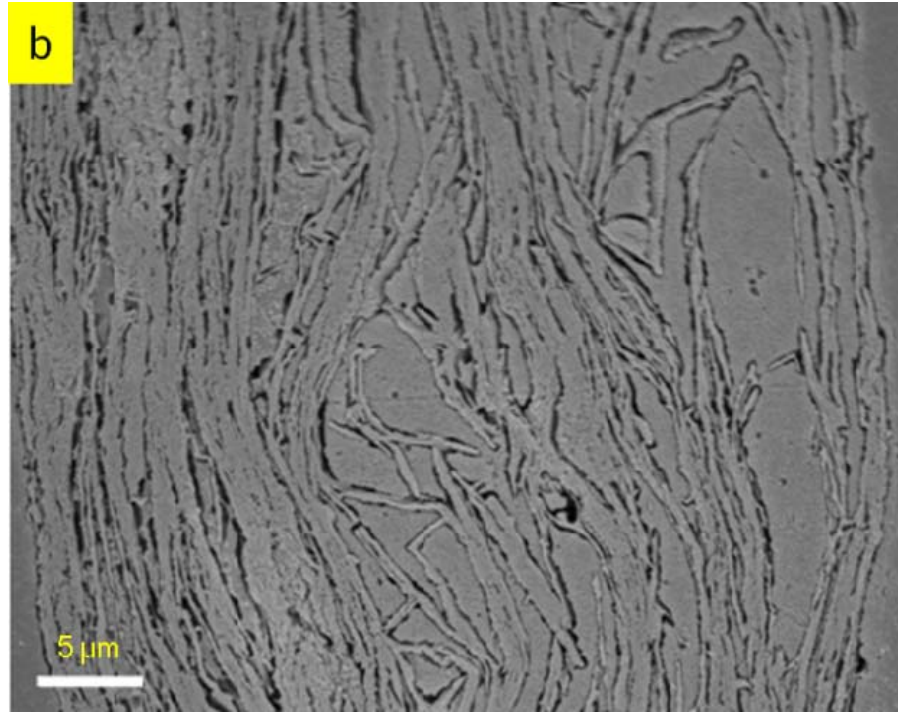


Figure 5-6: (a) Representative cross sectional SEM image of “as-made” GNP paper (scale bar: 5 μm). (b) as-made Au/GNP hybrid paper prepared at 0.3wt% PEI (scale bar: 5 μm).

Figure 5-6(cont'd)



The cross sections of both as-made GNP and Au/GNP papers for SEM observation were prepared by epoxy embedding shown in Figure 5-6. The neat as-made GNP paper shows a highly aligned structure while preserving certain porosity introduced during filtration. However, porosity is higher in the Au/GNP hybrid paper. The observed difference in morphology is attributed to the presence of Au nanoparticles on GNP. The Au nanoparticles act as spacers, creating more gaps between individual nanoplatelets when they were assembled into a paper. Due to the more open structure of the hybrid ‘paper’, epoxy can easily penetrate into the gaps as shown in Figure 5-6b. However, a highly ordered and highly condensed structure was formed after annealing and cold compaction. The increase in porosity for Au/GNP hybrid sample can also be supported by a reduction in the apparent density of the paper which is shown in Table 5.1.

Table 5-1: Average densities of GNP and Au/GNP hybrid papers measured as-made, annealed, annealed & cold compacted (standard deviation < 0.05g/cm³).

Density (ρ : g/cm ³)	As-made	Annealed	Annealed & cold compacted
GNP paper	0.62	0.62	1.5
Au/GNP (0.3wt% PEI)	0.58	0.57	1.5
Au/GNP (0.6wt% PEI)	0.58	0.58	1.5

5.4.2 Thermal diffusivity and thermal conductivity of Au/GNP hybrid paper

Thermal diffusivity of the samples prepared at different experimental conditions (as-made, annealed, annealed and cold compacted) were measured. Given the density of the sample, and the specific heat, which was measured by differential scanning calorimetry, thermal conductivity of the sample can be obtained: $\kappa = \alpha \rho C_p$ where κ is thermal conductivity with a unit of W/m²K, α is thermal diffusivity with a unit of mm²/s, and C_p is specific heat with a unit of J/g^oK.

As shown in Figure 5-7a, the through-plane thermal diffusivity of all the samples followed the same trend with a slight increase after thermal annealing and a reduction after cold compaction. Previous study (Chapter 4) showed that the enhancement brought by annealing was due to the thermal decomposition of polyethyleneimine at 300 °C [33 and Supporting Information]. It is believed PEI adsorbed either on the GNP surface or on the Au nanoparticles scatter the phonons in this paper-like structure, contributing to a larger thermal interface resistance which is a major impediment to phonon transport. A thermal annealing treatment removed most of the PEI in the paper, presumably reducing the interfacial resistance as suggested by a 20% improvement in through-plane diffusivity. However, upon annealing and cold compaction, thermal diffusivity decreased for all the samples. Compaction of the sample

effectively eliminated large pores within the paper created during filtration and the nanoplatelets were more aligned due to the compressive stress. The better orientation of the nanoplatelets reduced the through-plane phonon transport due to the intrinsically low thermal conductivity of GNP with multiple layers of graphene held together with weak Van der Waals forces and the high probability of interface scattering between individual nanoplatelets. It is also found that the through-plane diffusivity of the Au/GNP hybrid paper is lower than the neat GNP paper. Gold nanoparticles on GNP are likely to interfere with GNP from making contact with each other and the paper becomes more porous. As a result, thermal diffusivity reduced with an increasing concentration of Au nanoparticles on the GNP surfaces.

Cold compaction densifies the “loose” porous nanostructure. Despite the fact that macro sized pores collapse upon compaction in neat GNP paper, there are still numerous slit pores inside it that would interfere with the transport of electrons and phonons. With the hybrid paper, Au nanoparticles on the surface of GNP now have a much higher probability of contact with each other, serving as bridging agents or mini columns which might facilitate propagation of phonons within the paper structure. Nonetheless, the experimental results for “annealed and cold compacted” samples indicated a reduction in the through-plane diffusivity for the Au/GNP hybrid paper. In this case, a phonon is forced to go through a Au nanoparticle to go from one GNP to another, which slows down the heat transfer, thus the thermal diffusivity. The same trend can be observed for thermal conductivity of the samples. In particular, the cross sectional area of heat conduction is reduced due to the presence of Au nanoparticles. As a result, the through-plane thermal conductivity of the Au/GNP hybrid sample is lower than the neat GNP paper after annealing and cold compaction. The result is shown in Figure 5-7b. The reported through-plane

thermal conductivity for the highly oriented pyrolytic graphite measured by pump-probe thermoreflectance technique is $6.1 \text{ W/m}^{\circ}\text{K}$ [34].

The in-plane thermal diffusivity and conductivity are shown in Figure 5-7(c,d). Thermal annealing caused decomposition and removal of PEI from within the sample, improving the “thermal contact area” by reducing interface resistance. A moderate increase of around 10% was observed for samples measured after annealing. Cold-compaction of the samples restores the orientation of the nanoplatelets, making the paper more anisotropic in heat conduction. It is worth noting that both thermal diffusivity and conductivity of the Au/GNP hybrid samples are lower than the neat GNP paper, which is in accord with the trend observed from through-plane measurements. It is believed that those Au nanoparticles are more likely to serve as phonon scattering centers than mini heat conduction channels within the hybrid samples. Recent work by Wang et al used a thermal bridge configuration to measure the in-plane thermal conductivity of supported few layer graphene nanosheets and concluded that the conductivity is $1250 \text{ W/m}^{\circ}\text{K}$ at room temperature is comparable to bulk graphite [35]. The value reported here is lower because of the strong interface scattering which is absent in either individual graphene nanosheets or bulk graphite.

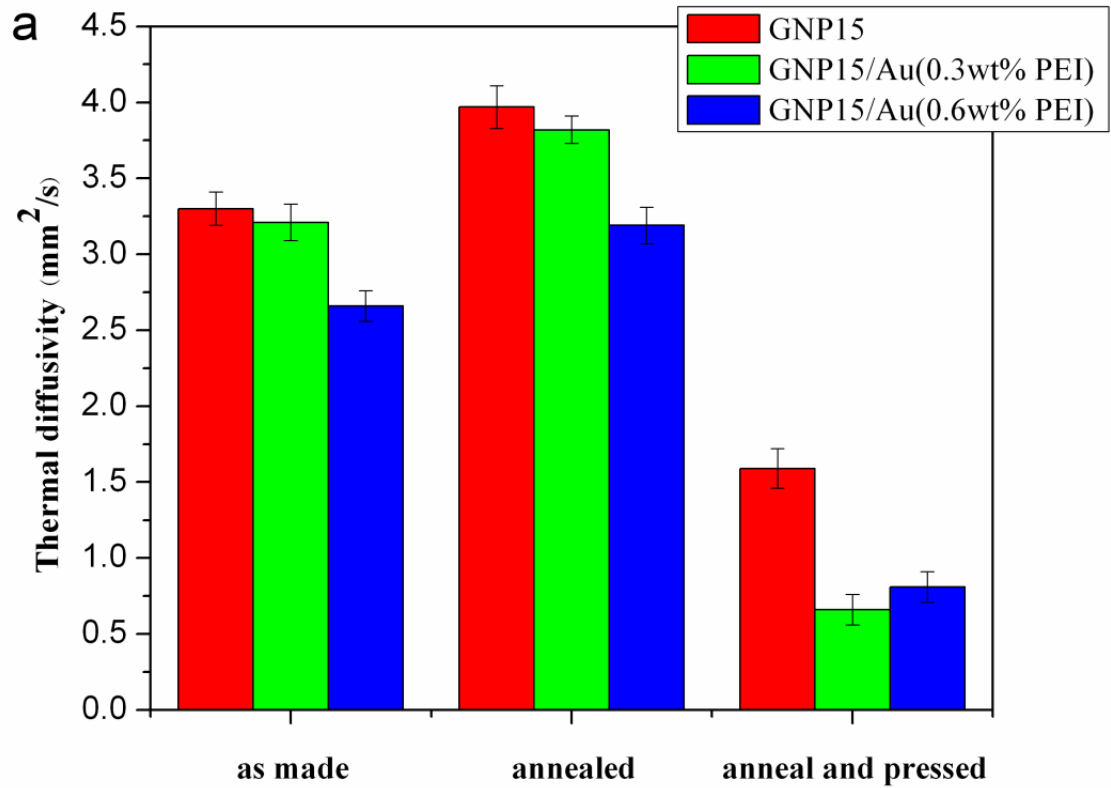


Figure 5-7: (a) Through-plane thermal diffusivity of GNP and Au/GNP paper. b: Through-plane thermal conductivity of GNP and Au/GNP paper. c: In-plane thermal diffusivity of GNP and Au/GNP paper. d: In-plane thermal conductivity of GNP and Au/GNP paper. Note: left column represents GNP15, middle column represents GNP15/Au(0.3wt% PEI), right column represents GNP15/Au(0.6wt% PEI)

Figure 5-7(cont'd)

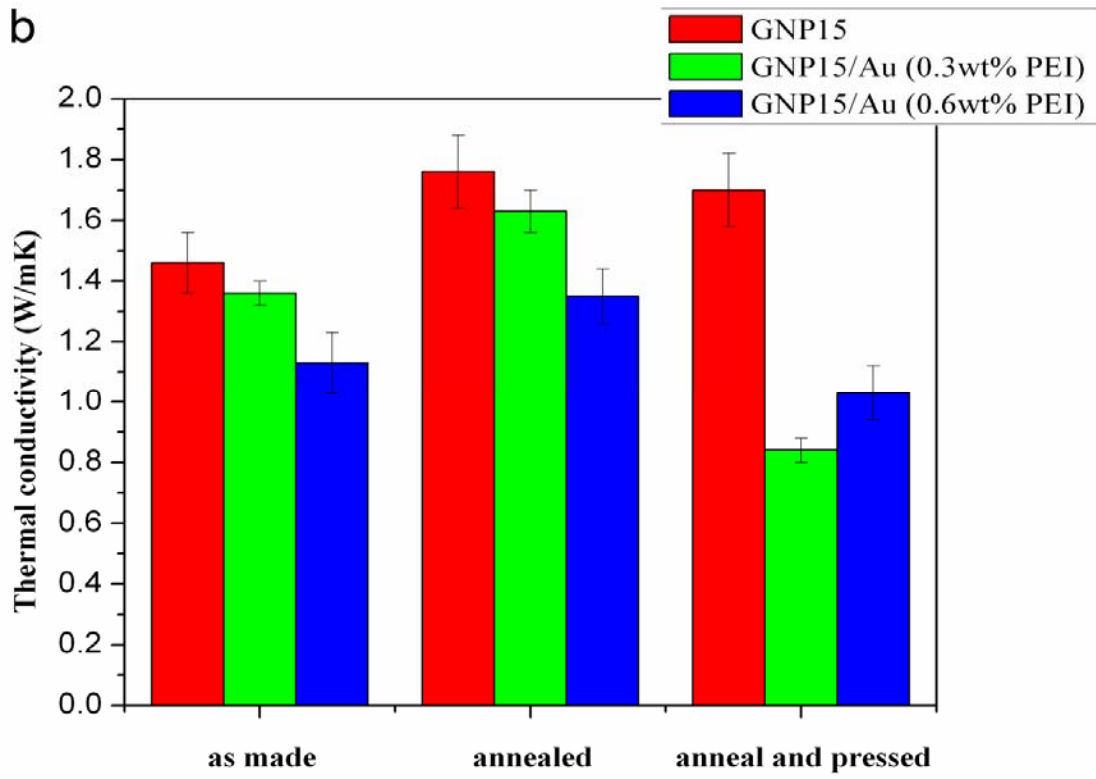


Figure 5-7(cont'd)

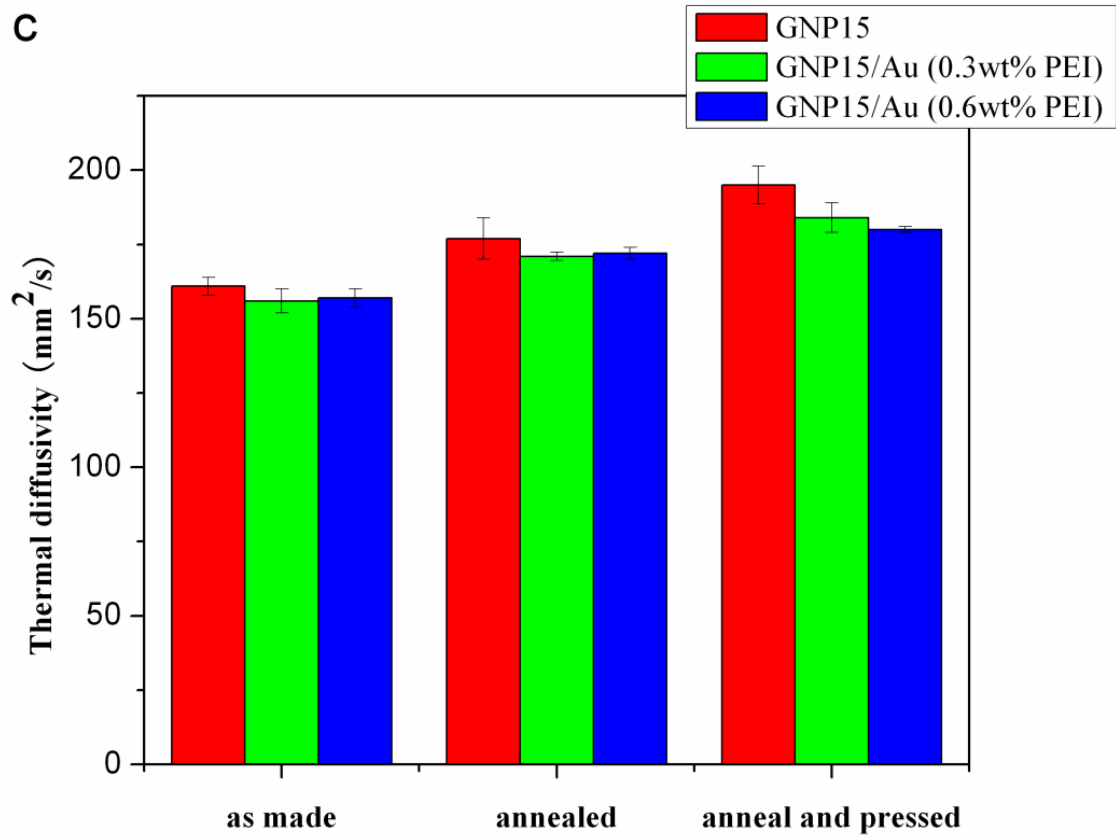
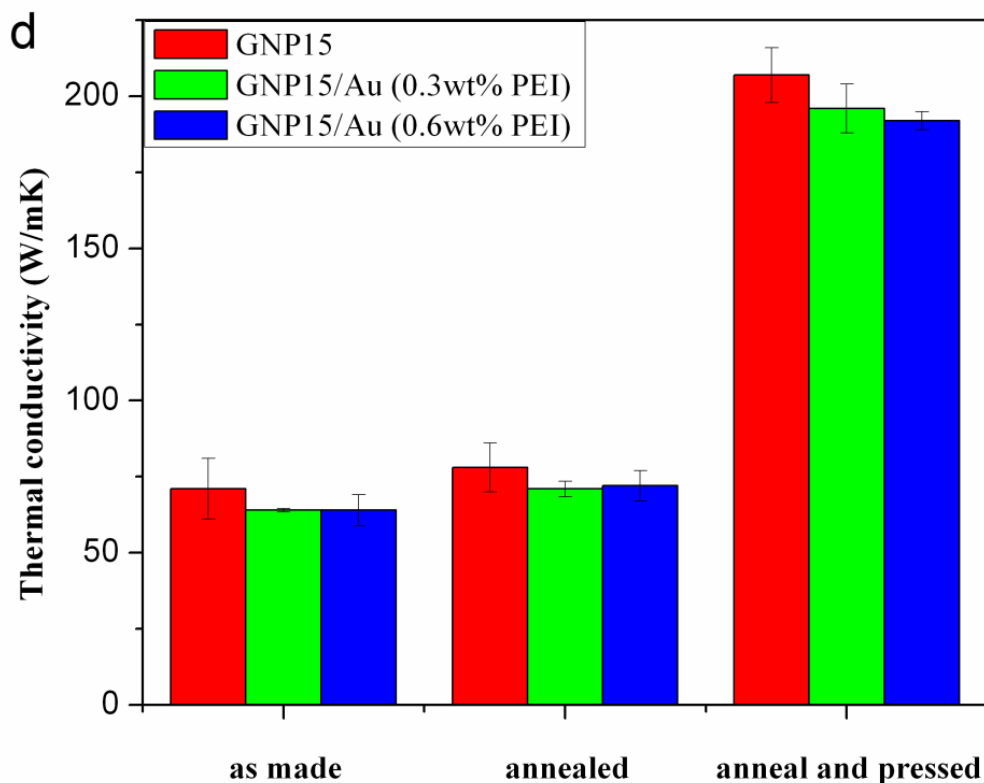


Figure 5-7(cont'd)



5.4.3 Electrical properties of Au/GNP hybrid paper

The self assembly of GNP with and without Au nanoparticles did have an impact on the thermal conductivity of the samples. In particular, the gold nanoparticles that were expected to provide additional heat channels through the plane of the paper structure to improve the heat conduction turned out to be ineffective. To investigate if the same phenomenon observed in phonon transport also applies to electrons, both the through-plane and in-plane electrical conductivity of these papers were measured and reported in Figure 5-8.

From Figure 5-8a, the in-plane electrical conductivity of the papers increased with annealing and cold compaction. The improvement can be explained by the effective

decomposition of electrically insulating PEI from the samples through thermal annealing and significant reduction of pore volumes through cold compaction, both contributing to decreasing electron tunneling resistance. In particular, the GNP paper decorated with Au nanoparticles of different size and distribution density showed higher conductivity than the neat GNP paper. Hybrid GNP papers with individual nanoplatelets decorated with smaller and higher coverage of Au nanoparticles exhibited higher in-plane electrical conductivity. Upon cold compaction, the collapse of macro pores in the sample brings more Au nanoparticles into immediate contact, effectively bridging previously isolated nanoplatelets. It is worth noting that the in-plane conductivity reaches a value as high as 1500 S/cm for Au/GNP (0.6wt% PEI) hybrid paper, which is almost 70% higher than the neat GNP paper (880 S/cm) at the same condition. It is worth noting that the in-plane electrical conductivity is measured to be 2×10^4 S/cm for bulk graphite [36], one order of magnitude higher than the value reported here for Au/GNP hybrid sample.

The through-plane electrical resistivity of the papers was measured by a two-point method (see Supporting Information) on the samples that have been annealed and cold compacted. The result is shown in Figure 5-8b. The results from as-made and annealed samples are not reported because the measured electrical resistance fluctuates a large amount possibly due to the open porous structure inside the sample. The measurements on the annealed and cold compacted samples were stable enough thanks to the dense and compact structure of the paper. The Au nanoparticles effectively bridged adjacent GNPs, creating mini channels for the cross plane electron transport as evidenced by the drop in the through-plane resistivity. It is thus evident that although the through-plane conductivity is small due to a greater anisotropic electronic conduction induced by cold compaction, the Au nanoparticles did facilitate the

electron transport within the paper structure, making individual nanoplatelets more electrically connected. As a comparison, the through-plane resistivity for bulk graphite is 0.1~1 ohm cm, a few orders of magnitude lower than the highly ordered layer structure reported here [36].

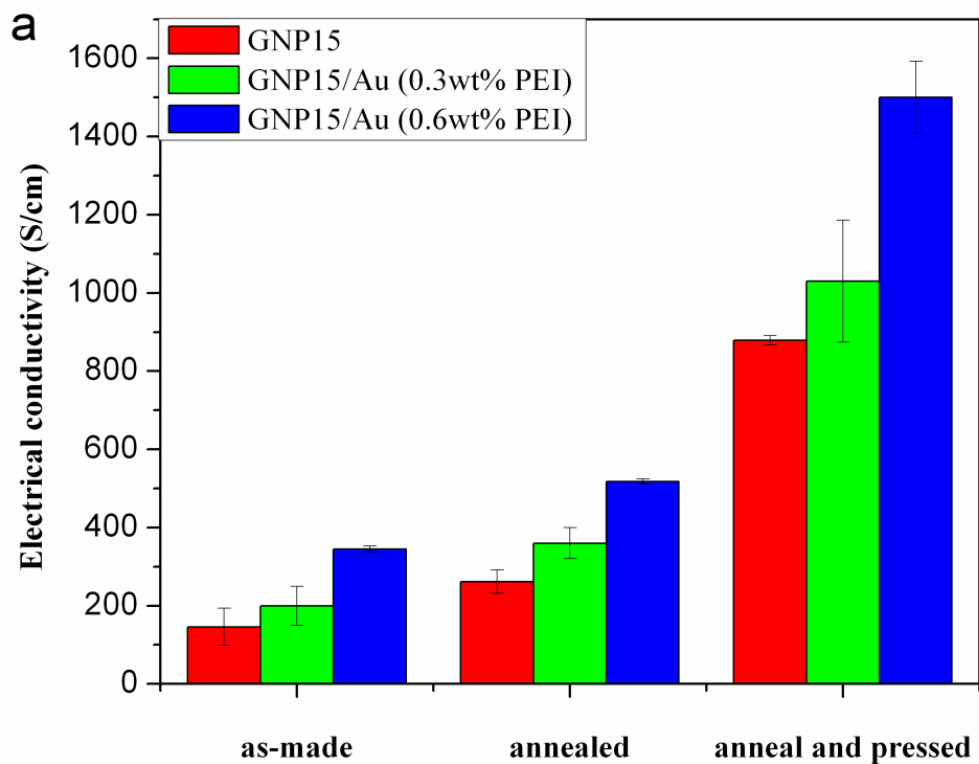
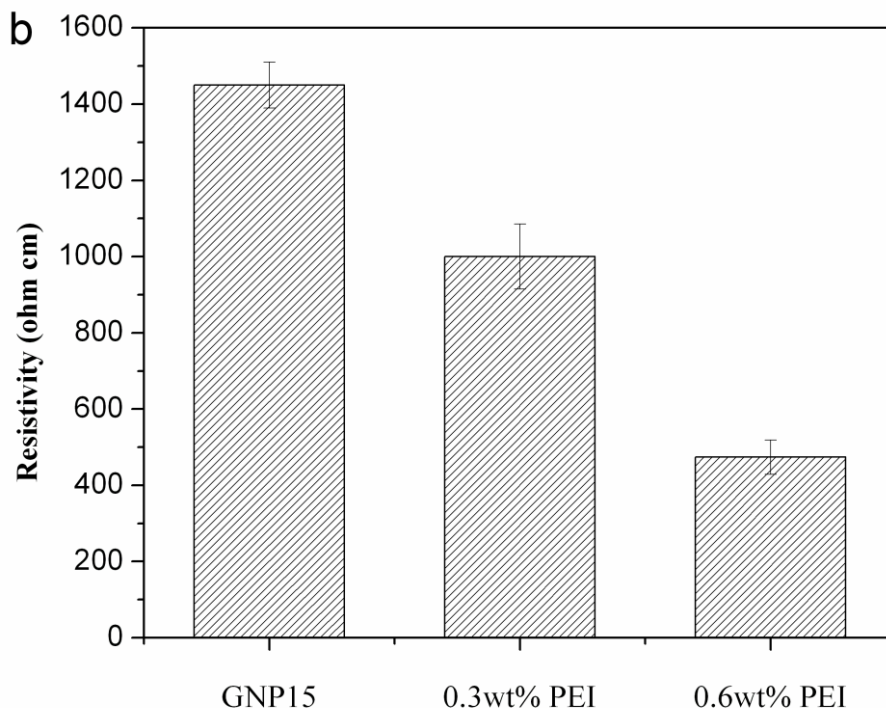


Figure 5-8: (a) In-plane electrical conductivity of anneal & cold compacted GNP and Au/GNP paper. (b) Through-plane electrical resistivity of anneal & cold compacted GNP and Au/GNP paper.

Figure 5-8(cont'd)



The findings reported here indicate that electron and phonon transport are affected differently by the presence of Au nanoparticles within the hybrid sample. Phonons travel at different frequencies in two materials of different densities (e.g. Au and graphite). Non-equilibrium molecular dynamic studies show that when a large mismatch in the phonon vibrational density of states (VDOS) exists in two distinctive mediums, direct coupling and propagation of phonons across the interface will be reduced. As a result, the thermal energy can only be transferred across the interface indirectly through anharmonic scattering which enables phonon-phonon interactions and gives rise to a high thermal interface resistance [37]. Despite the fact that Au nanoparticles could bridge the small gaps between individual nanoplatelets, the anharmonicity in VDOS in gold and carbon result in strong interface scattering that reduces the

efficiency of heat transfer. However, the improvement observed in electrical conductivity suggests that the Au nanoparticles allow more electrons to tunnel through, making the hybrid paper structure more electrically connected as compared with the neat GNP paper.

A few literature citations point out that few-layer graphene shows improved electrical conductivity when Au precursor were spontaneously reduced to Au nanoparticles driven by the redox potential difference between the Au^{3+} and the graphene nanosheets [38-40]. As a result, the few-layer graphene was p-type doped with electrons being transferred away from it to the metal precursor. The mere increase of the carrier concentration (i.e. holes) contributes to an increase in the electrical conductivity. However, the microwave assisted synthesis of nanoparticles in PEI matrix reported here did not involve transfer of electrons from individual graphite nanoplatelets to Au^{3+} ions. The fact that electrons mainly come from polyethyleneimine instead of GNP eliminates the possibility that the individual nanoplatelets would be p-type doped. Therefore, the enhancement in electrical conductivity observed here originates from the reduction in the interface resistance instead of doping, i.e. more electrons can find routes with least resistive pathways within the hybrid paper structure because of the highly electrically conductive Au nanoparticles.

5.5 Conclusion:

Gold nanoparticles of a uniform size distribution were successfully synthesized on exfoliated graphene nanoplatelets by microwave assisted heating in a polyethyleneimine/water solution. It is believed that fast super-saturation of metal atoms with low surface tension is desired for producing monodispersed small nanoparticles. A self-standing, mechanically robust Au/GNP nanostructured multilayered ‘paper’ was prepared by vacuum assisted self assembly.

Thermal annealing to decompose and remove PEI improves both electrical and thermal conductivities. Paper porosity was significantly reduced by cold compaction which produces closer contact between individual nanoplatelets. Au nanoparticles on the surface of GNP reduce phonon transport by introducing more scattering sites at the interface due to a vast difference in the density of states for phonons in gold and GNP and by reducing the total cross sectional area for heat conduction. However, the Au nanoparticles act as electron super highways that make nanoplatelets more electrically connected. The decoupled transport phenomenon observed here provided valuable insights into designing GNP paper based thermoelectric materials.

Acknowledgement

The authors wish to acknowledge the Army Research Office for financial support of this research, Grant # W911NF-09-1-0451, Dr. Robert Mantz, Technical Program Manager.

Supporting information

TGA (decomposition of PEI)

TGA curve of the neat polyethyleneimine decomposed in air is shown in Figure 5-9. It is noted that PEI begins a major decomposition event at around 300°C. In addition, the TGA curves of the as-made GNP paper, annealed GNP paper and as-made Au/GNP hybrid prepared at 0.6wt% PEI are shown in Figure 5-10. PEI decomposition can be observed in both the as-made GNP and Au/GNP hybrid samples. While for the annealed GNP sample, major decomposition event occurs at the oxidation temperature of GNP itself, indicating that PEI is removed from the sample.

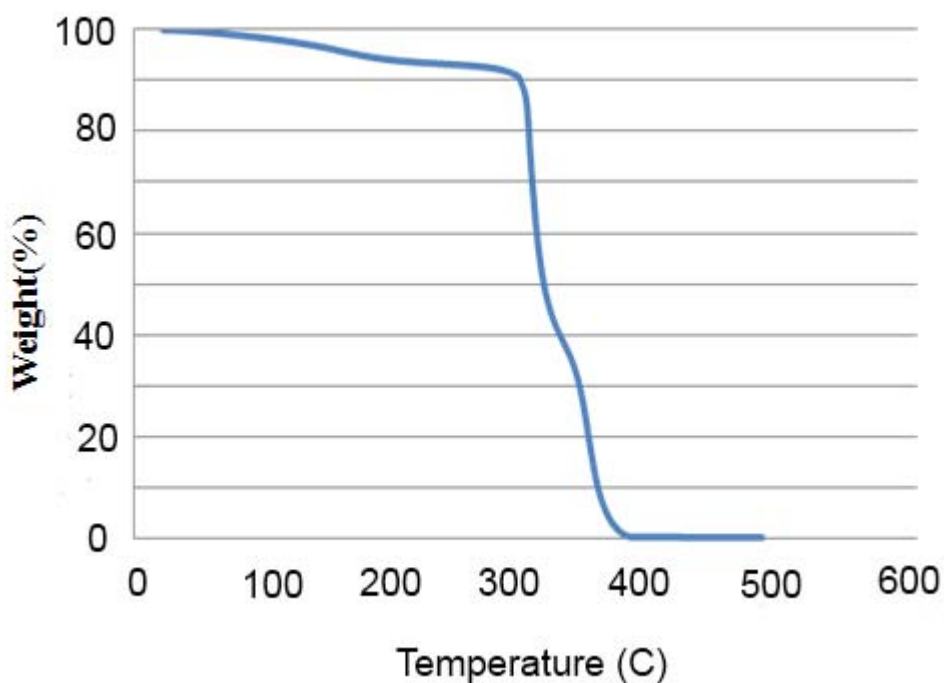


Figure 5-9: TGA curve of neat PEI in air

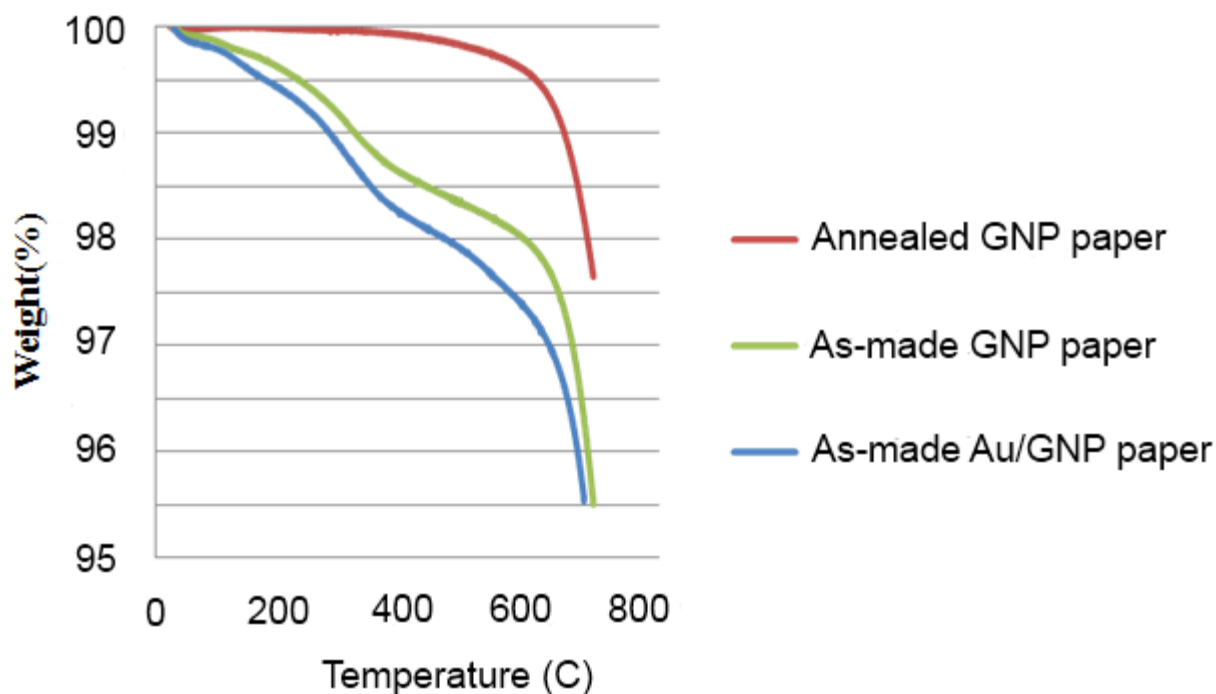


Figure 5-10: TGA curves of annealed GNP paper, as-made GNP paper and as-made Au/GNP paper in air.

Size distribution of Au nanoparticles on GNP by Image-Pro

The size distribution data shown in Figure 5-3 was obtained by analyzing the SEM images in Image-Pro, which is a software commercially available. The general procedures are described below: select a SEM image with a magnification of at least 80k, adjust the contrast until the Au nanoparticles stand out from the background. Let the software pick out the Au nanoparticles according to the pre-determined selection criteria (e.g. diameter $\geq 4\text{nm}$, $1 \leq \text{aspect ratio} \leq 1.5$). The average diameter of each nanoparticle on the analyzed SEM is shown and the histogram is plotted according to this information. Figure 5-11 is a representative SEM that was analyzed by the software. Figure 5-12 is the statistics of the nanoparticle distribution.

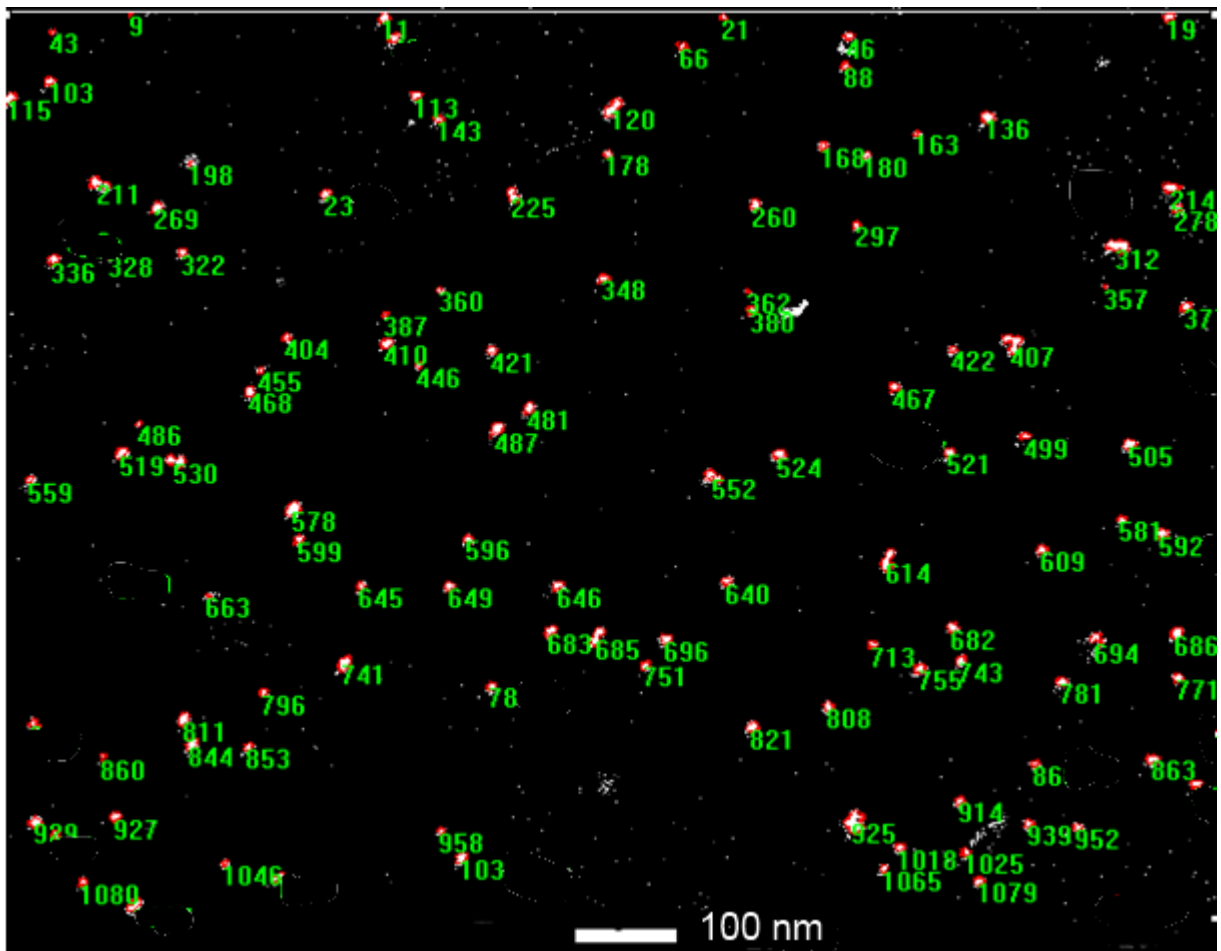


Figure 5-11: Example SEM images analyzed by Image-Pro to determine the distribution of nanoparticle size (scale bar 100nm)

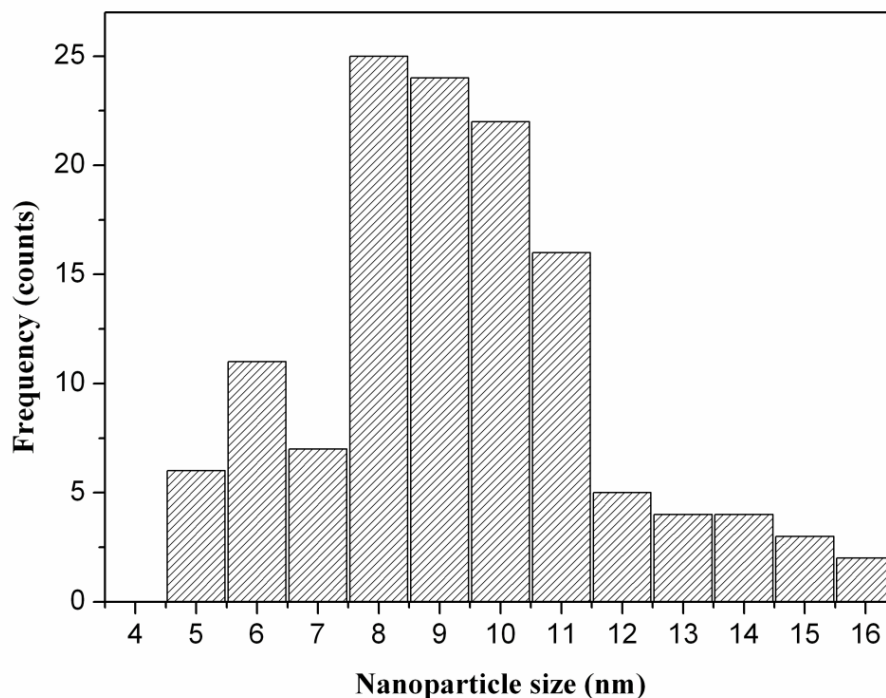


Figure 5-12: Particle size distribution obtained from Figure 5-11.

Two point through-plane electrical resistivity measurements of thin film (<math><100\mu\text{m}</math>)

The reported through-plane electrical resistivity is measured by the two point probe method because of the inherent geometric constraints of working with a thin film. However, the configuration is different from the in-plane four point probe measurement where a tip probe is in contact with the sample, giving rise to a very large contact resistance. In order to eliminate the effect of contact resistance, strips of adhesive copper foils were used to cover the top and bottom surfaces of the sample to spread the electrical current. Figure 5-13 shows cross sectional schematics of the measurement:

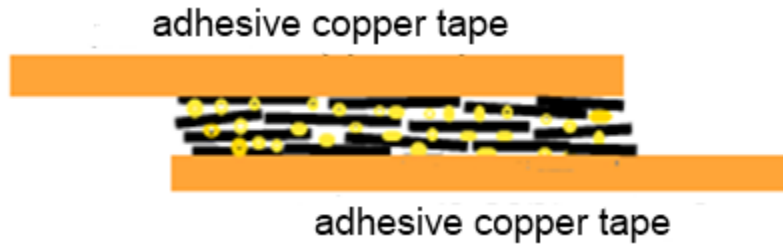


Figure 5-13: Schematic representation of through-plane resistivity measurement of thin film sample

It is noted that the resistance measured include the resistances of the copper tapes, the contact and the resistance of the sample. To account for the effect of copper and the contact, a gold foil with similar geometry to the samples (100 μ m in thickness, 99.99%, Sigma Aldrich) was used to estimate copper and contact resistance because the resistance of the gold foil in this case is negligibly small. The measured resistance is 0.26 ohm which is around 10% of the measured sample resistance. Therefore, the data reported is modified by subtracting 0.26 ohm from the measured sample resistance to obtain the electrical resistivity.

REFERENCES

References

1. Xu, C.; Wang, X.; Zhu, J.; Graphene-metal particle nanocomposites. *J. Phys. Chem. C.* **2008**, *112*, 19841-19845.
2. Yoo, E.; Okata, T.; Akita, T.; Kohyama, M.; Nakamura, J.; Honma, I. Enhanced electrocatalytic activity of Pt subnanoclusters on graphene nanosheets surface. *Nano Lett.* **2009**, *9*, 2255-2259.
3. Li, Y. M.; Tang, L. H.; Li, J. H.; Preparation and electrochemical performance for methanol oxidation of Pt/graphene nanocomposites. *Electrochem. Commun.* **2009**, *11*, 846-849.
4. Serger, B.; Kamat, P. V.; Electrocatalytically active graphene-platinum nanocomposites. Role of 2-D carbon support in PEM fuel cells. *J. Phys. Chem. C.* **2009**, *113*, 7990-7995.
5. Zhu, C.; Guo, S.; Zhai, Y.; Dong, S.; Layer-by-layer assembly for constructing a graphene/platinum nanoparticle three-dimensional hybrid nanostructure using ionic liquid as a linker. *Langmuir.* **2010**, *26*, 7614-7618.
6. Lu, J.; Do, I.; Drzal, L. T.; Worden, R. M.; Lee, I.; Nanometal-decorated exfoliated graphite nanoplatelet based glucose biosensors with high sensitivity and fast response. *ACS Nano.* **2008**, *2*, 1825-1832.
7. Guo, S.; Wen, D.; Zhai, Y.; Dong, S.; Wang, E.; Platinum nanoparticle ensemble-on-graphene hybrid nanosheet: One-pot, rapid synthesis, and used as new electrode material for electrochemical sensing. *ACS Nano.* **2010**, *4*, 3959-3968.
8. Si, Y.; Samulski, E.; Exfoliated graphene separated by platinum nanoparticles. *Chem. Mater.* **2008**, *20*, 6792-6797.
9. Li, Y.; Lv, X.; Lu, J.; Li, J.; Preparation of SnO₂-Nanocrystal/Graphene-nanosheets composites and their lithium storage ability. *J. Phys. Chem. C.* **2010**, *114*, 21770-21774.
10. Kamat, P. V.; Graphene-based nanoarchitectures, Anchoring semiconductor and metal nanoparticles on a two-dimensional carbon support. *J. Phys. Chem. Lett.* **2010**, *1*, 520-527.
11. Muszynski, R.; Seger, B.; Kamat, P. V.; Decorating graphene sheets with gold nanoparticles. *J. Phys. Chem. C.* **2008**, *112*, 5263-5266.
12. Goncalves, G.; Marques, P. A. A. P.; Granadeiro, C. M.; Nogueira, H. I. S.; Singh, M. K.; Gracio, J. Surface modification of graphene nanosheets with gold nanoparticles: the role of oxygen moieties at graphene surface on gold nucleation and growth. *J. Chem. Mater.* **2009**, *21*, 4796-4802.
13. Padgett, C. W.; Brenner, B. W.; Influence of chemisorption on the thermal conductivity of single-walled carbon nanotubes. *Nano Lett.* **2004**, *4*, 1051-1053.

14. Kongkanand, A.; Vinodgopal, K.; Kuwabata, S.; Kamat, P. V.; Highly dispersed Pt catalyst on single walled carbon nanotubes and their role in methanol oxidation. *J. Phys. Chem. B*, **2006**, *110*, 16185-16188.
15. Ostojic, G. N.; Ireland, J. R.; Hersam, M. C.; Noncovalent functionalization of DNA-wrapped single walled carbon nanotubes with platinum-based DNA cross-linkers. *Langmuir*, **2008**, *24*, 9784-9789.
16. Bayati, M.; Abad, J. M.; Nichols, R. J.; Schiffrin, D. J.; Substrate structural effects on the synthesis and electrochemical properties of platinum nanoparticles on highly oriented pyrolytic graphite. *J. Phys. Chem. C*. **2010**, *114*, 18439-18448.
17. Ren, G.; Xing, Y.; Deposition of metallic nanoparticles on carbon nanotubes via a fast evaporation process. *Nanotechnology*. **2006**, *17*, 5596-5601.
18. Lin, Y.; Watson, K. A.; Fallbach, M. J.; Ghose, S.; Smith, J. G. Jr; Delozier, D. M et al. Rapid, solventless, bulk preparation of metal nanoparticle-decorated carbon nanotubes. *ACS Nano*, **2009**, *3*, 871-884.
19. Teranishi, T.; Miyake, M.; Size control of palladium nanoparticles and their crystal structures. *Chem. Mater.* **1998**, *10*, 594-600.
20. Leff, D. V.; Thermodynamic control of gold nanocrystal size: experiment and theory. *J. Phys. Chem.* **1995**, *99*, 7036-7041.
21. Do. I.; Metal decoration of exfoliated graphite nanoplatelets for fuel cell applications, Ph.D dissertation, Michigan State University, East Lansing, Michigan, **2006**.
22. Meguro, K.; Torizuka, M.; Esumi, K.; The preparation of organo colloidal precious metal particles. *Bull. Chem. Soc. Jpn*, **1988**, *61*, 341-345.
23. Mohamed, M. B.; Wang, Z. L.; El-Sayed, M. A.; Temperature-dependent size-controlled nucleation and growth of gold nanoclusters. *J. Phys. Chem. A*. **1999**, *103*, 10255-10259.
24. Jasuja, K.; Linn, J.; Melton, S.; Berry, V.; Microwave-reduced uncapped metal nanoparticles on graphene: tuning catalytic, electrical, and Raman properties. *J. Phys. Chem. Lett.* **2010**, *1*, 1853-1860.
25. Vinodgopal, K.; Neppolian, B.; Lightcap, I. V.; Grieser, F.; Ashokkumar, M.; Kamat, P. V. Sonolytic design of graphene-Au nanocomposites. Simultaneous and sequential reduction of graphene oxide and Au(III). *J. Phys. Chem. Lett.* **2010**, *1*, 1987-1993.
26. Bai, L.; Zhu, H.; Thrasher, J. S.; Street, S. C.; Synthesis and electrocatalytic activity of photoreduced platinum nanoparticles in a poly(ethylenimine) matrix. *ACS App. Mater. Interfaces*. **2009**, *1*, 2304-2311.

27. Kuo, P. L.; Chen, W. F.; Huang, H. Y.; Chang, I. C.; Dai, S. A.; Stabilizing effect of pseudo-dendritic polyethyleneimine on platinum nanoparticles supported on carbon. *J. Phys. Chem. B.* **2006**, *110*, 3071-3077.
28. Sun, X.; Dong, S.; Wang, E.; One-step synthesis and characterization of polyelectrolyte-protected gold nanoparticles through a thermal process. *Polymer.* **2004**, *45*, 2181-2184.
29. Zhang, J.; Xu, Q.; Ye, F.; Lin, Q.; Jiang, D.; Iwasa, M.; Effect of citric acid on the adsorption behavior of polyethyleneimine (PEI) and the relevant stability of SiC slurries. *Colloids Surf A.* **2006**, *276*, 168-175.
30. Oxtoby, D. W.; Nucleation of first order phase transitions. *Acc. Chem. Res.* **1998**, *31*, 91-97.
31. Furedi-Millhofer, H.; Spontaneous precipitation from electrolyte solutions. *Pure Appl. Chem.* **1981**, *53*, 2041-2055.
32. Peng, X. G.; Wickham, J.; Alivisatos, A. P.; Kinetics of II-VI and III-V colloidal semiconductor nanocrystal growth: "Focusing" of size distribution. *J. Am. Chem. Soc.* **1998**, *120*, 5343-5344.
33. Xiang, J.; Drzal, L. T.; Thermal conductivity of exfoliated graphite nanoplatelet paper *Carbon*, **2011**, *49*, 773-778.
34. Schmidt, A. J.; Chen, X.; Chen, G.; Pulse accumulation, radial heat conduction, and isotropic thermal conductivity in pump-probe transient thermoreflectance. *Rev. Sci. Instrum.* **2008**, *79*, 114902(1-9).
35. Wang, Z.; Xie, R.; Bui, C. T.; Liu, D.; Ni, X.; Li, B et al. Thermal transport in suspended and supported few-layer graphene. *Nano Lett.* **2011**, *11*, 113-118.
36. Morgan, G. J.; Uher, C.; The C-axis electrical resistivity of highly oriented pyrolytic graphite. *Philos. Mag. B.* **1981**, *44*, 427-430.
37. Luo, T.; Lloyd, J. R.; Non-equilibrium molecular dynamics study of thermal energy transport in Au-SAM-Au junctions. *Int. J. Heat Mass Transfer*, **2010**, *53*, 1-11.
38. Kong, B. S.; Geng, J.; Jung, H. T.; Layer-by-layer assembly of graphene and gold nanoparticles by vacuum filtration and spontaneous reduction of gold ions. *Chem Commun*, **2009**, *16*, 2174-2176.
39. Shi, Y.; Kim, K. K.; Reina, A.; Hofmann, M.; Li, L. J.; Kong, J.; Work function Engineering of graphene electrode via chemical doping. *ACS Nano*, **2010**, *4*, 2689-2694.
40. Kim, K. K.; Reina, A.; Shi, Y.; Park, H.; Li, L. J.; Lee, Y. H et al. Enhancing the conductivity of transparent graphene films via doping. *Nanotechnology*, **2010**, *21*, 285205(1-6).

Chapter 6 Templated Growth of Polyaniline on GNP and Its Thermoelectric Properties

6.1 Abstract:

Polyaniline (PANI)/exfoliated graphene nanoplatelets (GNP) nanocomposites were prepared by in situ polymerization of aniline monomer in the presence of GNP for thermoelectric applications. PANi has a strong affinity for GNP due to π electron interactions, forming a uniform nanofibril coating. A paper-like nanocomposite was prepared by controlled vacuum filtration of an aqueous dispersion of PANi decorated GNP. The Seebeck coefficient of the resulting nanocomposite changes with initial concentration of aniline in the solution as well as the protonation of PANi, reaching as high as 33 $\mu\text{V/K}$ for nanocomposites containing approximately 40wt% of PANi and with a protonation ratio of 0.2. The presence of GNP improved the electrical conductivity of the nanocomposites to 59 S/cm. As a result, thermoelectric figure of merit ZT of the nanocomposites is 2 orders of magnitude higher than either of the constituents, exhibiting a significant synergistic effect. This chapter is based on a journal publication: Xiang, J., Drzal, L. T.(2012). Templated growth of polyaniline on exfoliated graphene nanoplatelets (GNP) and its thermoelectric properties. *Polymer*, 2012 (in press)

6. 2 Introduction:

Previous research (Chapter 5) has shown that it is possible to separate the electron and phonon transport in gold nanoparticle modified GNP paper nanocomposites. Given the high price of gold nowadays, this method proves the concept but is not practical for real application. Instead of using metal nanoparticles to serve as spacers, a conductive polymer can be similarly

deposited at the interfaces of GNP to preferentially reduce thermal conductivity. Figure 6-1 is a schematic representation of replacing Au with a polymer. This chapter is dedicated to the investigation of thermoelectric properties of this novel nanocomposite.

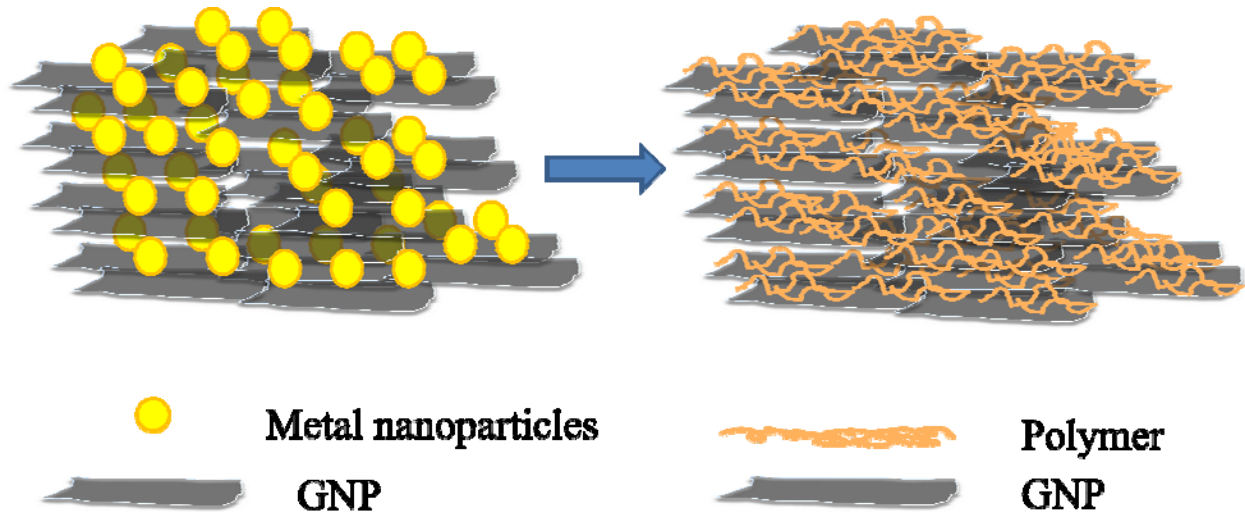


Figure 6-1: A schematic representation of replacing the Au nanoparticle spacers in the highly ordered GNP paper with a layer of polymer.

Thermoelectric materials have great potential in applications such as power generation and solid state heating/cooling, realizing direct conversion between thermal energy and electrical energy without involving moving mechanical components or hazardous working fluids [1,2]. The efficiency of thermoelectric materials is dependent on a dimensionless figure of merit ZT , defined by $(S^2\sigma/\kappa)T$ (S , σ , κ , T are the Seebeck coefficient, electrical conductivity, thermal conductivity and absolute temperature, respectively and $S^2\sigma$ is the power factor) The major challenge in designing a good thermoelectric material is to separate the interdependence of parameters in ZT . For example, improving electrical conductivity by increasing carrier concentration usually results in a reduction in Seebeck coefficient, while improving the carrier mobility is generally considered as the most effective way to increase both electrical

conductivity and Seebeck coefficient [3,4]. Until now, inorganic semiconductors and their compounds have received the most attention because of their high power factor [5,6]. Recently, there has been research underway directed at developing low dimensional nanomaterials or their composites to replace bulk components to achieve a higher ZT [7]. However, the relative high cost of raw materials and lack of scalability of production has created a great need for inexpensive, easy to process materials for emerging novel applications.

Polymer based thermoelectrics are gaining ever increasing interest because of their low cost and low thermal conductivity [8-10]. In particular, conductive polymers such as polyaniline has been extensively studied and are known for their environmental stability and facile acid base doping and de-doping characteristics [11-13]. The thermoelectric properties of polyaniline have also been extensively studied [14-17]. However, the performance is usually limited by its low power factor which presents a significant challenge for polymers to compete with inorganic semiconductors. To further improve the thermoelectric properties of conductive polymers, Grunlan et al. first proposed a segregated-network polymer composite where highly conducting CNTs were introduced to the emulsion polymer matrix to create electrically connected but thermally disconnected pathways in an effort to decouple the electron and phonon transport [18]. This composite approach was then adopted in conductive polymer systems and a synergistic effect was observed [19-23], counterintuitive to what was commonly believed that a simple mixture of two components will not lead to an enhancement in performance [24,25].

Given the fact that the performance of carbon nanotubes based thermoelectric materials is still low with a highest reported room temperature ZT in the range of 10^{-3} - 10^{-2} , a very large area of active material is needed to generate the same amount of power as the conventional bismuth telluride module. Therefore, the high cost of producing high quality carbon nanotubes in a

commercial scale might still be the bottleneck for wide spread application of CNT based nanocomposites.

While PANi can be successfully grown on the surface of carbon nanotubes due to their structural similarity [26,27], the actual interaction area between individual CNT and PANi could be very small due to the extremely small diameter of the nanotubes. Rapid synthesis of PANi in the presence of GNP by in situ polymerization was carried out at various concentrations of aniline. The 2D platelet morphology provides a much larger "interaction surface area" with PANi than CNT and possibly enables a templating effect for ordered growth of individual PANi nanofiber. Due to the strong affinity of PANi for the basal plane of GNP, a uniform coating of PANi can be formed. It is also mentioned in several literature citations that the Seebeck coefficient of conjugated polymers is related to its electrical conductivity, which is primarily determined by the dopant used and doping strength [28,29]. Protonation (deprotonation) of PANi on the surface of GNP was altered by exposing the as-made PANi/GNP to different acid/base concentrations. A highly ordered composite film was prepared on a filter membrane which showed good flexibility and mechanical robustness upon drying and compaction. The thermoelectric properties (Seebeck coefficient, thermal and electrical conductivity) of the PANi/GNP nanocomposites with various composition of polymer and various degree of protonation are discussed.

6.3 Experimental:

Production of exfoliated graphene nanoplatelets

GNP are produced by exfoliating the graphite intercalated compounds (Asbury Inc.) in a conventional kitchen microwave oven following the procedures described previously. The

intercalation and exfoliation does not damage the sp^2 carbon scaffold in the basal plane, therefore maintaining the undisrupted carrier transport. The GNP particles used in this experiment are GNP200 with an average diameter of $5\mu\text{m}$ and BET surface area of about $200\text{ m}^2/\text{g}$.

Synthesis of PANi/GNP core-shell nanostructure (as-made)

120 mg of GNP200 was dispersed in 60 ml 1M HCl with slight sonication. Certain weight of aniline (M_w : 93.13g/mol from Sigma Aldrich) was added to the suspension and sonicated for 60 mins at 5°C . Ammonium persulfate (M_w : 228 g/mol from Sigma Aldrich) as the oxidant was pre-dissolved in 5 ml 1M HCl at 5°C and added within 1 min to the aniline chloride solution with GNP particles. The solution was further bath sonicated for 15 mins and the reaction was kept for 24 h under magnetic stirring. The reaction product was washed with centrifugation with 1M HCl and ethyl alcohol many times. A polyaniline/GNP thin film structure was then formed on a PVDF (Durapore, $0.22\mu\text{m}$) filter membrane by vacuum assisted self assembly. The film was then dried in a vacuum oven at 60°C for 48h.

Synthesis of neat emeraldine salt polyaniline

Ammonium persulfate (APS, 0.05 mole, 11.5g) was dissolved in 200 ml 1M HCl at $0-5^\circ\text{C}$. Aniline (20 ml, 0.219 mole) was dissolved in 300 ml 1M HCl at $0-5^\circ\text{C}$. APS was added to the solution of aniline hydrochloride within 1 min. The solutions were mixed by strong stirring for 2 mins followed by continuous stirring at around $0-5^\circ\text{C}$ for 24 h. The reaction product was filtered and washed with several portions of 1M HCl first and ethanol to get rid of un-reacted products and oligomer. The dark green sample cake was vacuum dried at 60°C for 48 h and is known as the emeraldine salt form of polyaniline.

Achieving polyaniline with different levels of protonations:

To achieve a higher protonation of PANi, the as-made PANi coated particles were suspended in 0.1M HCl for 2 h with stirring. The re-protonated powder was then filtered on a PVDF membrane to form a thin film and subsequently dried in dynamic vacuum at 60°C. A deprotonated PANi/GNP was prepared by suspending the particles in 0.1M NH₄OH solution for 2 h. The resulting powder was filtered on PVDF membrane to form a thin film and subsequently dried in dynamic vacuum at 60°C.

Seebeck coefficient and thermal conductivity measurement:

Thermal conductivity, Seebeck coefficient measurements were conducted on the thin film nanocomposite in a Janis model ST-100 cryostat cooled with flowing liquid nitrogen. Due to the small thickness of the sample (usually around 100 μm), the metal-film resistor cannot be attached to heat the sample, therefore a polyimide backed strain gauge (350 Ω) was used as a resistive heater. A silver-filled epoxy was used to fix the gauge to the side of the film, the other end to a "L-shaped" copper block, and two thin copper strips along the length of the sample. (See Figure 6-2) Two thermocouples made from copper and constantan wires were soldered directly to the copper strips. The Seebeck coefficient (S) and thermal conductivity (κ) were measured simultaneously by passing a current through the metal film resistor (I_h), thereby generating a temperature gradient (ΔT) in the sample. The Seebeck coefficient was then calculated according to equation (6.1) when the system reached steady-state.

$$S = \frac{\Delta V}{\Delta T} \quad (6.1)$$

where ΔV is the thermoelectric voltage measured using the copper leads of the thermocouples. Thermal conductivity was calculated according to equation (6.2):

$$\kappa = \frac{V_h I_h l}{\Delta T s} \quad (6.2)$$

where V_h , l and s are the measured voltage across the resistor, distance between thermocouples and the cross sectional area of the sample. Measurements were conducted under vacuum ($<10^{-5}$ torr) to minimize heat conduction and convection through the surrounding medium. A fused quartz sample was used as a calibration standard for thermal conductivity and the data reported here have been corrected for parasitic and radiation heat losses. Labview software was used for automated data acquisition.

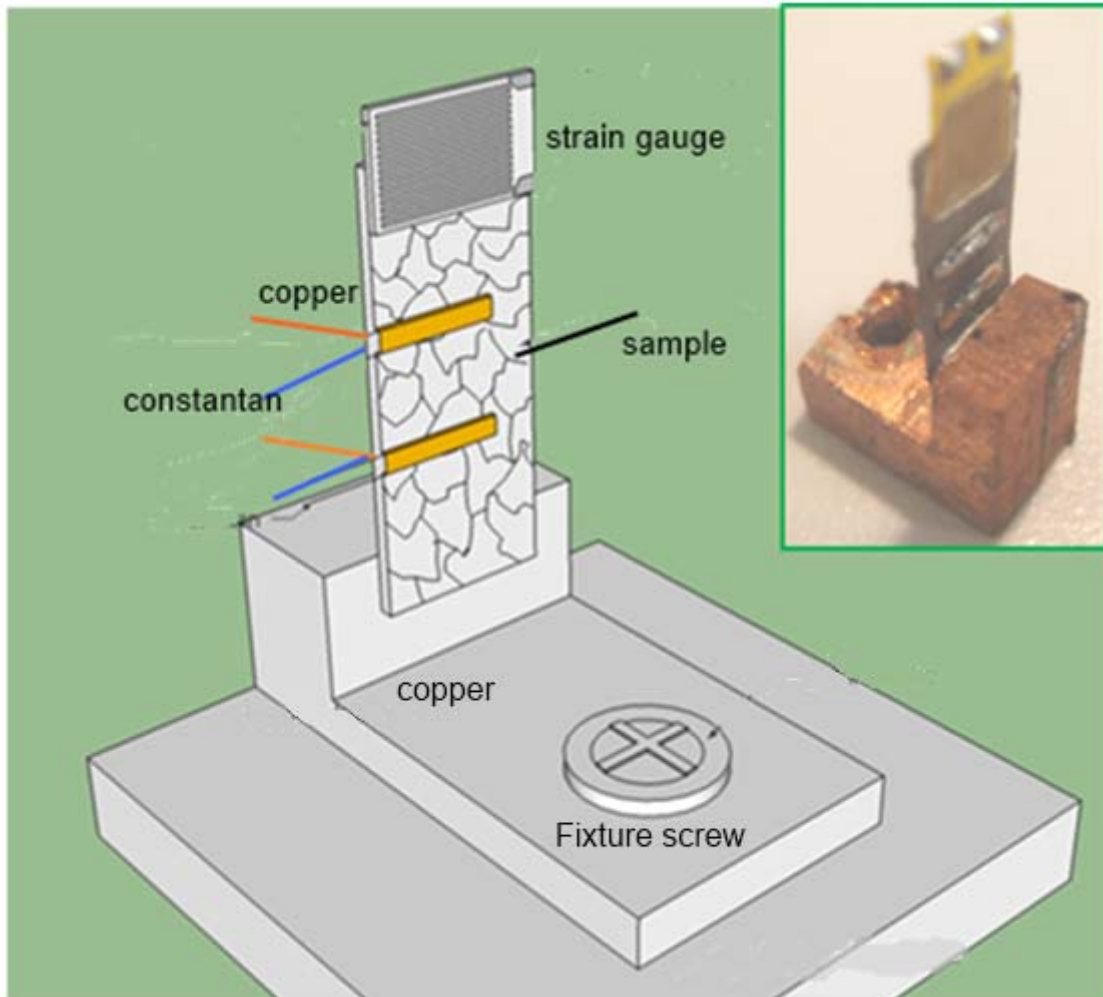


Figure 6-2: Schematic representation of the experimental setup for measuring the Seebeck coefficient and thermal conductivity of thin film sample. Inset is the photo of the actual sample mounted to the "L-shaped" copper block.

Electrical conductivity measurement (room temperature):

In-plane electrical conductivity was measured with a Keithley 2400 sourcemeter in a four point configuration with a probe spacing d of 1 cm on thin rectangular film. Electrical resistance was measured and the conductivity of the rectangular film was calculated by equation (6.3):

$$\sigma(S / cm) = \frac{d \cdot i}{v \cdot w \cdot t} \quad (6.3)$$

where d is the probe spacing in cm, i is the current in mA, v is the voltage in mV, w is the width of the film in cm, and t is the film thickness in cm.

Scanning electron microscopy:

A scanning electron microscope (Auriga 39, Carl Zeiss Microscopy, LLC) was used to image PANi/GNP nanocomposites with an accelerating voltage of 2 kV and a working distance around 2 mm. The sample was placed on a aluminum holder.

X-ray photoelectron spectroscopy:

XPS results of PANi/GNP with different levels of protonation were obtained from a Physical Electronics PHI 5400 ESCA system with a Mg Ka x-ray source (1253.5eV photons). All samples were mounted on standard sample holders by means of double-sided adhesive tapes. Regional scans of N 1s and Cl 2p spectra were collected to investigate the presence of various nitrogen species and chlorine species in order to estimate the protonation ratio of polyaniline.

Raman spectroscopy:

A LabRAM ARAMIS laser Raman spectrometer (Horiba Scientific) with 532 nm 50mW DPSS laser was used to inspect the samples. Neat PANi powder, the as-made GNP film as well as PANi/GNP film were used for the measurement.

TGA analysis:

A thermogravimetric analyzer (TA instruments Q500) was used. 10-15 mg of PANi/GNP sample was loaded into a Pt pan. The sample was heated at 10°C/min at a resolution of 4°C/min to 700°C in air.

6.4 Results and discussions:

6.4.1 Synthesis of PANi/GNP and characterizations:

Direct dispersion of GNP particles in 1M HCl is difficult because of the highly hydrophobic basal planes. Bath sonication is essential prior to the addition of the oxidizing agent to help break down the agglomerates of GNP in the aqueous solution so that more GNP surface area is accessible for PANi nucleation. A few minutes into the reaction, nucleation started and the color of the solution turned dark at which point sonication can be turned off. The nuclei of PANi grew on the basal plane of GNP due to strong π - π interaction, which helped overcome the van der Waals attraction and facilitated dispersion of GNP in the aqueous solution. PANi continued to grow on the nuclei during synthesis until all monomer dissolved in the solution was reacted. The amount of PANi coated on the surface of GNP is directly related to the initial concentration of aniline in the solution. In particular, a higher concentration of aniline in the vicinity of GNP led to the formation of more PANi nuclei and a longer growth period. In all the experiments, the as-synthesized PANi/GNP hybrid particles after the reaction dispersed well in the aqueous solution possibly due to the slight positive charges carried by the polymer backbone as a result of proton doping on the imine nitrogen [30]. The film prepared at 50mM aniline exhibited a dark brown color to it after vacuum drying while it was much lighter in color for film

prepared at 30mM aniline. Figure 6-3 depicts the synthesis of PANi/GNP hybrid particle by in-situ polymerization and the resulting paper-making process by vacuum assisted self-assembly.

Detailed morphology of the PANi/GNP samples as well as PANi synthesized in the absence of GNP were revealed by scanning electron microscopy shown in Figure 6-4(a-f). Neat polyaniline has an interconnected granular feature with PANi nanofibers growing from the surface. This distinctive morphology with the formation of needle-like nanostructure could result from a heterogeneous nucleation and growth since the later formed PANi are more likely to grow onto the "seeds" that were already formed in the solution. In comparison, PANi grew onto the surface of GNP and formed a uniform coating. Depending on the initial concentration of monomer, the as-formed PANi grew longer and formed a high density, highly ordered PANi fibril forest in the nanocomposite prepared at 50mM aniline solution. The structural similarity between PANi and GNP plays an important role in creating this highly ordered nanostructure. Unlike the bulk synthesis of PANi, GNP provided a strong and flat template for adhesion of as-synthesized PANi. It is expected that π electron interaction is the primary interaction to hold PANi and GNP together. Further increasing the concentration of monomer in the solution is found to be ineffective in "loading" more nanofibrils on GNP surface because only the aniline in close vicinity of GNP particles would be attracted to the surface while the rest of the monomer undergoes homogeneous nucleation and growth. Polyaniline nanofibers synthesized in the bulk did not bind to the surface of GNP and remained dispersed in the aqueous solution. The excessive unbound PANi can be easily washed off by repeated centrifugation and washing. In order to make a film from the PANi decorated GNP particles, multi-filtration was carried out to ensure that a higher particle alignment can be achieved in the final nanocomposite film.



Figure 6-3: Schematic representation of in-situ polymerization of aniline in the presence of GNP particles and a photo showing the flexibility of the final nanocomposite film.

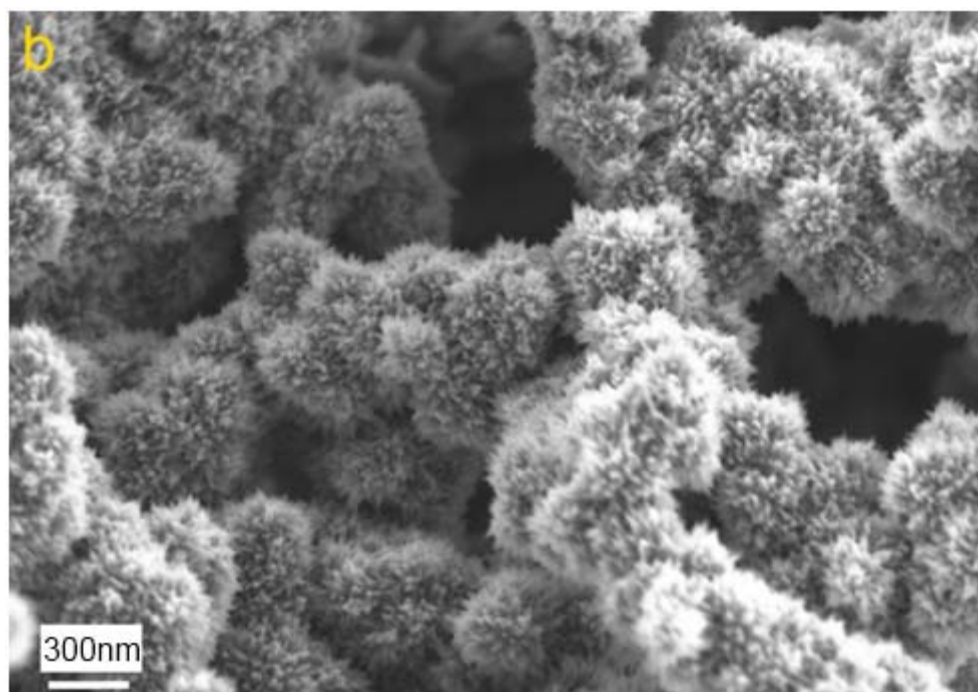
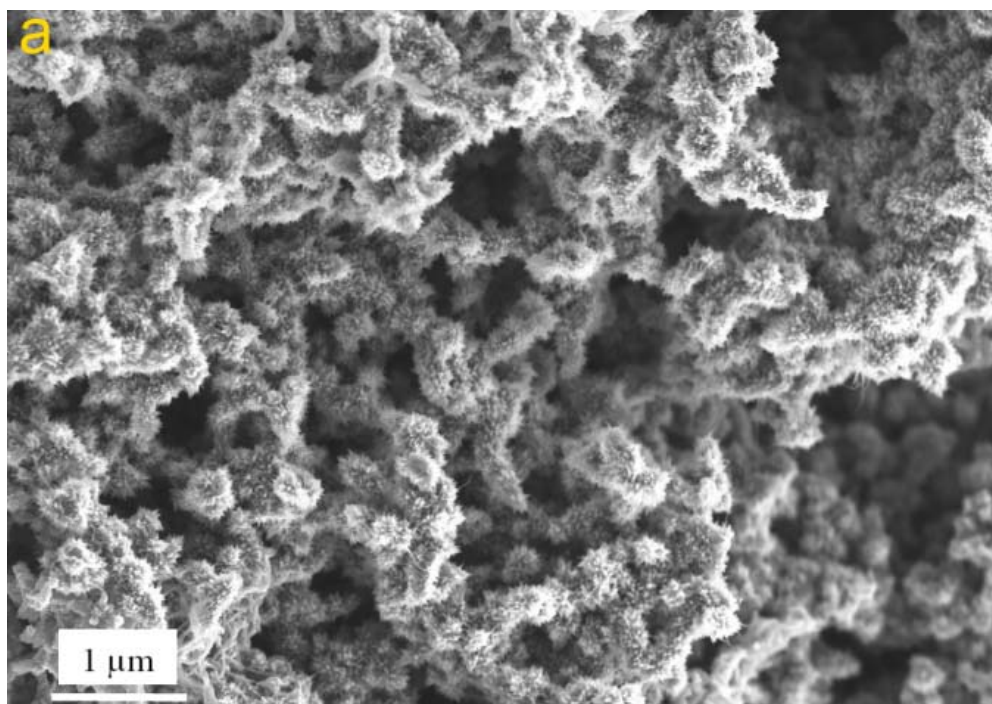


Figure 6-4: (a,b) SEM micrographs of neat polyaniline salt showing the granular structure and small needle-like nanostructure growing out of the surface. (c,d) surface morphology of PANi/GNP particles (in-situ polymerization of aniline in the presence of GNP particles in 1M HCl at 0.03M aniline). (e,f) surface morphology of PANi/GNP particles (in-situ polymerization of aniline in the presence of GNP particles in 1M HCl at 0.05M aniline).

Figure 6-4(cont'd)

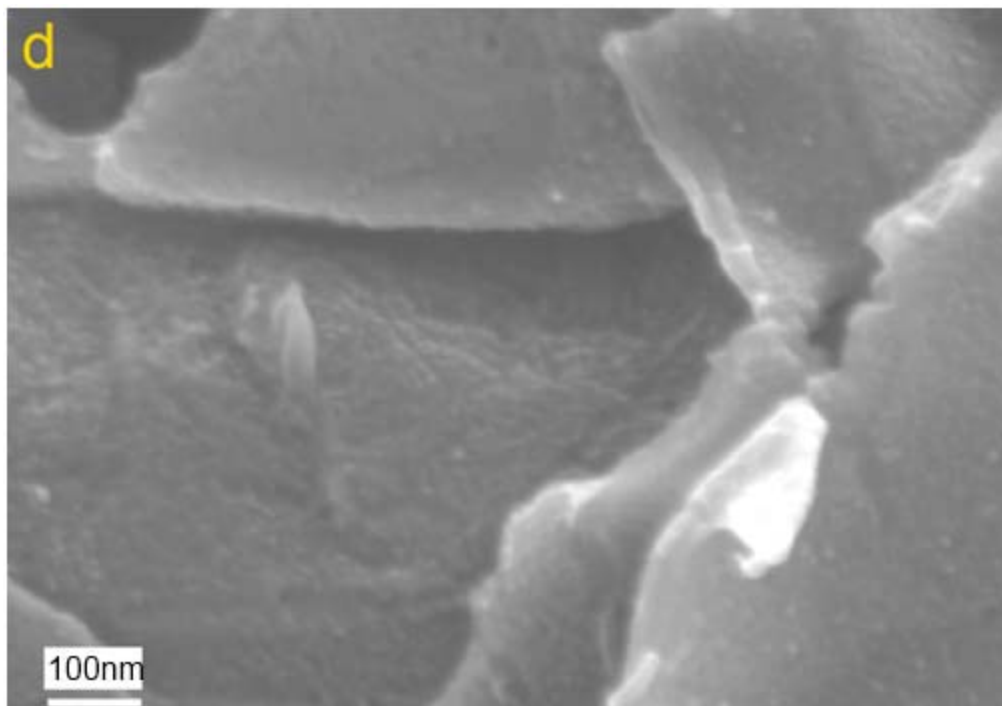
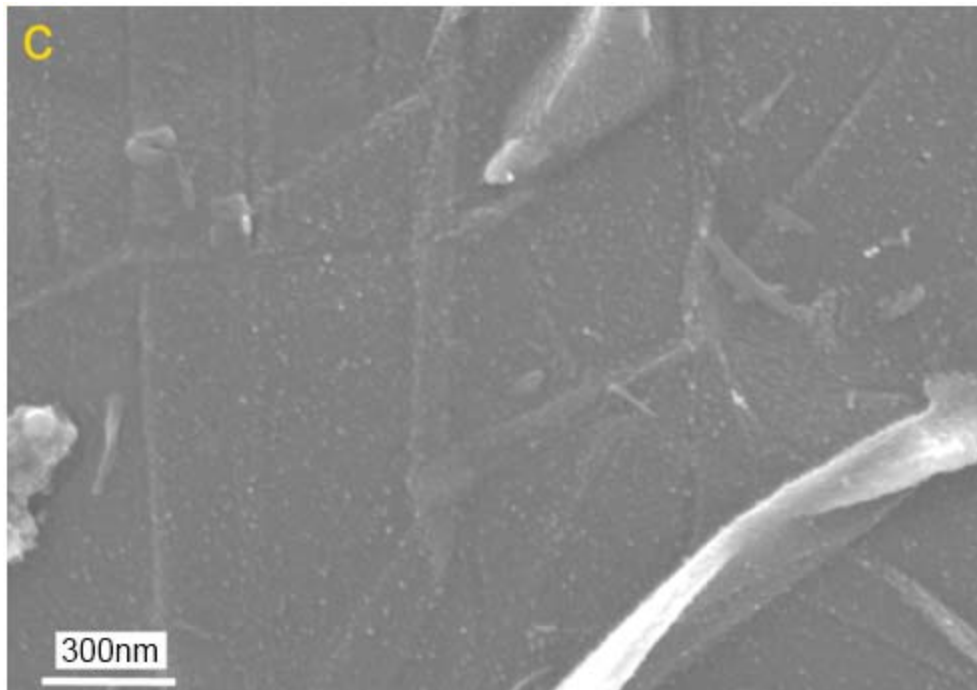
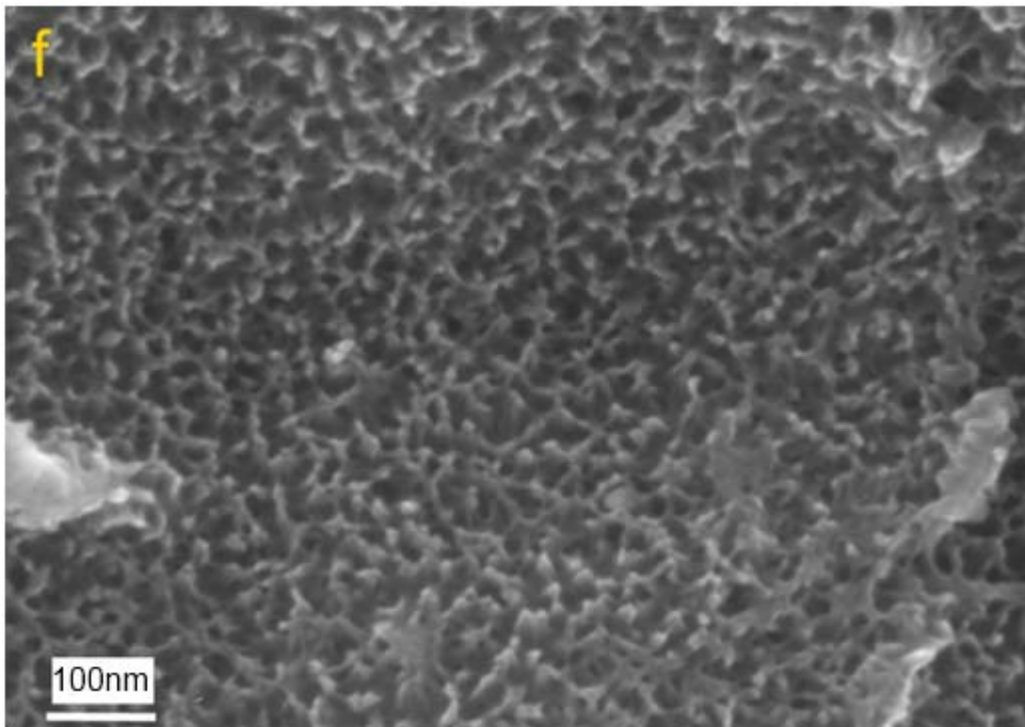
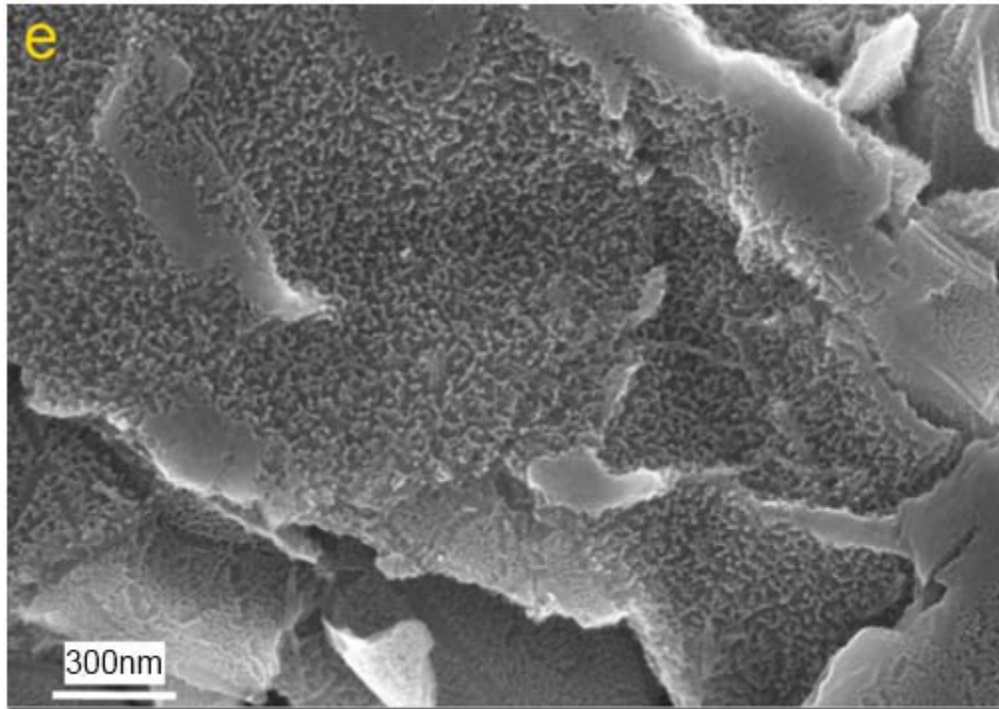


Figure 6-4(cont'd)



The amount of polyaniline coated on the surface of GNP can be estimated from TGA weight loss curve and the derivative of weight loss vs. temperature shown in Figure 6-5(a-b). In particular, the weight loss before 100°C is due to some volatile species and the moisture adsorbed on PANi while the weight loss within 200 to 250°C could originate from the loss of bound water molecules acting as secondary dopant in PANi since synthesis was carried out in an aqueous medium. It is observed in Figure 6-5b that neat PANi has a much sharper peak at 233°C as compared to the PANi/GNP composites, suggesting a lower amount of bound water molecules on the composites possibly due to a more hydrophobic surface of PANi coated GNP than the neat PANi surface. The major weight loss started from 300°C with a maximum thermal decomposition at approximately 461°C for neat PANi. For PANi/GNP samples, the major weight loss did not start until 350°C with maximum decomposition occurring at 480°C which is 20°C higher than the neat PANi. These results provide additional evidence that PANi is interacting with the surface of GNP, leading to an enhanced thermal stability. While GNP itself decomposes at 650-700°C, it can be estimated from the curve that the amount of PANi synthesized on GNP is around 30wt% for PANi/GNP (0.03M aniline) and 40wt% for PANi/GNP (0.05M)

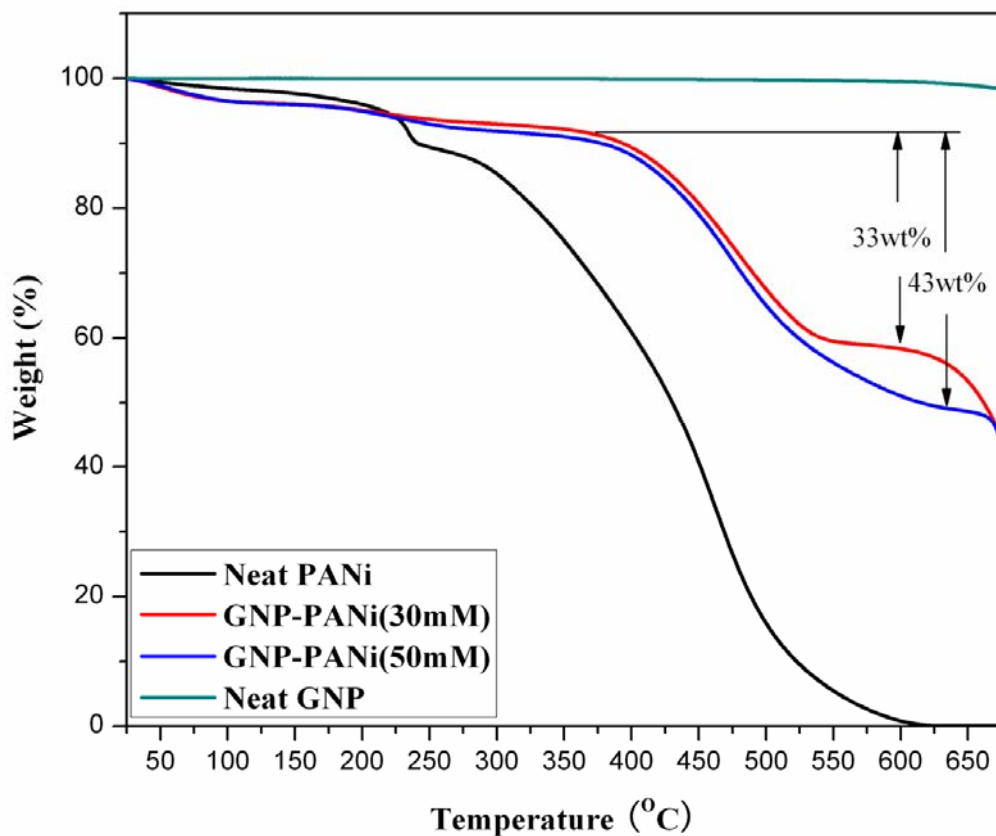
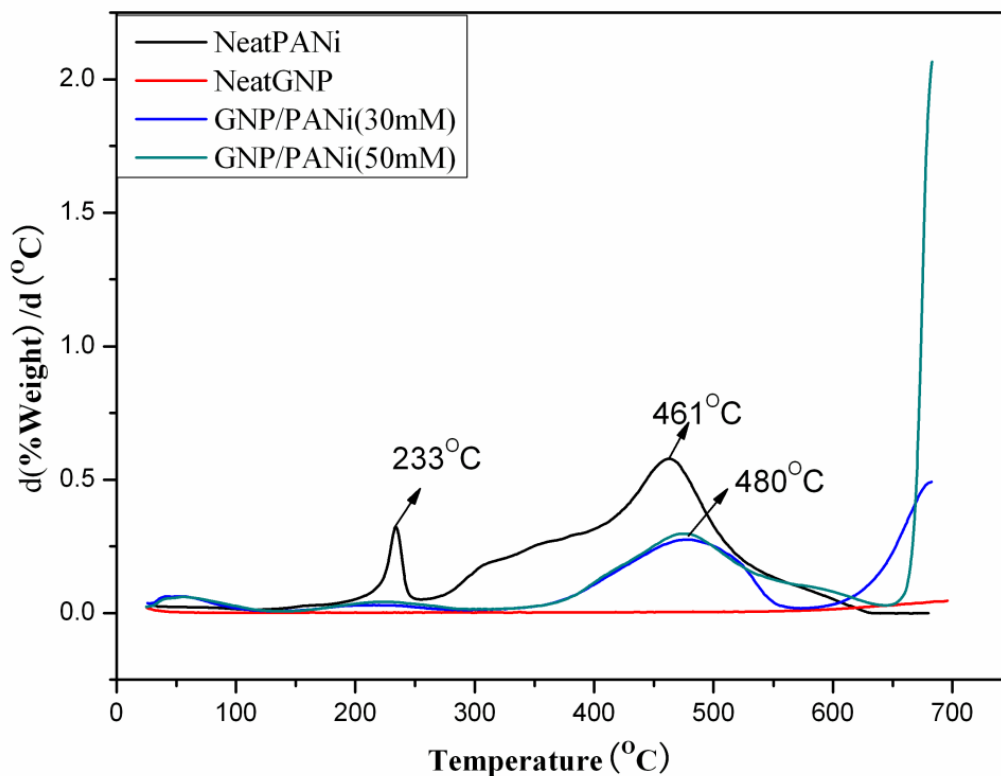


Figure 6-5: a: TGA of neat polyaniline salt, neat GNP, and PANI/GNP synthesized at 0.03M and 0.05M initial concentration of aniline. b: Derivative of weight loss vs. temperature for neat PANi, neat GNP, and PANI/GNP synthesized at 0.03M and 0.05M initial concentration of aniline.

Figure 6-5(cont'd)



Polyaniline synthesized by current oxidative polymerization is in its emeraldine oxidation state and it has also been established in the literature that the imine nitrogens are preferentially protonated by hydrochloric acid [12]. Different levels of protonation are believed to alter the electronic structure of the polyaniline as well as the thermoelectric properties of the nanocomposite. Figure 6-6(a-b) shows the N1s core level spectrum of PANi/GNP (@0.05M aniline) showing there are primarily three distinctive nitrogen species in the sample. In particular, the imine nitrogen (-N=) with binding energy at 399.1eV, amine nitrogen (-NH-) with binding energy at approximately 400eV and the positively charged nitrogen (N⁺) between 401eV and 402eV due to protonation in close vicinity of the Cl⁻ anions [31,32]. The Cl2p core-level

spectrum suggested the presence of two major components at about 197.2 and 200.1eV which can be attributed to the chloride anion and the covalently bonded chlorine shown in Figure 6-6(c-d). While it is difficult to directly quantify protons by XPS, the amount of counter ion (i.e. chloride anion) can be readily estimated from XPS. Therefore, a good indicator of the level of protonation achieved is to quantify the negative Cl species with protonation expressed by the ratio between Cl anion and total N atoms (i.e. $[Cl^-]/[N]$). Theoretically, the maximum protonation that can be achieved is 0.5 which means all the imine nitrogens in the polymer are protonated [33]. Table 6-1 shows the atomic percentage of different nitrogen and chlorine species in the samples with different protonation levels. It is found from the table that the as-made GNP/PANi has a relatively low protonation, similar to the neat polyaniline salt which is around 0.2.

Table 6-1: Typical atomic percentage of nitrogen and chlorine species on PANi/GNP samples prepared at 0.05M aniline and estimation of the protonation level

	-N= ($\approx 399.1\text{eV}$)	N ⁺ ($>401\text{eV}$)	Cl total	Cl ⁻	N total	Protonation: $[Cl^-]/[N]$
neat PANi	3.65	0.79	1.47	1.41	6.88	0.20
PANi/GNP as made	5.65	1.5	2.75	2.27	11.76	0.19
PANi/GNP reprotonated	4.2	2.8	4.37	3.9	9.85	0.4
PANi/GNP deprotonated	8.88	0.8	0.5	0.18	10.81	0.02

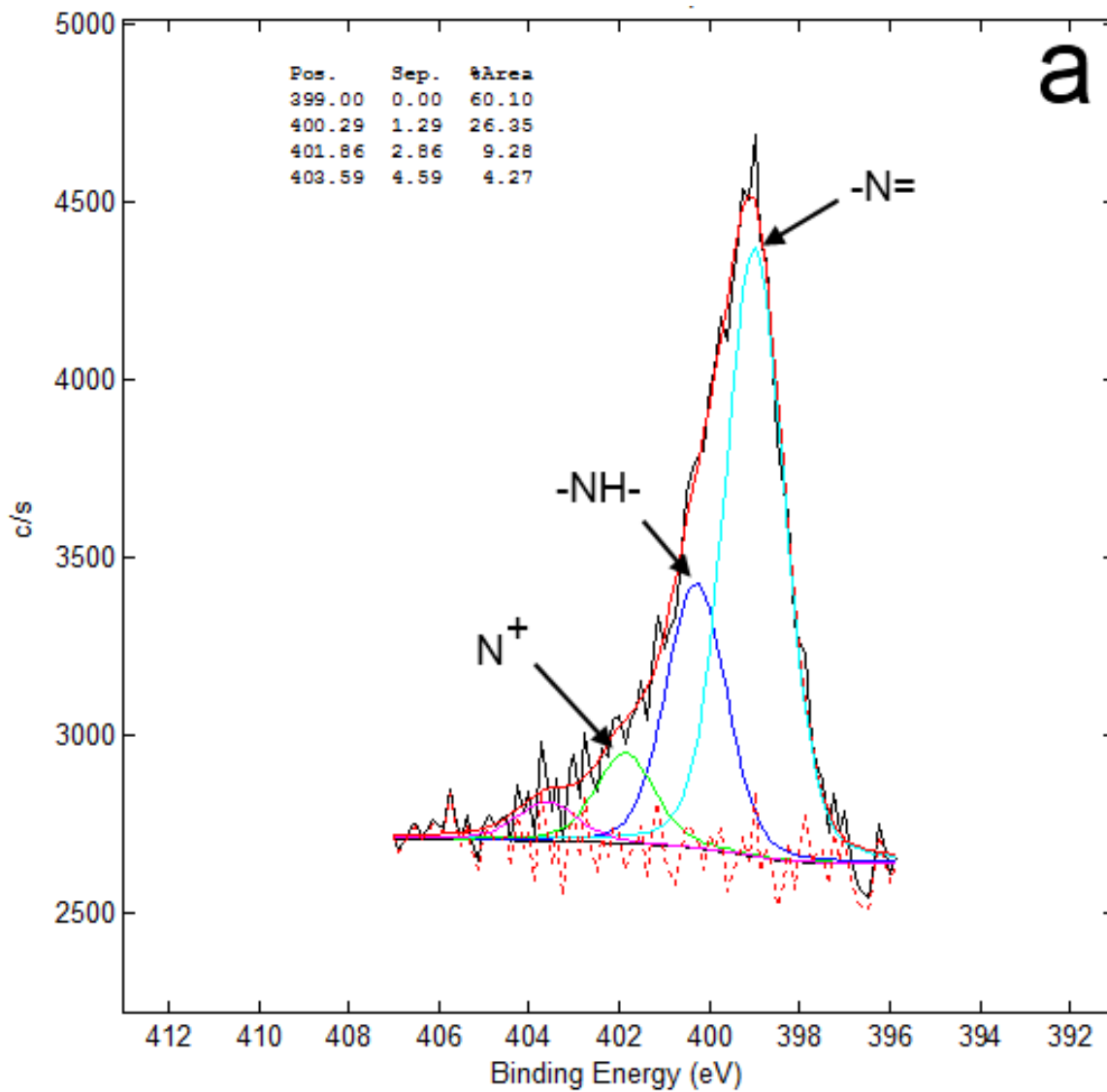


Figure 6-6: (a) Regional scans of N1s core-level spectra of as-made polyaniline salt showing the presence of imine nitrogen(-N=), amine nitrogen (-NH-) and positively charged nitrogen (N⁺) (b): regional scan of Cl2p core-level spectra of as-made polyaniline salt showing Cl anions. (c): regional scans of N1s core-level spectra of as-made PANi/GNP prepared at 0.05M of aniline. (d): regional scans of Cl2p of PANi/GNP(0.05M).

Figure 6-6 (cont'd)

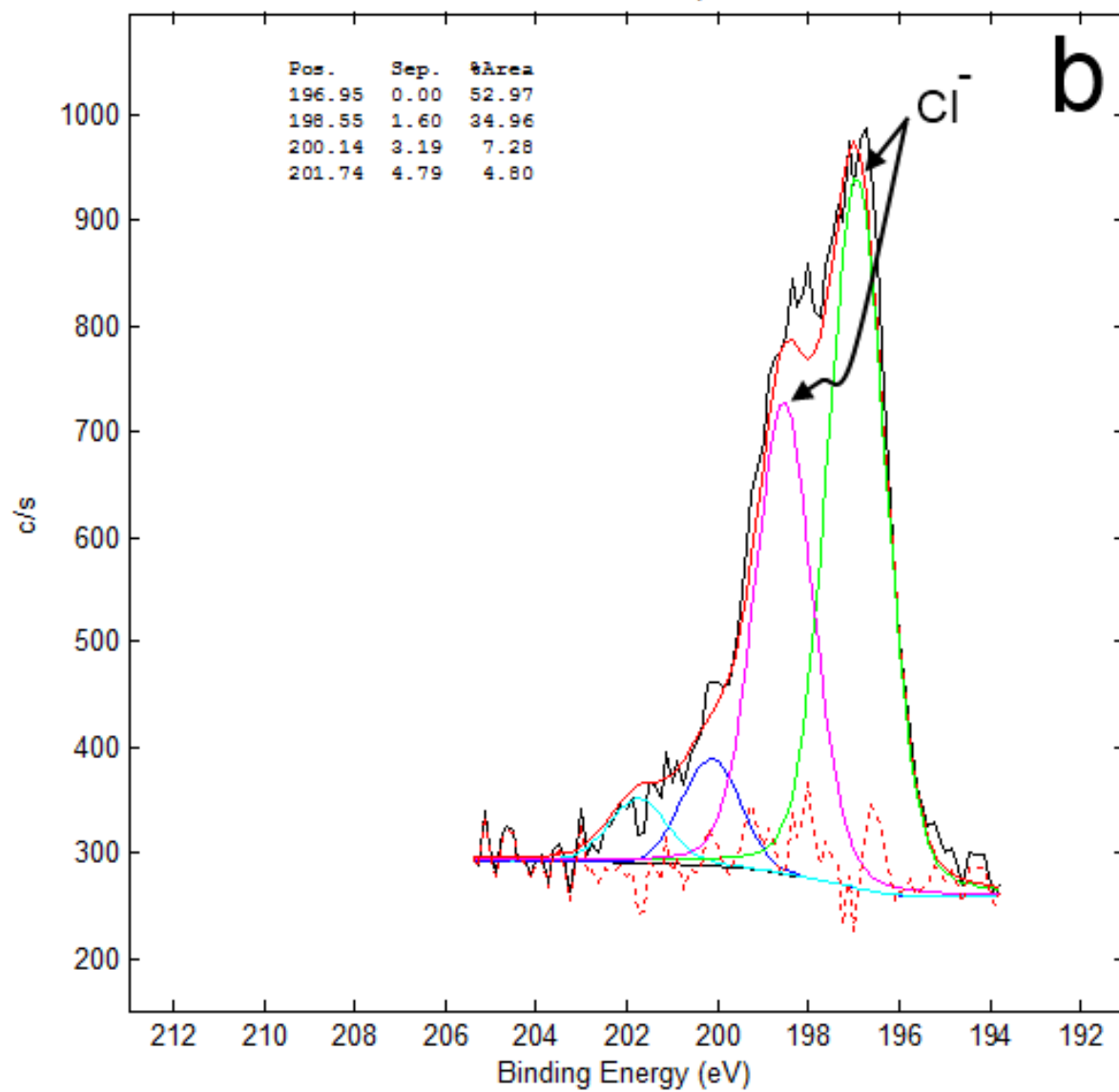


Figure 6-6 (cont'd)

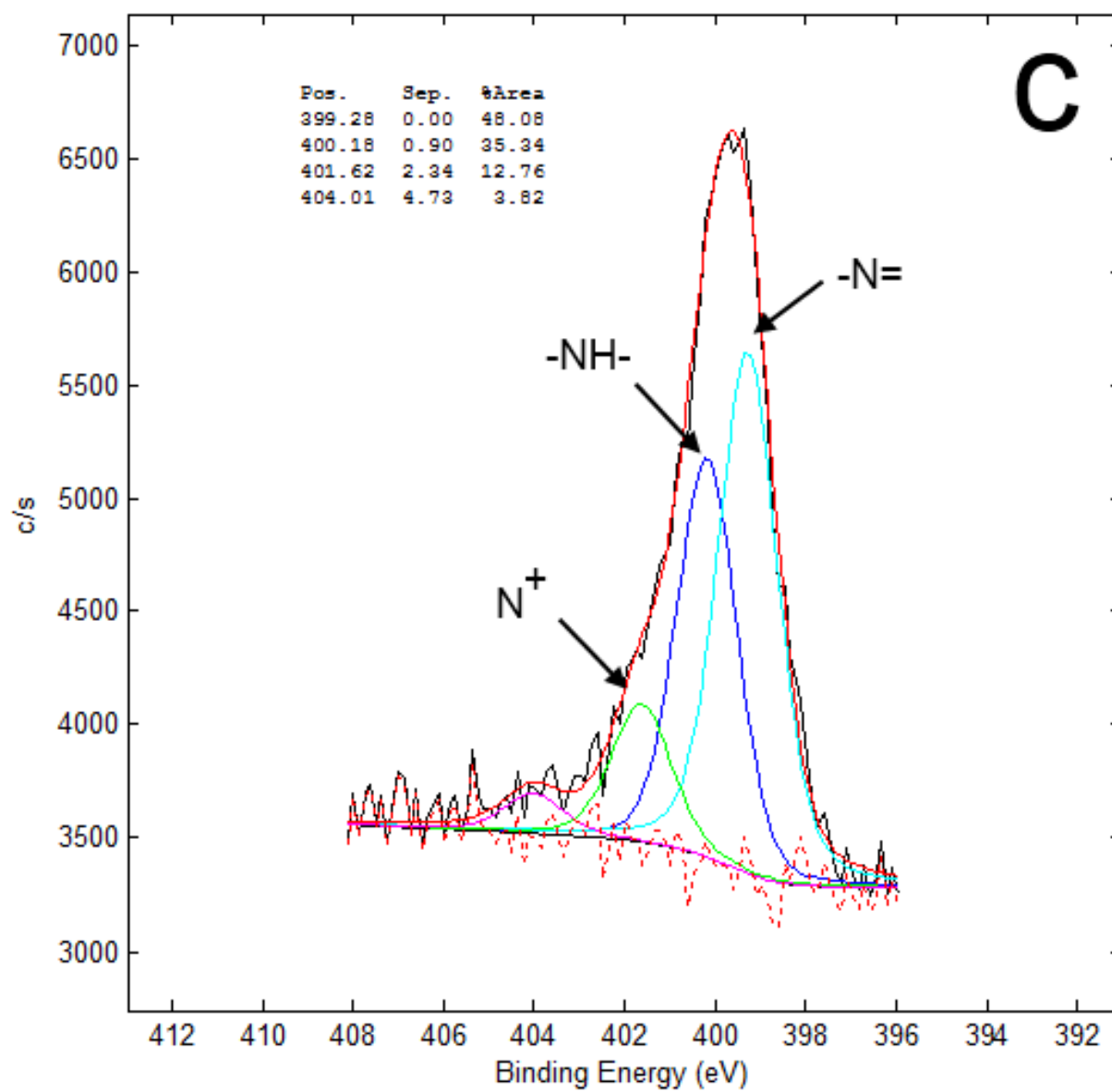
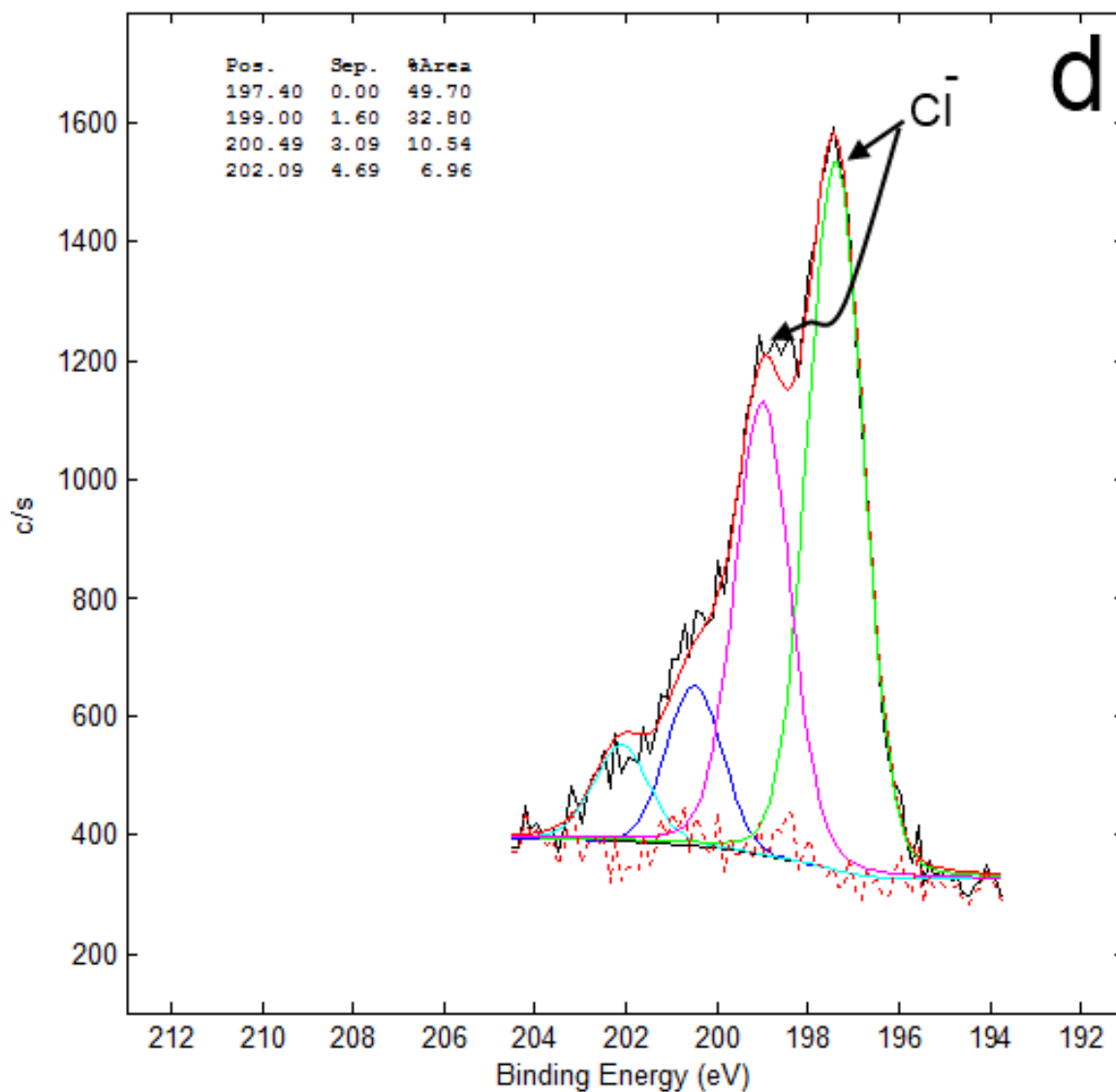


Figure 6-6 (cont'd)



Raman spectroscopy also verifies the presence of polyaniline on the surface of GNP as shown in Figure 6-7. In particular, several characteristic peaks of polyaniline were observed at 1162 cm^{-1} (C-H bending of the quinoid and benzenoid rings), 1218 cm^{-1} (weak C-N stretching), 1485 cm^{-1}

(C=N stretching of the quinoid ring), 1580 cm^{-1} (C-C stretching) as well as the peaks characteristics of GNP itself such as 1350 cm^{-1} (D peak), overlapping 1580 cm^{-1} (G peak) and the 2D peak at 2700 cm^{-1} .

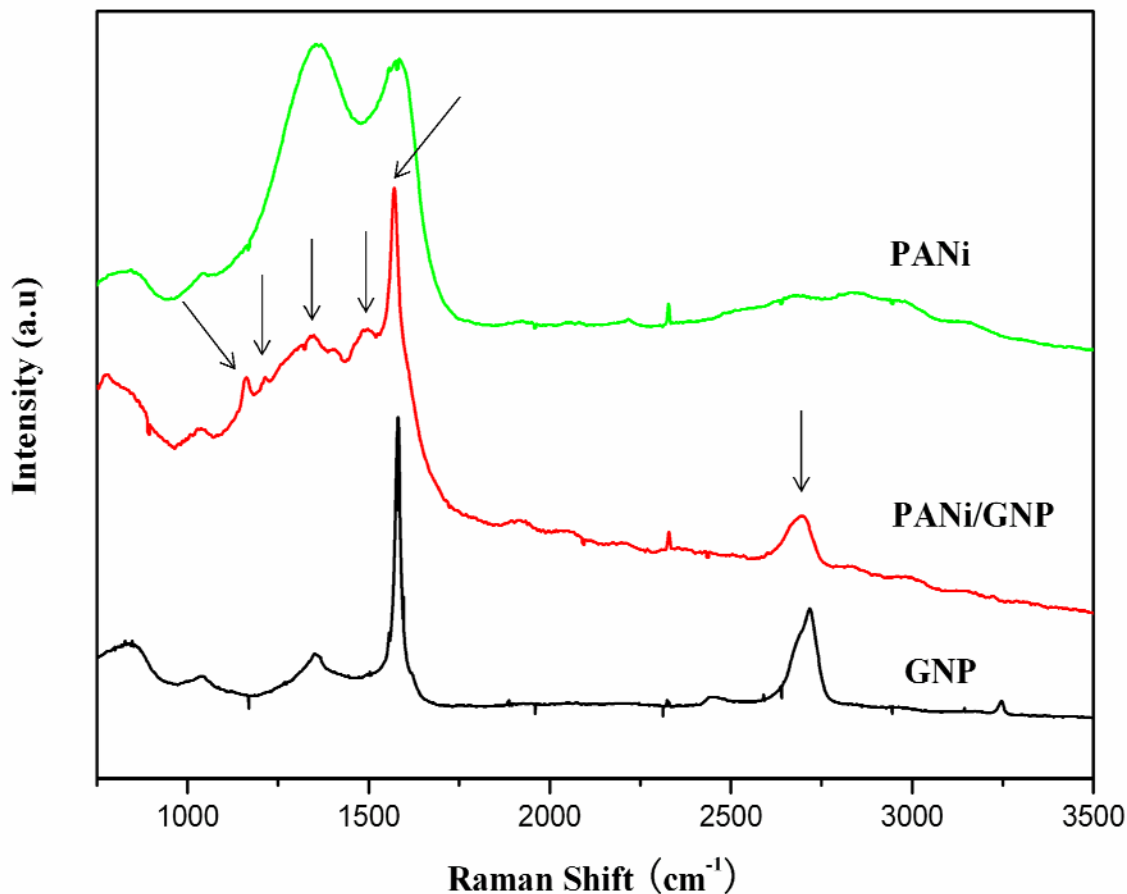


Figure 6-7: Raman shift of neat PANi powder, neat GNP film and the as-made PANi/GNP film prepared at 50mM aniline concentration.

6.4.2 Thermoelectric properties of PANi/GNP:

The Seebeck coefficient of a material is dependent on the concentration as well as the mobility of the charge carriers (i.e. holes and electrons). It is generally believed that bi-carrier material systems are not preferred for thermoelectric applications because electrons and holes

have opposite Seebeck coefficients that offset each other according to the equation (6.4) shown below:

$$S = \frac{S_e \sigma_e + S_h \sigma_h}{\sigma_e + \sigma_h} \quad (6.4)$$

where S_e , S_h , σ_h and σ_e are electron Seebeck coefficient, hole Seebeck coefficient, hole conductivity and electronic conductivity. Since graphite is known to be a bi-carrier system with an overlapping band structure, both electrons and holes contribute to the establishment of Seebeck voltage under a temperature gradient which unfortunately counteract each other, resulting in a low overall Seebeck coefficient [34]. Figure 6-8a shows the Seebeck coefficient (S) of various GNP/PANi samples from 200K to 300K. It is observed that neat GNP paper has a low S of about $5\mu\text{V/K}$ at room temperature as a result of bi-carrier transport. However, the GNP/PANi nanocomposite prepared at 0.03M of initial aniline concentration reached $19\mu\text{V/K}$ at 300K while it further increased to $33\mu\text{V/K}$ for samples prepared at 0.05M of aniline.

Loading of more PANi on the GNP surface is contributing to the Seebeck voltage that can be generated. The positive value also suggested very clearly that holes are the dominating charge carriers in the nanocomposites because protons carrying positive charges are being incorporated to the polymer during the protonation process. On the other hand, the Seebeck coefficient of the as-made polyaniline is only $7\mu\text{V/K}$ at room temperature. While a similar improvement in the Seebeck coefficient has been observed on PANi coated CNT network [19,20], the CNT network itself has been p-type doped by oxygen during synthesis, therefore leading to a higher base line value. The highest enhancement ratio reported ($\Delta S/S_{\text{cnt}}$) is about 80% [19]. However, the highest enhancement ratio reported here with respect to neat GNP paper is

$(33-5)/5=560\%$. One of the possible reasons that could contribute to the large improvement in Seebeck coefficient for GNP samples compared with CNT is that GNP provides a much larger and flatter surface for polyaniline to grow on as opposed to a surface with very high curvature in the case of CNT. Therefore, the polymer chains synthesized in the presence of GNP will be more ordered and aligned as a result of the templating effect. While the charge transport in a polymer is dependent on the interchain and intrachain hopping, a more aligned conformation of the molecular chains is likely to reduce the carrier hopping resistance, therefore leading to higher carrier mobility and a higher Seebeck coefficient. The schematic representation of the difference in charge carrier transport in PANi synthesized with and without the presence of GNP was proposed and shown in Figure 6-9. Another perspective to look at it is that PANi on GNP is chemically stretched so that the chains are more ordered. In fact, similar improvement in Seebeck coefficient was reported in which the solution cast PANi film was mechanically stretched in order to improve the orientation of the polymer chains, resulting in an enhanced carrier mobility as well as a higher Seebeck coefficient [35,36].

Thermal conductivity of the nanocomposites are presented in Figure 6-8(b) with neat GNP having the highest conductivity of about 72W/mK at 300K. The conductivity reduces to 39W/mK for samples prepared at 0.03M aniline (corresponding to about 30wt% PANi in the composite) and further reduces to 13W/mK for samples prepared at 0.05M aniline (corresponding to about 40wt% PANi). The fine feature of PANi fibrils on GNP surface is believed to strongly scatter heat carrying phonons, leading to a lower interfacial thermal conductance. Although there is a significant reduction in thermal conductivity for the nanocomposites as a result of polymer encapsulation, they are still one order of magnitude higher than the thermal conductivity of neat PANi measured to be 0.6W/mK at room temperature.

Despite the absolute value of thermal conductivity is still too high for a good thermoelectric material, nanoengineering the GNP surface by a uniform coating of polymer proved effective in reducing interfacial thermal conductance, therefore decreasing the overall thermal conductivity. It is also worth noting that nanostructuring techniques such as the paper making process and polymer encapsulation could potentially completely alter the heat conduction capability of a highly thermally conductive particle like GNP that has an estimated intrinsic thermal conductivity greater than 1000W/mK.

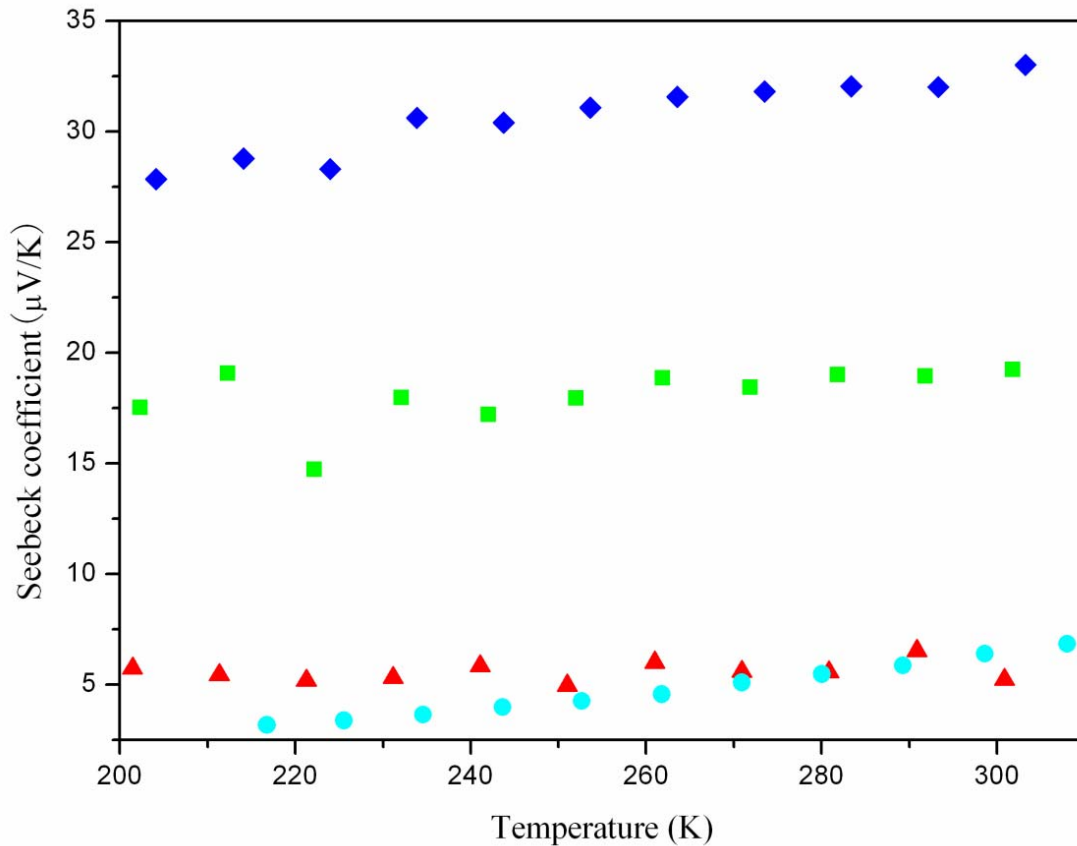
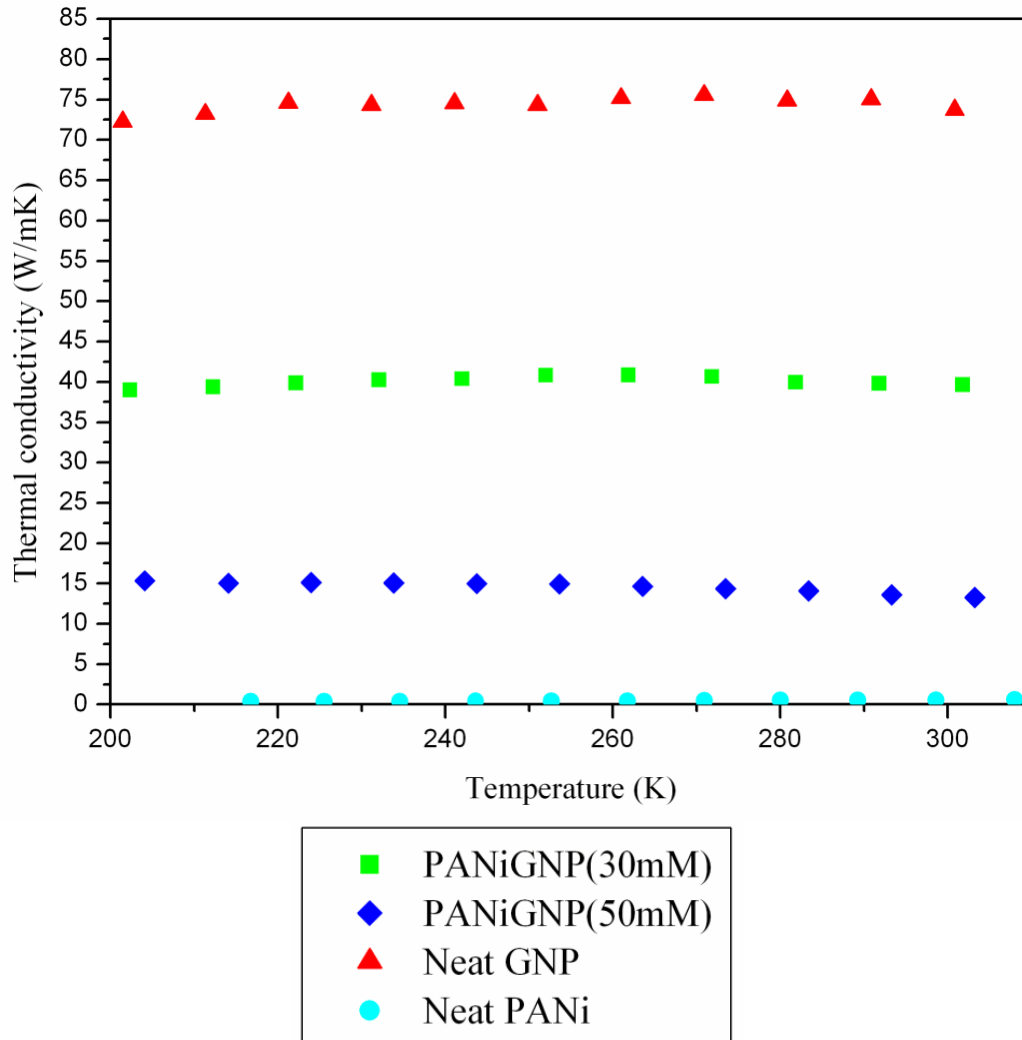


Figure 6-8: (a) Seebeck coefficient of GNP/PANi nanocomposites prepared at different aniline concentrations (0.03M and 0.05M) as well as the performance for neat GNP paper and neat polyaniline salt measured from 200K to 300K. (b). Thermal conductivity of GNP/PANi (0.03M and 0.05M) as well as neat GNP paper and neat polyaniline salt from 200K to 300K.

Figure 6-8 (cont'd)



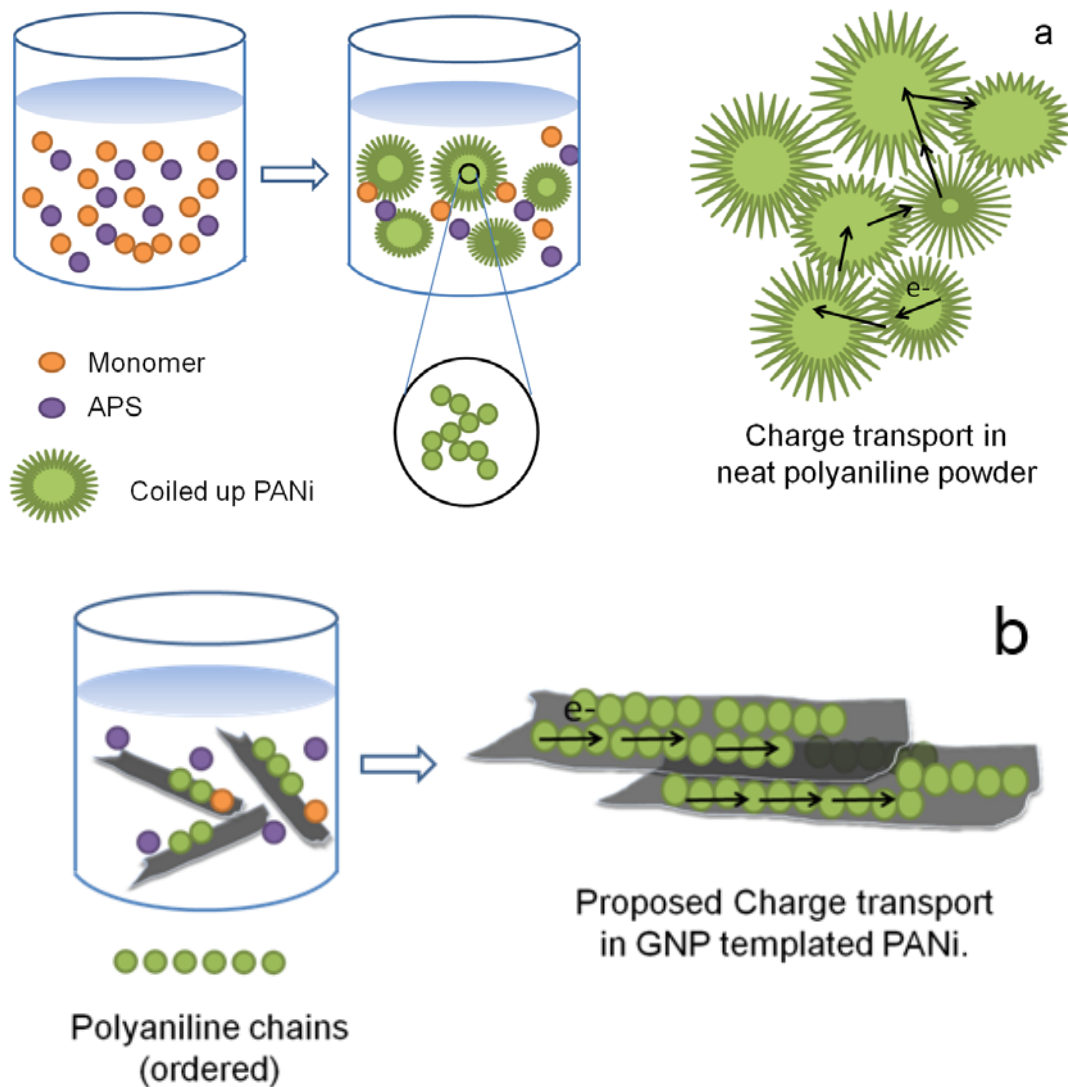


Figure 6-9: (a) Proposed polymerization process for polyaniline in the absence of GNP and the charge transport mechanism by inter and intrachain hopping. (b) Proposed polymerization of PANi in the presence of GNP and the proposed charge transport mechanism in the composites.

The electrical conductivity of the nanocomposites is reported in Figure 6-10. It is observed that the encapsulation of GNP with PANi led to a decrease in the conductivity. For the nanocomposites with the highest amount of PANi ($\approx 40\text{wt}\%$), conductivity reduced from 200 S/cm to 59 S/cm. The same surface PANi fibrils that grew out of GNP also scatter the electrons in addition to phonons. Although PANi fibrils are electrically conductive, they are far from being

fully doped to achieve the maximum conductivity as evidenced by its relatively low protonation level determined by XPS. Given that PANi can be thought of as conducting (protonated) islands intermixed in a sea of non-conducting regions, electron transport took place primarily by hopping both interchain and intrachain, significantly lowering the mobility of the carriers [37]. In particular, if the PANi chain is less ordered, the electron scattering is likely to further reduce conductivity as in the case of PANi synthesized without the templating effect of GNP particles. For comparison, the electrical conductivity of neat PANi in compressed pellets form is 1.5 S/cm at room temperature.

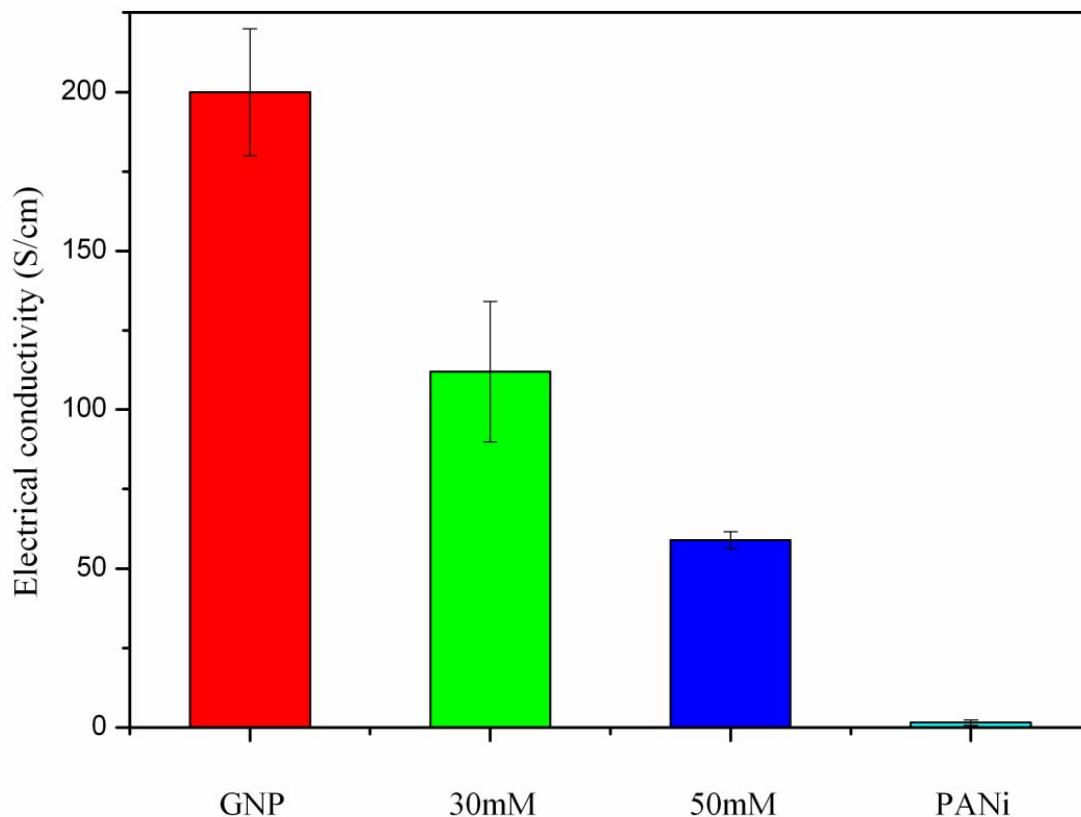


Figure 6-10: Electrical conductivity of GNP/PANi (0.03M and 0.05M) as well as neat GNP paper and neat polyaniline salt at room temperature.

6.4.3 Effect of protonation on thermoelectric properties of PANi/GNP nanocomposites:

It has been reported that there is an inverse relationship between Seebeck coefficient and electrical conductivity for solvent cast PANi film (i.e. higher protonation correlates to a lower Seebeck coefficient). One purpose of this article is to further investigate if the trend still holds for PANi synthesized in an aqueous environment that cannot be dissolved in the solvent (i.e. PANi in its aggregated form). The maximum protonation that can be achieved theoretically on PANi is 0.5 with two imine nitrogens being protonated every four nitrogen atoms on PANi chains. Figure 6-11a shows the Seebeck coefficient of PANi/GNP prepared at 0.05M aniline at different protonation levels. It is found that Seebeck coefficient reached a maximum for the as-made samples (protonation: 0.15-0.2) while further reprotonation or deprotonation decreased the Seebeck coefficient. This is in analogy to a recently published work that claims highest thermoelectric performance of PEDOT can be achieved through controlling the oxidation level [38]. No matter it is the oxidation level or the protonation level, one possible explanation for this phenomenon is that different protonation ratio or oxidation level in a conductive polymer results in a shift of the Fermi level to regions with different curvature in electronic density of states. Park et al. reported the highest Seebeck coefficient of neat PANi salt in compressed pellets form to be approximately $35\mu\text{V/K}$ at room temperature but the conductivity is only 0.03 S/cm [16]. While the GNP/PANi nanocomposite achieved a similar Seebeck coefficient at 300K, the electrical conductivity is 3 orders of magnitude higher because of the presence of GNP particles. In essence, GNP particles effectively make up the loss in electrical conductivity caused by insufficient protonation of PANi in an effort to achieve the highest thermoelectric performance. Thermal conductivity of PANi/GNP, however, is not directly affected by the protonation as shown in Figure 6-11(b). Phonon transport is dependent on the interfacial thermal conductance

which is determined by bonding strength, phonon spectrum matching and geometrical contact area. Protonation is not likely to alter any of the above mentioned properties, therefore the thermal conductivity at 300K remained at approximately 15 W/mK.

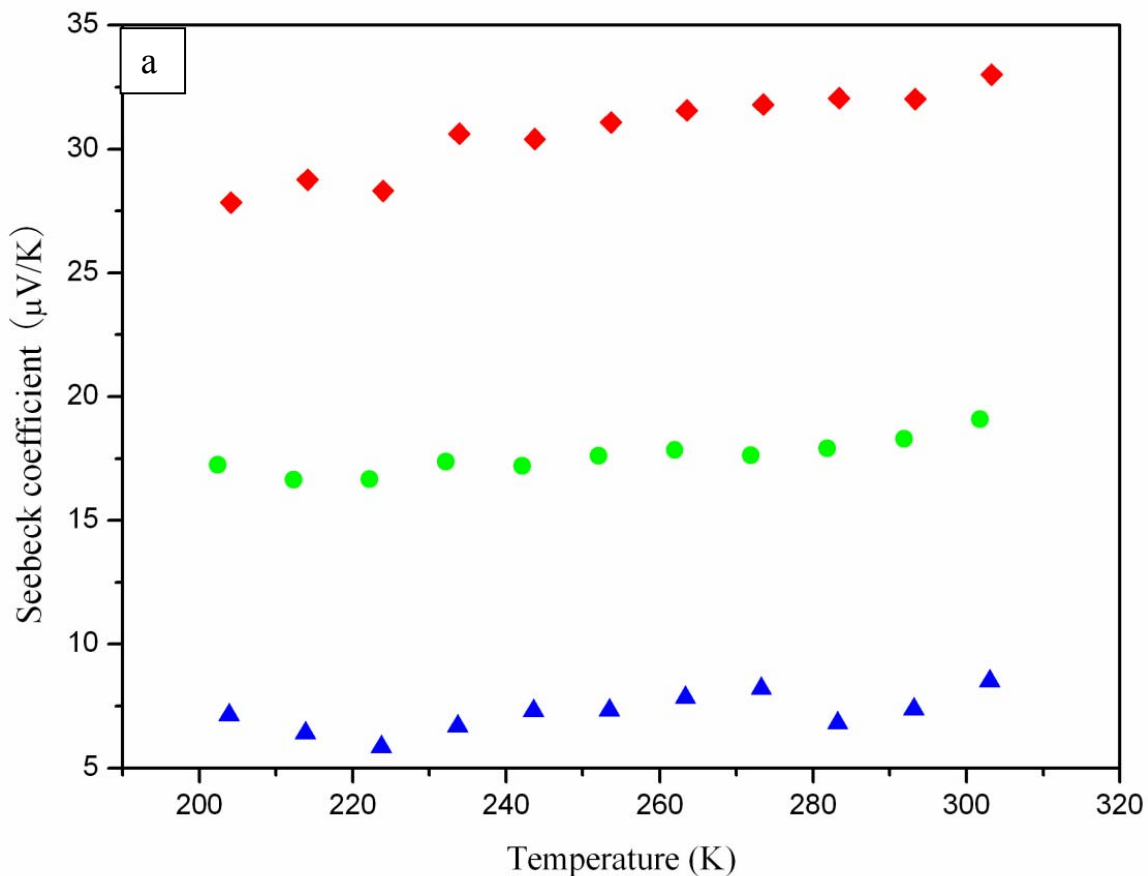
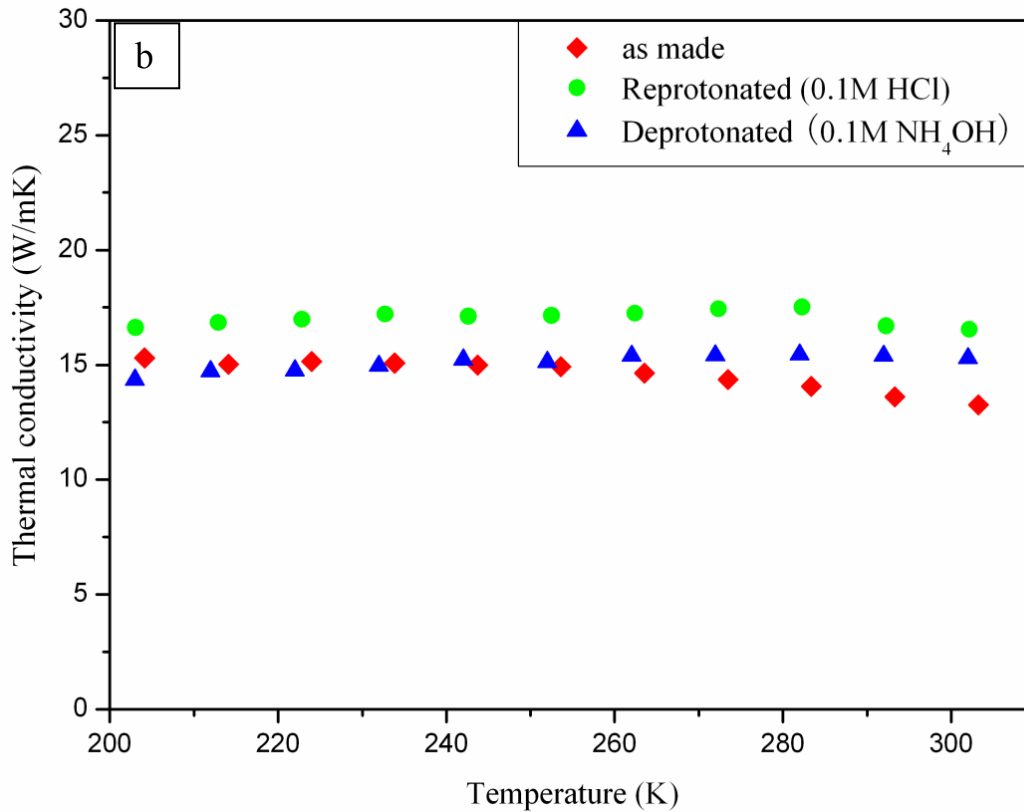


Figure 6-11: (a) Seebeck coefficient of PANi/GNP prepared at 0.05M aniline with different protonation levels. (b) Thermal conductivity of PANi/GNP (50mM) with different levels of protonations.

Figure 6-11 (cont'd)



Electrical conductivity of the nanocomposites is immediately affected by protonation as shown in Figure 6-12. A higher protonation of PANi suggests a higher concentration of charge carriers which leads to a higher electrical conductivity. It is also worth noting that re-protonation of PANi/GNP nanocomposites can only be carried out in a very dilute acid concentration to avoid possible hydrolysis of PANi which would alter the molecular structure of PANi, making it non-conducting [39]. For the nanocomposite that was re-protonated in 0.1M HCl, electrical conductivity reached as high as 174 S/cm.

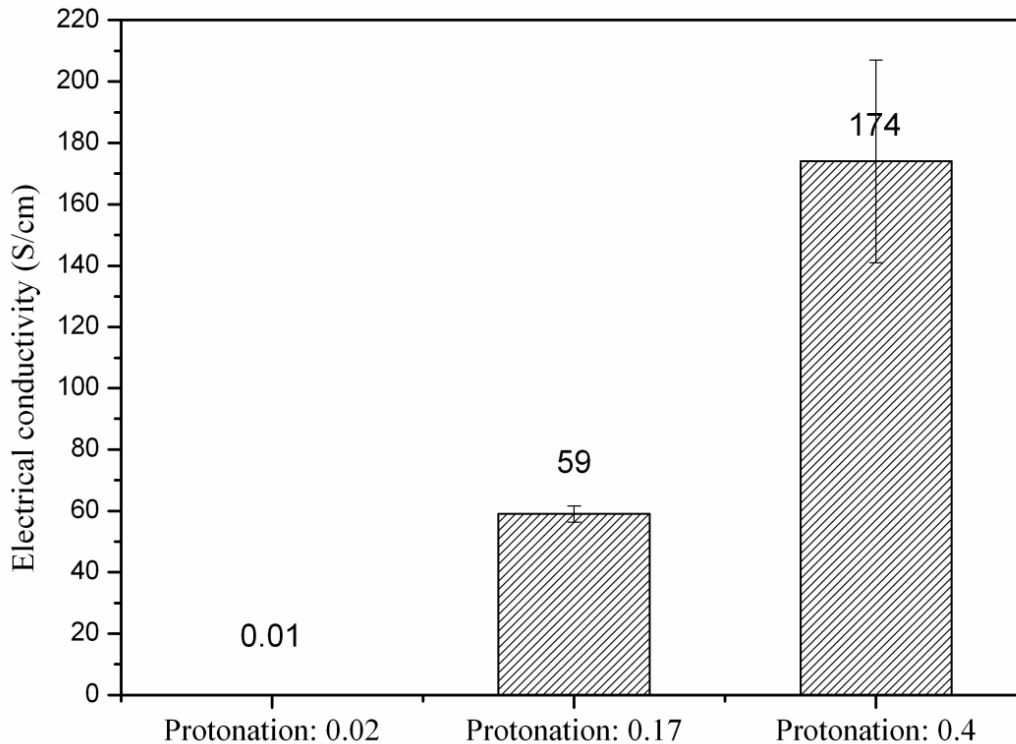


Figure 6-12: Electrical conductivity of PANi/GNP samples prepared at 0.05M aniline with different protonation ratio.

The thermoelectric properties, the σ/κ ratio as well as the thermoelectric figure of merit ZT at room temperature are compared in Table 6-2 for neat GNP, neat PANi, PANi/GNP(50mM, as-made) as well as the PANi/GNP(50mM, re-protonated). In particular, σ/κ ratio increases significantly from 2.5 to around 12 suggesting a successful separation of electrical and thermal conductivity of the nanocomposites. At the same time, ZT remains basically the same for neat GNP and neat PANi. The highest ZT was obtained for the nanocomposite prepared at 0.05M aniline with a protonation of around 0.2 reaching 1.51×10^{-4} . The fact that both ZT and Seebeck coefficient of the composites are almost 2 orders of magnitude larger than either of its constituents calls into question the previously established viewpoint that thermoelectric properties cannot be enhanced through simple mixture of two components. Although ZT is still

low, the unique flexibility and mechanical robustness of this nanocomposite makes it possible for them to be installed to the surface of irregular geometry such as the roof and exterior of the house, potentially complementing electricity generated by solar cells.

Table 6-2: The thermoelectric properties, σ/κ and ZT of neat PANi, neat GNP and PANi/GNP (50mM aniline, as-made) and PANi/GNP(50mM aniline, reprotonated) at room temperature.

Samples	σ (S/cm)	κ (W/m K)	σ/κ ratio	S (μ V/K)	ZT(300K)
Neat PANi	1.5	0.6	2.5	7	3.68×10^{-6}
Neat GNP	200	74	2.7	5	3.04×10^{-6}
PANi/GNP (50mM, as made)	59	13	4.6	33	1.51×10^{-4}
PANi/GNP(50mM, reprotonated)	174	15	11.6	19	1.26×10^{-4}

6.5 Conclusion:

Polyaniline was synthesized in the presence of exfoliated graphene nanoplatelets to make lightweight, low cost, flexible nanocomposite for thermoelectric applications. Depending on the initial concentration of aniline, highly ordered, highly densified PANi nanofibril were grown on the surface of GNP as a result of a strong π electron interaction. The Seebeck coefficient of the nanocomposites depended on the weight composition of PANi with the best performance achieved at 50mM as the starting concentration of monomer. The degree of protonation of PANi determined by the dopant strength was estimated by the ratio of chloride anion to the total nitrogen atoms in the composites and was found to be closely related to the thermoelectric properties. A higher protonation did not necessarily lead to better performance because of the inverse relationship between electrical conductivity and Seebeck coefficient. As a result of this trend, a composite approach by using GNP not only preserved the high Seebeck coefficient of PANi but also significantly increased the electrical conductivity of the nanocomposites. In

addition, it appears that GNP served as a "template" for PANi to grow, potentially stretching the molecular chains of PANi chemically to enhance carrier mobility. The combined improvement of power factor overcomes the increase of thermal conductivity, resulting in a net gain in performance. This flexible, lightweight, inexpensive nanocomposite based on exfoliated graphene is an alternative organic thermoelectrics that are still primarily dominated by carbon nanotubes composites. The combination of low cost and high availability of GNP/PANi nanocomposites make them attractive for solar thermal electric conversion generating extra electricity from the sun.

Acknowledgement:

I would like to thank Prof. Don Morelli and Dr. Kevin Zhou from the department of Chemical Engineering and Materials Science for their assistance in this project.

REFERENCES

References

1. Snyder, G.J.; Toberer, E.S. Complex thermoelectric materials, *Nat. Mater.* **2008**, *7*, 105-114.
2. Tritt, T.M.; Bottner, H.; Chen, L.D. Thermoelectrics: Direct solar thermal energy conversion. *MRS Bull.* **2008**, *33*, 366-367.
3. Makala, R.S.; Jagannadham, K.; Sales, B.C.J. Pulsed laser deposition of Bi₂Te₃-based thermoelectric thin films. *J. Appl. Phys.* **2003**, *94*, 3907-3918.
4. Liufu, S.C.; Chen, L.D.; Yao, Q.; Wang, C.F. Assembly of one-dimensional nanorods into Bi₂S₃ films with enhanced thermoelectric transport properties. *Appl. Phys. Lett.* **2007**, *90*, 112106.
5. Yan, X.; Poudel, B.; Ma, Y.; Liu, W. S.; Joshi, G.; Wang, H et al. Experimental studies on anisotropic thermoelectric properties and structures of n-type Bi₂Te_{2.7}Se_{0.3}. *Nano Lett.* **2010**, *10*, 3373-3378.
6. Martin, J.; Wang, L.; Chen, L.; Nolas, G. S. Enhanced Seebeck coefficient through energy-barrier scattering in PbTe nanocomposites. *Phys. Rev. B.* **2009**, *79*, 115311(1-5).
7. Dresselhaus, M.S.; Chen, G.; Tang, M. Y.; Yang, R. G.; Lee, H.; Wang, D. Z et al. New directions for low-dimensional thermoelectric materials. *Adv. Mater.* **2007**, *19*, 1043-1053.
8. Dubey, N.; Leclerc, M. Conducting polymers: efficient thermoelectric materials. *J. Polym. Sci. Part B. Polym. Phys.* **2011**, *49*, 467-475.
9. Toshima, N. Conductive polymers as a new type of thermoelectric material. *Macromol. Symp.* **2002**, *186*, 81-86.
10. Chang, K.C.; Jeng, M. S.; Yang, C. C.; Chou, Y. W.; Wu, S. K.; Thomas, M. A et al. The thermoelectric performance of poly(3,4-ethylenedioxythiophene) /poly(4-styrenesulfonate) thin films, *J. Electron. Mater.* **2009**, *38*, 1182-1188.
11. MacDiarmid, A.G.; Chiang, J.C.; Richter, A.F.; Epstein, A.J. Polyaniline: A new concept in conducting polymers. *Synth. Met.* **1987**, *18*, 285-290.
12. Chiang, J.C.; and MacDiarmid, A.G. 'Polyaniline': Protonic acid doping of the emeraldine form to the metallic regime. *Synth. Met.* **1986**, *13*, 193-205.
13. Epstein, A.J.; Ginder, J. M.; Zuo, F.; Bigelow, R. W.; Woo, H. S.; Tanner D. B et al. Insulator to metal transition in polyaniline. *Synth. Met.* **1987**, *18*, 303-309.

14. Li, J.; Tang, X.; Li, H.; Yan, Y.; Zhang, Q. Synthesis and thermoelectric properties of hydrochloric acid-doped polyaniline. *Synth. Met.* **2010**, *160*, 1153-1158.
15. Sun, Y.; Wei, Z.; Xu, W.; Zhu, D. A three-in-one improvement in thermoelectric properties of polyaniline brought by nanostructures. *Synth. Met.* **2010**, *160*, 2371-2376.
16. Park, Y. W, Lee, Y. S, Park, C.; Shacklette, L.W.; Baughman, R. H. Thermopower and conductivity of metallic polyaniline, *Solid State Commun*, **1987**, *63*, 1063-1066.
17. Yao, Q.; Chen, L.; Xu, X.; Wang, C. The high thermoelectric properties of conducting polyaniline with special submicron-fiber structure. *Chem. Lett.* **2005**, *34*, 522-523.
18. Yu, C.; Kim, Y.S.; Kim, D.; Grunlan, J.C. Thermoelectric behavior of segregated-network polymer nanocomposites. *Nano Lett.* **2008**, *8*, 4428-4432.
19. Meng C.; Liu, C.; Fan, S. A promising approach to enhanced thermoelectric properties using carbon nanotube networks. *Adv. Mater.* **2009**, *21*, 1-5.
20. Yao, Q.; Chen, L.; Zhang, W.; Liufu, S.; Chen, X. Enhanced thermoelectric performance of single-walled carbon nanotubes/polyaniline hybrid nanocomposites. *ACS Nano*, **2010**, *4*, 2445-2451.
21. Kim, D.; Kim, Y.; Choi, K.; Grunlan, J.C.; Yu, C. Improved thermoelectric behavior of nanotube-filled polymer composites with poly(3,4-ethylenedioxythiophene) polystyrenesulfonate. *ACS Nano*, **2010**, *4*, 513-523.
22. Yu, C.; Choi, K.; Liang, Y.; Grunlan, J.C. Light-weight flexible carbon nanotube based organic composites with large thermoelectric power factors. *ACS Nano*, **2011**, *5*, 7885-7892.
23. Chen, J.; Gui, X.; Wang, Z.; Li, Z.; Xiang, R.; Wang, K et al. Superlow thermal conductivity 3D carbon nanotube network for thermoelectric applications, *ACS Appl. Mater. Interfaces*, **2012**, *4*, 81-86.
24. Bergman, D. J.; Levy, O. Thermoelectric properties of a composite medium. *J. Appl. Phys.* **1991**, *70*, 6821-6833.
25. Lin-Chung, P. J.; Reinecke, T. L. Thermoelectric figure of merit of composite superlattice systems, *Phys. Rev. B.* **1995**, *51*, 13244-13248.
26. Zengin, H.; Zhou, W.; Jin, J.; Czerw, R.; Smith, D.W. Jr. Carbon nanotube doped polyaniline. *Adv. Mater.* **2002**, *14*, 1480-1483.
27. Sainz, R.; Benito, A. M.; Martinez, M. T.; Galindo, J.F. Soluble self-aligned carbon nanotube/polyaniline composites. *Adv. Mater.* **2005**, *17*, 278-281.

28. Mateeva, N.; Niculescu, H.; Schlenoff, J.; Testardi, L.R.; Correlation of Seebeck coefficient and electric conductivity in polyaniline and polypyrrole. *J. Appl. Phys.* **1998**, *83*, 3111-3117.
29. Maddison, D.S.; Unsworth, J.; Roberts, R.B. Electrical conductivity and thermoelectric power of polypyrrole with different doping levels. *Synth. Met.* **1988**, *26*, 99-108.
30. Li, D.; Kaner, R. B.; Processable stabilizer-free polyaniline nanofiber aqueous colloids. *Chem. Commun.* **2005**, *26*, 3286-3288.
31. Tan, K.L.; Tan, B.T.G.; Kang, E.T.; and Neoh, K.G. X-ray photoelectron spectroscopy studies of the chemical structure of polyaniline. *Phys. Rev. B*, **1989**, *39*, 8070-8073.
32. Yue, J and Epstein, A.J. XPS study of self-doped conducting polyaniline and parent systems. *Macromolecules*, **1991**, *24*, 4441-4445.
33. Zuo, F.; Angelopoulos, M.; MacDiarmid, A.G.; Epstein, A.J. Transport studies of protonated emeraldine polymer: A granular polymeric metal system. *Phys. Rev. B*. **1987**, *36*, 3475-3478.
34. Uher, C. Thermopower of exfoliated graphites between 1.7 and 300K. *Phys. Rev. B*. **1982**, *25*, 4167-4172.
35. Yan, L.; Ohta, N.; Toshima, N. Stretched polyaniline films doped by (\pm)-10-Camphorsulfonic acid: Anisotropy and improvement of thermoelectric properties. *Macromol. Mater. Eng.* **2001**, *286*, 139-142.
36. Holland, E.R.; Monkman, A.P. Thermoelectric power measurements in highly conductive stretch-oriented polyaniline films. *Synth. Met.* **1995**, *74*, 75-79.
37. Lin, Y.F.; Chen, C. H.; Xie, W. J.; Yang, S. H.; Hsu, C. S.; Lin, M. T et al. Nano approach investigation of the conduction mechanism in polyaniline nanofibers. *ACS Nano*, **2011**, *5*, 1541-1548.
38. Bubnova, O.; Khan, Z. U.; Malti, A.; Braun, S.; Fahlman, M.; Berggren, M et al. Optimization of the thermoelectric figure of merit in the conducting polymer poly(3,4-ethylenedioxythiophene). *Nat. Mater.* **2011**, *10*, 429-433.
39. Gospodinova, N.; Mokreva, P.; Terlemezyan, L. Influence of hydrolysis on the chemical polymerization of aniline. *Polymer*, **1994**, *35*, 3102-3106.

Chapter 7 Improving Thermoelectric Properties of Exfoliated Graphene Nanoplatelet Paper by Folding

7.1 Abstract:

A highly ordered, highly flexible paper-like structure consisting of individual exfoliated graphene nanoplatelets (GNP) was folded, turning a 2D paper into a 3D structure with improved thermoelectric properties. As a result of this nano-structuring of the graphene nanoplatelets through folding, an electrically connected, thermally disconnected structure was created due to the interconnected edges within the folded paper that allowed electrons to conduct freely while increasing phonon scattering. In addition, the folded sample can be made into a p-type thermoelectric material by coating the surfaces of the GNP paper with a thin layer of polyaniline by rapid mixture polymerization. Mechanical compaction on the folded sample was found to be essential because a net gain in power factor achieved outweighed the increase in thermal conductivity, leading to an overall improvement in ZT at room temperature.

7.2 Introduction:

Solid state heating/cooling using thermoelectrics are gaining ever increasing interest and are projected to be one of the promising technologies that could potentially revolutionize the way people produce energy [1]. As discussed previously, a thin film nanocomposite consisting of PANi polymerized on the surface of GNP not only reduced thermal conductivity of GNP paper, but also improved the Seebeck coefficient without significantly reducing the electrical conductivity. The research reported here describes the ability to nano-structure the GNP by three dimensional folding in order to decouple the electron and phonon transport. Electron-crystal

phonon-glass material systems such as skutterudites, clathrates, etc. have been extensively studied in the past for their promising thermoelectric properties [2-4]. Research has also identified inorganic materials having delicate nanostructures to scatter more phonons than electrons [5,6]. However, the high cost of raw material, complex material design, sensitivity of the desired nanostructure to processing conditions are major hurdles for commercial applications of these nanocomposites [7,8]. In addition, there are very few choices apart from bismuth telluride alloys when it comes to room temperature application [9,10]. The development of inexpensive, easy to produce alternatives for low grade heat conversion is a potential significant opportunity for clean, solar energy generation.

While various nano-structuring techniques have been demonstrated to successfully separate the electron and phonon transport in previous publications, this report tackles this challenge from a different perspective. In particular, simple folding of flexible GNP paper was performed that completely altered the way electron and phonon transport takes place in this paper. A GNP paper consisting of polyelectrolyte stabilized graphene nanoplatelets in water can be prepared by vacuum assisted self-assembly following the same procedures described elsewhere. When folded, electrons are still able to pass through the folded GNP paper due to the interconnected edges but phonon transport is significantly reduced due to the high anisotropy of the individual fold. On the other hand, the Seebeck coefficient, which is approximately $5\mu\text{V/K}$ for neat unfolded GNP paper can be greatly enhanced by synthesizing a thin layer of polyaniline by rapid mix polymerization [11] on the surface of GNP paper. The thermoelectric properties of the folded PANi/GNP are improved and the effect of consolidation on folded paper is discussed.

7.3 Experiments:

Preparation of GNP paper

GNP was produced as usual. The detailed procedures can be found in Chapter 4. In brief, PEI solution was prepared containing 0.1 wt% of the polyelectrolyte in DI water. 0.1 g GNP was dispersed in 100 ml PEI solution and bath sonicated for 30 min under constant stirring. The suspension was kept stirred for 24 h and filtered through a 0.2 μm Durapore PVDF filter paper to make the GNP paper.

Preparation of PANi coated GNP paper

GNP paper was prepared using the procedures described above. However, an extra thermal annealing was carried out at 340°C for 2h to "burn off" residual polyethyleneimine. Upon annealing, the paper was further compacted in the press with a pressure of 1000psi. A solution containing 0.6g aniline dissolved in 110 ml 1M HCl (0.05M) and another solution containing 1g ammonium persulfate (APS) dissolved in 20 ml 1M HCl were prepared. Two solutions were then mixed rapidly with magnetic stirring for 3 mins before the GNP paper was immersed. The reaction took place for 12 h at 0-5°C. The PANi coated GNP paper was then washed with DI water and isopropanol repeatedly and dried at 60°C for 24h. The schematic representation was shown in Figure 7-1:

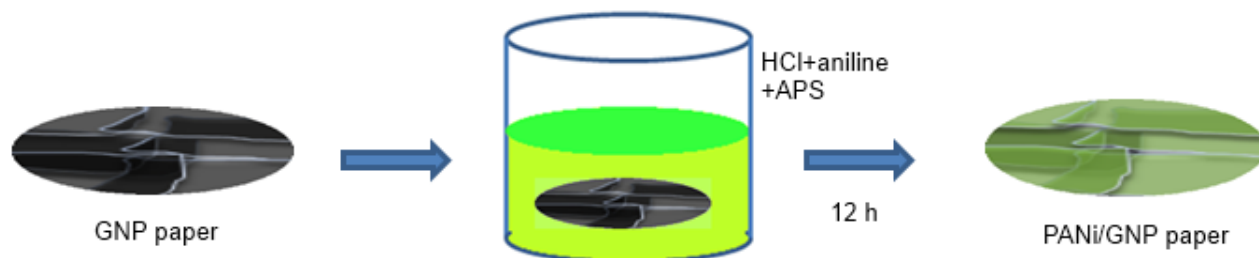


Figure 7-1: Schematic representation of experimental procedures to prepare PANi coated GNP paper by rapid mixture polymerization.

Folding by the mold, (pressed and unpressed)

Folding of the paper was carried on a custom made mold shown in Figure 7-2. In brief, a 5mm × 5mm acrylic rod of 6' was cut into bars of 3" in length, these bars were then arranged in the diamond fashion with one side fixed to a 12" long acrylic rod side rail, and the bottom fixed to an acrylic substrate. The GNP paper was laid on top of the mold, and individual folds were introduced to the paper with two additional rods pressed gently down on the cavity of the mold. Individual folded paper strips prepared from the mold was then arranged in another mold and compressed to make a sample of desired thickness. To prevent the sample from springing back, silicone caulk was applied at the open edges of folded sample (referred to as the unpressed sample). To further consolidate the folded paper, the sample was further compressed to 50% of its original length in a custom made mold (not shown here) and was referred to as the pressed sample. It is worth noting that ideally, the sample should consist of only one folded paper. Multiple strips were used here because a minimum sample length is required for attaching the thermocouples to the side of the folded paper. (note: thermocouples were attached to the connected edge of the folds instead of the open edges)

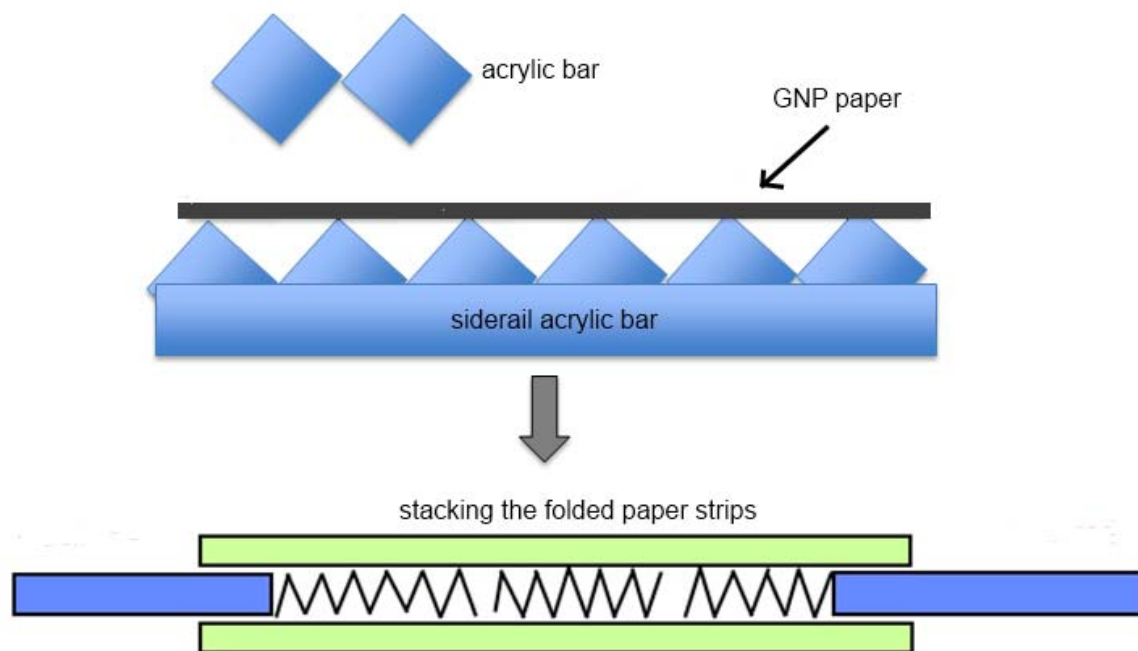


Figure 7-2: custom made mold for paper folding, and stacking of folded paper strips into desired thickness for subsequent measurements.

Thermoelectric property measurements (Seebeck coefficient and thermal conductivity)

Near room temperature (270K-320K) thermal conductivity, Seebeck coefficient measurements were conducted on the folded GNP sample (either pressed or unpressed) in a Janis model ST-100 cryostat cooled with flowing liquid nitrogen. A silver-filled epoxy was used to fix one end of the sample to a copper block, the other end to a 1000 Ω metal-film resistor, and two thin copper strips along the length of the sample. (See Figure 7-3) Two thermocouples made from copper and constantan wires were soldered directly to the copper strips. The Seebeck coefficient (S) and thermal conductivity (κ) were measured simultaneously by passing a current (7mA) through the metal film resistor (I_h), thereby generating a temperature gradient (ΔT) in the sample. (The experimental section in Chapter 6 has detailed calculations of the Seebeck coefficient and thermal conductivity.)

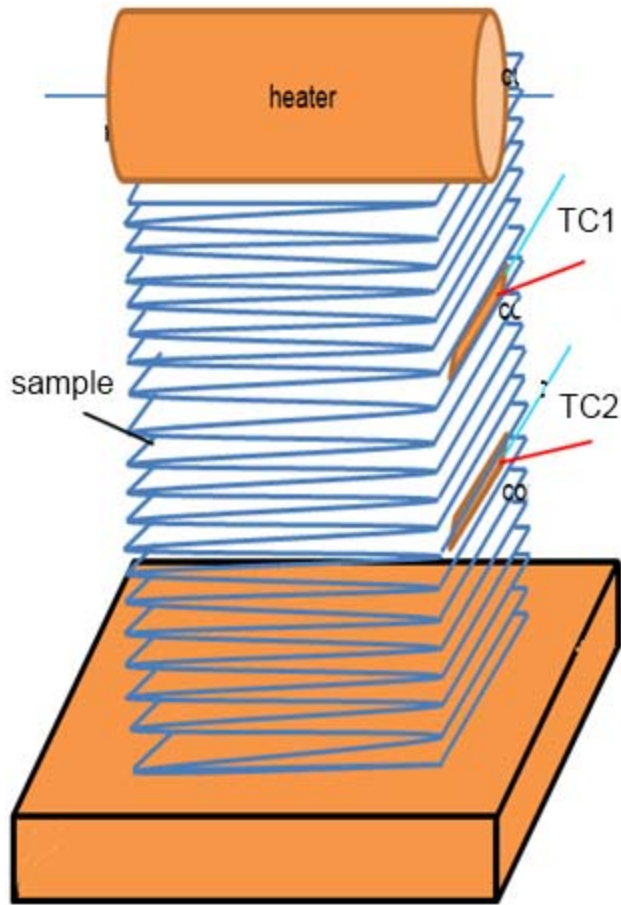


Figure 7-3: (a) schematic representation of experiment setup for Seebeck coefficient, thermal conductivity, electrical conductivity measurement for the folded sample. (b) a photo of the folded PANi/GNP paper mounted on the cryostat before measurement.

Electrical conductivity measurement

Electrical conductivity of the folded paper was measured by the standard 4-point method where two thin adhesive copper strips were attached to the "interconnected edge" as the voltage probes, while a current passed through the entire sample. The resistance was measured and the conductivity (σ) taking into account the geometric factor was obtained by equation (7.1):

$$\sigma = \frac{l}{R \cdot A} \quad \text{Equation (7.1)}$$

where l is the distance between voltage probes, R is the measured resistance, A is the cross sectional area of the folded paper.

Scanning electron microscopy:

A scanning electron microscope (Auriga, Carl Zeiss Microscopy) was used to image polyaniline nanofiber on the surface of GNP paper with an accelerating voltage of 2kV and a working distance around 2 mm.

TGA analysis:

A thermogravimetric analyzer (TA instruments Q500) was used. 10-15mg of PANi/GNP, neat GNP and neat polyaniline was loaded into a Pt pan. The sample was heated at 10°C/min at a resolution of 4°C/min to 700°C in air.

7.4 Results and discussions:

7.4.1 GNP paper folded

Micropores are introduced during the paper making process by vacuum filtration, which negatively affects the mechanical robustness of the paper. Therefore, it is essential to compress the paper first to get rid of the pores and create a highly aligned structure inside the paper. The enhanced alignment of the nanoplatelets results in a large improvement in its flexibility and "foldability". It was reported previously that the through-plane electrical conductivity of compressed GNP paper is very low (in the order of 10^{-2} S/cm) while the in-plane electrical conductivity exceeds 1000 S/cm because of high anisotropic conduction in the plane of the paper [12]. In the folded paper, electrons are now able to utilize the high in-plane conduction paths established by the interconnected edges rather than rely on the limited cross plane conduction. The ability of electrons to tunnel across conductive particles that are not in contact with each other offers another advantage. When the edges are partially damaged due to large folding stress, electrons can still travel between particles without being scattered. On the other hand, the through-plane thermal conductivity has been reported to be very low in comparison to the high in-plane value. In a nanostructured GNP paper, heat transport takes place through phonons (i.e. lattice vibration) and is primarily determined by the interfacial thermal conductance. In particular, the matching of phonon density of states, the type of interaction or bonding strength, and the geometrical overlapping area are the three major factors in interfacial heat conduction. It is expected that the strong bending at the folds significantly reduced the geometrical overlapping areas of GNP, leading to a reduced contribution from the high in-plane thermal conductivity due to strong phonon scattering. Figure 7-4 depicts the concept of the electrically connected,

thermally disconnected paper after folding. Figure 7-5 depicts the process of cutting the paper into strips and folding them on the custom-made mold.

Although the GNP paper did not fracture completely at the edge after experiencing severe deformation at the folds introduced during the folding process, SEM micrographs did identify some breakage and discontinuity at the fold areas for the folded paper as shown in Figure 7-6. However, it seems that the exterior (convex side) of the folded GNP was fractured while the interior (concave side) experienced much less damage due to the different tensile and compressive stresses incurred in the folding process. Despite partial damage at the outer layers of the edge, the "inner core" of the paper was still connected, contributing some mechanical integrity to the folded structure.

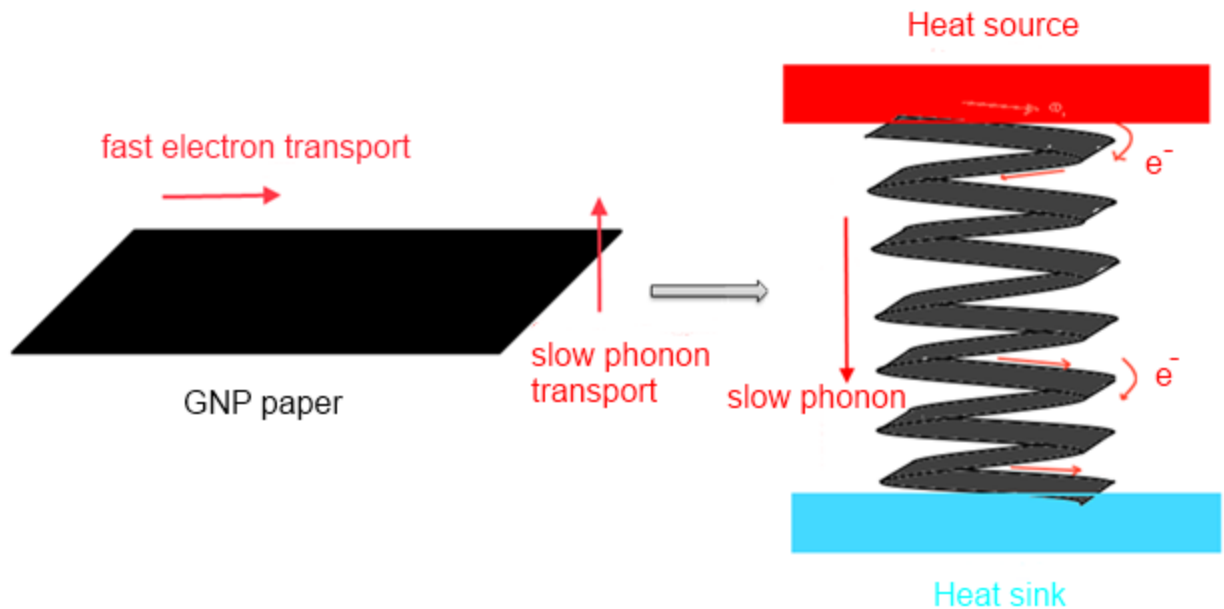


Figure 7-4: schematic representation of electron transport within the folded paper, the air gaps between individual fold is exaggerated.

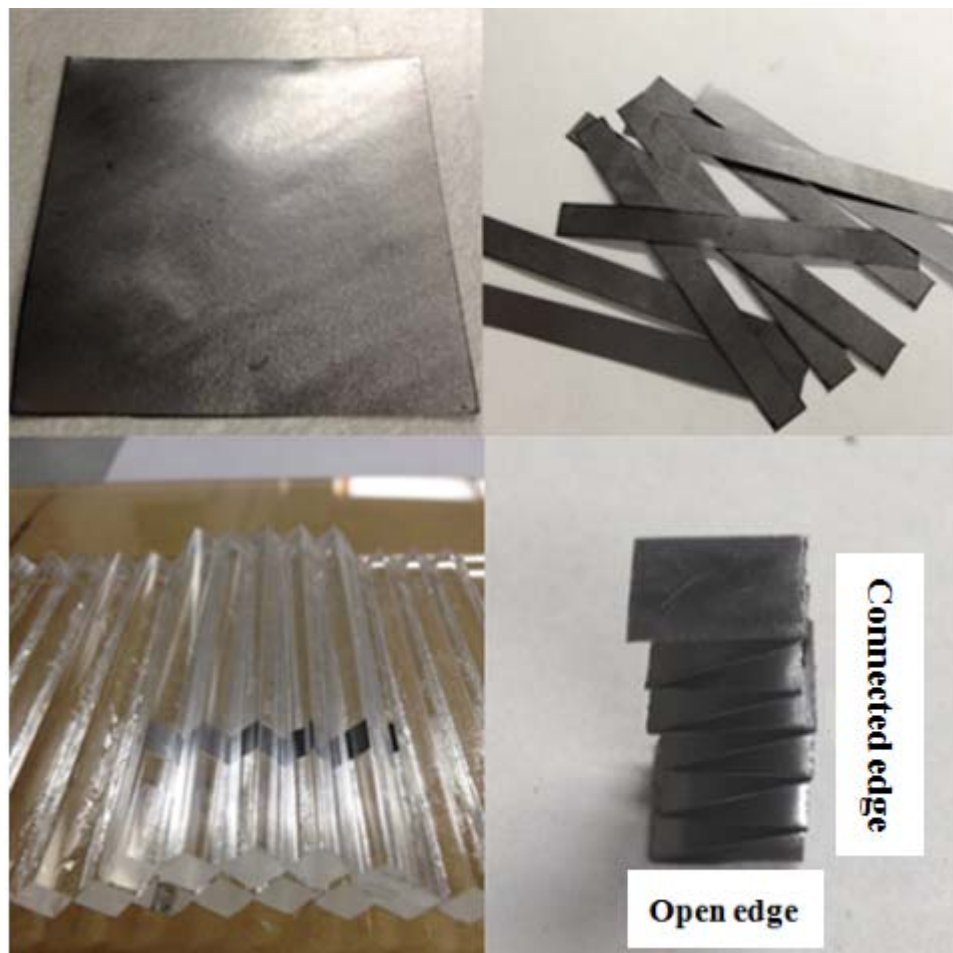


Figure 7-5: Photos of flat GNP paper, GNP paper cut to strips, folding the GNP strips on the custom-made acrylic mold, and the folded paper.(from top left to bottom right)

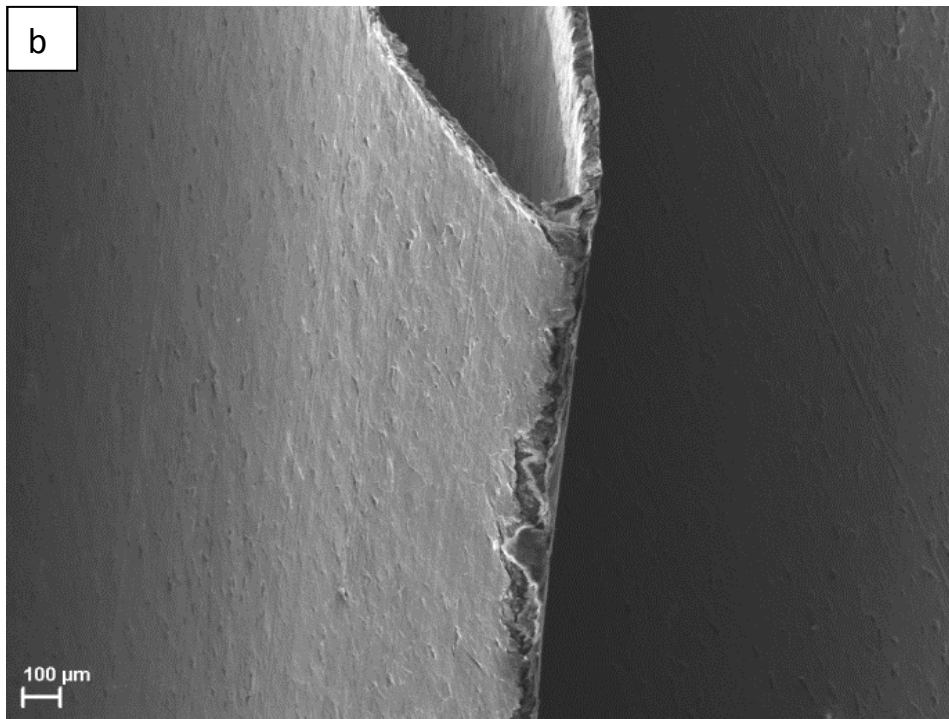
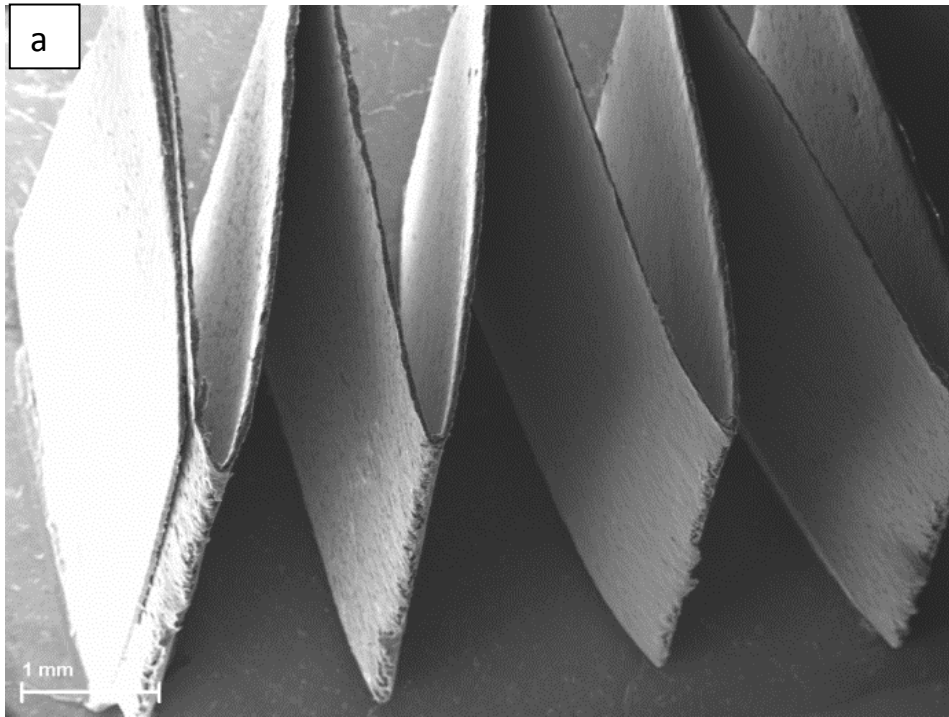
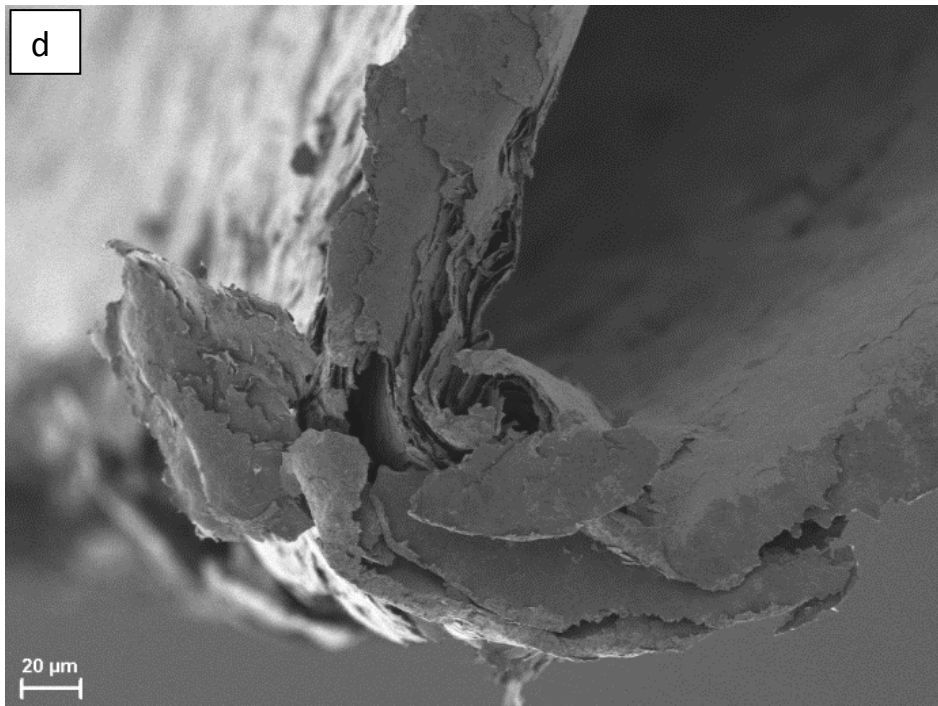
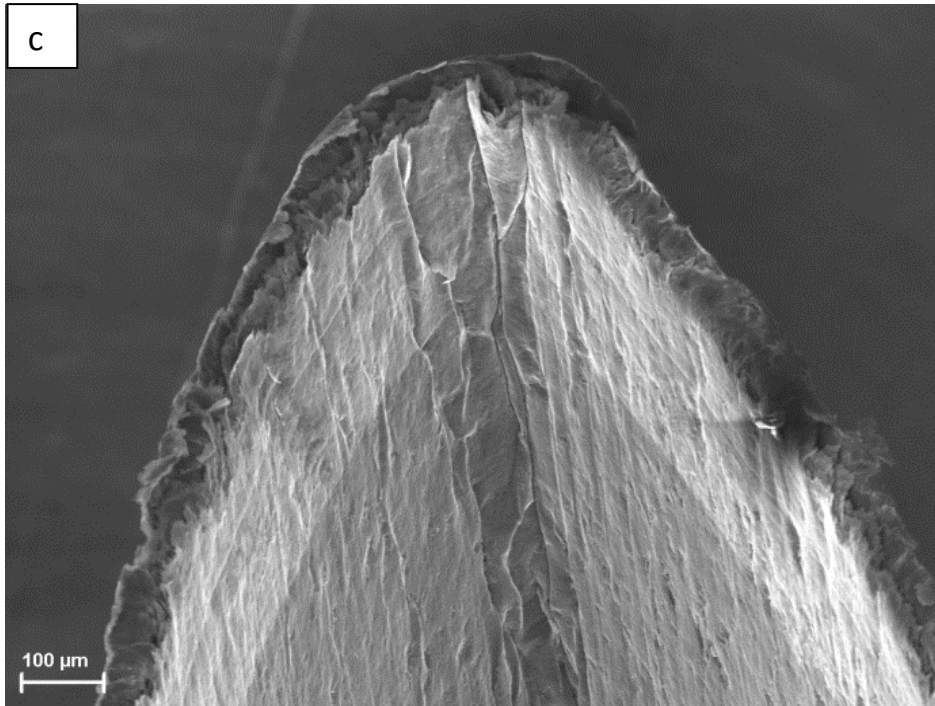


Figure 7-6: (a) SEM micrographs of a folded strip at low magnification (scale bar: 1mm), (b) the convex side of the folding edge (scale bar: 100μm), (c) the concave side of the folding edge (scale bar: 100 μm), (d) a magnified view of the tip of the folding edge (scale bar: 20 μm)

Figure 7-6(cont'd)



7.4.2 Electronic conduction of the folded paper

From the SEM micrographs shown above, folding did partially damage the structural integrity of the paper at the fold. Depending on the intrinsic "folding strength" of the GNP paper and its thickness, the damage can be controlled. However, the paper remained as an entire coherent piece without breaking apart at the fold no matter how much they were folded. The change in resistance of the folded GNP paper and the mechanical integrity was expected to change with the density of folds. The electrical resistance of a flat strip of paper, a slightly folded paper strip (Figure 7-7a) and a highly folded paper (Figure 7-7b) with either one fold or two folds between the probes were measured and tabulated in Table 7-1 and 7-2 below:

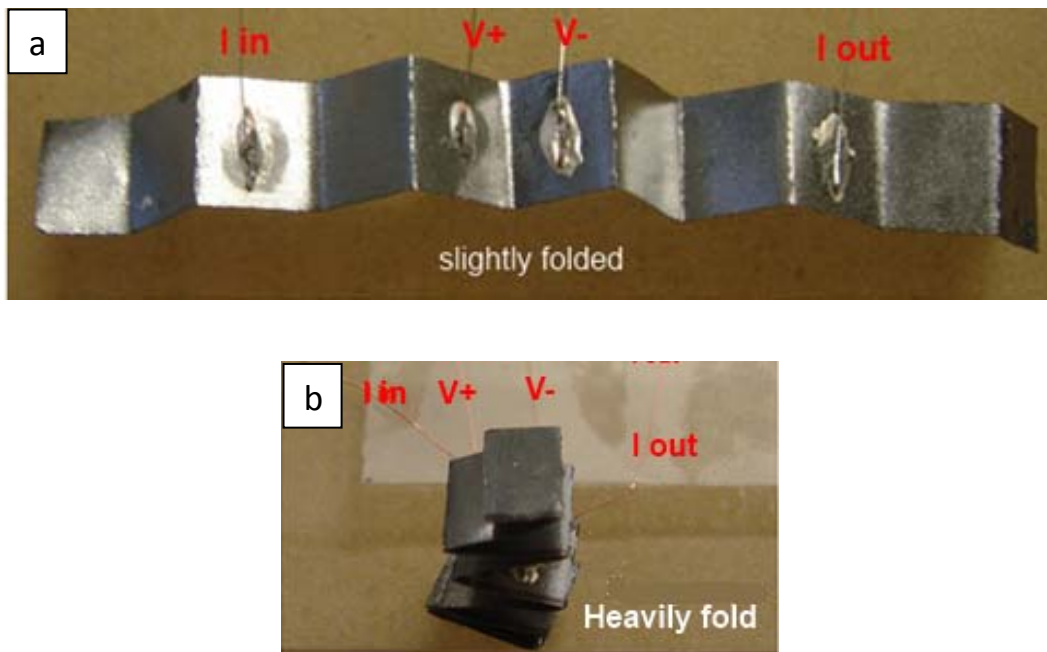


Figure 7-7: (a) Photos of four-point electrical resistance measurement on the slightly folded GNP paper and (b) a heavily folded GNP paper with one fold between the voltage probes.

Table 7-1: Electrical resistance measurement on the folded paper (1 fold between voltage probes)

Sample (1 fold)	Resistance (Ω)
Flat	0.27
Slightly folded	0.28
Heavily folded(pressed)	0.28

Table 7-2: Electrical resistance measurement on the folded paper (2 folds between voltage probes)

Sample (2 folds)	Resistance (Ω)
Flat	0.54
Slightly folded	0.56
Heavily folded(pressed)	0.4

The resistance basically remained the same value after folding. For the measurement conducted on the folded paper with 2 folds in between the voltage probes, the electrical resistance dropped when a pressure was applied on the heavily folded sample. It is possible that in this case electrons not only traveled along the plane of the paper, but also took advantage of the through-plane transport because adjacent folds were now in close contact with each other. Therefore, folding the paper with slight compression can improve the contact to maintain and even reduce the electrical resistance of the folded sample. It is therefore believed that partial breakage at the edge did not increase the resistance of the paper because the "core" of the paper is still connected, sufficient for electronic conduction.

7.4.3 Folded PANi/GNP paper as a p-type thermoelectric material

Thermoelectric properties of neat polyaniline as well as their carbon nanotube composites have been extensively documented in the literature [13,14]. Due to the structural similarity between PANi and GNP, PANi has also been successfully synthesized on individual GNP particles by π electron interaction. A hybrid PANi/GNP paper in which every single GNP particle was coated with a layer of PANi has been prepared by vacuum assisted self-assembly [Chapter 6]. However, the flexibility and foldability of such paper is reduced and breakage at the edge is more likely to occur as compared to the neat GNP paper, failing the purpose of creating a continuous pathway inside this folded structure. Rapid mix polymerization provided a solution to this problem by creating a thin layer of conductive polymer coating only on the surfaces of GNP paper while leaving the interior intact, preserving the foldability and introducing multifunctionality to GNP paper.

The PANi coated paper appeared dark purple in color after washing and drying (Figure 7-8a). The surface morphology of PANi grown on GNP paper were shown in Figure 7-8(b,c). A highly ordered and dense structure of PANi nanofibrils were observed, forming a homogeneous layer encapsulating the top and bottom surfaces of the GNP paper. It is worth noting that the inner core of the paper was still connected by individual GNP although the surface layer was disconnected under folding. (Figure 7-8d)

The amount of PANi synthesized on GNP was verified by TGA shown in Figure 7-9. A significant increase of the decomposition temperature of PANi was observed, possibly due to the strong interaction between PANi and GNP and a possible templating effect of GNP during the course of polymerization. It was found that a major weight loss began at about 350°C, indicating the onset of PANi decomposition until a second major weight loss occurred at around 600°C,

characteristic of oxidation of GNP itself. Therefore, the total weight of PANi in the composite was estimated to be about 10wt%.

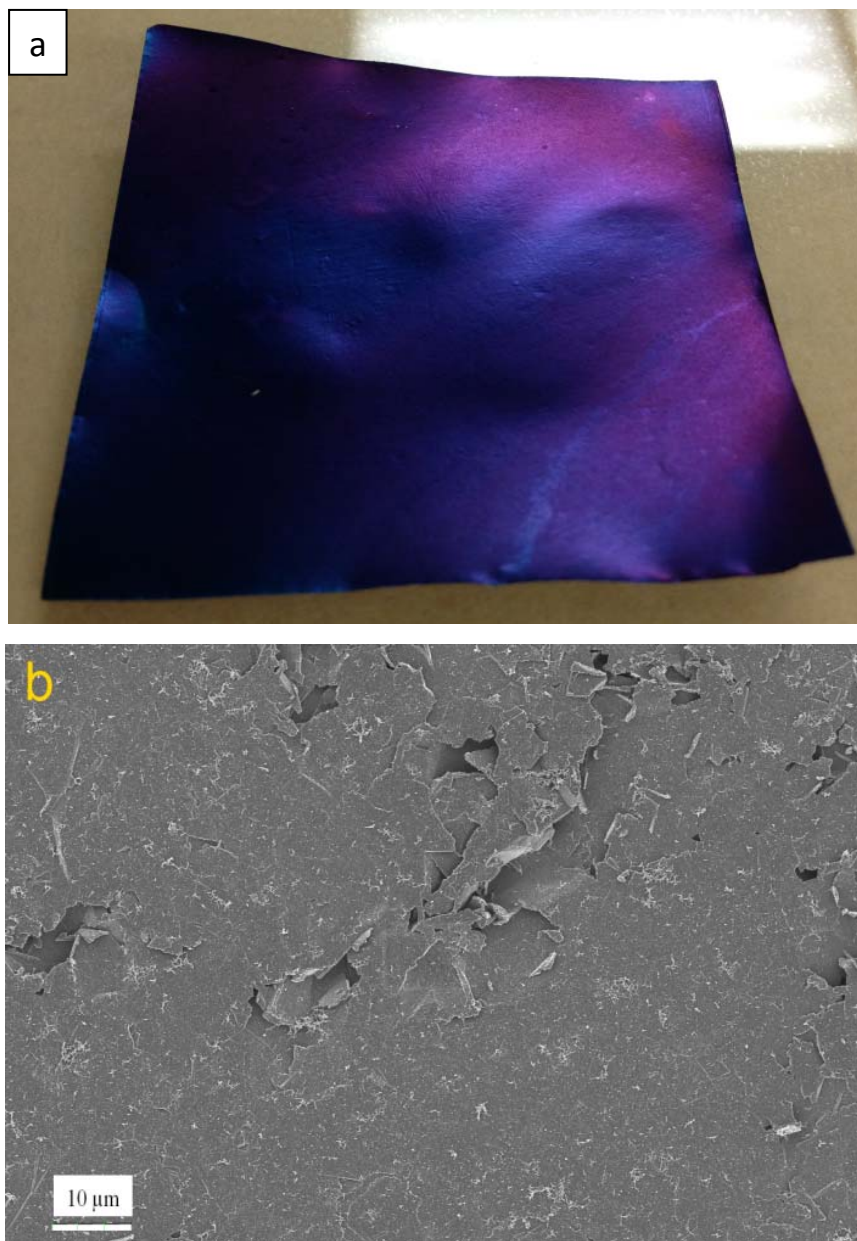
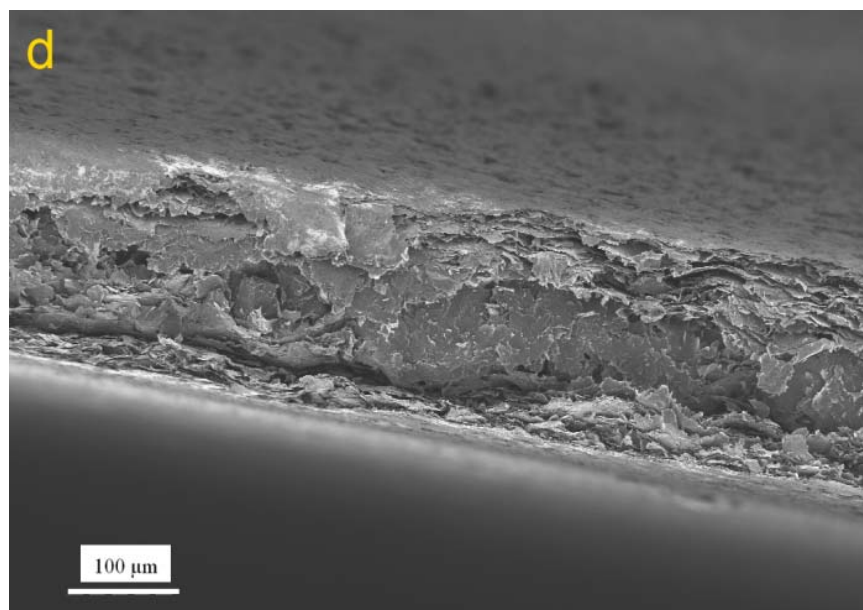
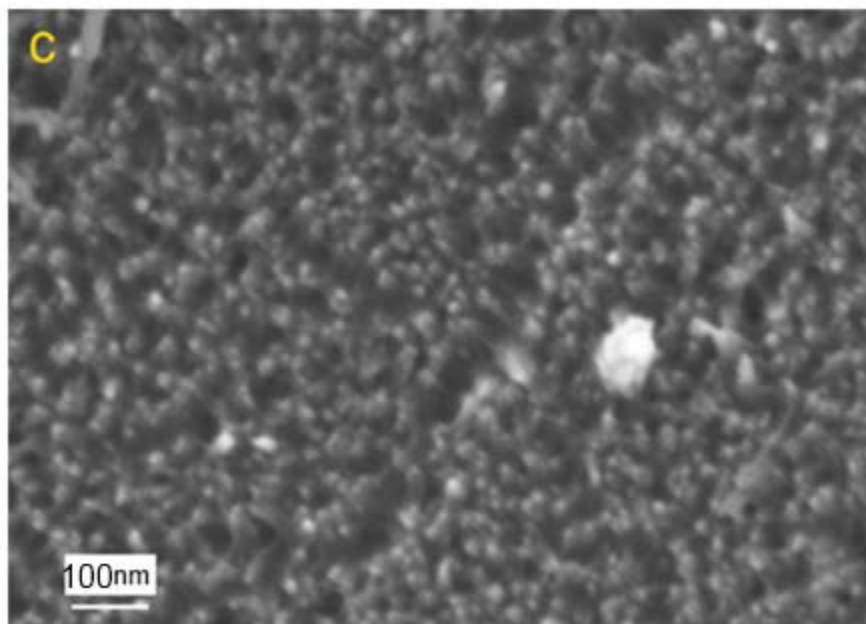


Figure 7-8: (a) Photo of the as-synthesized PANi/GNP paper (5 cm × 5 cm). (b) An overview of the surface morphology of PANi/GNP paper by SEM (scale bar: 10 μm). (c) SEM micrograph of PANi nanofibrils grown on the surface of GNP (scale bar: 100 nm). (d) folding edge of the PANi/GNP paper showing the interconnected "core" (scale bar: 100 μm).

Figure 7-8(cont'd)



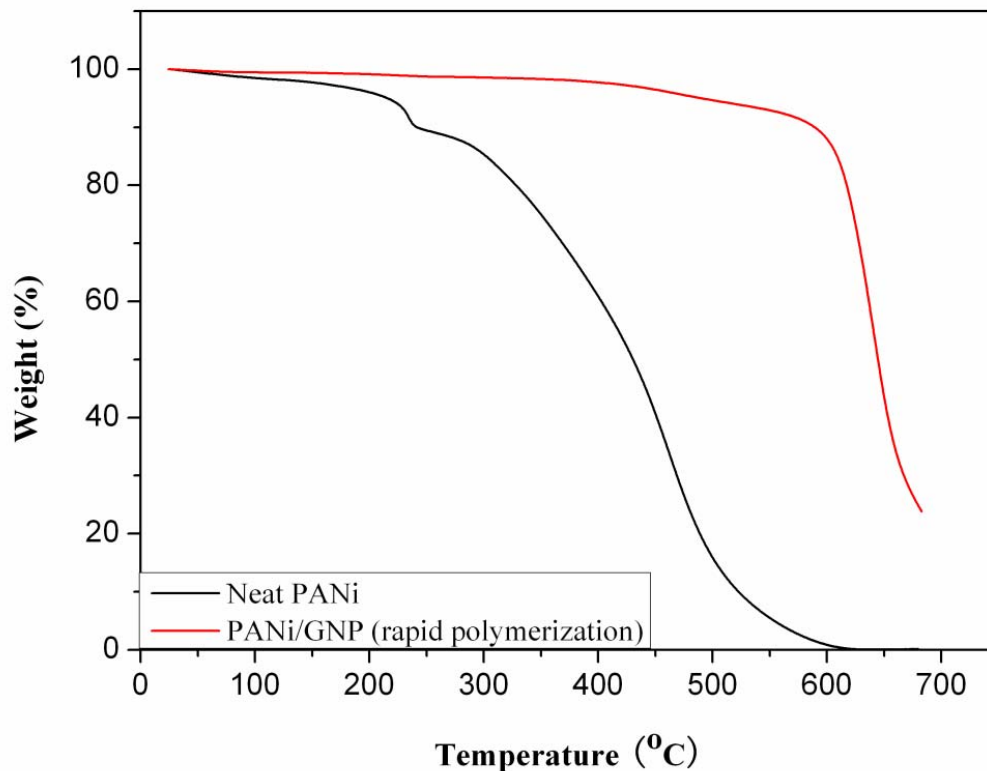


Figure 7-9: TGA analysis of the as synthesized PANi/GNP paper and the neat polyaniline in air.

The thermoelectric properties of both the pressed and un-pressed folded PANi/GNP papers were measured on the liquid nitrogen cooled cryostat platform. For the un-pressed sample, it is expected that gaps existed between the individual folds, leading to a possible "air-paper" composite. The existence of air gaps could be detrimental to the performance of the folded paper. Upon compaction in the press, the air gaps were effectively eliminated, creating solid contact between the individual folds. The presence of the nanofibril structure could be acting as "interlocking nanohooks" that helped achieve a more condensed structure. As a result, the Seebeck coefficient increased from $8\mu\text{V/K}$ to $21\mu\text{V/K}$ at room temperature despite the fact that the thermal conductivity went up from 0.09W/mK to 0.7W/mK due to increased density. The positive Seebeck coefficient also indicates holes are the dominant charge carriers in the sample,

in agreement with the fact that protons were incorporated into polymer during synthesis. As a result of the compaction, electrons could find more conduction paths inside the folded sample as the porosity was significantly reduced compared with the un-pressed sample. The conductivity shown in Table 7-3 also increased by almost an order of magnitude to 0.7 S/cm. While the absolute value of conductivity is still low due to the geometric design of the sample (i.e. a 5mm ×5mm cross section area, constrained by the side length of the acrylic rod in the mold), a model for estimating the conductivity of the folded paper as well as ways to enhance conductivity is discussed below.

Table 7-3: Electrical conductivity of the folded PANi/GNP paper with and without compaction

	Probe distance (mm)	Resistance (Ω)	Conductivity (S/cm)
Unpressed	2	17	0.04
Pressed	2	1.2	0.7

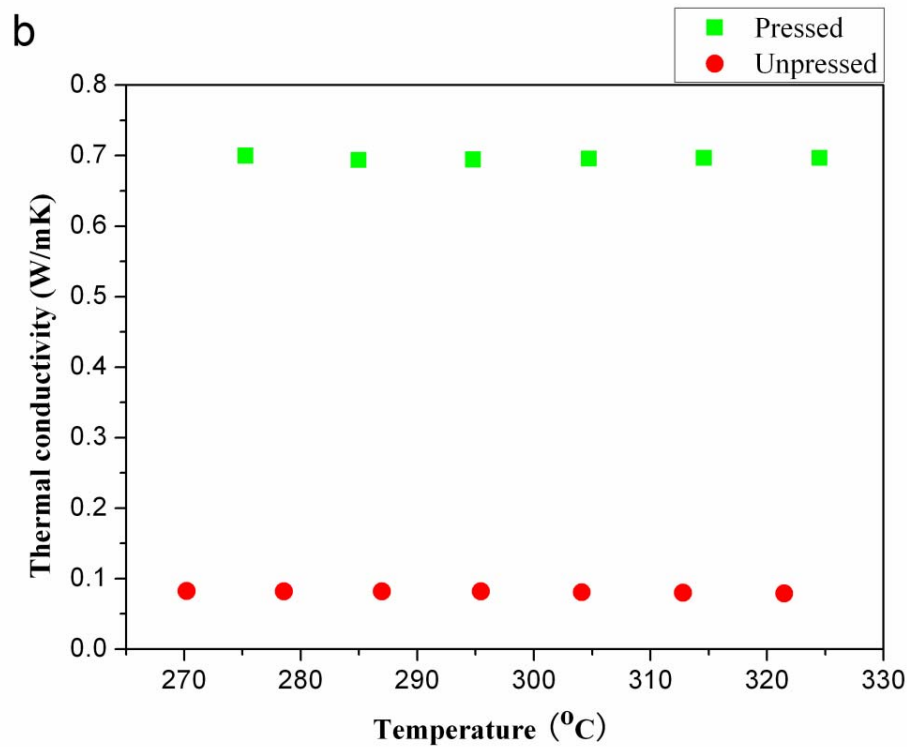
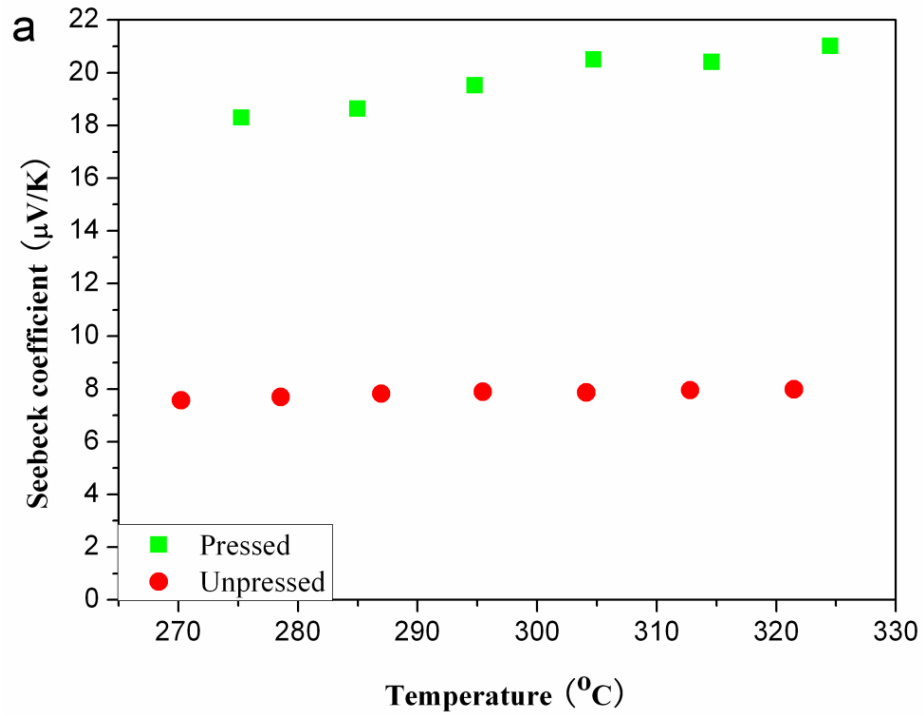


Figure 7-10: (a) Seebeck coefficient of the folded PANi/GNP paper (pressed vs. unpressed) from 270K to 320K (b) Thermal conductivity of the folded PANi/GNP paper (pressed vs. unpressed) from 270K to 320K.

The electrical conductivity of the folded GNP/PANi paper is directly related to how the paper was being folded. The folding width is dependent on the side length of the acrylic rod used to construct the mold for folding. A simple mathematical model was built to estimate the electrical conductivity of the folded paper. It is known from earlier discussion that the high curvature introduced in the folding process did not increase the resistance of the paper compared to when it was not folded. Take an individual folded strip as an example shown in Figure 7-11: the important parameters relevant to the calculation are the thickness of the unfolded paper (t), the number of folded segments (n), the folding period (f_p , dependent on the mold), as well as the width of the strip (w). The resistance of this folded strip (R) is assumed to be the same as the unfolded paper. A consolidated sample is obtained by compaction so that all the gaps inside the folded paper are eliminated. The length of the bulk sample (l) now becomes the thickness of the paper times the number of folding segments, with the cross sectional area to be 25mm^2 ($5\text{mm} \times 5\text{mm}$). The electrical conductivity of the folded paper (σ) can be obtained by the following equation given that the resistivity (ρ) of a flat GNP paper is known.

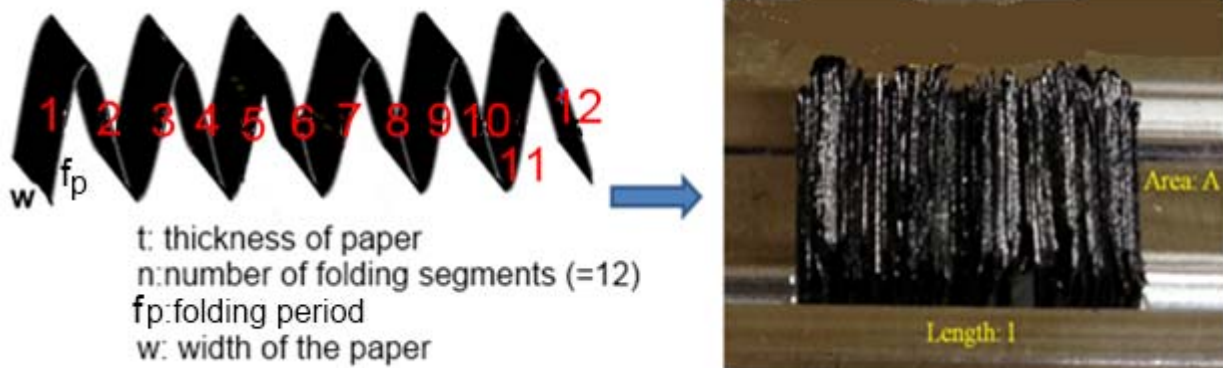


Figure 7-11: schematic representation of the folded paper for estimating the bulk electrical conductivity and mathematic derivation.

$$\sigma = \frac{l}{A \cdot R} = \frac{t \cdot n}{(w \cdot f_p) \cdot (\rho_{paper} \cdot \frac{n \cdot f_p}{w \cdot t})} = \left(\frac{t}{f_p}\right)^2 \cdot \frac{1}{\rho_{paper}}$$

From the above estimation, electrical conductivity of the folded paper is proportional to $(t/f_p)^2$, given that the thickness of the paper is around 50 μ m, folding period is 5mm, the resistivity of the unfolded paper is >1000S/cm, the estimated electrical conductivity of the folded paper is at least 0.1 S/cm, in good agreement with the measured value of about 0.7 S/cm. The reason why the measured value is higher is because the model described above does not take the cross-plane tunneling of electrons into account, thus leading to the lower limit of conductivity. In terms of thermoelectric figure of merit ZT at room temperature, the unfolded GNP paper has an estimated ZT around 3.7×10^{-6} while the folded GNP/PANi paper achieves a ZT of 1.3×10^{-5} .

To further improve electrical conductivity, one can increase the ratio between t and f_p by making a thicker paper (e.g. 100 μ m) and decrease the folding width to 1mm (which may require a custom made interlocking gears to make the folds instead of making it by hand), the projected electrical conductivity could be improved to 10 to 20 S/cm, which leads to a room temperature ZT in the range of 10^{-4} . Another advantage brought by folding is that the original thin film material is transformed back to the bulk material, which is conducive to establishing a temperature difference perpendicular to the surface of the thermoelectric module. For thin films, the maximum temperature difference attainable is limited by the thickness of the film, creating new challenges as to how to heat the film in the plane of the film because lateral temperature difference is not easily established. (e.g. think about the wrist watch example, the temperature difference between body heat and ambient is more easily achieved if heat gradient is established

perpendicular to the surface of the module, which requires a bulk configuration). Therefore, this approach by simple mechanical folding opens up plenty of opportunities for flexible GNP paper to be used for ambient temperature thermoelectric applications.

7.5 Conclusion:

An electrically connected, thermally disconnected structure was achieved by mechanically folding a highly ordered, highly flexible GNP paper. The high anisotropic features of the GNP paper allowed electrons to travel undisturbed in the folded paper, yet significantly discouraged the transport of phonons thanks to the highly curved but still interconnected folding edges that scattered most of the phonons. Polyaniline was successfully synthesized on the surface of GNP paper that resulted in a significant improvement in the Seebeck coefficient of the folded sample after sample compaction without compromising the "foldability" of the paper. This is the first article that discusses the potential of decoupling electron and phonon transport of a flexible thin film material by simple mechanical manipulation. In addition, this approach overcomes the difficulty of establishing a temperature difference across thin films by converting them to a highly ordered bulk material, making the folded structure compatible with current thermoelectric module design.

REFERENCES

References

1. Tritt, T. M. Thermoelectrics run hot and cold. *Science*, **1996**, *272*, 1276-1277.
2. Sales, B. C.; Mandrus, D.; Chakoumakos, B. C.; Keppens, V.; Thompson, J. R. Filled skutterudite antimonides: electron crystals and phonon glasses. *Phys. Rev. B*, **1997**, *56*, 15081-15089.
3. Nolas, G.S.; Morelli, D.T.; Tritt, T.M.; Skutterudites: A phonon-glass-electron crystal approach to advanced thermoelectric energy conversion applications. *Annu. Rev. Mater. Sci.* **1999**, *29*, 89-116.
4. Nolas, G.S.; Slack, G.A.; Schujman, S. B. Semiconductor clathrates: a phonon glass electron crystal material with potential for thermoelectric applications. *Semiconduct Semimet.* **2001**, *69*, 255-300.
5. Zebarjadi, M.; Esfarjani, K.; Shakouri, A.; Bahk, J. H.; Bian, Z.; Zeng, J et al. A. Effect of nanoparticle scattering on thermoelectric power factor. *Appl. Phys. Lett.* **2009**, *94*, 202105(1-3).
6. Kim, W.; Zide, J.; Gossard, A.; Klenov, S.; Stemmer, A.; Shakouri, A et al. Thermal conductivity reduction and thermoelectric figure of merit increase by embedding nanoparticles in crystalline semiconductors. *Phys. Rev. Lett.* **2006**, *96*, 045901(1-4)
7. Snyder, G. J and Toberer. E. S. Complex thermoelectric materials. *Nat. Mater.* **2008**, *7*, 105-114.
8. Minnich, A. J.; Dresselhaus, M.S.; Ren, Z. F.; Chen, G. Bulk nanostructured thermoelectric materials: current research and future prospects. *Energy Environ. Sci.* **2009**, *2*, 466-479.
9. Yamashita, O.; Tomiyoshi, S.; Makita, K. Bismuth telluride compounds with high thermoelectric figures of merit. *J. Appl. Phys.* **2003**, *93*, 368 (1-7).
10. Poudel, B.; Hao, Q.; Ma, Y.; Lan, A.; Minnich, B.; Yu, X et al. High-thermoelectric performance of nanostructured bismuth antimony telluride bulk alloys. *Science*. **2008**, *320*, 634-638
11. Yan, X.; Chen, J.; Yang, J.; Xue, Q.; Miele, P. Fabrication of free-standing, electrochemically active, and biocompatible graphene oxide-polyaniline and graphene-polyaniline hybrid papers. *ACS Appl. Mater. Interfaces*, **2010**, *2*, 2521-2529.
12. Xiang, J.; Drzal, L. T. Electron and phonon transport in Au nanoparticle decorated graphene nanoplatelet nanostructured paper. *ACS Appl. Mater. Interfaces*, **2011**, *3*, 1325-1332.
13. Li, J.; Tang, X.; Li, H.; Yan, Y.; Zhang, Q. Synthesis and thermoelectric properties of hydrochloric acid-doped polyaniline. *Synth. Met.* **2010**, *160*, 1153-1158.

14. Sun, Y.; Wei, Z.; Xu, W.; Zhu, D. A three-in-one improvement in thermoelectric properties of polyaniline brought by nanostructures. *Synth. Met.* **2010**, *160*, 2371-2376.

Chapter 8 Summary and Recommended Studies

8.1 Summary:

Graphene nanoplatelets (GNP) produced from thermal expansion of graphite intercalated compounds with microwave assisted heating have excellent electrical, thermal and mechanical properties as a result of the preserved conjugation in the basal plane of graphene. To investigate how these unique physical properties can be transferred to a polymer matrix, these GNP particles were incorporated into paraffin wax and the resulting electrical and thermal conductivity of the nanocomposites prepared by casting were measured. It is found that nanocomposites with GNP of larger aspect ratio achieved electronic percolation at a lower loading. Interestingly, the thermal conductivity at the percolation threshold of the nanocomposites remained almost the same although the conductive network has already been established inside the composite. This distinction in the properties of the composites is attributed to the different conduction mechanisms of electrons and phonons across the polymer/GNP interfaces. For electronic conduction, direct physical contacts between conductive particles is not necessary because of the ability of electrons to tunnel across a non-conductive barrier of a finite thickness independent of the intrinsic resistivity of the film. On the other hand, heat is conducted by phonons of different vibration frequencies. The efficiency of heat transport in composites is largely dependent on the properties of the matrix-filler interfaces. In the GNP/polymer case, a large thermal interface resistance is likely to offset the contribution from the highly conductive GNP particles, thus leading to a marginal or even a decrease in the thermal conductivity especially at a filler loading close or slightly above the percolation threshold of the nanocomposites. However, the significant

increase of electrical to thermal conductivity ratio (σ/κ) at percolation threshold provides insight to developing GNP/polymer based nanocomposites for thermoelectric energy conversion.

From SEM micrographs, it is found that the GNP particles in the composite prepared by casting assumed random orientation with some particle folding, wrinkling, fracture incurred during sample processing. To avoid this, a GNP scaffold was pre-established by dispersing individual GNP particles in a polyelectrolyte/water solution followed by vacuum assisted self-assembly, forming a highly ordered, highly condensed paper structure with excellent flexibility as well as mechanical robustness. As a result, the electrical conductivity of this GNP paper is significantly improved from 150 S/cm to 880 S/cm after annealing and compaction due to a combined reduction of tunneling and contact resistances as a result of the decomposition of the polyelectrolyte, increased contact area between GNP particles and a better alignment of the particles. Thermal conductivity also increased significantly to as high as 200W/mK after annealing and compaction because of a reduction in interfacial thermal resistance.

In order to take advantage of the high electrical conductivity of the paper for thermoelectric application, thermal conductivity needs to be reduced. One approach to modify and separate the electronic and phononic conduction in the GNP paper was achieved by depositing metal nanoparticles on the surfaces of GNP to act as spacers that prevented immediate physical contact between adjacent GNP particles. After annealing and compaction, the electrical conductivity of GNP/Au hybrid paper increased by 80% from 880 S/cm to 1500 S/cm while the thermal conductivity reduced by almost 10%. Metal nanoparticles created more tunneling channels for electrons inside the hybrid paper while the phonons are unable to tunnel across but scattered due to the difference in phonon spectra in metals and carbon. In addition, the weak van der Waals interaction between metals and GNP also scattered phonons without disrupting

electron flow. The separation of carriers in Au nanoparticle decorated GNP paper further illustrates the fundamental difference in electronic and phononic conduction that can be taken advantage of in optimizing nanocomposites based on GNP for thermoelectric energy conversion.

Built on this understanding on separation of electron and phonon transport, a conductive polymer polyaniline was used to replace the metal nanoparticles in an effort to further reduce thermal conductivity of the nanocomposites. Polyaniline was successfully synthesized on the surface of GNP forming a homogenous coating layer. Depending on the initial concentration of monomer prior to polymerization, the amount of PANi synthesized on GNP can be readily controlled with a highest composition of 40wt% PANi in the composite prepared at 50mM of aniline starting concentration. SEM micrographs indicated a highly ordered, highly condensed PANI nanofibrils growing from the surface of GNP. In contrast, PANi synthesized in the absence of GNP has a random granular structure very distinctive from PANi/GNP nanocomposite. The difference in morphology also suggests that GNP served as a template during PANi polymerization and contributed to a more ordered and aligned growth of molecular chains on the surface of GNP rather than a random coil-like conformation without GNP. The encapsulation effect of PANi on GNP successfully reduced the thermal conductivity of the nanocomposite film prepared by vacuum filtration from more than 70W/mK to around 13W/mK with 40wt% PANi in the composites. The ratio of electrical and thermal conductivity (σ/κ) increased from 2.85 for neat as made GNP paper to 4.6 for (40wt%PANI)/GNP nanocomposite.

From XPS, the protonation ratio of PANi on GNP can be readily estimated $[Cl^-]/[N]$ which is around 0.2 for the as-made nanocomposites. The as-made samples can be further doped to a higher protonation ratio by a facile dilute protonic acid treatment (e.g. 0.1M HCl solution for 2h). The electrical conductivity of the re-protonated sample increased from 60S/cm to 174S/cm

while the thermal conductivity, which relies much less on the incorporation or ejection of hydrogen proton, remained almost the same at around 15W/mK. This offers another interesting route to further separate the electrical and thermal conductivity, effectively increasing the σ/κ ratio from 4.6 for the as-made samples to 11.6 for the re-protonated samples.

The Seebeck coefficient (S), also benefited greatly by incorporation of PANi into the GNP paper. In particular, the as-made 40wt%PANi/GNP has a Seebeck coefficient around 33 μ V/K at room temperature while it is only 5 μ V/K and 7 μ V/K for the neat GNP paper and neat PANi. Since the Seebeck coefficient S is dependent on the mobility of the charge carriers, in the case of conductive polymers such as polyaniline, inter-chain and intra-chain hopping have a strong impact on carrier mobility. A highly oriented polymer chain can reduce the barriers of inter-chain and intra-chain hopping and allow the carriers to move easily because of the high conjugation in PANi/GNP. The templating effect of GNP is analogous to a chemical stretching applied to the chains of the conductive polymer, enhancing the carrier mobility. Compared with a mechanical stretching reported previously to enhance Seebeck coefficient [1], the chemical stretching could be more effective because it is in situ: every single chain is "stretched" if polymerization occurs in close vicinity of the template (i.e. GNP particle). One thing to note that in spite of the increased electrical conductivity achieved by re-protonation, the Seebeck coefficient dropped to around 20 μ V/K at room temperature for the highly protonated samples. One possible explanation is that re-protonation results in a shift of the Fermi level in the conductive polymer to regions with different curvature in the density of states function, which still needs to be verified in later studies.

This research has demonstrated with evidence that proper nano-structuring work wonders. The ability to separate the electron and phonon transport in GNP paper by engineering particle

interfaces significantly altered the properties of neat GNP. In the case of PANi decorated GNP, neither neat GNP nor neat polyaniline is considered as good thermoelectric materials possibly because of their certain undesired physical properties and a possible bi-carrier transport nature. Nevertheless, PANi/GNP nanocomposite possess much enhanced thermoelectric properties with a room temperature ZT of 1.5×10^{-4} almost 2 orders of magnitude higher than either of its constituents. These inexpensive graphene nanoplatelets and the ability to control their properties by nano-engineering will certainly open up numerous opportunities for graphene based nanocomposites for novel energy generation and conversion application.

8.2 Recommended future works:

8.2.1 Solvent processing of PANi/GNP:

Another possible way to prepare PANi/GNP nanocomposites is by solvent processing and film casting. Instead of synthesizing PANi by in-situ polymerization in the presence of GNP, neat PANi emeraldine salt can be prepared first. PANi can be dissolved in a proper solvent followed by addition of GNP, film casting and removal of solvent by evaporation. However, it is worth noting that the emeraldine salt (ES) form of polyaniline cannot readily dissolve in most of the solvents while the emeraldine base (EB) form of polyaniline has been found to dissolve well in solvents such as N-methyl pyrrolidinone (NMP), m-cresol, etc. Therefore, it is necessary to convert ES PANi to EB PANi first by suspending the as-made PANi in dilute base (e.g. 0.1M NH_4OH) for several hours to deprotonate. At the same time, NMP would be a nice solvent for GNP too because a recent paper by Hernandez et al. reported successful liquid phase exfoliation of graphite in NMP to produce thin layers of graphene because of the comparable surface energy between the solvent and graphene [2].

It is expected that PANi dissolved in NMP maintains a more extended and relaxed molecular conformation as compared to neat PANi powder whose molecular chains are more coil-like. The extended chains will still interact with the surface of GNP as a result of π electron stacking forming a coating layer on the surface. A film of PANi coated GNP can be prepared by film casting, vacuum assisted self-assembly, or doctor blading.

The as-made EB PANi/GNP film after elimination of solvent can be further protonated by simply dipping the self-standing film in a solution of protonic acids such as HCl, H₂SO₄, acetic acid, and etc. Depending on the concentration and dipping time, different protonations can be achieved. It would be interesting to compare the thermoelectric properties (electrical, thermal conductivity, Seebeck coefficient) with the samples made by in-situ polymerization reported in the previous chapters.

8.2.2 Carrier transport analysis for PANi/GNP:

Previous study showed PANi synthesized in the absence of GNP has granular morphology as opposed to a more ordered structure if synthesized in the presence of GNP particles. The enhanced alignment of polymer chains is likely to reduce the inter-chain and intra-chain carrier hopping barrier, leading to an increased carrier mobility that contributed to a higher Seebeck coefficient. A possible way to prove that there is indeed an increase in the carrier mobility is to perform a Hall measurement. This can be done in the Quantum design Versalab system (module and the schematics shown in Figure 8-1)

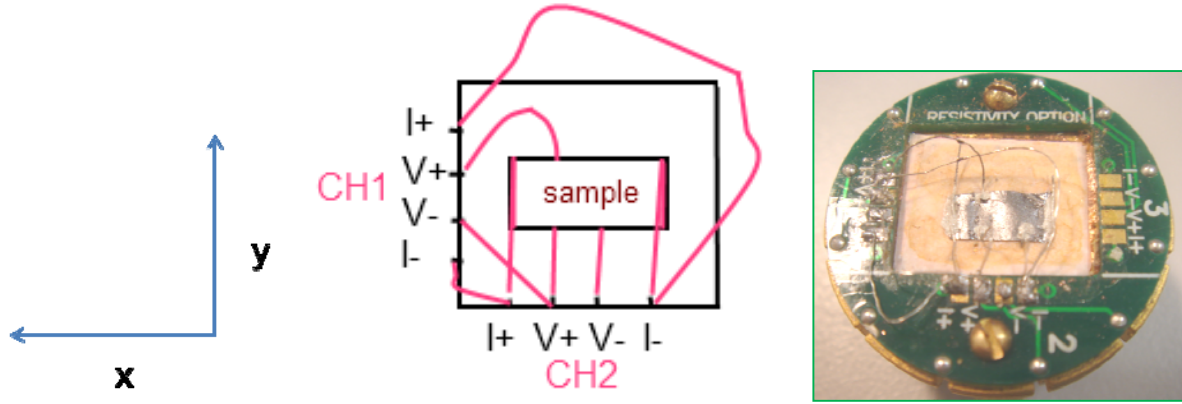


Figure 8-1: Schematics and actual photo of the quantum design versalab module and wiring, CH1 measures the Hall voltage, CH2 measures the in-plane resistivity of the sample. z direction: coming out of the paper.

By measuring the Hall voltage, it is possible to determine the carrier transport properties and estimate the carrier mobility from a known carrier concentration. The carrier concentration can be calculated from Hall coefficient R_H assuming the samples studied are considered heavily doped semiconductors and only one type of charge carriers (either electrons or holes) are present in the system. R_H and the carrier concentration n is expressed as:

$$R_H = \frac{E_y}{j_x B_z} = \frac{V_y t}{I_x B_z} = \frac{R_{xy} t}{B_z} = -\frac{1}{ne} \quad (8.1)$$

where E_y is the induced electric field in the y direction, j_x is the current density in the x direction, B_z is the magnetic field perpendicular to the sample (coming out of the paper), V_y is the Hall voltage, I_x is the current in the x direction, R_{xy} is the Hall resistance, t is the sample thickness and e is the unit charge. Therefore the slope of Hall resistivity ($R_{xy} \cdot t$) versus B_z is the Hall coefficient. However, preliminary results on the PANi/GNP samples suggest a non linear relationship between Hall resistivity and magnetic field, which provides evidence that the nanocomposite sample is still a bi-carrier system with both electrons and holes contributing to the Seebeck

coefficient. In order to calculate the carrier concentration and mobility of both electrons and holes, a more complicated bi-carrier transport model must be used to fit the experimental results [3]. It would be necessary to compare the transport properties of neat PANi with PANi/GNP samples combined with a bi-carrier model analysis before any solid conclusion can be drawn.

REFERENCES

References

1. Yan, H.; Ohta, T.; Toshima, N. Stretched polyaniline films doped by (\pm) 10-camphorsulfonic acid: anisotropy and improvement of thermoelectric properties. *Macromol. Mater. Eng.* **2001**, *286*, 139-142.
2. Hernandez, Y.; Nicolosi, V.; Lotya, M.; Blighe, F. M.; Sun, Z.; De, S et al. High-yield production of graphene by liquid phase exfoliation of graphite. *Nat. Nanotechnol.* **2008**, *3*, 563-568.
3. Morelli, D. T.; Canfield, P. C.; Drymiotis, P. Low-temperature transport properties of NdBiPt. *Phys. Rev. B.* **1996**, *53*, 12896-12901.